DISS. ETH NO. 28098

The imprint of the Amazon River on the marine carbon and nutrient cycles

A thesis submitted to attain the degree of
DOCTOR OF SCIENCES of ETH ZURICH
(Dr. sc. ETH Zurich)

presented by

DOMITILLE LOUCHARD

M.Sc. Oceonagraphy, Aix-Marseille University
born on May 28th, 1985
citizen of France

accepted on the recommendation of

Prof. Dr. Nicolas Gruber, examiner
Dr. Matthias Münnich, co-examiner
Prof. Dr. Timothy Egliton, co-examiner

2021

Summary

From the upstream lands to the open ocean, water acts as a driving force creating a land-to-ocean aquatic continuum that connects the terrestrial and marine worlds. As water travels through soils, aquifers, lakes, wetlands, and rivers, essential biogeochemical elements are transported, exchanged, transformed and eventually delivered to the ocean. This terrestrial input from rivers constitutes an important supply of carbon and nutrients, in particular nitrogen, phosphorus and silicon, to the ocean where they form the basis of all marine food webs. Meandering from estuaries to the open ocean, river plumes form a dynamic interface that leaves a complex imprint on marine biogeochemistry and phytoplankton dynamics. Although riverine inputs have been hypothesized to impact the marine biogeochemical cycles at the regional to global scale, the exact quantification of such an impact remains unresolved. Field measurements struggle to capture the average conditions of the highly variable plume environments, and coarse resolution models fail to reproduce critical processes driving the physical dispersal of the plume and lack the ecological complexity to account for the wide range of impacts on the marine food web.

In this thesis, I used a high-resolution regional model (ROMS) coupled to a biogeochemical/ecological model that explicitly considers four phytoplankton functional types (PFTs), i.e., small phytoplankton, free-living diatoms, Trichodesmium (free-living diazotroph) and a symbiotic assemblage of diatom-diazotrophs (DDAs). I applied this modeling framework to the Atlantic Ocean to assess the impact of the Amazon River on the cycling of carbon and nutrients in the Western Tropical Atlantic (WTA). To investigate the distinct and cumulative impact of the different riverine inputs, I first ran a set of nine factorial simulations where one or several elements are excluded from the Amazon inflow. Over the whole study region, the Amazon River spawns a substantial increase of the Net Primary Production (NPP), +115 Tg C yr^{-1}, that actually surpasses the potential increase based on riverine inorganic nitrogen or phosphorus. This amplification is supported in a major way by the enhancement of N_2 fixation i.e., the utilization of gaseous atmospheric dinitrogen (N_2) by diazotrophs. This increase in N_2 fixation is mostly driven by the large blooms of DDAs that benefit from the supply of riverine Dissolved Organic Phosphorus (DOP). The vertical export of carbon is also enhanced but proportionally, its increase exceeds the increase of NPP, indicative of a stronger biological pump. This change in the strength of the biological pump stems from a shift in the phytoplankton community towards the dominance of diatoms whose growth is fueled by riverine $Si(OH)_4$. The combined effect of the increase in NPP and the strengthening of the biological pump contributes the most to the changes in the air-sea CO_2 balance, inducing an uptake of atmospheric CO_2 in the shelf and plume waters and a reduc-

tion of the outgassing in the rest of the WTA. The delivery of riverine dissolved inorganic carbon and alkalinity reinforces this effect of the biological pump while the progressive remineralization of terrestrial dissolved organic carbon acts as a counteracting force. This first part of my thesis provides the first comprehensive quantification of the imprint of the world largest river on marine biogeochemistry and thereby demonstrates that these impacts are numerous, intertwined and non-linear.

In the second part of my thesis, I investigate the factors controlling the intense N_2 fixation that has proven to be so crucial in the previously assessed balance of the system. In agreement with observations, the model reproduces, the largest rates of N_2 fixation in the offshore plume waters that are mainly supported by DDAs. The analysis of the factorial simulations show that the Amazon River amplifies N_2 fixation by 74% (+ 3.8 Tg N yr^{-1}) and that this increase is highly reliant on the delivery of riverine phosphorus and $Si(OH)_4$. This supply of nutrients modifies the phytoplankton competition in favor of DDAs, with contrasting dynamics in different portions of the plume pathway. In the upstream pathway (0-1300 km), the competitive growth advantage of DDAs is associated with their capacity to fix N_2 when the non-diazotrophs quickly exhaust the inorganic nitrogen pool and are N-limited. In the rest of the plume pathway (1300-3500 km), phosphorus becomes the most limiting nutrient for all PFTs, and DDAs benefit from their ability to directly use DOP in PO4-starved conditions. However, my results demonstrate that bottom-up controls, while important, are not sufficient to explain the spatial patterns of N_2 fixation. Indeed, DDAs do not bloom in the upstream plume pathway, as their growth advantage is almost entirely suppressed by a strong grazing disadvantage, i.e., the grazing pressure experienced by DDAs is significantly higher than the one experienced by other PFTs. The relative strength of this top-down control weakens in the rest of the plume pathway, allowing DDAs to thrive in the offshore plume waters. These results highlight the combined importance of bottom-up and top-down controls in shaping the intensity and patterns of N_2 fixation and demonstrate the necessity to investigate both aspects in future observational and modeling research effort.

In response to anomalies in precipitation over the Amazon basin, driven in part by the El Niño-Southern Oscillation (ENSO), the river discharge varies on interannual timescales. The analysis of different hindcast simulations reproducing conditions from 1983 to 2019 in the third part of my thesis reveals that the variability of the Amazon discharge can modify the N_2 fixation rates by up to 15 % in the offshore plume waters. Additionally, N_2 fixation rates are altered by the variability of physical processes i.e., the deepening or shoaling of the mixed layer depth (MLD) and the strength of the equatorial upwelling, induced by the fluctuations of the Atlantic Meridional Mode and ENSO. While the discharge variability influences N_2 fixation in the northwestern part of the WTA, these two climate modes have the strongest impact on the southeastern region. Both the discharge and climate-related variability affect N_2 fixation through the availability of phosphorus. Anomalously high discharge provides more DOP and reinforces the excess P to N in the plume waters, conditions that further enhance N_2 fixation. In contrast, a deepening of the MLD and a strengthening of the upwelling brings waters with low DOP concentration and a N:P ratio close to 16:1, which mostly favor non-diazotrophs at the expense of DDAs and Trichodesmium. This study represents the first assessment of the factors controlling the variability of N_2 fixation in the WTA and demonstrates the crucial role of phosphorus and especially its absolute concentration, its composition i.e, organic versus inorganic, and its relative abundance to N.

Altogether, the three studies I present in this thesis offer a novel, integrative quantification of the multiple and intricate impacts of the Amazon River on the marine ecology and associated biogeochemical cycles, fostering the idea that the land to ocean continuum should be considered in its full extent and that its complexity should be accounted for in earth system models.

Résumé

Depuis les terres en amont jusqu'à la haute mer, l'eau agit comme une force motrice qui crée un continuum liquide liant les mondes terrestre et marin. Le passage de l'eau à travers les sols mais aussi les aquifères, les lacs, les zones humides et les rivières, contrôle le transport, les échanges et la transformation des éléments biogéochimiques jusqu'à leur arrivée dans l'océan. Cet apport fluvial d'éléments représente pour l'océan une importante source de carbone et de nutriments comme l'azote, le phosphore et la silice qui nourrissent la base de la chaine alimentaire marine: le phytoplancton. En serpentant des estuaires à l'océan ouvert, les panaches fluviaux forment une interface dynamique qui laisse une empreinte complexe sur la biogéochimie marine et la dynamique du phytoplancton. En effet, la quantification exacte des apports fluviaux sur les cycles biogéochimiques marins à l'échelle régionale et mondiale demeure irrésolue. Les mesures in situ capturent difficilement les conditions environnementales moyennes liées aux panaches fluviaux à cause de la très forte variabilité spatio-temporelle de ces derniers. Les modèles numériques océaniques à faible résolution ne parviennent pas à reproduire tous les processus clés régissant la dispersion physique du panache fluvial. De plus, ces modèles océaniques sont couplés à des modèles biogéochimiques qui n'ont souvent pas la complexité écologique requise pour représenter l'ensemble des impacts que les apports fluviaux peuvent avoir sur les cycles biogéochimiques et les écosystèmes marins.

Dans cette thèse, j'ai utilisé un modèle océanique régional à haute résolution (ROMS) couplé à un modèle biogéochimique/écologique qui représente explicitement quatre types fonctionnels de phytoplancton (TFPs), c'est-à-dire, le phytoplancton de petite taille, les diatomées, les *Trichodesmium* (diazotrophe vivant librement) et les assemblages symbiotiques de diatomées- diazotrophes (ASDD). J'ai utilisé ces modèles couplés pour évaluer l'impact du fleuve Amazone sur le cycle du carbone et des nutriments dans l'océan Atlantique tropical occidental (ATO). Afin d'étudier l'impact distinct et cumulatif des différents apports fluviaux sur la biogéochimie marine, un ensemble de neuf simulations factorielles au sein desquelles un ou plusieurs éléments ont été exclus de l'apport de l'Amazone ont été réalisées. Sur l'ensemble de la région étudiée, le fleuve Amazone engendre une augmentation significative de la production primaire nette (PPN), +115 Tg C an^{-1}, qui dépasse l'augmentation potentielle basée uniquement sur les apports fluviaux en azote et phosphore inorganique. Cette amplification est en majorité soutenue par l'augmentation de la fixation de l'N_2, c'est-à-dire l'utilisation du diazote atmosphérique gazeux (N_2) par les diazotrophes. Cette augmentation de la fixation du N_2 est principalement due aux larges efflorescences phytoplanctoniques de ASDD qui bénéficient de l'apport en phosphore organique dissous

(POD) fluvial. L'export de carbone vers les profondeurs est également accru, et ce manière disproportionnée par rapport à l'augmentation de la PPN, ce qui indique que la pompe biologique est devenue plus efficace. Cette augmentation de l'efficacité de la pompe biologique est due à un changement de composition au sein de la communauté phytoplanctonique : les diatomées, qui exporte plus efficacement le carbone et dont la croissance est alimentée par le $Si(OH)_4$ fluvial, ont vu leur contribution à la production augmenter. L'effet combiné de l'augmentation de la PPN et du renforcement de la pompe biologique contribue le plus aux variations des échanges de CO_2 a l'interface air-mer. En effet, ces facteurs induisent une absorption accrue du CO_2 atmosphérique dans les eaux localisées sur le plateau continental et/ou dans le panache de l'Amazone, tout en réduisant le dégazage de CO_2 dans le reste de l'ATO. L'apport fluvial en carbone inorganique dissous et en alcalinité renforce cet effet de la pompe biologique, un effet qui est contrebalancé par la reminéralisation progressive du carbone organique dissous d'origine terrestre. Cette première partie de ma thèse fournit la première quantification complète de l'empreinte du plus grand fleuve du monde sur la biogéochimie marine et démontre ainsi que ces impacts sont nombreux, interconnectés et non linéaires.

Dans la deuxième partie de ma thèse, j'ai étudié les facteurs contrôlant la fixation du N_2 qui s'est avérée intense et déterminante pour l'équilibre du système tel qu'évalué dans la première partie. En accord avec les observations, le modèle biogéochimique reproduit les plus grands taux de fixation de N_2 mesurés dans les eaux du panache, fixation qui est principalement soutenue par les ASDD. L'analyse des simulations montre que le fleuve Amazone amplifie la fixation du N_2 de 74% (+ 3,8 Tg N yr^{-1}) et que cette augmentation dépend fortement de l'apport fluvial en phosphore et en $Si(OH)_4$. Cet apport en nutriments modifie la compétition phytoplanctonique en faveur des ASDD, qui montrent des dynamiques contrastées dans les différentes portions du panache. Dans la partie située en amont du panache (0-1300 km), l'avantage compétitif des ASDD est associé à leur capacité à fixer le N_2 alors que le phytoplanctone non-diazotrophe épuise rapidement le pool d'azote inorganique et sont ainsi vite limités par la concentration en azote. Dans le reste de la trajectoire du panache (1300-3500 km), le phosphore devient le nutriment le plus limitant pour tous les TFPs, mais les ASDD bénéficient de leur capacité à utiliser directement le POD dans des eaux pauvres en PO4. Cependant, mes résultats démontrent que les contrôles *bottom-up* sont insuffisants pour expliquer les patrons spatiaux de fixation du N_2. En effet, les ASDD accumulent peu de biomasse en amont du panache, car leur avantage en termes de croissance est presque entièrement annulé par leur plus forte sensibilité au broutage par le zooplancton. En d'autres termes, l'intensité du broutage du zooplancton sur les ASDD est significativement plus élevée que celle modélisée pour les autres TFPs. L'intensité du broutage s'affaiblit dans le reste de la trajectoire du panache, ce qui permet aux ASDD de se développer plus au large. Ces résultats soulignent l'importance des contrôles *bottom-up* par les nutriments et de mortalité due au zooplancton vis à vis de la fixation du N_2 et sa distribution spatiale. Il est donc nécessaire d'étudier ces deux mécanismes pour les recherches futures, qu'elles soient basées sur des observations des modèles numériques.

Le débit des rivières varie de manière interannuelle en réponse aux anomalies des précipitations sur le bassin de l'Amazone, qui sont déterminées en partie par El Niño-Southern Oscillation (ENSO). Dans la troisième partie de ma thèse, j'ai analysé différentes simulations texthindcast reproduisant les conditions atmosphériques de 1983 à 2019. Celles-ci ont montré que la variabilité du débit de l'Amazone modifie les taux de fixation de N_2 jusqu'à 15 % dans les eaux du panache au large. De plus, les taux de fixation de N_2 sont modifiés par la variabilité spatiale des processus physiques, c'est-à-dire l'approfondissement ou la réduction de la profondeur de la couche de mélange et la force de l'upwelling équatorial, qui sont induits par les fluctuations du mode méridional de l'Atlantique et de l'ENSO. Alors que la variabilité du débit influence la fixation de N_2 dans la partie nord-ouest de l'ATO, les deux modes climatiques cités ci-dessus ont l'impact le plus fort sur la région sud-est. La variabilité du débit et la variabilité climatique affectent la fixation de N_2 par la disponibilité en phosphore dissous. Un débit anormalement élevé fournit plus de DOP et renforce donc l'excès de phosphore par rapport aux nitrates dans les eaux du panache, des conditions qui favorisent la fixation du N_2. En revanche, un approfondissement de la couche de mélange et un renforcement de l'upwelling apportent des eaux charactériées par de faibles concentrations en DOP et un rapport N:P proche de 16:1. Ceci favorise principalement les non-diazotrophes aux dépens des ASDD et des Trichodesmium. Cette étude représente la première évaluation des facteurs contrôlant la variabilité de la fixation de N_2 dans l'ATO. Elle démontre le rôle crucial du phosphore, et particulièrement de sa concentration, de sa composition (organique *versus* inorganique) et de son abondance relative par rapport à l'azote.

Dans l'ensemble, ma thèse offre une nouvelle quantification intégrative des impacts multiples et complexes du fleuve Amazone sur les écosystème marins et les cycles biogéochimiques associés. Mes travaux encouragent l'idée que le continuum terre-océan devrait être considéré dans toute son étendue et que sa complexité devrait être prise en compte dans les modèles du système Terre.

Contents

Summary **iii**

Résumé **vii**

1 Introduction **1**

1.1 The Land-Ocean Aquatic Continuum (LOAC) in the context of the Anthropocene 1

1.1.1 LOAC: definition and relevance 1

1.1.2 LOAC and the global carbon cycle 2

1.1.3 LOAC and the cycling of nutrients 4

1.2 The Amazon River Plume 6

1.2.1 The Amazon River: a giant river in the midst of rising anthropogenic disturbance 6

1.2.2 The impact and dispersal of the freshwater input 8

1.2.3 The input of nutrients and its consequences 11

1.2.4 The impact of the marine carbon cycling 14

1.3 N_2 fixation in the Western Tropical Atlantic 16

1.3.1 The importance of N_2 fixation 16

1.3.2 The biodiversity of diazotrophs 17

1.3.3 Factors controlling N_2 fixation 20

1.3.4 Modeling N_2 fixation 21

1.4 Open questions 23

1.5 Thesis structure 23

1.5.1 Objectives 23

1.5.2 Approach 24

1.5.3 Chapter overview 24

2 The impact of the Amazon on the biological pump and the air-sea CO_2 balance of the Western Tropical Atlantic 27

2.1 Introduction 28

2.2 Methods 30

2.2.1 ROMS-BEC with explicit DDAs 30

2.2.2 External sources of nutrients 33

2.2.3 Simulations and analyses 34

2.2.4 Model evaluation 36

2.2.4.1 Circulation 36

2.2.4.2 Biogeochemistry and ecology 37

2.2.4.3 Air-sea CO_2 exchange 40

2.3 Changes in the biological pump 41

2.3.1 Overview 41

2.3.2 The enhancement of primary production 46

2.3.3 The enhancement of carbon export 47

2.3.3.1 Changes in *e*-ratios 47

2.3.3.2 Phytoplankton community structure and POC production . . . 49

2.3.3.3 Depth of production and the *s*-ratio 51

2.4 Changes in the air-sea CO_2 balance 52

2.4.1 Air-sea CO_2 balance of the WTA 52

2.4.2 Factors contributing to the air-sea CO_2 balance 54

2.5 Caveat and limitations 56

2.6 Comparison to previous work 57

2.7 Summary and Synthesis 59

3 The intensification of N_2 fixation driven by the Amazon river: the role of phytoplankton competition 63

3.1 Introduction 64

3.2 Methods 65

3.2.1 ROMS-BEC 65

3.2.2 Simulations 67

3.2.3 Masks and pathways 68

3.2.4 Analysis framework: growth and grazing ratios 69

3.2.5 Model evaluation 70

3.3 Results 71

3.3.1 N_2 fixation and the importance of DDAs in the WTA 71

3.3.2 The impact of the Amazon on the phytoplankton community structure and the relative contribution of DDAs 74

3.3.3 Changing competition in the northward upstream plume pathway (0-1300km) 77

3.3.3.1 Bottom up controls 77

3.3.3.2 Growth versus grazing 78

3.3.4 Changing competition in the northward downstream plume pathway (1300-3500km) 79

3.3.4.1 Bottom up controls 80

3.3.4.2 Growth versus grazing 80

3.4 Discussion 81

3.4.1 The Amazon, boosting N_2 fixation in the WTA 81

3.4.2 DDAs versus Non-Diazotrophs: bottom up controls 82

3.4.3 DDAs versus Non-Diazotrophs: top down controls 83

3.4.4 DDAs versus *Trichodesmium* 83

3.4.5 Limits and caveat 84

3.5 Conclusion 85

4 The Interannual Variability in Marine N_2 Fixation and its Drivers in the Western Tropical Atlantic 87

4.1 Introduction 88

4.2 Methods 90

4.2.1 Model 90

4.2.2 Model Forcing 91

4.2.3 Simulations and Analyses 92

4.2.4 Model Evaluation 95

4.2.4.1 Sea Surface Temperature 95

4.2.4.2 Sea Surface Salinity and Plume Size 96

4.2.4.3 N_2 Fixation 97

4.3 Results and discussion 99

4.3.1 Variability in N_2 Fixation 99

4.3.2 Bottom-up Controls Drive Variability in N_2 Fixation 103

4.3.3 The Amazon River as a Source of Variable Nutrient Input 108

4.3.4 The Role of Climate Variability 109

4.4 Caveats 112

4.5 Conclusion 114

5 Synthesis & Outlook 117

5.1 Major scientific findings and conclusions 118

5.2 Implications 121

5.3 Limits and shortcomings 124

5.4 Outlook and suggestions for future research 128

A Appendix to Chapter 2 131

B Appendix to Chapter 3 137

C Appendix to Chapter 4 **141**

List of Figures **154**

List of Tables **165**

Bibliography **169**

Aknowledgments **197**

Curriculum Vitae **199**

Chapter 1

Introduction

1.1 The Land-Ocean Aquatic Continuum (LOAC) in the context of the Anthropocene

1.1.1 LOAC: definition and relevance

Anthropogenic greenhouse gas emissions have lead to a steady increase in atmospheric carbon dioxide (CO_2) concentrations, resulting in a global rise of air temperature (Stocker et al., 2013). In this context, research in global biogeochemistry has been focusing more and more on the pressing question of the cycling and redistribution of carbon on Earth (Bianchi, 2021). Rivers constitute an important flowpath, exporting carbon laterally from the different biotic and abiotic terrestrial reservoirs to the ocean. While intimately interconnected, each component is generally studied in isolation. This artificial partition can limit scientific exchanges and taper off our ability to build a comprehensive budget. In contrast, the Land-Ocean Aquatic Continuum (LOAC) refers to research that aims to bridge land to ocean processes (Bouwman et al., 2013; Xenopoulos et al., 2017). LOAC encompasses the study of many different systems (e.g, soils, lakes, reservoirs, streams, floodplains, estuaries, coastal oceans) that transform and transport biogeochemical elements from headwaters to the open ocean (Billen et al., 1991). On top of carbon (C), biogeochemical constituents of particular importance for the ecosystems are the macronutrient elements Nitrogen (N), Phosphorus (P) and Silicon (Si). Together they play a key role in controlling the growth of plants, both terrestrial and aquatic. In various forms i.e particulate or dissolved, inorganic or organic, these elements are filtered and transferred from land to the aquatic network through different pathways, mainly flows from soils, aquifers and surface runoff (figure 1.1).

The LOAC is currently facing an increasing anthropogenic stress owing to the growing demand for land, energy, food and water (Best, 2019). The multiple human perturbations have cascading effect on all the components of the LOAC, with consequences on the CO_2 evasion and uptake of both freshwater and marine surface waters. Yet, until now, these perturbations are neglected in global carbon budgets (Regnier et al., 2013; Friedlingstein et al., 2020, 2021). In this context, the C-CASCADES project, in which this thesis is embedded, aimed to better understand the processes that shape the lateral flux of carbon and the human related disturbance of this flux (https://c-cascades.ulb.ac.be/).

1.1.2 LOAC and the global carbon cycle

Large amounts of carbon are washed in from the surrounding landscape and processed across the LOAC. Regnier et al. (2013) estimated the C flux to the aquatic inland network to approximate 2.9 Pg C yr^{-1} (Figure 1.2). From the moment raindrops start to precipitate in the atmosphere until they reach the streams and rivers, the water content gets enriched with Dissolved Organic Carbon (DOC) and Particulate Organic Carbon (POC) as the water flows through vegetation layers and overland (Ward et al., 2017). Along this journey, part of this organic matter gets already degraded and converted to dissolved inorganic carbon (DIC). Unless they are completely saturated, soils also absorb part of the rainfall that subsequently participates in the leaching and below-ground transport of organic matter (Figure 1.1). The scarcity of the data coverage and the heterogeneity of soil environments render this flow path difficult to constrain at the global scale. Using a process based modelling framework, Nakhavali et al. (2021) estimated that leaching only is responsible for a flux of 0.28 ±0.07 Pg C yr^{-1} of DOC. According to this study, the largest fluxes of leached DOC are located in the rain forest where they represent up to 22% of the Net Ecosystem Productivity (NEP defined as the difference between the net primary production and soil respiration).

Within the fluvial environment, this terrestrial C flux is further processed. During its down-

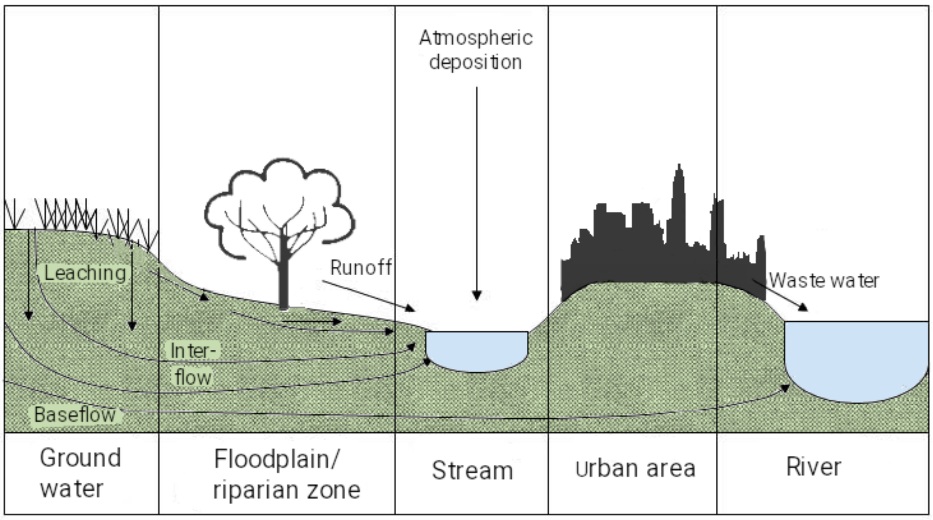

Figure 1.1 Schematic of a generic river basin: its main components (rectangles) and the main processes delivering water, particulate matter and dissolved solutes to the river network (arrows). Adapted from Bouwman et al. (2013).

stream advection, the land-derived organic carbon is continuously decomposed, fueling the production of greenhouse gases, primarily CO_2 and methane (CH_4) (Battin and Luyssaert, 2009). Typically oversaturated compared to the atmosphere, the freshwater aquatic network tends to release CO_2 and CH_4. While rivers and streams were perceived for a long time as passive conduits, these emissions of CO_2 from inland waters are more and more accounted for in carbon budgets (figure 1.2). Over the last decade or so, estimates for present-day CO_2 evasion from inland waters have been increasing: 0.8 Pg C yr^{-1} (Cole et al., 2007), 1.2 Pg C yr^{-1} (Battin and Luyssaert, 2009), 1.9 Pg C yr^{-1} (Global Carbon Budget, 2018 - see figure 1.2), 2.1 Pg C yr^{-1}(Raymond et al., 2013), 2.45 Pg C yr^{-1} (Sawakuchi et al., 2017). This increase reflects advances that were made recently in the quantification of the remineralization of organic carbon in aquatic systems, the estimation of gas transfer velocity in freshwaters and the measuring of its areal extent of inland waters (Allen and Pavelsky, 2018). However, the exact quantification is still disputed and the heterogeneity and complexity of the inland water systems warrant the ongoing research effort. For example, multiple lines of evidence demonstrated the importance of the priming effect i.e., the enhancement of the breakdown of terrestrial organic carbon when mixed with autochthonous carbon (Guenet et al., 2014; Bianchi et al., 2015; Ward et al., 2016) and yet, the phenomenon is still widely overlooked when assessing the CO_2 evasion from streams and rivers. Although terrestrially-derived organic carbon is rapidly degraded in the freshwater network, a significant fraction can be stored in the sediments (Figure 1.2), especially in lakes and reservoirs where the

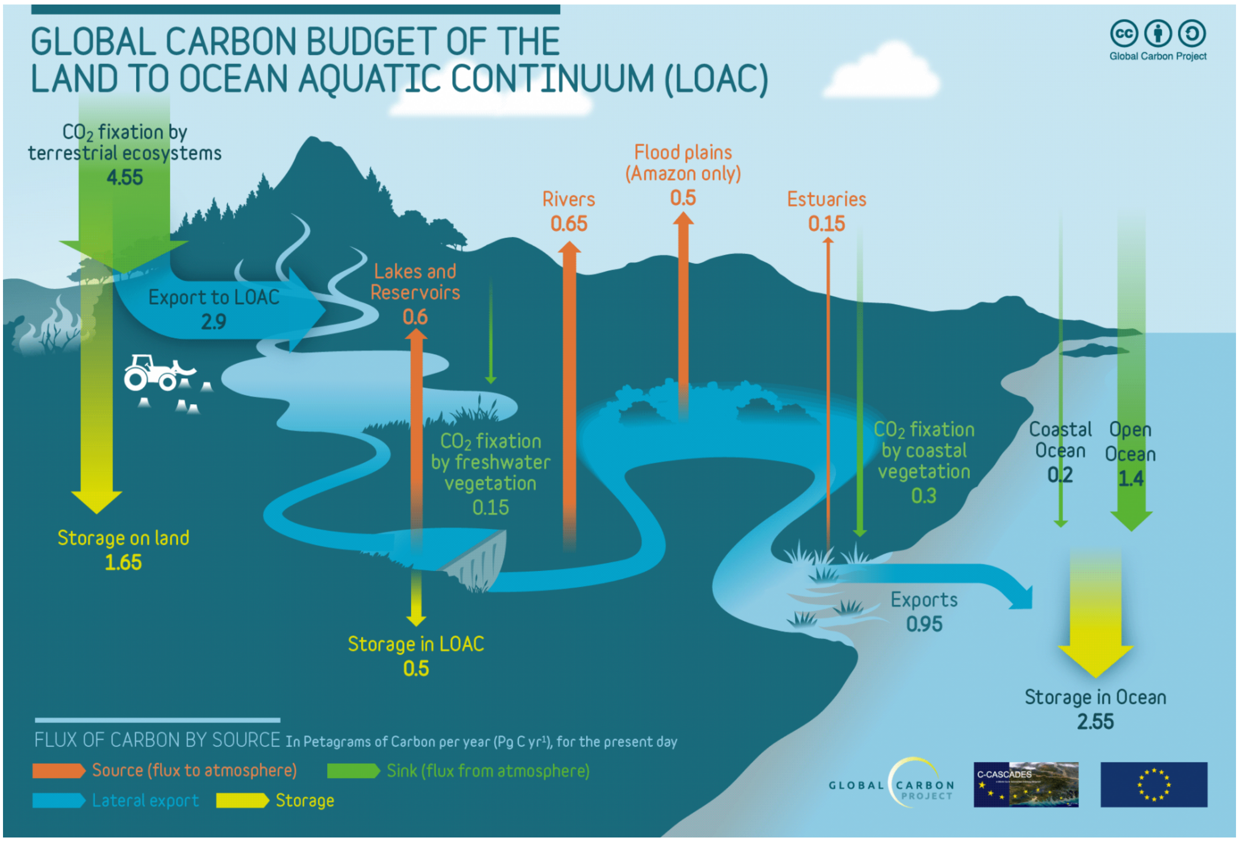
GLOBAL CARBON BUDGET OF THE
LAND TO OCEAN AQUATIC CONTINUUM (LOAC)
Global Carbon Project
CO2 fixation by terrestrial ecosystems 4.55
Export to LOAC 2.9
Lakes and Reservoirs 0.6
Rivers 0.65
Flood plains (Amazon only) 0.5
Estuaries 0.15
CO2 fixation by freshwater vegetation 0.15
CO2 fixation by coastal vegetation 0.3
Coastal Ocean 0.2
Open Ocean 1.4
Storage on land 1.65
Storage in LOAC 0.5
Exports 0.95
Storage in Ocean 2.55
FLUX OF CARBON BY SOURCE In Petagrams of Carbon per year (Pg C yr¹), for the present day
Source (flux to atmosphere)
Sink (flux from atmosphere)
Lateral export
Storage
GLOBAL CARBON PROJECT
C-CASCADES

Figure 1.2 Global carbon budget for the LOAC combining both natural and human-induced emissions and uptake. Source: Global Carbon Budget (http://www.globalcarbonproject.org/).

burial rates are hypothesized to be 1 to 4 times higher than in the ocean (Tranvik et al., 2009).

Carbon fluxes across the LOAC are subject to change due to anthropogenic perturbation. Overall, the C flux to inland waters is expected to increase in response to human activities such as deforestation and intensive agricultural practices. Regnier et al. (2013) estimated this increase to amount to 1.0 ± 0.5 Pg C yr^{-1} compared to pre-industrial times. This additionnal carbon undergoes the same processes as the ”natural” carbon and is partly buried, partly respired and partly transported to the ocean.

Eventually, only a small fraction of the terrestrial C flux, both ”natural” and anthropogenic, reaches the coastal ocean (Figure 1.2). Recent estimates of this global C load vary from 0.78 Pg C yr^{-1} (Resplandy et al., 2018) to 0.95 Pg C yr^{-1} (Regnier et al., 2013). Behind these values lies a large spatial variability, with some catchments contributing significantly more than others. Using weathering and export organic matter models, Lacroix et al. (2020) estimated the riverine carbon and nutrient load in pre-industrial conditions. They identified the tropical Atlantic as the largest supplier of carbon to the ocean (20 % of the global riverine C flux), highlighting the importance of large rivers, here the Amazon River and the Congo River, in the global carbon budget. Implementing the riverine loads in a global coupled oceanic model resulted in an CO_2 outgasing of 231 Tg C yr^{-1} but also created an additional sink of 80 Tg C yr^{-1}, in response to the stimulation of primary and export production (Lacroix et al., 2020). This study illustrates the great value of models to run idealized scenarios and provide quantifications that would be almost impossible to derive from observations only. It also underlines the importance for global models to account for the riverine load and more specifically, to include both the carbon and nutrient inputs. However, in models, the dispersal of river plumes is very sensitive to the representation of the runoff point source, the grid resolution and the refinement of the shelf bathymetry, all aspects that are ill-represented in coarse resolution global models (Feng et al., 2021). Overcoming these limitations is key to adequately reproduce both the physical and biogeochemical dynamics of these highly variable environments.

1.1.3 LOAC and the cycling of nutrients

The inland freshwater network receives N, P and Si in various chemical forms and loads from groundwater flows and weathering. Many factors influence this input of nutrients including precipitation patterns, temperature, soil properties and geomorphology of the basin (Bouwman et al., 2013). This flux of terrigenous nutrients is also perturbed by human activities such as land-use change, utilization of fertilizer, discharge of agricultural and industrial waste, etc. Beusen et al. (2016) estimated that these perturbations are responsible for an increase of the global delivery of N and P to the inland aquatic system of more than +80% over the past century. In contrast, the input of Si to the rivers is likely to be reduced by land-use change and intense agricultural Si harvest (Struyf et al., 2010; Vandevenne et al., 2012).

Biogeochemical constituents are further transformed within the river, mainly through microbial decomposition and incorporation in the biological loop. These transformations are crucial as they determine the ultimate content of the inflowing waters entering the ocean. Here again, natural processes are suffering from anthropogenic alterations. The multiplication of reservoirs and dams has been showed to be associated with an increased in-stream retention of nutrients that changes both the absolute and relative concentration of nutrients in the downstream waters (Beusen et al., 2016; Maavara et al., 2020). Damming might lead to a global increase the N:P ratio in river outflows (Maavara et al., 2020). P is indeed more efficiently eliminated in reservoirs than N, although the driving mechanisms have not been fully elucidated. Leading hypotheses include the sorption of P to minerals and the wide-spread P-limitation of freshwater ecosystems (Maranger et al., 2018). At low hydraulic residence time, Si has been shown to be also disproportionately lost compared to N and even P (Ran et al., 2013). The enhanced nutrient removal of P and N within the streams does not offset the increased supply from land which leads to a global increase of riverine N and P inputs in the ocean Beusen et al. (2016). Summing the particulate and dissolved forms, Lacroix et al. (021b) estimated that the global flux of N and P increased from 27 to 46 Tg N yr^{-1} and from 3.7 to 5.3 Tg P yr^{-1} between 1905 and 2010. In contrast, the global supply of Si by river is hypothesized to be decreasing in response to anthropogenic disturbance (Laruelle et al., 2009; Bernard et al., 2011).

The amount and stoichiometry of riverine nutrients are key determinants to the functioning and composition of marine ecosystems in the coastal ocean. It is especially crucial as the coastal ocean supports up to 30% of the primary production and provides critical ecosystems services while facing a strong societal pressure (Barbier et al., 2011). Over the past century, the human-induced changes in riverine nutrient inputs have disrupted the natural stability of coastal environments, with regionally dramatic effects on ecosystems (Fennel and Testa, 2019). Globally, the increase of the riverine nutrient load is likely to induce an increase of NPP in the coastal ocean (Lacroix et al., 021b). However, the primary production is also very sensitive to changes in nutrient stoichiometry. Thus, the excess of nitrogen in certain river outflows is associated with eutrophication and the expansion of hypoxic zones (Diaz and Rosenberg, 2008; Fennel and Testa, 2019). The relative decrease of Si to N and P leads to shift in phytoplankton communities to the detriment of coastal diatoms (Gong et al., 2006).

The impact of rivers is not limited to the coastal ocean. Part of the terrigenous nutrients is eventually transported offshore, influencing the biogeochemical cycles at a global scale. In estuaries and shelf seas, the processes that retain, break down, and bury nutrients are complex and differ widely, depending on the morphology of the shelf, the sediment dynamics and the local physical and biogeochemical environment. Hence, studies that take on the challenge of estimating the eventual flux of riverine nutrients from the coastal to the open ocean are rare, especially at the global scale. Global mass balance models have proved to be useful in providing global estimates of nutrient fluxes in and out the coastal ocean but they rely on numerous simplifications and do not account for individual rivers (Laruelle et al., 2009). To resolve the geographic heterogeneity of rivers and shelf physical settings, Sharples et al. (2017) proposed a mechanistic description of the plume dynamics and built empirical relations between the plume residence time and the proportion of nutrients crossing the shelf break. With this approach, they estimated that 75% of the dissolved inorganic nitrogen (DIN) and 80% of the dissolved inorganic phosphorus (DIP) supplied by the rivers reach the open ocean. Building on this work, Izett and Fennel (2018) ran different simulations and developed additional empirical relationships to further constrain the plume export. In a companion article (Izett and Fennel, 2018), they present estimates of the riverine nutrient lateral export that are significantly lower than those of Sharples et al. (2017): 2.8–44.3% for DIN, 3.5–45.9% for DIP, 5.7–52.3% for Dissolved Silicate (DSi). The study identifies a band around the equator, between 15° S and 15° N, where nutrients are the most efficiently exported from the shelf.

Global ocean models can be used to assess the impact of this flux of riverine nutrients on the open ocean biogeochemistry. Coupling a general circulation model (MPI-OM) and a biogeochemical model (HAMOOC), Bernard et al. (2011) identified hot spots of oceanic silica such as the Amazon River plume and demonstrated the necessity to account for riverine DSi inputs to properly reproduce surface DSi in global models. To investigate the effect of the increasing nutrient load from rivers from 1905 until 2010, Lacroix et al. (021b) used an updated version of the HAMOOC model, that better reproduces shelf processes (Lacroix et al., 021a). In response to the rising anthropogenic perturbations, Lacroix et al. (021b) estimated an increase of N and P cross-shelf export of +12 Tg N yr^{-1} and +0.4 Tg P yr^{-1}, respectively. These enhanced lateral fluxes of nutrients result in an increase of NPP of 4% over the whole open ocean, with a few regions such as the Tropical Atlantic Ocean and the Indian Ocean driving most of the increase (Lacroix et al., 021b).

1.2 The Amazon River Plume

This present thesis takes a regional approach and focuses on the Amazon River, an aquatic system of global importance.

1.2.1 The Amazon River: a giant river in the midst of rising anthropogenic disturbance

Among the world rivers, the Amazon is the river of all superlatives: It has the vastest watershed, the largest discharge, and the second largest delta after the Ganges (GRDC, 2020; Dai et al., 2009; Syvitski and Saito, 2007). With an area of 6 millions of km^2, the Amazon basin encompasses a diverse landscape of Andean glaciers, dense rain forests, extensive flood plains, and savannas (Sioli, 1984; McClain and Naiman, 2008; Hess et al., 2015). The basin is drained by a capillary network of meandering and biogeochemically diverse rivers and streams that drive seasonal inundation pulses (figure 1.3).

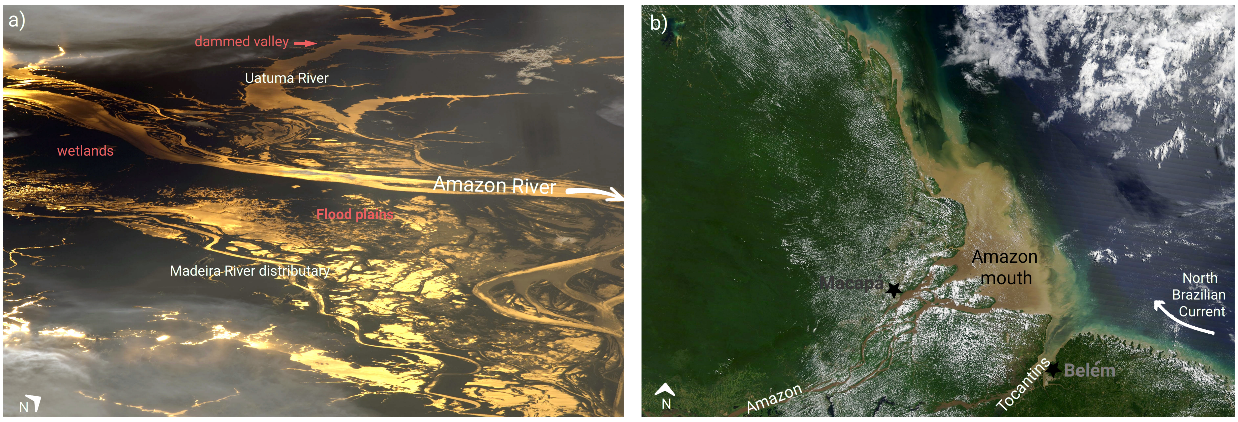

Figure 1.3 Both pictures were retrieved from NASA Observatory and annoted by myself. a) Picture taken from space on August 19, 2008. The region shown here is located around 1000 km inland from the mouth of the river and is indicated by a red cross on figure 1.4. The yellowish color is the result of the setting sun glinting off the water and the smoke particles from forest fires in the air reflecting light. The sun's reflection reveals features that are normally dark and hard to see from space. Image provided by the ISS Crew Earth Observations experiment and the Image Science & Analysis Laboratory, Johnson Space Center. The arrow indicates the flow direction. b) Image of the Amazon from Lauren Dauphin, using the Moderate Resolution Imaging Spectroradiometer on Nasa's Terra satellite (July 29, 2020).

Its immensity and its location in the very productive wet tropical environments make the Amazon River an aquatic system of global importance in the cycling of carbon. Due to the large inputs of terrestrial organic carbon and the high rates of remineralization, the freshwater network acts as a source of atmospheric CO_2 (Richey et al., 2002). The quantification of the CO_2 flux comes with large uncertainties owing to the low coverage of observations and the difficulty to estimate the areal extent of the waterways (Allen and Pavelsky, 2018), but estimates agree on the prominence of this flux. Raymond et al. (2013) predicted this CO_2 evasion to amount to ~0.6 Pg C yr^{-1}, representing almost 30% of the global CO_2 flux from inland water bodies. More recently, Sawakuchi et al. (2017) demonstrated the importance of a better assessment of the lower part of the Amazon River - from Òbidos to the mouth - and revised upwards the estimated flux to 0.95 Pg C yr^{-1}.

Compared to other large Asian or European rivers cutting through highly populated and industrialized areas, the Amazon river experiences lower anthropogenic disturbance. Nevertheless, the pressure of human activities in the Amazon basin has been steadily increasing and impacting both the main stream and tributaries to varying degree depending on the type of activity (McClain and Elsenbeer, 2001; Castello et al., 2013). The development of mining is responsible for an increased load of sediments as well as a contamination of the streams by mercury and other pollutants (McClain and Elsenbeer, 2001). The deforestation and slash-and-burn agriculture also increases the fluxes of sediments and different solutes to the streams. These changes in land cover might also affect the discharge of streams. At the local scale, they induce an increase in the freshwater input by reducing the evapotranspiration, while at the large scale, they reduce the regional precipitation and thus decrease the discharge (Coe et al., 2009; Lee et al., 2018). The balance between the two processes eventually determines the net effect. Another main cause of perturbations is the development of cities. While the urban coverage is still limited in the tropical wilderness areas, the Amazon region has undergone an intense process of both planned and informal urbanization over the past decades, especially in the vicinity of waterways (Guedes et al., 2009; Cabrera-Barona et al., 2020). This has resulted in a increasing load of particulate organic matter and diverse contaminants to the freshwater system (Schmidt et al., 2019; Fabregat-Safont et al., 2021; Gerolin et al., 2020).

The expansion of cities is also associated with a rising demand in energy, and hence a boom in the construction of dams and hydroelectric facilities (Stickler et al., 2013; Winemiller et al., 2016). According to the last counting in 2019, 158 hydropower dams are currently in operation in the Amazon basin, while 351 more are planned to be constructed in the coming decades. This progressively turns most of the major free-flowing streams into a succession of reservoirs (Almeida et al., 2019). While hydropower can be seen as a climate-friendly source of energy (Muller, 2019), large dams have a wide range of effects, involving multi-scale social costs, disrupting biogeochemical cycles and altering both land and freshwater ecosystems (Latrubesse et al., 2017). Multiple lines of evidence have shown that dams in the Amazon basin result in an enhanced outgasing of CO_2 and CH_4 (Fearnside, 2015), although strategic planning and optimal operating could reduce this effect (Song et al., 2018; Almeida et al., 2019). Impeding the flow, increasing the residence time, dams also affect the cycling of nutrients (Maavara et al., 2020). For instance, using historical data and a mechanistic model, Forsberg et al. (2017) estimated that in response to the construction of 6 large dams in the Andean region, the P and N load to the entire Amazon basin will be reduced by 51% and 23% respectively.

The properties of the Amazon river are constantly evolving from the upstream source to the outflow in the ocean. Physical and biogeochemical processes driving these changes are numerous, variable and experiencing rising human disturbance. When the Amazon river eventually meets the Atlantic, the inflow combines the integral signals of the different headwater streams. The ongoing research effort to characterise and quantify the inland processes is critical to elucidate the eventual impacts of the Amazon in the marine realm.

1.2.2 The impact and dispersal of the freshwater input

The Amazon river flows into the Western Tropical Atlantic at around 0.5° N - 50.5°. The muddy brown inflow contrasts sharply with the dark blue of the ocean as observed from space (figure 1.3-b). This freshwater discharge is unique by its magnitude, accounting for around 50% of the surface river inflow to the Atlantic and 15 to 20% of the global river discharge (Dai et al., 2009; Coe et al., 2008; Callède et al., 2010; Salisbury et al., 2011). The volume of water increases by a factor of 2 to 3 between its low regime in winter (December-February) and its peak in spring (April-June). Precipitation within the basin drives its seasonality, although with a lag due to terrestrial water storage and a loss of around half of the rainfall to evapotranspiration (Salati and Vose, 1984; de Paiva et al., 2013). The Amazon discharge varies in response to precipitation anomalies induced, e.g., by the El Niño-Southern Oscillation (ENSO) phenomenon (Richey et al., 2002). El Niño years result in anomalously low discharge, while La Niña years are characterized by anomalously high discharge (figure 1.4-b). Local evapotranspiration on the continent and anomalies in the sea surface temperatures (SST) in the Tropical Atlantic also modulate the rainfall regimes over the Amazon basin (Zeng et al., 2008; Espinoza et al., 2014; Lee et al., 2018). Over the past two decades, extreme droughts and floods have been more frequent (Marengo et al., 2011; Espinoza et al., 2011; Marengo et al., 2013; Marengo and Espinoza, 2016) and the hydrological cycle has been intensifying, resulting notably in a wetter wet season and consequently a more prevalent high discharge regime (Gloor et al., 2013; Friedman et al., 2021). As for now, climate models disagree on the overall future trend of rainfall within the Amazon catchment, but the majority of them predict contrasting patterns of wetting and drying over the region and agree on an increase of the hydrological extremes (Duffy et al., 2015; Baker et al., 2021).

The Amazon inflow generates an extensive fresh lens atop the water column, which enhances surface stratification and the trapping of solar radiations, with implications for the formation of hurricanes (e.g. Grodsky et al. (2012)). Despite a strong seasonal signal, the magnitude of the discharge is not the dominant factor determining the plume pathways and extent. Much more important is surface circulation (Coles et al., 2013). After reaching the ocean, the river water inflow is kept onshore by the North Brazilian Current (NBC), a strong northward current whose flow varies seasonally between 10 and 30 Sv (Philander and Pacanowski, 1986) (figure 1.4-d). From the equator to 5° N, the plume waters remain on the continental shelf, forming a 10-30m deep cap of brackish water, above a landward flow of marine waters (Lentz and Limeburner, 1995). Further North, the plume is entrained by the Guyana Current that begins at the western edge of the NBC. This northward pathway is open throughout the year, but how far north the plume travels varies seasonally, following the variation of the strength of the surface current (Coles et al., 2013). In winter and early spring, the plume is pressed against the coastline by the strong trade winds (figure 1.4-d). In contrast, in summer, the influence of the Amazon plume can be traced up to the Caribbean Sea, more than 3500 km away from the mouth of the river (Hu et al., 2004). Additionally, around 5-8° N, the NBC retroflects eastward. The strength of the NBC retroflection varies seasonally from remnant in April to a maximum peak in November (Lumpkin and Garzoli, 2005). In late summer-fall, the retroflection extends its meandering pattern into the North Equatorial Counter Current (NECC). The NECC is a seasonal current bounded by the South Equatorial Current (SEC) and the North Equatorial Current (NEC) (figure 1.4). Non-existent or even reversed in winter and spring, the NECC reaches its seasonal maximum strength in fall in relation with the northward migration of the Intertropical Convergence Zone (ITCZ) (Bourlès et al., 1999). The NECC establishes a seasonally-locked eastward pathway for the plume waters

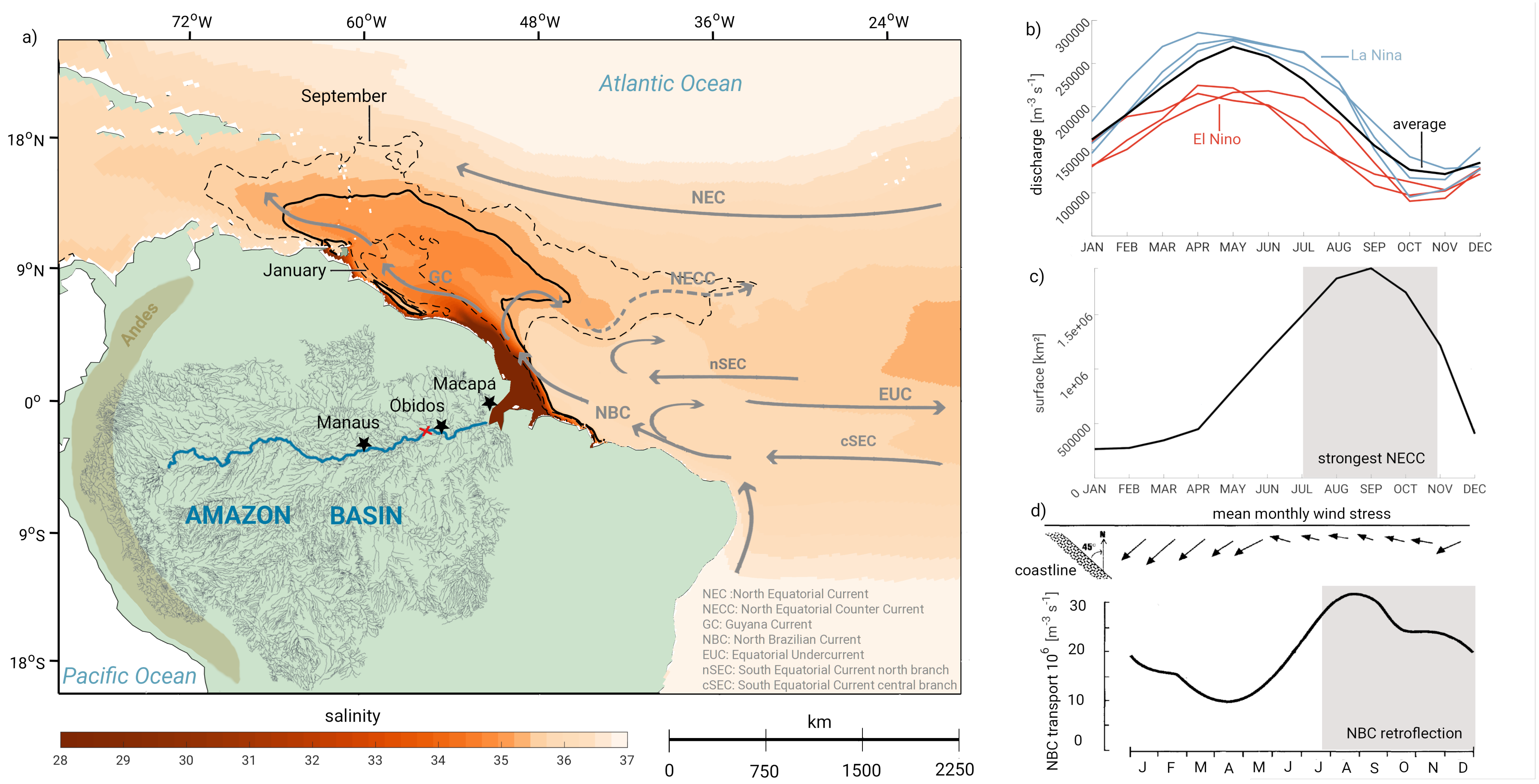
a)
72°W
60°W
48°W
36°W
24°W
18°N
9°N
0°
9°S
18°S
Atlantic Ocean
Pacific Ocean
September
January
NEC
NECC
GC
nSEC
EUC
NBC
cSEC
Andes
Macapá
Óbidos
Manaus
AMAZON BASIN
NEC :North Equatorial Current
NECC: North Equatorial Counter Current
GC: Guyana Current
NBC: North Brazilian Current
EUC: Equatorial Undercurrent
nSEC: South Equatorial Current north branch
cSEC: South Equatorial Current central branch
salinity
28 29 30 31 32 33 34 35 36 37
km
0 750 1500 2250
b)
discharge [m-3 s-1]
100000 150000 200000 250000 300000
La Nina
average
El Nino
JAN FEB MAR APR MAY JUN JUL AUG SEP OCT NOV DEC
c)
surface [km²]
0 500000 1e+06 1.5e+06
strongest NECC
JAN FEB MAR APR MAY JUN JUL AUG SEP OCT NOV DEC
d)
mean monthly wind stress
45°
N
coastline
NBC transport 10^6 [m-3 s-1]
0 10 20 30
NBC retroflection
J F M A M J J A S O N D

Figure 1.4 a) Geographical setting of the Amazon basin, major circulation features and sea surface salinity in the Western Tropical Atlantic. The Amazon stream network is the result of a topography-independent analysis method (Mayorga et al., 2012) (last access: October 14, 2021). The sea surface salinity corresponds to the annual average conditions simulated by ROMS (*All* simulation described in chapter 2). The lines locate the plume limits (salinity below 35.25) on average (solid line) and at its minimum and maximum extent (dashed line). b) Monthly average discharge of the Amazon (1979-2016) and discharge during 3 years of El Niño (1983, 1992, 1998) and La Niña (2000, 2008, 2011), data from HYBAM (last access: December 13, 2019). c) Monthly average surface of the plume with the same data as in a. d) Mean trade winds and North Brazilian Current velocity adapted from DeMaster and C. (2001)

(figure 1.4-a). Its jet structures prevent any southward flow and advect waters all the way to Africa in a time scale of <5 months (Coles et al., 2013). The Amazon plume reaches its maximum spread in late summer, covering a total of 1.8 millions of km^2 in my climatological simulation (figure 1.4-c), very similar to the 1.5 millions of km^2 estimated from satellite data for the 2000-2004 period (Molleri et al., 2010).

Beyond the consequences on the physical properties of the surface waters, tracking the plume pathways is critical to understand the impact of the Amazon on marine biogeochemistry and ecology. The dispersal pathways determine which type of environments is affected (e.g., marginal sea or open ocean) and how far-reaching the Amazon influence is. Surface salinity is often used in biogeochemical studies to differentiate different states of the plume (e.g., Subramaniam et al. (2008a)) or to determine a conservative mixing line from which deviations in carbon and nutrient content can be investigated (e.g., Goes et al. (2014)).

1.2.3 The input of nutrients and its consequences

The Western Tropical Atlantic (WTA), like most tropical oceans, is a stratified, nutrient-starved environment and the addition of exogenous nutrients by the Amazon sparks large phytoplankton blooms (Gouveia et al., 2019). This extensive imprint on marine productivity is visible from space, with levels of Chlorophyll *a* comparable to the levels of the productive boundary upwelling regions (figure 1.5). A quantitative assessment linking the Amazon nutrients and the enhancement of the primary production is arduous to determine owing to (i) the uncertainties associated with the estimates of the nutrient input and its seasonality and (ii) the complexity of the fate of nutrients once in the ocean.

Most estimates of the riverine input of nutrients are based on measurements made at the Òbidos station, 800 km upstream of the mouth of the river (figure 1.4). This alone casts uncertainty on the exact magnitude of the fluxes as nutrients are likely to be continuously transformed and exchanged in the last stretch of the fluvial network. Furthermore, measurements are instantaneous snapshots of highly variable conditions and so far, no agreement has been reached with regard to the seasonal variation of nutrient concentrations. The results from Moquet et al. (2016) tend to suggest that the solutes respond chemostatically to the discharge, i.e., concentrations remain constant, making the seasonal variation of the flow the driving factor of the dissolved load seasonality. In contrast, others studies indicate a mobilization effect, with an increased concentration of the dissolved elements during the high discharge regime and inversely a decrease during the low discharge regime (Araujo et al., 2014; Almeida et al., 2015). A recent study by Drake et al. (2021) offers a more complex picture, with dissolved organic carbon (DOC) and nitrogen (DON) experiencing a mobilization effect, PO_4 and SiO_2 being in chemostasis and NO_3 having two seasonal peaks. Reducing the uncertainties around these assessments would require an unprecedented effort of sampling at the mouth of the Amazon, with high resolution, both spatially and temporally (Ward et al., 2015).

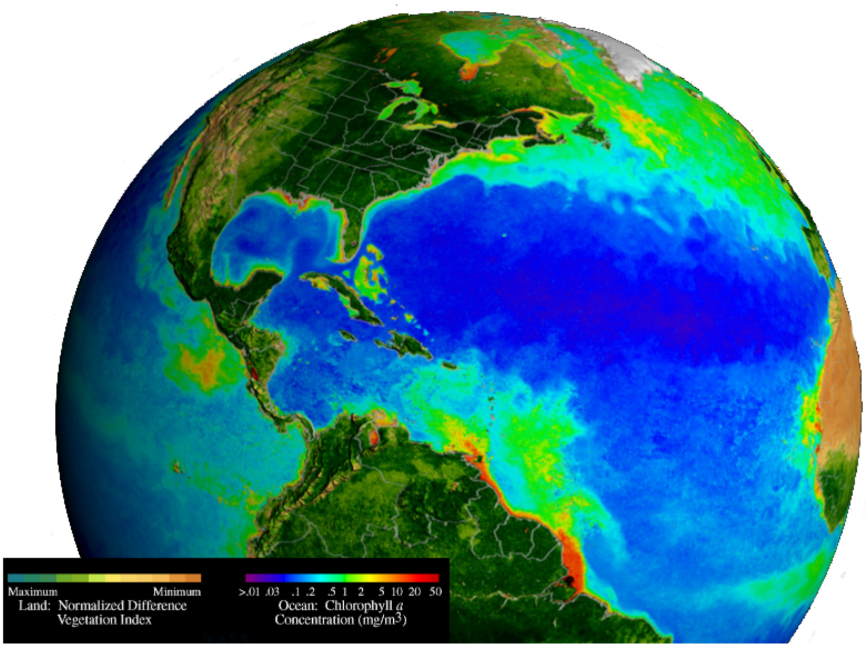
Maximum
Minimum
Land: Normalized Difference Vegetation Index
>.01 .03 .1 .2 .5 1 2 5 10 20 50
Ocean: Chlorophyll a Concentration (mg/m3)

Figure 1.5 Surface oceanic Chlorophyll a and land vegetation index as observed from space. Screenshot of one day conditions in spring 2006. The data originates from Sea-viewing Wide Field-of-view Sensor (SeaWiFS) Ocean Color Data and the visualization was made by NASA's Goddard Space Flight Center.

First receptacle of the river water, the Amazon shelf plays a pivotal role in modifying land-derived nutrients, thus determining the biogeochemical characteristics of the offshore plume. The Amazon shelf offers a very energetic and fluctuating setting, combining the effects of a large river discharge, pervasive waves induced by the trade winds, complex marine hydrodynamics, and tidal forces (Nittrouer and DeMaster, 1996). This dynamic environment entraines the large load of riverine sediments - estimated at around 754 x 10^6 t yr^{-1} (Martinez et al., 2009) - which, together with chromophoric-dissolved-organic-matter (CDOM), reduces the light availability and limits phytoplankton growth (Del Vecchio and Subramaniam, 2004). Once the water clarity has improved, phytoplankton begins to benefit from the riverine nutrients, resulting in sizeable blooms. Over the shelf, the phytoplankton community structure is dominated by coastal diatoms species such as *Skeletonema costatum* and *Pseudonitzschia sp* (Subramaniam et al., 2008a; Araujo et al., 2017; Demaster et al., 1996). They notably benefit from the large inputs of $Si(OH)_4$ that is delivered by the Amazon in excess compared to N, with an average N:Si ratio of 1:11 (Brzezinski et al., 2003; Araujo et al., 2014). As a result, the $Si(OH)_4$ inputs from the river combined with the onshore advective fluxes are sufficient to sustain the primary production while N and P require recycling (DeMaster and C., 2001).

The predominance of large siliceous diatoms promotes a strong flux of particulate organic matter (POM) down to the seabed. The burial of POM represents the main sink for most riverine nutrients, although marine organic matter has been shown not to be efficiently preserved in the sediment on the Amazon shelf (DeMaster and C., 2001). Eventually, the fraction of externally supplied nutrients that is exported from the shelf varies depending on the nutrient. DeMaster and C. (2001) estimated that virtually all of the phosphorus and the majority of the silicate (91-97%) escape from the shelf as either dissolved or biogenic material, while only half of the nitrogen is exported to the open ocean. Nitrogen is in relative terms more retained on the shelf than other nutrients, as it is also affected by sediment denitrification, i.e., the reduction of fixed nitrogen to dinitrogen (N_2) (Hulth et al., 2005). Since N_2 is a form of nitrogen unavailable for most microorganisms, denitrified N is considered lost to the system (DeMaster and C., 2001). Due to the scarcity of measurements, estimates of the total loss of N via sediment denitrification on the Amazon shelf vary from 7.7 - 8.4 x 10^{10} mol N yr^{-1} (Nixon et al., 1996) to 8.4 x 10^{10} yr^{-1} (Seitzinger and Giblin, 1996). These values represents roughly half of the estimated input of N from land, which agrees with the hypothesis that a large fraction of N supplied by the Amazon never leaves the shelf. This singular loss of N on the shelf might be an important factor driving the P and Si excess observed in the offshore plume waters (Zhao et al., prep), a distinct N:P:Si stoichiometry that appears to be crucial for the phytoplankton dynamics (section 3.3). Overall, processes on the shelf are determinant in shaping the biogeochemical properties of the downstream plume waters. Yet the link between inshore and offshore is still poorly constrained.

In the offshore plume, the remaining nutrients that are laterally exported from the shelf have been hypothesized to modify the phytoplankton community (Subramaniam et al., 2008a; Goes et al., 2014; Weber et al., 2017). A common approach to study the shift in phytoplankton dynamics is to use salinity as a proxy of the progressive mixing of plume and marine waters. Over the past decade or so, most studies have used a set of salinity ranges proposed initially by Subramaniam et al. (2008a), each range representing a different stage of the plume life: <30 as ”low-salinity” i.e., the early stage the plume dispersal, >30 and <35 as ”mesohaline” representing the core of the offshore plume waters and >35 as ”oceanic” representing the non-plume or weakly influenced waters. The low-salinity sub-region encompasses roughly the shelf environment described above, although this type of waters sometimes extends offshore. In the mesohaline waters, diatoms still represent an important fraction of the total biomass, on average $\sim$30% (Shipe et al., 2006). However, the most interesting emergent property is the development of large blooms of diatom-diazotroph-assemblages (DDAs), a symbiotic association between a diatom and a diazotroph (Subramaniam et al., 2008a; Goebel et al., 2010). DDAs never really dominate the phytoplankton community (Subramaniam et al., 2008a; Stukel et al., 2014), but their presence results in very high rates of N_2 fixation, making the Western Tropical Atlantic a globally significant hotspot of marine N_2 fixation (Luo et al., 2012; Landolfi et al., 2018). Biological N_2-fixation corresponds to the enzymatic reduction of N_2 to ammonia and is performed by a wide range of diazotrophs. N_2 fixation is such an important feature of the WTA that I dedicated a whole section to its introduction (section 3). In the oceanic type of waters, the phytoplankton community is more typical of oligotrophic tropical waters, characterized by a mixture of smaller phytoplankton and the prevalence of *Trichodesmium* in the N_2-fixing assemblage (Goes et al., 2014). This shift of the phytoplankton community along the salinity gradient reflects the changes in environmental conditions. The mechanisms that underlay this shift and more specifically the prevalence of DDAs in the mesohaline waters have been the focus of numerous studies and are exposed in section 3.3.

1.2.4 The impact of the marine carbon cycling

Carbon is delivered by the Amazon in various forms, mainly DIC, DOC and POC. The estimated POC load varies depending on the study, with estimates based on observations suggesting lower values (5.8 Tg C yr^1 (Moreira-Turcq et al., 2003) and 6.1 Tg C yr^1 (Bird et al., 2008)) than estimates computed from models (17.1 Tg C yr^1 (Lacroix et al., 2020)). However, all studies agree on the fact that POC represents the smallest fraction of the total carbon load. In the vicinity of the Amazon mouth and shelf, terrestrial POC progressively settles down to the seabed, where it can be further entrained within a layer of fluid sediments. Indeed the energetic physical setting of the shelf creates an extensive mobile mudbelt that stretches up to the mouth of the Orinoco River at 9.5° N (Gensac et al., 2016; Nittrouer et al., 2021). The composition of this muddy sediment topset evolves along the way from mostly terrestrial (around 60-70%) in the proximal delta to mostly marine (Aller and Blair, 2006). The constant reworking and reoxidation of the mudbelt result in very high C remineralization rates, making it a ”gigantic sedimentary incinerator” (Aller and Blair, 2006). Even though most of the terrestrial POC tends to get remineralized, DeMaster and C. (2001) suggested that the preservation efficiency of terrestrial POC within the sediments might be ten times greater than that of marine POC.

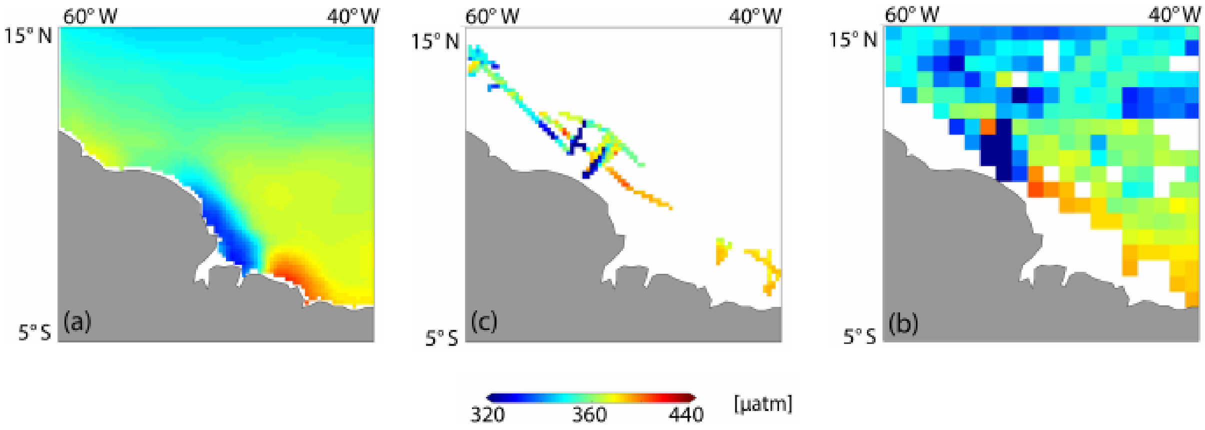

Figure 1.6 The climatological mean pCO_2 is reported for (a) a merged climatology based on two neural network-based pCO_2 products (Landschützer et al., 2020), (b) all available SOCATv5 data for the open ocean, covering the 1998-2015 period, and (c) all coastal SOCATv5 data. Adapted from Landschützer et al. (2020)

According to the most recent estimate (Drake et al., 2021), the Amazon supplies around 25.5 Tg C yr^{-1} in the form of DOC. Previous estimates were quite similar, although slightly higher e.g., 29 Tg C yr^{-1} (Araujo et al., 2014) or 28.2 Tg C yr^{-1} (Lacroix et al., 2020). This DOC load represents around 10% of the global flux of DOC to the ocean (Hedges et al., 1997). The labile fraction of terrestrial DOC, whose pool is replenished up to the mouth to the river by important lateral inputs (Seidel et al., 2016), is rapidly consumed upon its entry in the ocean, while a more refractory fraction is laterally transported on the shelf and beyond (Ward et al., 2013b). Medeiros et al. (2015) estimated that between 50 and 76 % of the terrestrial DOC flushed by the Amazon remains stable throughout the plume and is exported offshore. The Amazon thereby contributes significantly to the supply of long-lived terrestrial DOC to the open ocean.

DIC constitutes the largest fraction of the total carbon load delivered by the Amazon (32.7 Tg C yr^{-1} estimated by Araujo et al. (2014); 33.2 Tg C yr^{-1} estimated by Lacroix et al. (2020)). More important than the absolute value of DIC is its ratio to alkalinity. The Amazon River exhibits a high DIC concentration and low total alkalinity (472 mmol m^3), driving oversaturated conditions. This chemical CO_2 system balance is then modified in the ocean by the mixing with alkalinity-rich marine waters and the drawdown of DIC by biological activity Cooley et al. (2007).

The eventual effect of the Amazon river on the air-sea CO_2 balance is difficult to evaluate. In a recent global pCO_2 climatology that combines a coastal and an open ocean neural network-based products, the Amazon plume waters exhibit lower pCO_2 values over the shelf area in comparison to the surrounding waters (Figure 1.6-a). Offshore, the imprint of the Amazon is less evident and seems to dissipate rapidly. However, in the SOCAT observations, the low pCO_2 values extend further away from the river mouth, both on the shelf and in the open ocean (Figure 1.6-b-c). Landschützer et al. (2020) note that the paucity of observations, especially in the nearshore, and the large variance in observed pCO_2 are important challenges for neural-network based techniques to reconstruct the pCO_2 in the region.

In regional studies, the Amazon outflow has been shown to actually drive an initial CO_2 outgasing to the atmosphere, with measured CO_2 fugacity (fCO_2) ten times greater than oceanic fCO_2 (Sawakuchi et al., 2017; Lefèvre et al., 2017). The breakdown of reactive terrestrial DOC, combined with the delivery of already oversaturated river waters, is hypothesized to maintain high pCO_2 concentration (Sawakuchi et al., 2017; Ward et al., 2013b). Additionally, the high turbidity prevents any significant CO_2 uptake by photosynthesis that could have dampened this CO_2 evasion (Salisbury et al., 2011). The net heterotrophy of the system could be also the result of the high remineralization rates within the muddy fluid sediments as described above.

Further away from the mouth, the CO_2-oversaturated waters become undersaturated (Lefèvre et al., 2017). Numerous studies have provided estimates of the net air-sea CO_2 flux of the plume waters (table 1.1). These studies established first a relationship between oceanic pCO_2 and salinity based on field measurements and then extrapolated the measurements to the whole plume using sea surface salinity (SSS) data provided by the World Ocean Atlas (Körtzinger, 2003) or different remote sensing products (other studies). All studies predict that the Amazon plume is a sink of atmospheric CO_2, although estimates vary up to threefold. Strikingly, one recent study suggests that the plume is actually a source of atmospheric CO_2 (Valerio et al., 2021). In this study, the estimated outgasing in the inshore areas close to the river mouth offsets the CO_2 uptake of the rest of the plume. However, using the same observational dataset i.e., three sampling expeditions made in May–June 2010, September–October 2011, and July 2012, Mu et al. (2021) came to a different conclusion, indicating that a robust linear relationship between SSS and pCO_2 could only be established for a salinity range between 15 and 35. This study also highlights that SSS-pCO_2 relationships can diverge for certain months, suggesting to temporally refine these correlations. Eventually, Mu et al. (2021) do not provide an annual net air-sea CO_2 flux estimate, arguing that more observations are needed and that the effect of the biology and export should be better assessed.

Table 1.1 Estimates of net air-sea CO_2 flux within the plume waters

Study	Salinity range	Plume area [$km^{-}2$]	Tg of C yr^{-1}
Körtzinger (2003)	15 - 34.9	2.4 x 10^6	-14
Cooley et al. (2007)	28 - 35	0.73 x 10^6	-15 ± 6
Lefévre et al. (2010)	15 - 34.9	1.10 x 10^6	-5 ± 0.48
Ibánhez et al. (2015)	below 35[1]	0.89 x 10^6	-7.85 ±1.02
Valerio et al. (2021)	below 35	N/A	+8.6 ±7.1

[1] removing the influence of rainfall

The difficult of the research community to concur on the overall effect of the Amazon plume on the air-sea CO_2 balance stems from the high spatio-temporal variability of the physical and biogeochemical processes driving the surface pCO_2. Among these various processes, the increase of primary production and the enhancement of the biological pump's efficiency have been put forth as the two main factors driving the CO_2 undersaturation in the offshore plume waters (Yeung et al., 2012). More specifically, extensive blooms of DDAs have been documented in the vicinity of the plume (Carpenter et al., 1999; Foster et al., 2007; Subramaniam et al., 2008a; Weber et al., 2017) and are hypothesized to drive an efficient carbon export out of the euphotic zone (Korte et al., 2020). Subramaniam et al. (2008a) suggested that DDAs could be responsible for the carbon sequestration of up to 20 ± 8 Tg of C yr^{-1}. Thus, the stimulation of N_2 fixation by the Amazon appears to play a crucial role not only for nutrient cycling (section 2.2) but also for export production and the air-sea CO_2 balance of the WTA.

1.3 N_2 fixation in the Western Tropical Atlantic

1.3.1 The importance of N_2 fixation

N_2-fixation is a key component of the nitrogen cycle and represents an important source of bioavailable N, an essential macronutrient that limits the primary production in large portions of the ocean (Moore et al., 2013b). N_2 fixation rates are traditionally measured by acetylene C_2H_2 reduction or using the isotopic ^{15}N tracer methodology, although a plethora of new methods have been developed in recent years, including functional gene analysis and stable isotope probing (Zehr and Capone, 2021a). A current community-wide effort is ongoing to homogenize the measurements as well as understand and reduce the discrepancies between different methods. As part of the MARine Ecoystem DATa (MAREDAT) project, a first database gathered measurements of N_2 fixation rates, abundances and biomasses from the global ocean (Luo et al., 2012) and was recently further updated (Tang et al., 2019b). Although this database constitutes an indispensable benchmark, deriving from it a global estimate of total N_2 fixation remains a challenge, mostly due to the poor spatial and temporal coverage (figure 1.7-a). Different models were applied to infer this global estimate, giving quite a large range of results (table 1.2). Each method has its strengths and weaknesses and their lack agreement illustrates gaps in our understanding in the controls, diversity, variability of marine diazotrophy and the need of further investigation. I will present in more details the recent efforts in prognostic modeling as it is the method used in the present thesis (see section 3.4).

Table 1.2 Recent global estimates of N_2 fixation

Study	Method	Tg of N yr^{-1}
Luo et al. (2014)	equation derived from multiple linear regression	74 [51 - 110]
Paulsen et al. (2017)	prognostic ocean modeling	135.6
Tang et al. (2019b)	machine learning - Random Forest	68
Tang et al. (2019b)	machine learning - Support Vector Regression	90
Wang et al. (2019)	inverse biogeochemical & prognostic modeling	163.2 [125.6 - 222.9]

Modeling efforts and field measurements might not yet provide us with a definitive quantification of global N_2 fixation but they do agree on the global patterns, notably the higher abundances and rates in the tropical and subtropical regions (Pierella Karlusich et al., 2021). The Western Tropical Atlantic has been identified as a hot spot and as such, worthy of more scrutiny (Tang and Cassar, 2019). This region exhibits among the highest areal rates of N_2 fixation in the global ocean, with up to 10 000 μmol N m^{-2} d^{-1} (Tang et al., 2019b). The WTA is also the most sampled region in terms of N_2 fixation rates and N_2-fixer abundances (figure 1.7-a), which is an asset for the design of robust modeling framework. Lastly, the WTA is also a hot spot of N_2-fixers biodiversity, harboring the most important diazotrophic groups (figure 1.7-b).

1.3.2 The biodiversity of diazotrophs

Diazotrophs encompass a very diverse group of microorganisms (Zehr and Capone, 2020). First N_2-fixer to be formally identified in the ocean, *Trichodesmium* is a colonial cyanobacterium that does not form any heterocyst i.e, a specialized cell that fixes nitrogen (figure 1.8). *Trichodesmium* primarily inhabits oligotrophic tropical oceans where they are hypothesized to fix nearly half of the N_2 that sustains the local biomes (Jiang et al., 2018). They form colonies at shallow depths thanks to their gas vesicles providing natural buoyancy. Well suited for the high-irradiance regime of the surface tropical ocean, their photosynthetic apparatus reaches its maximum efficiency at high light and is resistant to photoinduced alteration (Capone et al., 1997). Their location at the surface and their phycoerythrin pigment make their large blooms detectable by remote sensing (Westberry et al., 2005). Both field measurements and laboratory data suggest that *Trichodesmium* are slow growing (Letelier and Karl, 1998; Mulholland and Capone, 2001; Holl and Montoya, 2008).

Other widespread diazotrophs are the heterocystous cynabacteria, *Richelia* and *Calothrix*, that live in symbiosis with diatoms of various genera, notably *Hemiaulus*, *Rhizolenia* or *Chaetoceros*. Their symbiosis is generically referred to as Diatom Diazotroph Assemblages (DDAs), although it is important to note that DDAs are host specific (Foster and Zehr, 2006). In fact, a recent phylogenetic study uncovered an ancient co-evolution of the symbiont/host pair (Caputo et al., 2019). In the WTA, the most sampled DDAs are composed of a *Richelia intracellularis* symbiont associated with a *Hemiaulus hauckii* or *Rhizosolenia clevei* diatom (Carpenter et al., 1999; Stenegren et al., 2017). The symbiont forms a trichome that comprises a heterocyst that fixes N_2 and several vegetative cells (figure 1.8). Multiple lines of evidence suggest that the majority of the N fixed by the diazotroph is then transferred to the host (Foster et al., 2011, 2021). It is assumed that the host provides shelter and essential nutrients to the symbiont although this has not been explicitly proven yet. Similarly, while both the symbiont and the host possess the

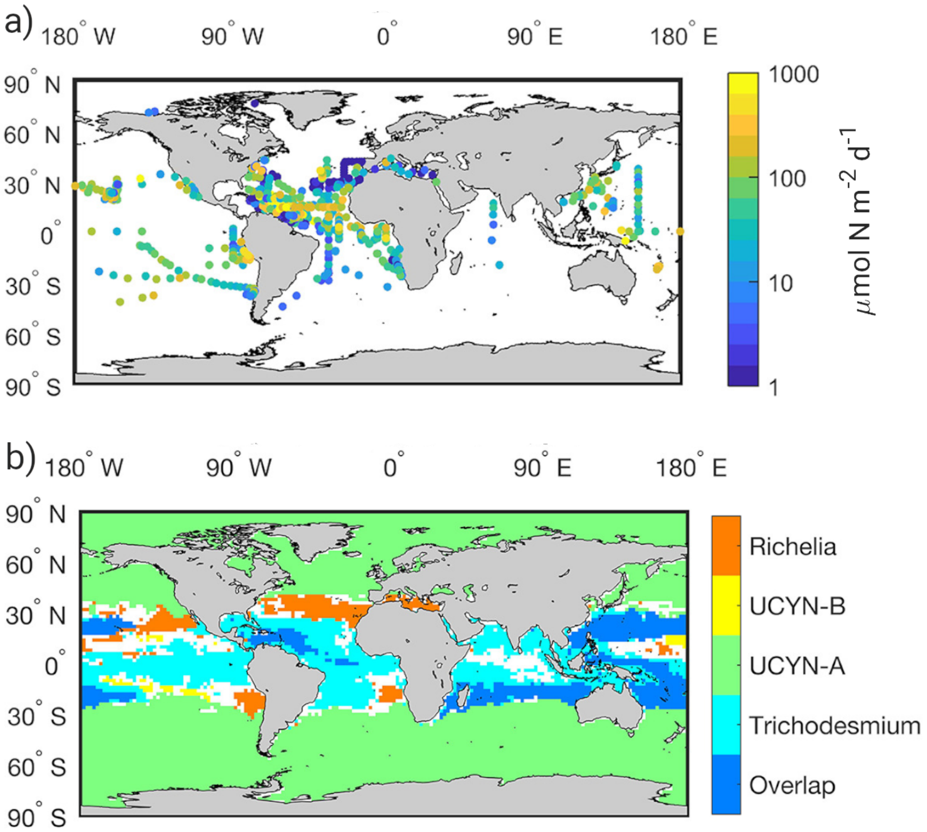

Figure 1.7 a) Field observations of depth-integrated N_2 fixation rates, map from Tang et al. (2019a). b) Simulated distribution of diazotrophs using a random forest machine learning technique, map from Tang et al. (2019b)

machinery to perform photosynthesis, uncertainties remain on which partner actually fixes C and how they might exchange C (Foster et al., 2021). Recent modeling efforts have demonstrated that the exchange of resources could explain the fact that the observed growth and N_2 fixation rates of DDAs are significantly higher than the rates of any other marine diazotroph (Inomura et al., 2020). A lot of open questions persist and the many intricacies of this singular partnership are currently the subject of a compelling research effort (Harke et al., 2018; Pyle et al., 2020; Foster et al., 2021).

More recently, the methodological advances and particularly the wide use of nitrogenase gene sequencing have uncovered the importance of unicellular cyanobacteria: UCYN-A, UCYN-B (*Crocosphera*) and UCYN-C. They represent a very diverse group of small size diazotrophs. UCYN-A is found in symbiosis with an haptophyte, a photosynthetic picoeukaryote. UCYN-A is highly dependant on its host as it does not fix C (Zehr et al., 2017). UCYN-B has been found both free-living and in association with a diatom (Foster et al., 2011). The physiology of UCYN-C remains unclear. Their ubiquity in the ocean and their N_2 fixation rates that are equivalent to those of *Trichodesmium* give them an unsuspected role in the global N_2 fixation (Montoya et al., 2004; Benavides and Voss, 2015; Landa et al., 2021). UCYN also challenge the current paradigm that confines N_2 fixation to the low-nutrient warm waters. For instance, UCYN-A appears to abound in colder and deeper waters (Langlois et al., 2005), in nutrient-rich upwelling regions (Tang et al.,

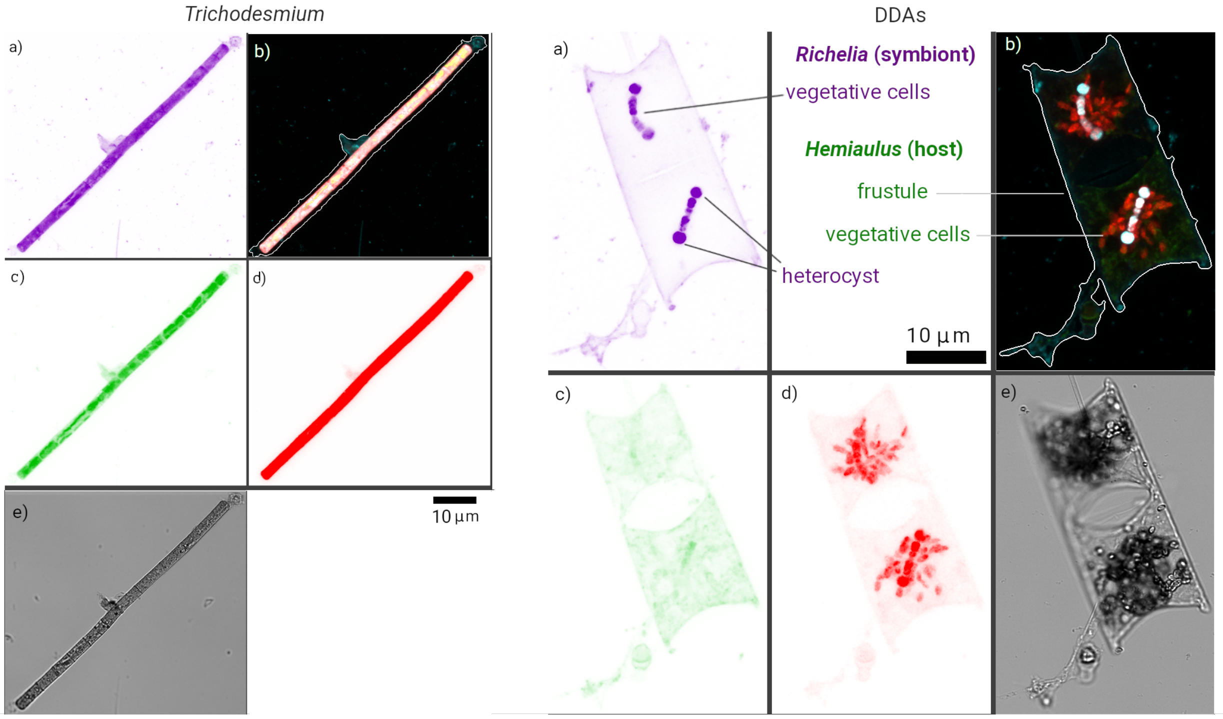

Figure 1.8 Images of *Trichodesmium* (left pannel) and *Hemiaulus inter Richelia* (right panel) retrieved during the Tara Ocean expedition using Environmental High-Content Fluorescent Microscopy (eHCFM). For both panels, each micrograph is displayed here and represents a) the cell surface, b) the cellular membranes, c) the chlorophyll autofluorescence, d) the bright field and e) the merged channels. Source: https://www.ebi.ac.uk/biostudies/S-BSST529 (last access: Oct21, 2021), compiled by Pierella Karlusich et al. (2021).

2019b) and has even been detected in the Arctic Ocean (Shiozaki et al., 2018; Harding et al., 2018).

All three of these major diazotrophic groups have been detected in the WTA. UCYN-A, B and C were present only at low abundance (Goebel et al., 2010), while DDAs and *Trichodesmium* dominate the regional diazotrophic flora (e.g., Carpenter et al. (1999); Capone et al. (2005); Subramaniam et al. (2008a)).

1.3.3 Factors controlling N_2 fixation

Similar to other phytoplankton, the growth of diazotrophs is primarily controlled by light, temperature and nutrient availability. Temperature is associated to their physiological bounds and as such could partly explain the global distribution of N_2 fixation (Stal, 2009). However, UCYN appear to tolerate a wider temperature range than expected for a diazotroph. Besides temperature also correlates with many other factors such as nutrient concentrations. While important, temperature has been shown to not directly control the N_2 fixation biogeography (Monteiro et al., 2011; Zehr and Capone, 2021b).

More important in driving the global patterns of N_2 fixation is the availability of nutrients. Due to their lower growth rate, diazotrophs are assumed to be poor competitors in N-replete conditions. In contrast, the scarcity of N in the oligotrophic gyres gives them a competitive advantage against the non-diazotrophic phytoplankton. Nevertheless, their growth is limited by other nutrients, namely phosphorus and iron. Because nitrogenase i.e., the enzyme that catalyzes the reduction of N_2, comprises two Fe-rich proteins, the growth of diazotrophs is often limited by Fe (Sohm et al., 2011). However in regions that received large inputs of iron-rich atmospheric deposition, e.g the whole tropical North Atlantic, P is believed to constitute the main limiting nutrient (Dutkiewicz et al., 2014). Following the resource-ratio theory introduced by Tilman (1982), Ward et al. (2013a) suggested that the ratio in which N, P and Fe are supplied with regard to the physiological needs of each phytoplankton shapes the competition between diazotrophs and non-diazotrophs, determining the ecological success of N_2-fixers even more than the absolute concentration of nutrients. Building on that conceptual framework, Landolfi et al. (2018) demonstrated that DOP should also be considered as its direct utilization by N_2-fixers (e.g., Orchard et al. (2010); Watkins-Brandt et al. (2011); Meyer et al. (2016)) reinforces their competitive advantage especially in PO_4-depleted environment such as the North Atlantic.

In the WTA, early work focused on *Trichodesmium* (Carpenter et al., 2004; Capone et al., 2005). One exception is the study by Carpenter et al. (1999) that documented, for the first time in the WTA, large blooms of DDAs and speculated on the role of the Amazon in sustaining this intense N_2 fixation. Multiple lines of evidence have now established that several phytoplankton communities are cascading along the salinity gradient (see section 2.3). The transition from coastal diatoms to DDAs has been attributed to the progressive decline of inorganic N, giving room for DDAs to thrive on the remaining P and $Si(OH)_4$ (Subramaniam et al., 2008a; Goes et al., 2014; Weber et al., 2017). The eventual depletion of $Si(OH)_4$ would then explain the decrease of DDAs and the expansion of Trichodesmium in the oceanic waters. Stukel et al. (2014) tested these hypotheses using an ecological model ie., Diazotroph Interactions with Algae and Zooplankton in the Ocean (DIAZO), coupled to a physical model i.e., Hybrid Coordinate Ocean Model (HYCOM). In DIAZO, on top of *Trichodesmium*, two pairs of diazotroph-non-diazotroph analogs are represented: Cyanobacteria and unicellular diazotrophs; diatoms and DDAs. The analogs only differ in their N limitations and growth rates. With this modeling framework, Stukel et al. (2014) confirmed the central role of nutrient supply, and especially the excess of $Si(OH)_4$ to N, in the DDA bloom formation. However, their results also suggest that this explanation is incomplete and that two other prerequisites might be equally important to sustain the prevalence of DDAs in the mesohaline waters: the cessation of the grazing pressure and the duration of time spent by DDAs in their ideal habitat. The grazing pressure is hypothesized to decrease in response to physically driven dilution. Associated with DDA specific growth rates remaining elevated, the decrease of the top-down pressure allows DDAs to accumulate biomass, provided they remain at least 23 days in their environmental niches. In the oceanic waters, the DDA bloom termination is related to a strong Si limitation. This study comes nevertheless with a few shortcomings, some of which are underlined by Stukel et al. (2014) themselves. The bottom-up controls are somehow simplified as the model does not consider Fe nor DOP and does not differentiate the half saturation constants between the analogs. Furthermore, Stukel et al. (2014) did not explore the relative importance of bottom-up and top-down controls in relation to the competition between diazotrophs and non-diazotrophs and among diazotrophs nor did they investigate the consequences of the prevalence of DDAs on the carbon cycle.

Regardless of these limitations, this work by Stukel et al. (2014) is one the first studies to speculate on the role of top-down controls on the biogeography of N_2 fixation. This has prompted new field measurements (Conroy et al., 2016, 2017) which found evidence of the transfer of N_2 fixers biomass in the upper trophic levels through direct and/or indirect grazing. This putative importance of top-down controls has also been emphasized in a recent modeling study investigating the diazotrophic biogeography at the global scale Wang et al. (2019), suggesting that top-down controls might play a key role in the puzzling spatial decoupling of N_2 fixation and denitrification.

1.3.4 Modeling N_2 fixation

Modeling experiments have proved extremely important in pushing boundaries in our comprehension of N_2 fixation. The representation of N_2-fixers, especially the level at which processes are resolved, varies widely depending on the goal of the study and the computational capabilities. Numerous earth system models in the context of the Intergovernmental Panel on Climate

Change (IPCC) use an implicit representation of N_2 fixation (Ilyina et al., 2013; Landolfi et al., 2018). It consists in the restoring of the N:P ratio at the surface ocean. Some models using this restoring technique additionally accounts for other factors, e.g P and Fe limitations in the case of the PISCES model (Aumont et al., 2015). The explicit representation of N_2 fixation can be as detailed as coarse-grained models that resolves major cellular functions or, even more complex, as metabolic models that include genome-scale reactions (figure 1.9). Computationally expensive, these types of models are best suited for some scale experiments, as a complement to laboratory work (Inomura et al., 2020).

Monod-type equations that are usually implemented in ecological models, including in this present study, are intermediate in terms of complexity (figure 1.9). The growth rate of the considered N_2-fixer is generally described as a function of light, temperature and nutrient availability. The N_2 fixation rates are derived from the N required to sustain the C fixation, based on the elemental stoichiometry of the cells. This type of modeling comes down to a reduced number of equations and state-variables which is compatible with large-scale ocean simulations. However, when an explicit representation of N_2 fixation is implemented, only one type of N_2 fixer i.e *Trichodesmium* is generally accounted for (Moore et al., 2013c; Paulsen et al., 2017; Wang et al., 2019). The single diazotroph approach limits our capabilities to capture the distribution of N_2 fixation and to understand its controlling factors. Highlighting the ecophysiological diversity of N_2 fixers, Tang et al. (2019b) pleaded for a differentiation of the main diazotroph phylotypes in ocean modeling, which for now has only been the case in a few regional studies (e.g., Stukel et al. (2014); Follett et al. (2018)).

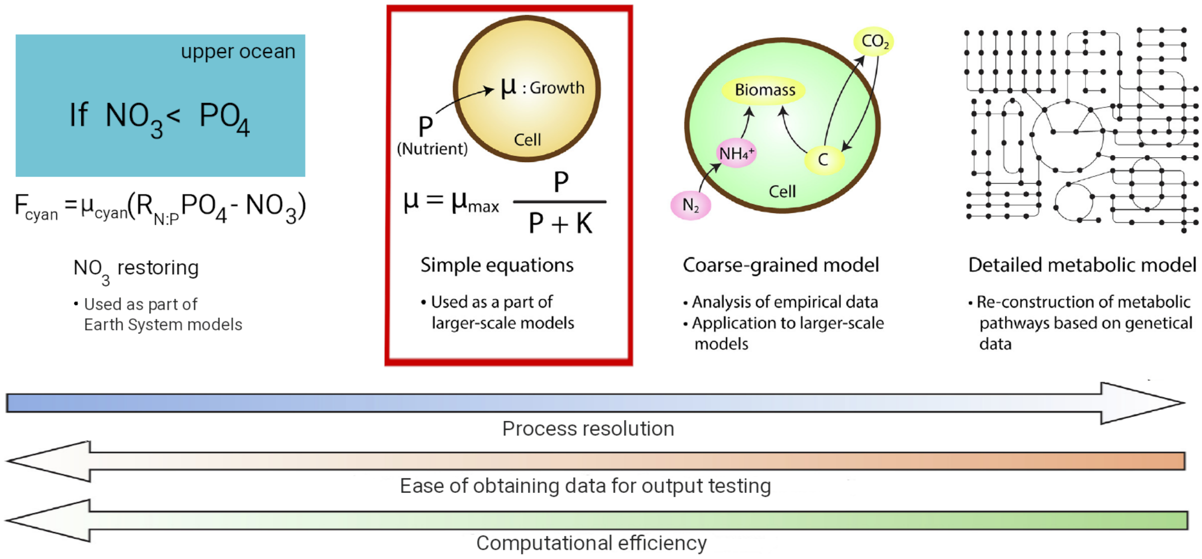
upper ocean
If $NO_3 < PO_4$
$F_{cyan} = \mu_{cyan}(R_{N:P} PO_4 - NO_3)$
NO_3 restoring
• Used as part of Earth System models
μ : Growth
P
(Nutrient)
Cell
$\mu = \mu_{max} \frac{P}{P+K}$
Simple equations
• Used as a part of larger-scale models
CO_2
Biomass
NH_4^+
C
N_2
Cell
Coarse-grained model
• Analysis of empirical data
• Application to larger-scale models
Detailed metabolic model
• Re-construction of metabolic pathways based on genetical data
Process resolution
Ease of obtaining data for output testing
Computational efficiency

Figure 1.9 Schematics of 4 different types of N2-fixation modeling. In the equation, μ_{max} is maximum growth rate, K is the half saturation constant that drives the growth depending on the nutrient concentration. The red square highlights the model used in this thesis. Adapted from: Inomura et al. (2020)

1.4 Open questions

Over the past decades, numerous field studies have started to reveal the extent of the Amazon's influence on the air-sea CO_2 balance, nutrient cycling and marine ecology of the WTA. In particular, the Amazon has been shown to alter phytoplankton communities, enhance N_2 fixation and drive negative pCO_2 anomalies. The running hypothesis is that the riverine nutrients favor the formation of large blooms of N2-fixing DDAs, which enhances the biological pump. The modification of the biological pump would then result in low surface pCO_2 concentrations, turning the plume waters into a sink of atmospheric CO_2. However, up until now, establishing quantitative links between all these processes has been hindered by the sparsity of observations in regard to the high variability of the system. Besides, a lot of questions persist on the distinct role the riverine nutrients in shaping the phytoplankton community, on the relative role of grazing, on the feedbacks of the modified community on the cycling of nutrients. It remains also unclear what is the relative importance of the biological pump compared to other physical and chemical processes affected by the Amazon, notably by the delivery of DOC, DIC and alkalinity. Lastly, the system experiences interannual variability that cannot be really investigated in the absence of regular measurements. High resolution modeling can contribute to overcome these challenges and fill the gaps in our comprehension of the underlying processes responsible for these pCO_2 anomalies.

1.5 Thesis structure

1.5.1 Objectives

The overarching goal of this thesis is to participate in a more comprehensive understanding of the impact of a large river system, the Amazon River, on the marine nutrient and carbon cycling. In more detail, I aim at (i) unfolding the cascading effects of the riverine inputs on the biological pump and (ii) determining the role of the Amazon in sustaining the high rates N_2 fixation of the Western Tropical Atlantic Ocean. My thesis thus addresses the following research questions:

(Q.1) *What are the individual and cumulative impacts of the riverine nitrogen, phosphorus and silicic acid inputs on the marine primary production? How do shifts in the phytoplankton community structure affect the export production?* (Chapter 2)

(Q.2) *How much does the Amazon River alter the air-sea CO_2 fluxes in the WTA? What are the different factors driving the changes in the air-sea CO_2 balance?* (Chapter 2)

(Q.3) *How much does the Amazon contribute to the high rates of N_2 fixation in the WTA? In what ways do the riverine inputs affect the bottom-up and top-down factors that control the phytoplankton competition and eventually determine the ecological success of Diatom-Diazotroph-Assemblages (DDAs)?* (Chapter 3)

(Q.4) *What is the response of N_2 fixation in the WTA to the Amazon discharge variability and the climate variability on interannual timescales? What are the mechanisms driving the negative and positive anomalies of N_2 fixation?* (Chapter 4)

1.5.2 Approach

To investigate the above stated research questions, I used a coupled physical-biogeochemical-ecological model, ROMS-BEC (Shchepetkin and McWilliams, 2005) that is configured for the Atlantic Ocean. The model runs on a telescopic grid, allowing a high spatial resolution (down to 4 km) in the Amazon plume region, especially the mouth of the river and the shelf area. I extended the standard version of BEC to include an explicit representation of DDAs, amounting the N_2-fixers represented in the model to two - the second being *Trichodesmium*.

Two types of simulations were performed: one forced by climatological conditions and one forced by realistic, variable conditions derived from reanalysis products and representing the conditions from 1979 until 2019. For both types, several factorial simulations were performed. The simulation in climatological conditions was ran 9 times, each time with a different riverine inflow e.g with the whole suite of nutrients, without nitrogen, without DOC etc. The hindcast simulation was ran 4 times, including or excluding the Amazon discharge variability and the climate variability.

More details on the model parametrizations and the exact configuration of the simulations can be found in the method section of chapters 2 and 4.

1.5.3 Chapter overview

Chapter 2 quantifies the alteration induced by the Amazon on the Net Primary Production (NPP), Export Production (EP) and air-sea CO_2 balance. For each process, we investigate the mechanisms driving the changes, based on the results of 9 factorial simulations. More specifically, we assess the role of the riverine nutrients and their stoichiometry in the differential enhancement of NPP and EP. We determine how these changes in the biological pump eventually affect the air-sea

CO_2 balance and quantify their relative contribution in comparison to other driving factors. This study intends to answer the research questions 1 and 2.

This study was published in Global Biogeochemical Cycles as:
Louchard, D., Gruber, N., & Münnich, M. (2021). The impact of the Amazon on the biological pump and the air-sea CO2 balance of the Western Tropical Atlantic. Global Biogeochemical Cycles, 35, e2020GB006818. https://doi.org/10.1029/2020GB006818

Chapter 3 quantifies how much N_2 fixation is enhanced by the Amazon inputs and determine the relative contribution of DDAs versus *Trichodesmium* in this increase. To understand why N_2-fixers and especially DDAs are favored, we investigate how the presence of the Amazon modifies the factors controlling the phytoplankton competition, focusing on both the bottom-up and top-down controls as well as the balance between the two.

This study is in preparation for Global Biogeochemical Cycles as:
Louchard, D., Gruber, N., & Münnich, M. Enhanced N_2 fixation in the Western Tropical Atlantic Ocean in response to the Amazon River and its modification of the phytoplankton competition

Chapter 4 investigates the variability of N_2 fixation in response to the variability of the Amazon discharge and different climate modes i.e the El Niño-Southern Oscillation (ENSO) and the Atlantic Meridional Mode (AMM). Using different hindcast simulations that isolate the discharge-related variability and the climate-related variability, we assess the driving mechanisms responsible for the changes in N_2 fixation.

This study is in preparation for Global Biogeochemical Cycles as:
Härri, J., Louchard, D., Gruber, N., & Münnich, M. The Interannual Variability in Marine N_2 Fixation and its Drivers in the Western Tropical Atlantic

Chapter 5 offers a synthetic overview of the main findings, answering the key questions detailed in section 4.1. This last chapter also discusses the limitations and shortcomings of the performed simulations and analysis. Finally, it provides ideas on how to expand on the present study and new research avenues to explore.

Appendix A, B, & C provide supporting information, such as model characteristics, additional results and additional figures for chapters 2, 3, and 4.

Chapter 2

The impact of the Amazon on the biological pump and the air-sea CO_2 balance of the Western Tropical Atlantic

D. Louchard, M. Münnich, N. Gruber

Environmental Physics, Institute of Biogeochemistry and Pollutant Dynamics, ETH Zurich, Universitätstrasse 16, 8092 Zürich, Switzerland.

This manuscript was published under the same title in ***Global Biogeochemical Cycles****, 2021, Citation*

Abstract

The Amazon River strongly modifies the biogeochemistry of the Western Tropical Atlantic (WTA). To disentangle the different mechanisms driving these modifications, we conduct a series of modelling experiments with a high resolution regional ocean model (ROMS) coupled to a biogeochemical/ecological model (BEC) that we augmented to include Diatom-Diazotroph-Assemblages (DDAs). In our model, the Amazon river increases net primary production (NPP) in the WTA by almost 10%, exceeding the stimulation expected from the supplied inorganic nitrogen and phosphorus by a factor of two. This amplification is fueled by new nitrogen stemming from DDA-driven N_2 fixation in the plume region, supported, in part, by the consumption of riverine dissolved organic phosphorus. The vertical export of organic carbon is enhanced by a shift of the phytoplankton community towards diatoms induced by the large amount of $Si(OH)_4$ delivered by the Amazon. These changes in NPP and export production induce a strong uptake of atmospheric CO_2. In contrast, the remineralization of the river-delivered terrestrial organic matter leads to a release of CO_2 over the WTA, which is partially offset by a net uptake induced by the riverine dissolved inorganic carbon and alkalinity. Overall, the Amazon reduces the strong outgassing of the WTA in our simulations by more than 50 %. Our study demonstrates how rivers modify the marine biological pump and the air-sea CO_2 fluxes in the downstream ocean through a myriad of cascading effects, highlighting the need to fully consider the land-ocean aquatic continuum in the modeling of the Earth System.

2.1 Introduction

From its upland basin to the open ocean, the Amazon River connects the world's most productive rainforest to the oligotrophic Western Tropical Atlantic (WTA), i.e., the region bounded by the equator in the south, 24° N in the north, the Lesser Antilles in the west, and 30° W in the east. Every second, the Amazon delivers about 190 000 m^3 of turbid freshwater rich in nutrients and organic matter, altering both the physical and biogeochemical properties of the ocean over up to 1.6 millions of km^2, i.e more than 15% of the WTA (Coles et al., 2013; Araujo et al., 2017; Ward et al., 2017; Gouveia et al., 2019).

Once most of the sediment load has settled and the water cleared up, the massive discharge of riverine nutrients spawns a large and persistent phytoplankton bloom (Smith and DeMaster, 1996; Dagg et al., 2004; Da Cunha and Buitenhuis, 2013). Many dedicated *in situ* sampling programs have demonstrated that this high productivity is sustained by coastal diatoms and predominantly located on the continental shelf and along the northward pathway of the plume (Smith and DeMaster, 1996; Demaster et al., 1996; Araujo et al., 2017; Gouveia et al., 2019). As the riverine nutrients are being drawn down by marine phytoplankton, the high ratio of $Si(OH)_4$ to NO_3 within the Amazon waters causes $Si(OH)_4$ in the plume waters further offshore to remain elevated when NO_3 becomes exhausted (Subramaniam et al., 2008a; Goes et al., 2014; Weber et al., 2017). This effect is exacerbated by the dynamics at the sediment interface: the Amazon plume initially follows the coast northward on the North Brazilian shelf, where benthic denitrification creates an additional sink for NO_3 (Aller et al., 1996). The resulting deficiency of NO_3 relative to PO_4 and $Si(OH)_4$ is thought to provide the conditions that foster high rates of N_2 fixation supported primarily by Diatom-Diazotroph-Assemblages (DDAs) (Foster and O'Mullan, 2008; Subramaniam et al., 2008a; Foster and Capone, 2012). DDAs are symbioses between diatoms of various genera (mostly *Hemiaulus* and *Rhizosolenia* in the WTA) and a diazotrophic cyanobacterial (*Richelia intracellularis*). The symbiont reduces nitrogen and provides ammonia to its host, while the host provides shelter and improves access to the limiting nutrients (Foster et al., 2011). As this symbiosis involves a large siliceous diatom, DDAs may be much more efficient in exporting the fixed organic carbon to depth compared to other more common diazotrophs such as *Trichodesmium*. Thus DDAs have been hypothesized to be the main pathway of carbon export within the plume waters (Subramaniam et al., 2008a; Yeung et al., 2012). Furthermore, the newly introduced fixed nitrogen can fuel more biological production downstream in the very oligotrophic WTA, where NO_3 levels are almost always below detection (Hansell and Follows, 2008).

The enhancement of the marine biological pump by the Amazon River is recognized as a crucial factor for the CO_2 undersaturation typical of the plume waters driving an uptake of CO_2 from the atmosphere (Subramaniam et al., 2008a; Yeung et al., 2012; Araujo et al., 2017). Estimates of this plume-related carbon sink range from 5 Tg C yr^{-1} (Leféyre et al., 2010) to 15 Tg C yr^{-1} (Cooley et al., 2007), reversing the expected paradigm of CO_2 release of the tropical ocean. But the impact of the Amazon on the air-sea CO_2 fluxes is more complex than just an enhancement of the biological pump. From the low-salinity waters, where terrestrial organic carbon is fueling heterotrophy (Lefèvre et al., 2017) and thus CO_2 out-gassing, to the open ocean, where the riverine input of Dissolved Inorganic Carbon (DIC) and Alkalinity (Alk) is diluted but still detectable (Leféyre et al., 1998; Cooley et al., 2007), the Amazon has a wide range of impacts that vary in space and time. Modeling experiments can help to disentangle the different contributions of the Amazon River to the air-sea CO_2 balance.

Only two studies have so far quantified the impact of the Amazon River on productivity and the air-sea CO_2 fluxes in the WTA. Da Cunha and Buitenhuis (2013) found a 5% increase in NPP and export production across the WTA, but the Amazon induced in their model only a modest reduction in the outgassing prevalent in the WTA. More recently, Lacroix et al. (2020) simulated an even larger relative enhancement of NPP, but they found the opposite effect on the air-sea CO_2 fluxes, i.e., that the Amazon makes the outgassing of the WTA even stronger. They argued that this is primarily a consequence of the large input of terrestrial organic carbon, whose remineralization within the WTA produces an excess of CO_2 that drives outgassing. Both studies used global models with resolutions of the order of 100 km or more, raising questions about the fidelity of their modeling the complex circulation of the WTA. In particular, their model resolutions were too coarse to resolve mesoscale dynamics, which have been shown to play a crucial role in the dispersal of the plume (Fontes et al., 2008; Coles et al., 2013; Gouveia et al., 2019). In addition, neither study looked at the relative ratios of the different river-delivered organic and inorganic nutrients and in what way their interaction can shift e.g., the phytoplankton community with potential consequences for export production. Most importantly, these studies did not include DDAs and thus potentially missed an important source of extra nitrogen that can fuel further ocean productivity downstream. DDAs were so far only accounted in the modeling study by Stukel et al. (2014). But they limited their focus on the factors controlling the blooms of DDAs, and thus did not investigate the impacts of the Amazon on the DDAs' export production or on the air-sea CO_2 exchange.

In the present study, using a modeling approach, we aim to capture and quantify most of the physical and biogeochemical/ecological complexities associated with the impact of the Amazon on the biological pump and the air-sea CO_2 fluxes in the WTA. To this end, we use an eddy-resolving configuration of the Regional Oceanic Modeling System (ROMS) (Shchepetkin and McWilliams, 2005) coupled to a biogeochemical/ecological module (BEC) (Moore et al., 2013c) that has been modified to include DDAs. We first investigate the response of NPP and carbon export based on different factorial simulations, where one or all the nutrients are removed from the Amazon river inflow (section 3). We then quantify the overall effect of the Amazon River on the air-sea CO_2 balance from the mouth of the river to the open ocean and assess the contribution of the different processes controlling this balance (section 4) paying special attention to the interaction of the different biogeochemical cycles and the cascading effects within these, i.e., the fact that the outcome of one process induces changes in another process further downstream.

2.2 Methods

2.2.1 ROMS-BEC with explicit DDAs

We use the UCLA-ETH version of the Regional Ocean Modeling system (ROMS, (Shchepetkin and McWilliams, 2005)), in which we updated the advection scheme for all tracers to the Weighted Essentially Non Oscillatory (WENO) scheme (Vandemeulebrouck, 2020), as this ensures higher accuracy while maintaining positivity. The model runs on a newly configured grid (576×450 grid points) that spans the whole Atlantic basin around two poles: one centered on the Amazon river mouth (0° N; 53° W) and the other one over Western Africa (18° N; 4° W) (Figure 2.1). This telescopic framework results in a high resolution in the tropical regions, from $\sim$4 km to $\sim$14 km and a coarser resolution in the outskirts of the grid (from ~ 50 to ~ 120 km). In the vertical, the model is discretized with 42 sigma layers, with an enhanced resolution in the top 100

m. As a result, 18 layers are usually found within this depth range. The northern boundary toward the Arctic and the eastern boundary within the Mediterranean are closed, while the southern boundary toward the Southern Ocean is open.

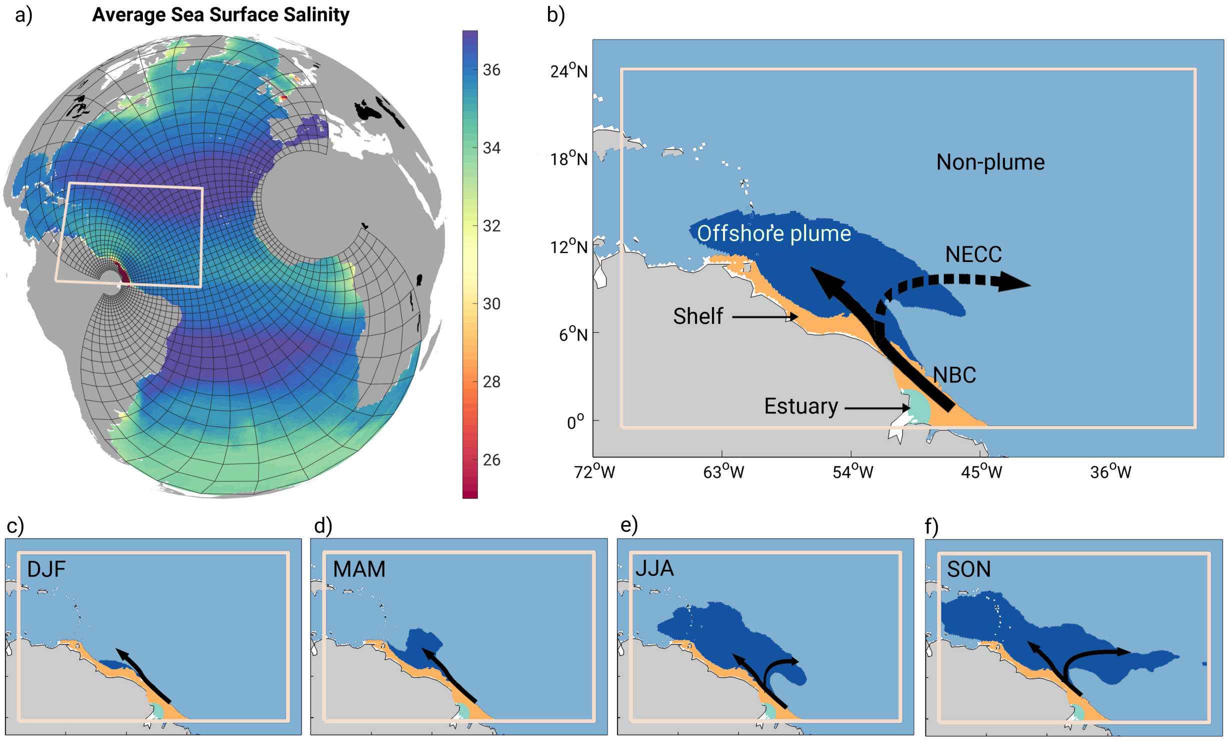

Figure 2.1 Maps of the model domain and the analysis regions: (a) Model domain showing the modeled annual average sea surface salinity, and the telescopic grid at by every 12th grid line. The white quadrilateral indicates our region of study (0.5° S-24° N; 30°-70° W) (b) Map of the analysis region with the annual average offshore and non-plume areas colored in dark and light blue, respectively. Black arrows indicate the North Brazilian current (NBC) and the seasonally varying North Equatorial Counter Current (NECC). (c-f) Seasonal maps illustrating the evolution of the offshore plume and non-plume waters. See text for how we delineated the different areas.

ROMS is coupled to an ecological/biogeochemical model (BEC, (Moore et al., 2013c)) that resolves the cycling of carbon, oxygen and different macro and micro nutrients, namely nitrogen, phosphorus, silicon and iron. These elements, along with light and temperature, govern the growth of four phytoplankton functional types (PFT). The standard version of BEC includes diatoms, a generic small phytoplankton class, diazotrophs (representing the most abundant marine diazotroph, *Trichodesmium spp*.) and one zooplankton class. A fraction of the small phytoplankton PFT is modeled to consist of coccolithophores, with their associated formation of calcite.

We added to this model an explicit representation of Diatom-Diazotroph-Assemblages (DDAs). We allowed two states for the DDAs, i.e., symbiotic and non-symbiotic, depending on the seawater NO_3 concentration. DDAs are assumed to be in a non-symbiotic state, i.e., without a diazotrophic symbiont, when NO_3 is above 0.5 mmol N m^{-3}. In this case, we regard the DDAs as regular diatoms with the same half saturation constant for NO_3 and ammonium as the normal diatom class. This threshold was determined by analyzing in the database from Luo et al. (2012) the environmental NO_3 concentration present when the biomass of DDAs drops to near zero (Figure A.1). Below our threshold, DDAs are truly represented as a symbiosis and are modeled by combining key traits of both diatoms and diazotrophs (Table A.1). As diazotrophs, DDAs can fix N_2 for their nitrogen needs, but require higher levels of iron to do so. In addition, DDAs, like *Trichodesmium*, can uptake dissolved organic phosphorus (DOP) with the same efficiency as they can take up PO_4, in agreement with several experimental studies (Watkins-Brandt et al., 2011; Girault et al., 2013) . As diatoms, the growth of the DDAs is limited by $Si(OH)_4$. Upon death or grazing, their contribution to the pool of particulate organic carbon (POC) is the same as that of the regular diatoms (Table A.1).

The C:N:P ratios of phytoplankton are fixed in BEC, with a stoichiometry close to the Redfield ratios: 117:16:1 for small phytoplankton, diatoms and DDAs (Anderson and Sarmiento, 1994), 117:45:1 for *Trichodesmium* (Letelier and Karl, 1998). The uptake and release of these macronutrients by phytoplankton follows the same ratios. If zooplankton is grazing on *Trichodesmium*, the phosphorus in excess compared to the standard Redfield ratio is assumed to be excreted immediately and split between the PO_4 pool (85%) and the DOP pool (15%). The ratios of Si:C, Fe:C and Chl:C are not fixed and can vary depending on the ambient nutrient levels. Thus, the Si:C ratio of diatoms and DDAs increases when iron is depleted leading to a stronger silification. Conversely, it decreases when $Si(OH)_4$ is scarce (less than 2 mmol m^{-3}).

In BEC, POC is directly produced by phytoplankton through non-grazing mortality and aggregation. The single zooplankton class grazing on all PFTs also produces POC as a result of sloppy feeding, egestion and mortality. The vertical sinking flux of POC and its remineralization is modeled following the ballast/protection model of Armstrong et al. (2001), which assumes that sinking material is either free or associated with ballasting minerals. Ballasting minerals in ROMS-BEC include calcite from coccolithophores, silica from diatoms and DDAs, and mineral dust from atmospheric deposition. The composition of the particulate matter determines its remineralization/dissolution length scale, from which the organic matter remineralization rates are determined given the implicit sinking scheme of BEC. A fraction of POC and other particulate organic matter arriving at the sediments is buried following Dunne et al. (2007) with a fixed maximum of 80%. Sediment denitrification represents an additional loss term for nitrogen. The remaining fraction of particulate organic matter is immediately remineralized based on the early diagenesis model of Soetaert et al. (1996), feeding back the inorganic carbon and nutrient pools.

Around 15% of the produced organic matter in the euphotic zone is simulated to be channeled to the dissolved organic matter (DOM) pool. Due to the decoupling between production and remineralization of its C, N and P fractions, DOM in BEC has a variable C:N:P stoichiometry. Upon production, a fraction of DOM is considered semi-labile, another refractory. Each DOM tracer has an assigned lifetime that varies depending on the light field in the considered grid cell. More specifically, it is assumed that the lifetime of DOM is shorter when the photosynthetically active radiation (PAR) is above 1% of surface irradiance and longer when PAR is below 1% (Table A.2). Our parameterization and parameter values lead to a typical lifetime for semi-labile DOM ranging from 5 months (PAR $> 1\%$) to 10 years (PAR $< 1\%$), and for the refractory pool of DOM from 2.5 years to 670 years, respectively.

2.2.2 External sources of nutrients

In the model, the Amazon river is represented as a three-dimensional influx boundary condition, supplying brackish water and dissolved constituents to the ocean (see Table A.3 in the supplementary section). We placed the boundary within the Amazon estuary, so that the inflowing waters reflect already some mixture of pure Amazon waters and marine conditions, resulting in an annual mean salinity of 3.8. We prescribe monthly variations of discharge at this boundary, including its temperature and salinity as well as the dissolved constituents: alkalinity, dissolved inorganic/organic nutrients and dissolved organic/inorganic carbon (Table A.3). We split the DIN estimate between NO_3 and NH_4 based on the NO_3:NH_4 ratio reported by DeMaster et al. (2001). The input concentration of all other state variables is set to zero. We obtained most of these input concentrations from a climatology that was derived from a comprehensive compilation of observations and model-based estimates (Araujo et al., 2014). We obtain the riverine input of dissolved organic nitrogen (DON) and dissolved organic phosphorus (DOP), by multiplying the input of DOC with a fixed stoichiometric ratio derived from the canonical C:N:P ratio of 117:16:1. Under this assumption, DON and DOP represent a significant component of the overall N and P inputs. Such a high organic nutrient contribution is typical for natural tropical river systems such as the Amazon (Seitzinger et al., 2005). We note that in light of the importance of DOP in our system, this assumption is nevertheless critical, which we will discuss in more detail in the caveat section. This contrasts with the stoichiometry of the inorganic nutrients (Table A.3): In the annual mean, the N:P:Si ratios of the inputs amount to 14:1:155, i.e., the Amazon input is characterized by a slight excess of P over N (relative to the canonical Redfield ratio), and a very large excess of Si over both N and P (iron replete diatoms tend to draw down the nutrients with a N:P:Si ratio of about 1:16:1 (Brzezinski et al., 2003). In the model, all dissolved constituents are added to their corresponding marine semi-labile corresponding state variables, i.e., once in the ocean, we do not differentiate between the terrestrial and marine sources of these constituents.

We do not consider the riverine input of any particulate matter in our model. The vast majority of the river supplied particulate matter sinks rapidly to the seafloor once the flow speed slows down upon arrival of the waters near the mouth of the river. At the seafloor, part of the material is buried, and part is remineralized, impacting the biogeochemistry of the water column indirectly. Although we do not explicitly model this process, we partly account for these remineralization fluxes through our parameterizations of the fluxes across the sediment-water interface.

In the estuary and near the mouth of the Amazon, where salinity is less than 31, we apply an attenuation coefficient to the photosynthetically active radiation (PAR) to account for the effects of river supplied colored dissolved organic matter (C-DOM) and turbidity on the vertical penetration of light. The attenuation coefficient is assumed to vary linearly with salinity, using a regression determined from *in-situ* measurements by Del Vecchio and Subramaniam (2004), i.e., $\text{PAR}_c = \text{PAR} \cdot (0.232 + S)$, where PAR_c is the PAR corrected for the additional attenuation, and S the local salinity (in practical salinity units). This parameterization leads to a substantial reduction of the vertical light penetration up to 700 km away from the mouth of the river during the high discharge regime in June.

The other major rivers within our Atlantic model domain are represented as surface freshwater and nutrient fluxes, spread over several grid points neighboring the river location, in the same manner as in previous ROMS-BEC simulations (Lovecchio et al., 2017; Frischknecht et al., 2018). These freshwater fluxes are derived from the observational data base of Dai et al. (2009) and the associated NO_3 and PO_4 fluxes are estimated from (Beusen, 2014).

Finally, we added forcing fields of atmospheric nitrogen, phosphorus and dust, based on the work of Mahowald et al. (2009) and assume that 3.5% of the dust constitutes iron, of which 2% is bioavailable. These inputs are added directly to the corresponding surface fields in ROMS. In using these fields the atmospheric N deposition in the WTA is of the same order of magnitude as the DIN delivered by the Amazon, i.e., 0.6 and 0.9 Tg N yr^{-1} respectively, while the deposition of P is substantially lower (Tables S4 and Table 2.3). For iron, atmospheric deposition is a key player in the WTA, providing almost twice the amount delivered by the Amazon: 0.07 Tg Fe yr^{-1} against 0.04 Tg Fe yr^{-1} for the river.

2.2.3 Simulations and analyses

The physical core of the model was first run for 30 years, starting from rest with initial conditions for salinity and temperature derived from the World Ocean Atlas (WOA, 2013) (Garcia et al., 2013; Levitus et al., 2015). The model was forced at the surface by monthly climatologies of wind stress, net solar radiation, and of the fluxes of heat and freshwater. All atmospheric variables were derived from ERA-Interim reanalysis covering the 1989-2009 time period (Dee et al., 2011).

The coupled model, i.e., including the ecology/biogeochemistry, was then run for another 20 years with the initial conditions for the physical variables taken from the first 30 years, and for the biogeochemical/ecological variables taken from different observation and model-based data sets. The main nutrients were derived from the climatology by WOA (2013) (Garcia et al., 2013; Levitus et al., 2015). DIC and alkalinity fields were interpolated from the climatology (1972-2013) of GLODAP gridded product (Global Ocean Data Analysis Project version 2, (Lauvset et al., 2016)). For the biogeochemical tracers that were not available in WOA or GLODAP such as iron and DOM, we relied on results from a simulation of the ocean component of the NCAR Community Earth System Model that employs the same ocean biogeochemistry/ecosystem model, i.e., CESM-BEC (Yang et al., 2017). The lateral boundary conditions at the open boundary in the South were derived from the same sources as the initial conditions with the seasonal cycle retained when available.

The atmospheric forcing included seasonally varying atmospheric pCO_2 based on the climatology created by Landschützer et al. (2014) over the period from 1998 through 2011. To compute the atmospheric pCO_2, they used the dry air mixing ratio for the marine boundary layer from (GLOBALVIEW-CO2, 2011), the atmospheric pressure from NCEP (Kalnay et al., 1996), and the water vapour correction from Dickson et al. (2007). The resulting climatology has an annual mean atmospheric pCO_2 over the domain of 365 μatm, corresponding roughly to the year 2006.

Of the 20 years of the coupled run, the first 14 years are considered as spin up. The last 6 years (years 15 to 20) were averaged and analyzed as a climatological mean state of our system.

To assess the effects of the Amazon River on the marine biogeochemistry, we performed a series of factorial simulations (Table 2.1), in which we systematically removed certain types of river fluxes in order to assess their relative contribution.

The *NoAmazon* simulation establishes the baseline, i.e., where the Amazon River is blocked and thus supplies neither any freshwater nor any of the dissolved constituents. We compare this simulation to the *All* simulation that represents the most realistic (standard) simulation with the Amazon delivering all dissolved constituents, i.e., the inorganic and organic nutrients as well as DIC, Alk and terrestrial DOC. The *NoNutr* simulation sits in between these two simulations: The Amazon River delivers only DIC, Alk but no terrestrial DOC nor inorganic and organic nutrients. The other sensitivity simulations allow us to explore the impact of each inorganic or organic nutrient individually as well as the role of the input of terrestrial DOC on the air-sea balance of CO_2.

We focus our analyses to that fraction of the Western Tropical Atlantic that is most affected by the Amazon river. We define this region as extending from 0.5° S –24° N and 70° –30° W to capture the full extent of the plume waters based on our model results (Figure 2.1). Within these boundaries, we delimit 4 sub-regions, each exhibiting similar physical and biogeochemical characteristics. The estuary region corresponds to the extended mouth of the river ($<$ 150 km from the point of entry of the Amazon River). The shelf region is defined as that part of the continental margin that is shallower than 100 meters, with the shelf-break marking the transition to the adjacent offshore region. The offshore plume region corresponds to the areas where the water column is deeper than 100 meters and the surface salinity is lower than 35.25. The offshore waters exhibiting a salinity above 35.25 constitute then the non-plume region. We use a threshold

Table 2.1 Summary of the ROMS-BEC simulations performed for this study. The concentrations of the Amazon river input and the resulting loads are given in table A.3

Name of the simulation	Description
NoAmazon	Base-line simulation: Amazon river is blocked.
All	Standard simulation: All nutrients and DIC & Alk are delivered.
NoNutr	Only DIC and Alk are delivered.
NoDIN	Same as All but without DIN load.
NoPO4	Same as All but without PO_4 load.
NoDOP	Same as All but without DOP load.
NoP	Same as All but without DOP and PO_4 loads.
NoSi	Same as All but without $Si(OH)_4$ load.
NoDOC	Same as All but without the input of terrestrial DOC.

of 35.25 instead of 35 as used in previous studies (e.g. (Subramaniam et al., 2008a; Coles et al., 2013; Stukel et al., 2014)). This is based on our analyses showing a substantial Amazon influence up to these salinities. Lowering it to a threshold of 35 would have removed from our plume analysis an important share of the river influence. As the pathways of the plume vary seasonally, the spatial limits of the offshore plume and non-plume regions change throughout the year (Figure 2.1c-f).

2.2.4 Model evaluation

2.2.4.1 Circulation

The general surface circulation of the Atlantic Ocean is well reproduced by ROMS-BEC, as exemplified by the very high correlation coefficient of 0.91 between the observed and the modeled annual mean sea surface height (Figure A.2). Especially encouraging is the model simulated Gulf Stream, which follows the North American coast until its branching at 40° N (Figure A.3). Thus our model does not suffer from a common bias in many ocean models in that they simulate a far too north branching of the Gulf Stream from the North American continent. The strength of the current is nonetheless underestimated by ROMS-BEC. The coarser resolution in our model in these high latitudes might impair the representation of eddies and other mesoscale dynamics, and thus temper the strength of the current. In the equatorial Atlantic, ROMS-BEC properly captures the complex structure of large scale westward currents and eastward counter currents that directly influence our region of study.

In the WTA, the model simulates the strong seasonal cycle of the currents in response to the seasonal variation of the wind field and the migration of the Intertropical Convergence Zone (ITCZ). The model captures the winter and spring dominance of the North Brazilian Current (NBC), which brings the plume waters northward along the South American continent (Figure 2.2). The model also represents correctly the transition to late summer and fall conditions, when the zonal equatorial currents move to a more northerly position, leading to the North Equatorial Counter Current (NECC) diverting part of the plume waters eastward (Stramma and Schott, 1999; Lumpkin and Garzoli, 2005). There are also some shortcomings. The NBC is somewhat weaker in ROMS-BEC compared to the drifter estimates (Lumpkin and Johnson, 2013). This might explain that the average limit of the plume does not go as far enough north in spring as the satellite estimates indicate.

2.2.4.2 Biogeochemistry and ecology

The basin-scale patterns of surface chlorophyll in the model match quite well the climatologies derived from satellite estimates (Figure A.4), with a correlation coefficient of the annual mean patterns of 0.6. Despite a slight underestimation of the productivity withing the eastern boundary upwelling systems, ROMS-BEC simulates across the whole domain a net primary production (NPP) of 16.7 Pg C yr^{-1} which is a bit higher than the 14.6 Pg C yr^{-1} estimated by SeaWiF's Vertically Generalized Production Model (VGPM) (Westberry et al., 2008). This difference is

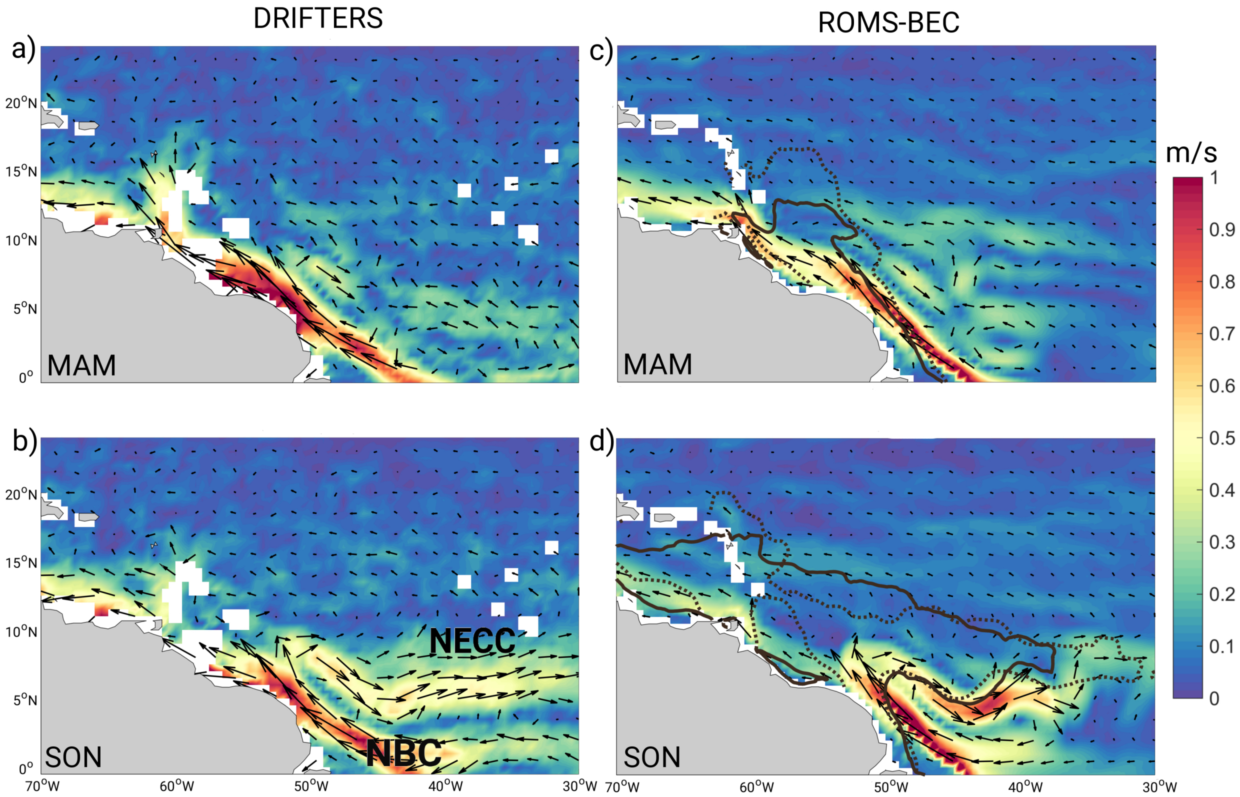

Figure 2.2 Maps of the seasonal mean surface ocean circulation in the Western Tropical Atlantic. (a-b) Average surface flow (m s^{-1}) in spring and fall estimated from drifters (Lumpkin and Johnson, 2013) and (c-d) in ROMS-BEC (integrated in the first 15 meters to be comparable to drifter data). Solid and dashed lines mark the boundaries of the plume waters (S<35.25) in ROMS-BEC and in the satellite estimates (SMAP 2015-2017), respectively. The North Brazilian Current (NBC) and the North Equatorial Counter Current (NECC) are indicated in (b).

mostly driven by the productivity in high latitudes that is stronger in the model.

In the WTA, our simulated surface chlorophyll is in good agreement with the estimates from remote sensing with an average negative bias of 0.2 mg Chl m^{-3} (Figure 2.3). The strongest discrepancies (locally > 10 mg Chl m^{-3}) are found very close to the mouth of the river (Figure 2.3). In these areas, the strength of our simulated blooms are very sensitive to the light attenuation coefficient that we apply (see section 2.2). This is also the type of turbid waters where remote sensing algorithms generally struggle the most to differentiate the different constituents and themselves might be highly biased (Tyler et al., 2016). In general, the model reproduces the offshore gradient detected in satellite estimates, with highest surface chlorophyll concentrations in the coastal areas and lowest concentrations in the oligotrophic open ocean, north of 15° N. However, the lateral extent of the blooms, especially in summer, is somewhat cut short compared to observations. This may be caused, in part, by our too weakly simulated NBC and NECC, leading to an insufficient downstream transport of the chlorophyll-rich waters.

Although a quantitative evaluation of the major nutrients is hampered by the sparsity of the *in-situ* measurements, the model succeeds in capturing the main seasonal and spatial variations of NO_3, PO_4 and $Si(OH)_4$ in the region (Figure 2.4). Following the plume pathways, riverine nutrients are transported from the mouth of the river to the open ocean, leaving a clear imprint on the spatial distribution of PO_4 and $Si(OH)_4$. In contrast, the NO_3 concentration simulated by

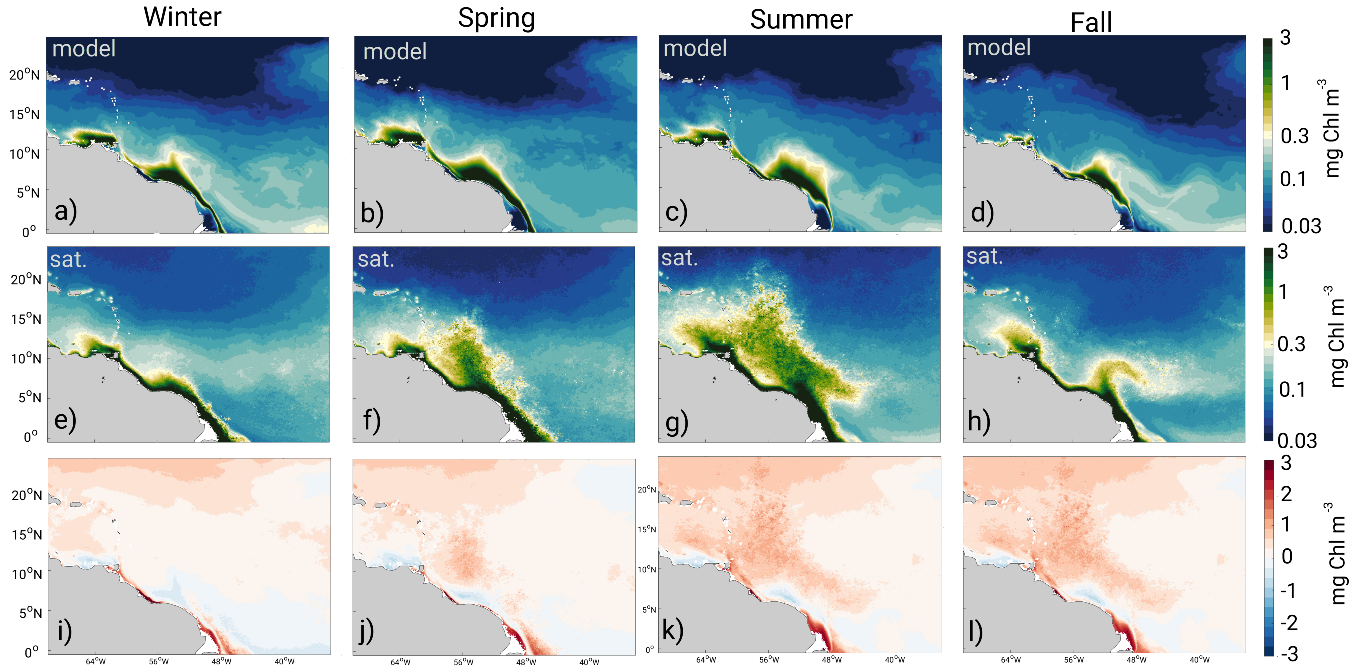

Figure 2.3 Maps of the seasonal mean surface chlorophyll concentration. (a-d) Average chlorophyll simulated by ROMS-BEC and (e-h) estimated from Sea-viewing Wide Field-of-view Sensor (SeaWiFS) Ocean Color Data (https://oceandata.sci.gsfc.nasa.gov/SeaWiFS/, data accessed and compiled in October 2012). (i-l) Difference between the two: SeaWiFs - ROMS-BEC. Winter is the mean of the months December through February, spring is March through May, summer is June through Augus and fall is September through November.

the model remains low in the offshore plume area, in agreement with observations. In our model, this is partly caused by a substantial amount of benthic denitrification simulated to occur on the North Brazilian shelf, imprinting the waters above with a deficit of NO_3, while keeping PO_4 high. As reported in several studies (Subramaniam et al., 2008a; Goes et al., 2014; Weber et al., 2017), this distinct fate of the riverine nutrients result in an excess of $Si(OH)_4$ and PO_4 over NO_3 in the offshore plume waters, with an average N:P:Si stoichiometry of 6:1:95. The area considered for this calculation exhibit a wide range of nutrient concentrations, but the concentrations are, on average, quite low: 0.2 mmol N m^{-3}, 0.04 mmol P m^{-3} and 3.8 mmol Si m^{-3}.

ROMS-BEC simulates a total N_2 fixation over the whole basin of 26 Tg N yr^{-1}, which is close to previous recent estimates: 34 ± 7 Tg N yr^{-1} (Luo et al., 2012), 46 Tg N yr^{-1} (Moore et al., 2013c), and 34 [24 - 50] Tg N yr^{-1} (Wang et al., 2019). In agreement with field measurements that were assembled in the MAREDAT database (Luo et al., 2012), N_2 fixation in ROMS-BEC is highest in the tropical North Atlantic and then decreases from there both northward and southward (Figure A.5). Around the latitude 40° N and again around the latitude 40° S, some regions exhibit a peak of total N_2 fixation before it decreases sharply toward the polar regions, due to temperature limitation in our model.

In the WTA, the measured rates of N_2 fixation are extremely variable as a result of the very dynamic hydrographic and environmental conditions. Nonetheless, Subramaniam et al. (2008a) showed that some general pattern emerges and proposed to divide the area into 3 sub-regions based on sea surface salinity (SSS): low-salinity ($SSS > 30$), mesohaline ($30 > SSS > 35$) and

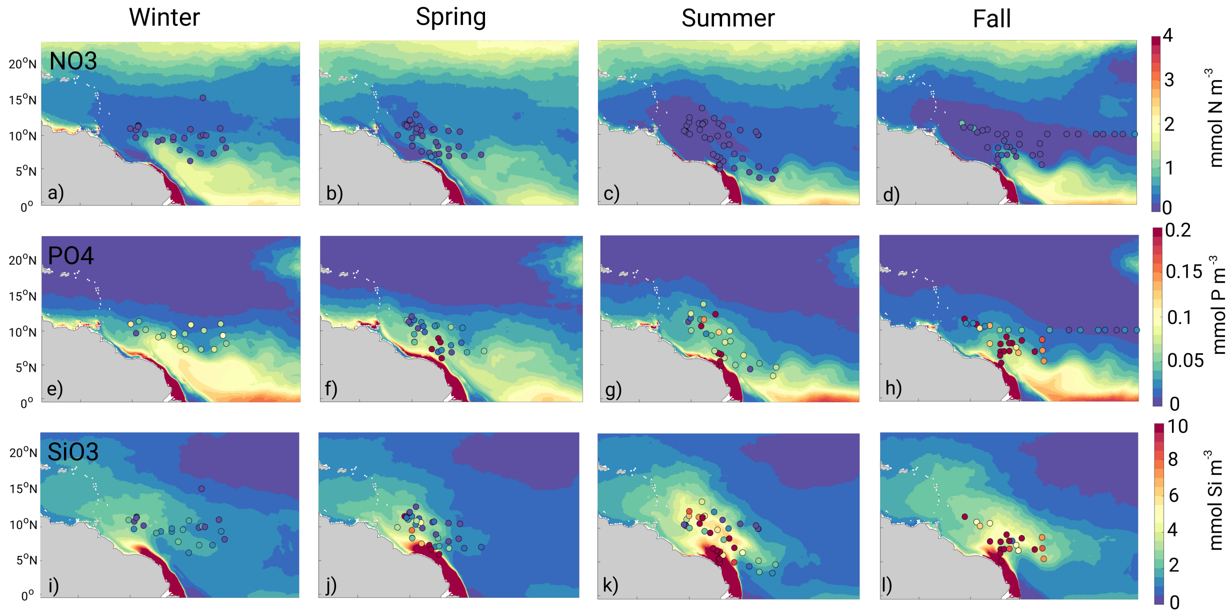

Figure 2.4 Maps of the seasonal mean surface concentrations of (a-d) NO_3, (e-h) PO_4 and (i-l) $Si(OH)_4$. The filled circles correspond to *in-situ* measurements collected during several different cruises (Langlois et al., 2008; Subramaniam et al., 2008a; Doherty et al., 2017a). Only surface measurements are plotted (depth < 15 m). The seasons are defined as in Fig. 3.

oceanic (SSS > 35). The average rate of N_2 fixation in the study by Subramaniam et al. (2008a) is the lowest in the low-salinity waters (35 ± 5 μmol m^{-3} d^{-1}) and the highest in the mesohaline waters (986 ± 373 μmol m^{-3} d^{-1}) while the oceanic waters exhibit an average rate of 157 ± 32 μmol m^{-3} d^{-1}. This general pattern is reproduced by the model with an average of N_2 fixation of 59 μmol m^{-3} d^{-1} (low-salinity), 503 μmol m^{-3} d^{-1} (mesohaline) and 152 μmol m^{-3} d^{-1} (oceanic).

2.2.4.3 Air-sea CO_2 exchange

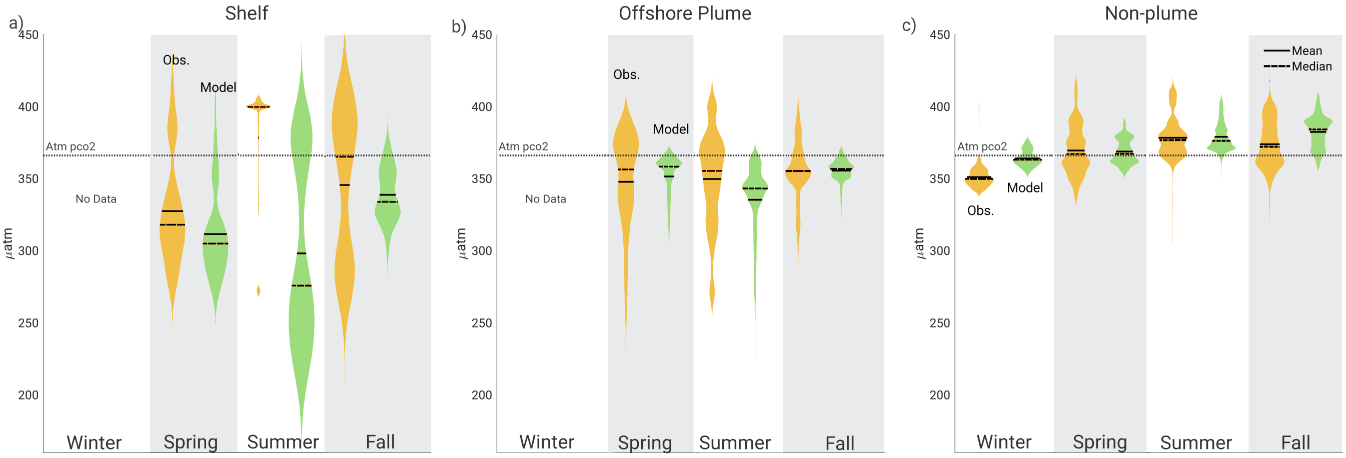

Figure 2.5 Evaluation of the surface ocean pCO_2: Depicted in this violin plot are the observations (yellow) and the results from ROMS-BEC (green) for every season (a) over the shelf area (b) in the offshore plume waters and (c) in the non-plume waters. The shape of the plots corresponds to the kernel density, the solid line to the mean and the dashed line to the median. The dotted line is the mean atmospheric pCO_2 within the domain. Observations are derived from the ungridded Surface Ocean CO_2 Atlas (SOCAT version 2020). All data (1970-2019) have been normalized to the year 2006 and concatenated by region and seasons. The model was sampled at the same locations as the observations. The seasons are defined as in Fig. 3.

Overall, the WTA is considered a source of CO_2 to the atmosphere (Goyet et al., 1998; Lefévre et al., 1998; Schuster et al., 2013). Except in winter, the areas that are not under the direct influence of the Amazon River (non-plume waters) are, on average, supersaturated in CO_2 with respect to atmospheric CO_2 (Figure 2.5-c). Nevertheless, surface pCO_2 within the region exhibit a clear north south gradient (Takahashi et al., 2009; Lefévre et al., 2010) which is well captured by the model (Figure A.6). The south of the domain (south of 11° N) displays higher surface pCO_2 than further north due to the supply of CO_2 rich waters from below by the equatorial upwelling (Lefèvre et al., 2014).

Under the influence of the Amazon River, the shelf and offshore plume waters are, on average, undersaturated with regard to atmospheric CO_2, in agreement with observations (Figure 2.5-a-b). Except in the summer on the shelf, where data are too scarce to draw a conclusion, ROMS-BEC successfully reproduces the mean conditions, with mean biases less than 16 μatm. Nevertheless, the simulated pCO_2 has much less variance compared to the observations, especially in the offshore plume region. The model might underestimate the full spectrum of the pCO_2 variations owing to it being forced with monthly climatological conditions, thus lacking the influence of storms and other perturbations.

2.3 Changes in the biological pump

The difference between the standard (*All*) and the *NoAmazon* simulations reveal the large impacts of the Amazon River on the marine biological pump (Table 2.2). This strong stimulation is foremost a consequence of the delivery of nutrients. The impact of the Amazon induced modifications of the circulation alone are relatively small (compare *All* with *NoAmazon* and *NoNutr*). Since our focus is on the role of the nutrients, and since the role of the circulation changes is small, we use the *NoNutr* as our new reference for exploring changes in NPP and export in response to the addition of the different nutrients (subsections 3.1 through 3.3). We first focus our analyses on the changes in NPP, and the associated export production (EP), diagnosed from the flux of particulate organic matter across 100 m depth. We then will use the factorial simulations to analyze the results more deeply.

2.3.1 Overview

The nutrients delivered by the Amazon stimulate NPP in the analysis region by 115 Tg C yr^{-1} (Table 2.2), representing an enhancement of 9%. The largest increase occurs on the shelf, with the influence of the Amazon River weakening as the waters travel from the mouth of the river to the open ocean (Figure 2.6a). This additional NPP increases EP by 32 Tg C yr^{-1}, representing an overproportional increase of +17%. Similar to NPP, the magnitude of the increase diminishes as the waters reach the offshore regions (Figure 2.6b). A noteworthy exception is the estuary zone, where NPP and EP remain low. This is because the phytoplankton in these regions remain light limited owing to the high levels of c-DOM and turbidity. This estuary zone will thus be excluded in our subsequent analyses.

The model simulated changes in NPP and EP are substantially larger than the potential changes one would expect from the nutrient input alone. To obtain these potential changes in NPP and EP, we assume (i) Redfield stoichiometry, (ii) that the added nutrients are completely biologically consumed in the WTA and then exported to depth, and (iii) that a constant fraction of the additional NPP is exported to depth, i.e., that the export ratio (*e*-ratio) is fixed. With these assumptions, the potential changes in NPP and EP expected for each nutrient i = NO_3+NH_4, PO_4, DON and DOP, i.e., $\Delta\text{NPP}^{i,pot}$ and $\Delta\text{EP}^{i,pot}$, can be estimated as follows:

Table 2.2 Mean NPP and EP in the *NoAmazon NoNutr* cases and the changes (δ NPP, δ EP) relative to these cases for the different sub-regions and the total across the WTA analysis region (see the Methods section for the definition of these sub-regions). Listed are the results for the standard case *All* and the different factorial simulations. The absolute values for all factorial simulations can be found in Table A.5.

Simulations	NPP [Tg C yr^{-1}]				EP [Tg C yr^{-1}]		
	Shelf	Offshore Plume	Non-Plume	Total[1]	Offshore Plume	Non-Plume	Total
NoAmazon	64	209.2	986.62	1259.9	35.4	162.7	198.1
NoNutr	60.8	201.5	966.9	1229.3	34	158.1	192.1
Simulations	ΔNPP [Tg C yr^{-1}]				ΔEP [Tg C yr^{-1}]		
	Shelf[1]	Offshore Plume	Non-Plume	Total	Offshore Plume	Non-Plume	Total
All - NoAmazon	23.6 (37%)	34.9 (17%)	26.1 (3%)	84.5 (7%)	12.5 (35%)	13.5 (8%)	25.9 (13%)
All - NoNutr	26.7 (44%)	42.6 (21%)	45.8 (5%)	115.1 (9%)	13.9 (41%)	18.1 (11%)	32 (17%)
NoDIN - NoNutr	18.8 (31%)	39.7 (20%)	48.8 (5%)	107.3 (9%)	13.2 (39%)	18.7 (12%)	32 (17 %)
NoPO4 - NoNutr	24.6 (40%)	38.4 (19%)	31.1 (3%)	94 (8%)	12.7 (37%)	16.1 (10%)	28.7 (15%)
NoDOP - NoNutr	18.6 (31%)	1.2 (0.6%)	-30.9 (-3%)	-11.2 (-1%)	6.5 (19%)	7.6 (5%)	14.1 (7%)
NoP - NoNutr	6.9 (11%)	-9.9 (-5%)	-45.9 (-5%)	-49 (-4%)	5 (15%)	6.1 (4%)	11.1 (6%)
NoSi - NoNutr	13.7 (22%)	61.6 (31%)	108 (11%)	183.3 (15%)	5.6 (16%)	10.9 (7%)	16.5 (9%)
NoAmazon - NoNutr	3.1 (5%)	7.7 (4%)	19.7 (2%)	30.6 (2%)	1.4 (4%)	4.6 (3%)	6 (3%)

[1] *This includes the estuary zone*

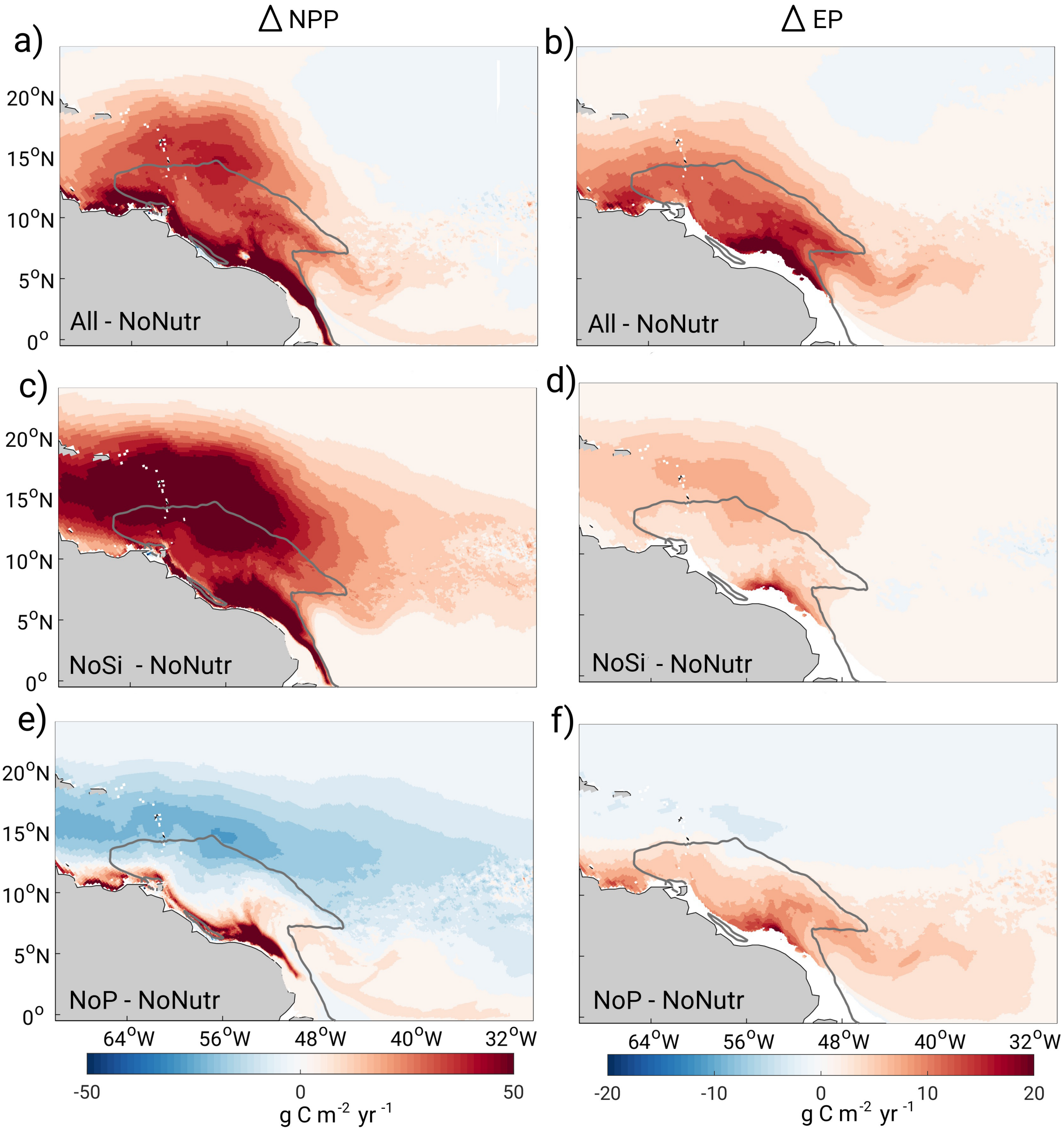

ΔNPP
ΔEP
a)
b)
c)
d)
e)
f)
20°N
15°N
10°N
5°N
0°
All - NoNutr
NoSi - NoNutr
NoP - NoNutr
64°W
56°W
48°W
40°W
32°W
-50
0
50
g C m^{-2} yr^{-1}
-20
-10
0
10
20
g C m^{-2} yr^{-1}

Figure 2.6 Maps illustrating the changes in annual mean net primary production (NPP) and export production (EP) in the western tropical Atlantic in response to the Amazon river input. (a) and (b) Differences between *All* and *NoNutr* simulations showing the overall impact of the Amazon on the ocean's biological pump. (c) and (d) Differences between the *NoSi* and *NoNutr* simulations showing the impact of all nutrients but $Si(OH)_4$. (e) and (f) Differences between *NoPO4* and *NoNutr* simulations showing the impact of all nutrients but PO_4. Gray lines mark the boundaries of the plume region (salinity < 35.25).

$$\Delta\mathrm{EP}^{i,pot} = J(N_i) \cdot r_{C:N_i} \tag{2.1}$$

$$\Delta\mathrm{NPP}^{i,pot} = \frac{\Delta\mathrm{EP}^{i,pot}}{e\text{-ratio}} \tag{2.2}$$

where $J(N_i)$ represents the total amount of (inorganic or organic) nutrient N_i delivered by the Amazon river. The symbol $r_{\mathrm{C}:N_i}$ is the carbon to nutrient phytoplankton uptake ratio of the nutrient N_i. We use a constant *e*-ratio of 0.16, which reflects the average value over the whole region of study in the *NoNutr* simulation; it implies a recycling of the nutrients in the upper ocean of more than 6 times.

These potential changes of NPP and EP (crosses in figure 2.7a), differ little between the addition of DIN (NO_3 + NH_4) or PO_4 as their ratio in the Amazon input is close to Redfield (Table A.3). But these potential changes are much lower than the actual realized increases in NPP and EP. In the *All* simulation (Table 2.2), the increase of NPP exceeds the potential increase based on DIN or PO_4 at least twofold (Figure 2.7a) and for EP, the realized increase is a staggering quintupling of the DIN or PO_4-based potential.

This strong amplification can only be reconciled by invoking other nutrient sources. Additional inputs of 4.2 Tg N yr^{-1} and 0.6 Tg P yr^{-1} are needed. One option is that a fraction of the river-supplied dissolved organic nutrients becomes bioavailable, since they have a very large potential for increasing NPP and export (Figure 2.7a), larger than actually needed to close the nutrient gap. But there are also other potentially important sources of new nutrients, primarily N_2 fixation. The stronger relative enhancement of the export production relative to NPP implies an increased export ratio, i.e., that a larger fraction of NPP is exported to depth. This requires changes in the phytoplankton community structure that alter the pathway of the fixed carbon through the upper ocean ecosystem. These results thus pose two questions: Where are the additional nutrients coming from, and what determines the changes in phytoplankton community structure that causes the increase in the *e*-ratio?

The factorial simulations, where we remove one riverine nutrient at the time, raise further questions. The omission of DIN in the Amazon river input in the *NoDIN* simulation has essentially no impact on the biological pump within the WTA (Figure 2.7a). This suggests that the removal of N from the Amazon input can be easily compensated for by other sources of N, giving riverine N no limiting role for phytoplankton growth in the region. In contrast, the *NoSi* case stimulates an even larger increase of NPP than seen in the *All* simulation, but a smaller increase in EP. Furthermore, in this simulation the realized change in export falls below the average e-ratio line. Finally, the most perplexing results emerge from the simulations in which DOP is missing in the riverine input, i.e., the *NoDOP* and the *NoP* cases. While the absence of PO_4 changes the results only somewhat, the absence of DOP leads to a decrease of NPP compared to the *NoNut*case, even though the other nutrients are still delivered. Even more surprising is the fact that despite these decreases in NPP, EP still increases in these two simulations. These responses of the WTA to the factorial nutrient experiments highlight the fact that riverine phosphorus, and especially DOP, plays a key role in the enhancement of NPP, but that the efficiency of export, i.e., the export ratio, might be driven by the presence of other riverine nutrients, namely $Si(OH)_4$.

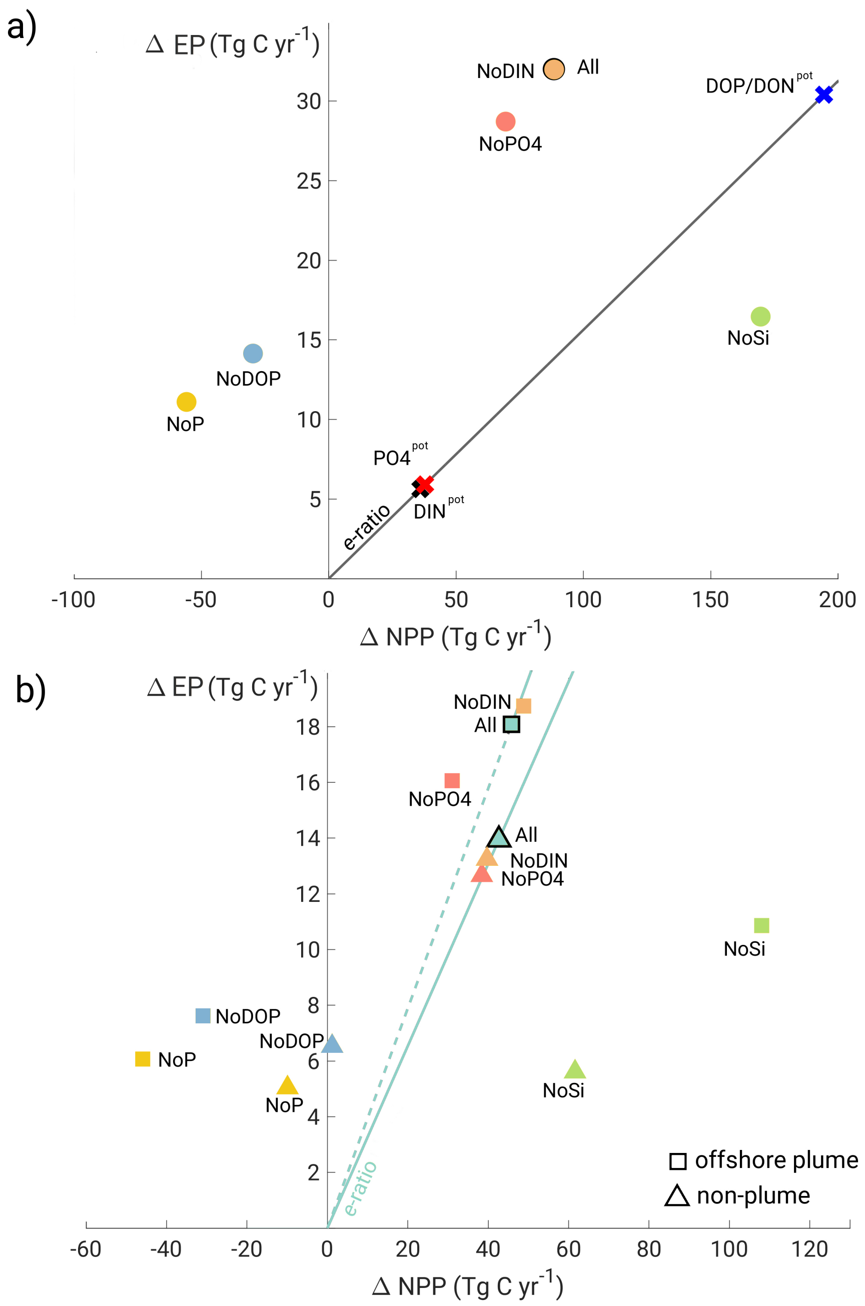

Figure 2.7 Relationship between the Amazon-river induced changes in NPP (integrated in the first 100 meters)(ΔNPP) and the changes in export production (at 100 m) (ΔEP) for (a) the entire WTA analysis region and (b) for the individual sub-regions. The regionally integrated changes in production and export were computed relative to the *NoNutr* case. Shown as crosses in (a) are the potential changes in NPP and export ($\Delta\mathrm{NPP}^{i,pot}$ and $\Delta\mathrm{EP}^{i,pot}$), estimated based on the nutrient delivery by the Amazon (see text for further details). The line corresponds to the average e-ratio of 0.16 across the whole WTA region in the *NoNutr* simulation. In (b) the shapes represent different zones in the region (see figure 2.1). The solid line and the dashed line indicate the e-ratio in the plume and non-plume regions, respectively, taken from the *All* simulation. In both (a) and (b), the colors correspond to the different simulations and will be used in subsequent figures.

These factorial simulations demonstrate a highly non-linear response of the WTA to the supply of nutrients by the Amazon River. More nutrients do not necessarily translate into higher production, and there is no proportional link between river-induced changes in NPP and EP, undermining the idea that the amount of carbon exported is primarily driven by changes in NPP. This suggests strong interactions between the cycling of the different nutrient elements, with important impacts on the phytoplankton community structure, ultimately affecting the strength and efficiency of the biological pump. Thus, at least one further question emerges from these factorial simulations: How does the input of the different nutrient elements lead to these very different responses in the biological pump? In the following, we provide further results and analyses to address this question as well as the two others raised before, i.e., the source of the additional nutrients and how the riverine nutrients are changing the phytoplankton community structure.

2.3.2 The enhancement of primary production

To identify the sources of additional bio-available nitrogen and phosphorus supporting the amplification of the potential response of NPP to the addition of nutrients by the Amazon, we determine all sources of extra inorganic nitrogen and phosphorus over the upper ocean (0-100 m) of the WTA. We do this for both the *NoNutr* and *All* simulations, and then compute their difference. Since the input from the ocean and atmosphere remain essentially unchanged, we need to consider only the extra inorganic nutrient sources from (i) the riverine input, (ii) the remineralization of dissolved and particulate organic matter, (iii) N_2 fixation and (iv) the uptake of DOP by phytoplankton (see Table 2.3).

Table 2.3 Annual mean sources of inorganic nitrogen and phosphorus in the *NoNutr* and *All* simulations integrated over the top 100m and the WTA.

	All (Tg N yr^{-1})	*NoNutr* (Tg N yr^{-1})	Difference in %	Additional Nutr. in *All* (Tg N yr^{-1})
N from river DIN input	0.9	0.0	100	0.9
N from N_2 fixation	8.9	5.1	74	3.8
N from DON remin.	36	30.1	19	5.8
N from PON remin.	28.1	22	28	6.1
P from river PO_4 input	0.13	0.0	100	0.13
P from DOP remin.	0.0067	0.0063	7	0.0004
P from DOP uptake	3.2	2.4	34	0.8
P from POP remin.	3.9	3	28	0.8

For nitrogen, N_2 fixation exhibits the largest increase in relative terms between the *All* and the *NoNutr* simulations (Table 2.3). Over the whole WTA analysis domain, the stimulation of N_2 fixation by the Amazon river supplies an additional 3.8 Tg N yr^{-1} of new bio-available nitrogen, representing an increase of 74%. However, in absolute terms, the intensification of the recycling of organic nitrogen in the *All* simulation represents the most important source of nitrogen to the WTA with an additional flux of 5.8 Tg N yr^{-1} (DON) and 6.1 Tg N yr^{-1} (PON). While this recycling is important for NPP, it does not represent a new source. Note that we cannot a priori determine what fraction of the DON comes from terrestrial DON remineralization, since our model does not differentiate between riverine and marine-sourced DON. Nevertheless, by matching the required N to support the enhanced NPP by N_2-fixation and a fraction of the terrestrial DON remineralization, we find a fraction of about 32%. The actual percentage could be a bit higher, owing to our lack of consideration of an increase in the losses of fixed nitrogen through enhanced benthic denitrification along the North Brazilian Shelf. Thus, only a relatively small fraction of the organic N sourced inorganic N is truly new nitrogen and the N_2 fixation represents the dominant source of new nitrogen.

The recycling of phosphorus is also intensified in the *All* simulation. The remineralization of POP is enhanced by 28%, providing an additional 0.8 Tg P yr^{-1}. While the remineralization of DOP exhibits only a small increase of 7 %, adding a small amount of PO_4 ($<$0.001 Tg P yr^{-1}), the uptake of DOP by phytoplankton constitutes a very important source of extra phosphorus to the phytoplankton community of the WTA, providing an additional 0.8 Tg P yr^{-1}.

In summary, the large amplification of the potential response of NPP in the WTA region to the nutrient input by the Amazon river is largely supported by the strong increase in N_2-fixation that more or less doubles the total amount of new nitrogen available to fuel growth of the phytoplankton. The large addition of new nitrogen is made possible by the diazotrophic organisms having access to river supplied PO_4 and particularly to the river supplied DOP. This explains also the very different responses of NPP to the different nutrient inputs (Figure 2.6 & 2.7, Table 2.2). In the *NoDIN* case, diazotrophic organisms are able to nearly completely compensate for the lack of DIN input, making up for this lack by strongly enhancing their rates of N fixation. Conversely, when the input of phosphorus is lacking especially in the *NoDOP* and *NoP* cases, the diazotrophic community cannot stimulate growth and export. In fact, this community even tends to suffer in these no phosphorus cases as a result of increased competition from the other groups, leading to a reduction in NPP relative to the *NoNutr* case (Table 2.2).

This budget analysis resolves thus the first question about the source of the nutrients and (part of the) third question on the role of the different nutrients. But it does not answer the second question, i.e., what causes the enhanced export beyond that expected by the increase in NPP, i.e., what causes the increase in the *e*-ratio?

2.3.3 The enhancement of carbon export

2.3.3.1 Changes in *e*-ratios

The overall increase in the *e*-ratio across the WTA analysis region stems predominantly from the plume waters, where it increases in the *All* simulation by nearly 17% (Figure 2.8a). In contrast, the *e*-ratio increases by only about 6% in the non-plume waters (Figure 2.8b). The changes are very similar across all factorial simulations, except for the *NoSi* case, where the *e*-ratio decreases.

This latter finding corresponds to the *NoSi* case lying below the potential line in figure 2.7a.

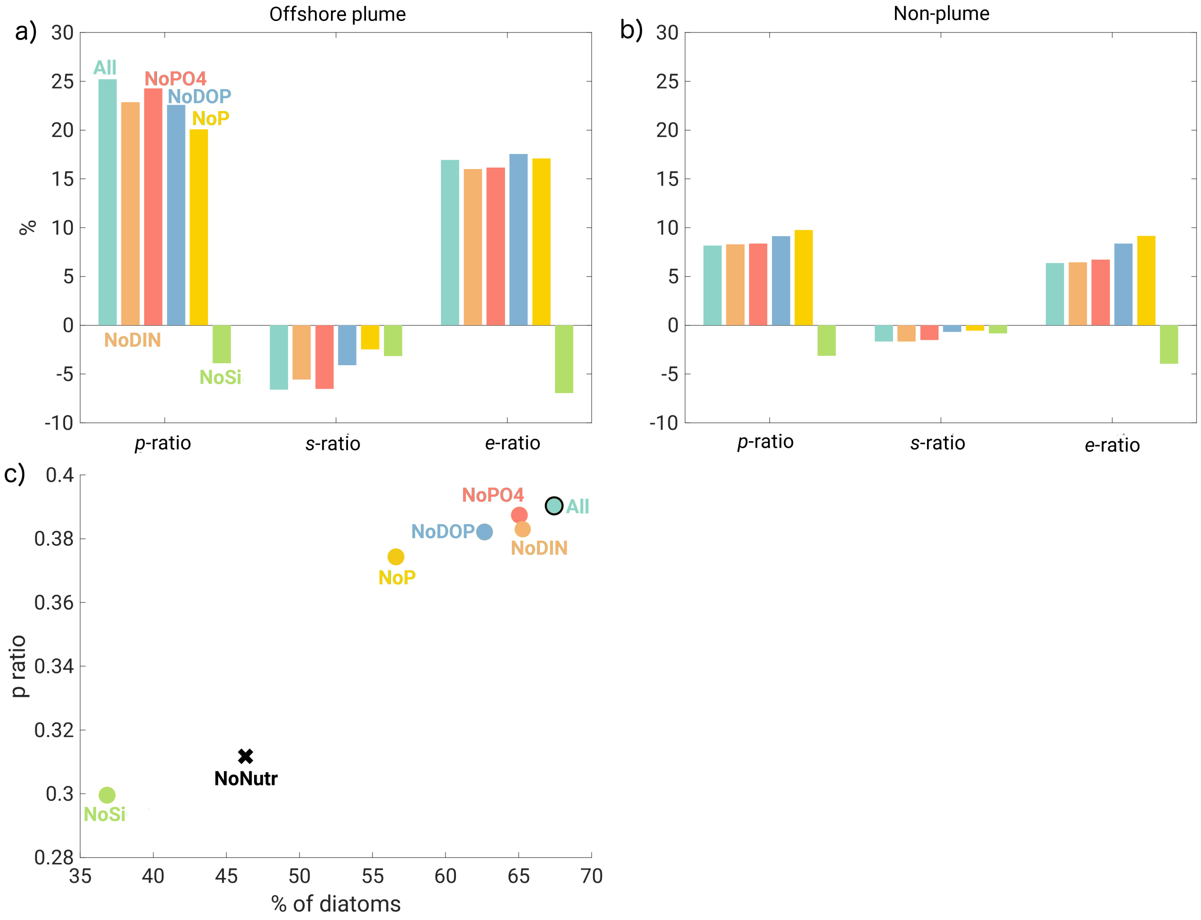

Figure 2.8 Amazon-river induced relative changes in the *e*-ratio and in its multiplicative factors, i.e., the *p*- and *s*-ratios. Shown are the changes simulated for the *All* case and the factorial experiments relative to the *NoNutr* simulation. (a) Changes in the offshore plume waters. (b) Changes in the non-plume waters. (c) Average *p*-ratio in the plume waters as a function of the percentage of diatoms in the total phytoplankton biomass. See figure 2.1 for the region boundaries.

To analyze the processes leading to these changes further, we split the *e*-ratio into two components: (i) the *p*-ratio, i.e., the fraction of NPP that is routed to detrital POC, and (ii) the *s*-ratio, i.e., the sinking efficiency of POC reflecting the fraction of the total POC produced that sinks below 100 meters (Laufkötter et al., 2016). This split reveals that the increase in the *e*-ratio is driven by the enhancement of the *p*-ratio, with the exception of the *NoSi* case (Figure 2.8). This conclusion applies to both plume and non-plume waters. In the former, this increase is slightly modified by a decrease of the *s*-ratio. In the non-plume waters the *s*-ratio is almost unchanged. For the *NoSi* case, the decrease in the *e*-ratio is driven by decreases in both the s- and *p*-ratios.

Thus, in order to understand the general increase in the *e*-ratio, we need to understand what enhanced the *p*-ratio, i.e., why a larger fraction of the POC produced by phytoplankton is routed to detrital POC? This routing is primarily governed by the phytoplankton community structure.

2.3.3.2 Phytoplankton community structure and POC production

In the absence of nutrient input by the Amazon river (*NoNutr* simulation), the phytoplankton community in the plume waters is dominated by diatoms, representing 46% of the total phytoplankton community there (Figure 2.9). This is a consequence of upwelling at the continental shelf break supplying the $Si(OH)_4$ needed to support the growth of coastal diatoms. Small phytoplankton, already abundant in the plume waters (37%), become dominant in non-plume waters (47%), reflecting the overall the oligotrophic conditions of the open ocean WTA. The addition of nutrients by the Amazon shifts the balance strongly toward the diatoms, as the latter tend to benefit the most when nutrients are being added. In the *All* simulation, diatoms increase in the plume waters their relative share to 67% of the total biomass, while the share of the small phytoplankton drops to 18%. The same trend can be observed in the non-plume waters, although with smaller changes. The rest of the community is split between DDAs and *Trichodesmium*. Their relative importance remains more or less unaffected by the nutrient delivery by the Amazon river with DDAs dominating the diazotroph community (Figure 2.9).

The productivity of the different PFTs change more substantially (Figure 2.10). Diatoms increase their productivity very strongly, with the highest changes occurring in the plume waters. The productivity of DDAs is also boosted in most of the domain although their absolute increase is more moderate. In contrast, the small phytoplankton increase only far downstream in the non-

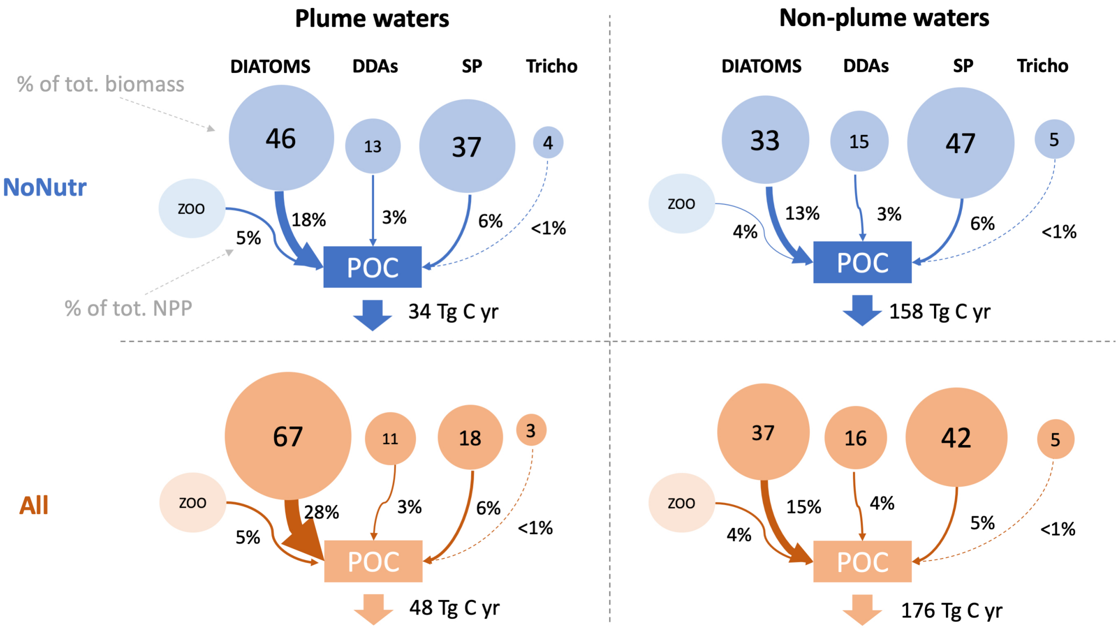

Figure 2.9 Phytoplankton community structure and pathways for the formation of detrital POC in the *NoNutr* simulation (top panel) and the *All* simulation (bottom panel). Indicated within each circle is the relative contribution in % of each PFT to the total phytoplankton biomass. Indicated by the arrows is the relative contribution of the different POC formation pathways associated with each PFT, given as % of total NPP in the top 100 m. The integrated POC fluxes are given separately for the plume and non-plume waters for the *NoNutr* and *All* simulations.

plume waters, while they experience a decrease of their productivity in the plume waters and south of our region of study. The productivity by *Trichodesmium* does not change much. Thus, the introduction of new nutrients to the WTA benefit only some PFTs, while the others might even suffer owing to a fiercer competition between them.

The fact that diatoms, and to a lesser degree DDAs, are benefiting from the delivery of riverine nutrients is highly relevant for our analysis, since diatoms constitute the dominant pathway for the formation of detrital POC in our model, i.e., they are the main PFT contributing to the high simulated *p*-ratio. In the *NoNutr* simulation, diatoms prevail in terms of POC production, even in the non-plume waters where the small phytoplankton represent the largest fraction of the community. Overall, diatoms are routing 18% and 13% of NPP to detrital POC in the plume and non-plume waters respectively (Figure 2.9). This flux combines the aggregate formation, the grazing loss and the non-grazing loss, but on average, more than 90% of this flux is generated by grazing. In the *All* simulation, the shift toward a diatom-dominated community translates into a larger fraction of NPP being transferred to the particulate pool, up to 28% solely through diatoms in the plume region (Figure 2.9).

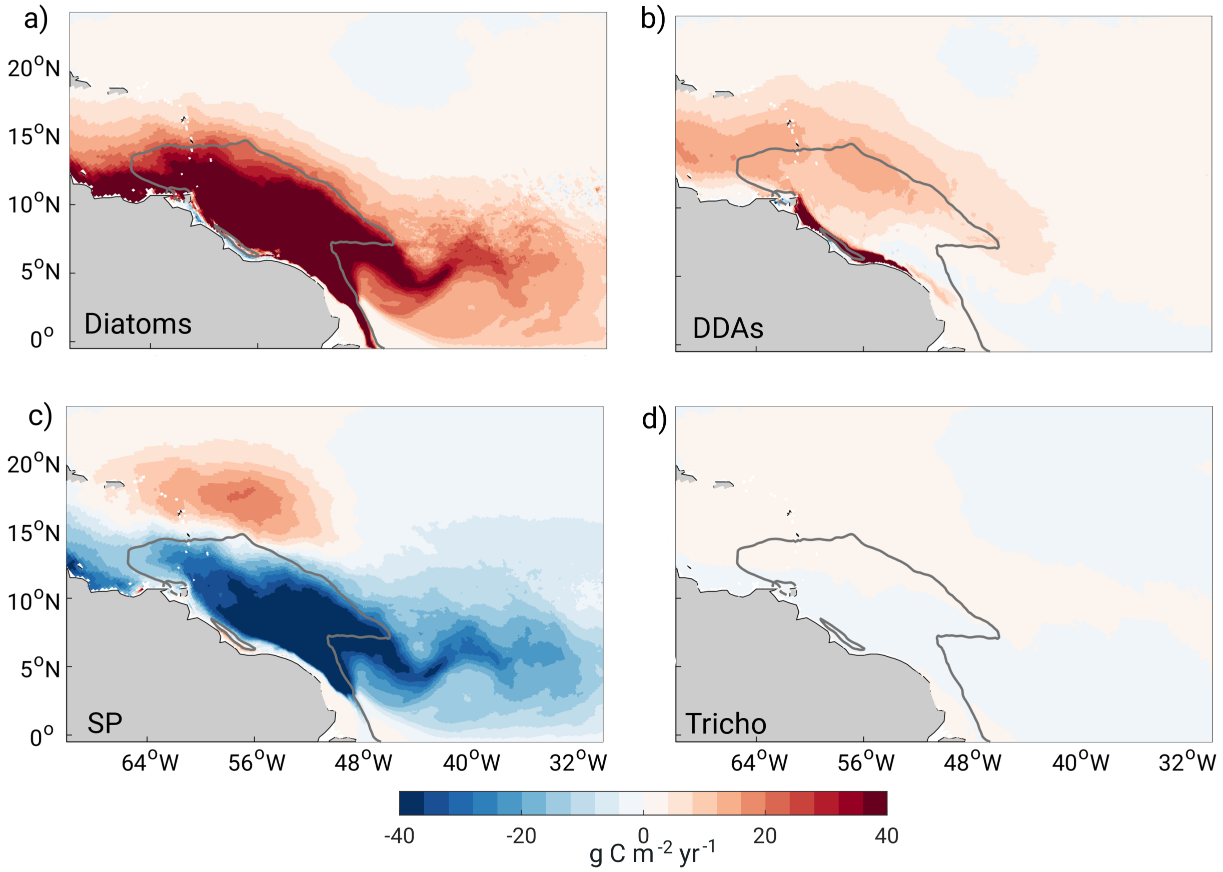

Figure 2.10 Maps of the changes in NPP integrated over the top 100 m in response to the nutrient addition by the Amazon river for the different Phytoplankton Functional Types, i.e., (a) the diatoms, (b) the diatom-diazotroph assemblage (DDA), (c) the small phytoplankton, and (d) the Trichodesmium groups. Shown are the differences between the *All* and the *NoNutr* simulations.

Thus, the prevalence of diatoms in the phytoplankton community is a key factor determining the *p*-ratio in all our simulations (Figure 2.8c). Overall, we can differentiate between two clusters of simulations: the simulations with a fraction of diatoms lower than 50% exhibit a *p* ratio lower than 0.32 and those with a fraction of diatoms above 55 % have a *p*-ratio higher than 0.36. The first cluster gathers the 2 simulations where riverine $Si(OH)_4$ is absent.

These findings provide us now an answer to the second question we raised, i.e., what determines the changes in phytoplankton community structure that causes the increase in the export ratio? It is primarily the nutrient delivery induced shift in the phytoplankton community structure toward diatoms that led to a higher fraction of NPP being exported. This shift is primarily induced by the riverine delivery of $Si(OH)_4$, which is clearly illustrated by the absence of this strong enhancement of export production in the *NoSi* case (Figure 2.7). The importance of diatoms in driving the *p*-ratio helps also to understand why the cases without phosphorus input, i.e., *NoPO4* and especially the *NoDOP* case, have actually higher export than the *NoNutr* case, even though their NPP is smaller (Figure 2.7). In these simulations, diatoms become more dominant, as they end up profiting most of the extra nutrients.

2.3.3.3 Depth of production and the *s*-ratio

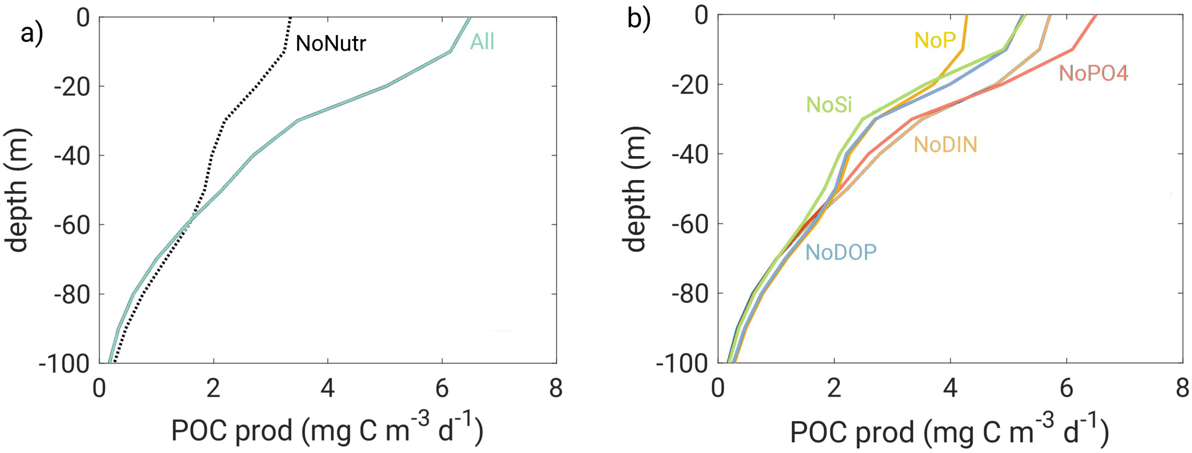

Figure 2.11 Annual mean rate of detrital POC production in the plume waters as a function of depth (a) in the *NoNutr* and *All* simulations, and (b) in all other factorial simulations.

While changes in phytoplankton community structure induced by the input of riverine nutrients explain the increase in the *p*-ratio, we have not yet addressed the possible reasons for why the *s*-ratio decreases, i.e., the fraction of detrital POC that escapes remineralization within the top 100 m and thus is exported to depth (Figure 2.8). It turns out that this is primarily a consequence of changes in the vertical distribution of organic matter production. Given that the remineralization of detrital organic matter tends to be swift, the lesser time particles spent in the top 100 m, the larger the fraction that gets exported vertically. If the particulate matter is mostly produced at depth, the time it requires to sink out of the top 100 m is much smaller compared to a particle that is produced near the surface. The *s*-ratio is thus directly impacted by the depth profile of POC production.

In the *All* simulation, a higher fraction of the POC is produced near the surface, reflecting the fact that the lighter and nutrient-rich waters of the river plume remain near the surface (Figure 2.11). In contrast, the distribution of POC production in the *NoNutr* simulation is more uniform throughout the depths, implying in relative terms that a smaller fraction of the total POC is produced atop the water column compared to the *All* simulation. The same is true for the factorial simulations. The *NoP* simulation in which the depth profile of POC production resembles the *NoNutr* case shows the smallest change in *s*-ratio. In contrast, the depth profile of POC production *NoPO4* simulation is close to the one in the *All* simulation and their changes in terms of *s*-ratio are similar.

Overall, our results suggest that the fate of the additional carbon that is fixed in response to the delivery of riverine nutrients depends for the most part on the phytoplankton community structure that drives the production of particulate matter. To a lesser extent, the vertical distribution of the POC production influences what fraction of the POC pool sinks below 100m and thus modulates the efficiency of the export measured by the *e*-ratio.

2.4 Changes in the air-sea CO_2 balance

The strong stimulation of the ocean's biological pump pushes the air-sea CO_2 balance of the WTA toward a sink, aided also by the riverine input of Alk. But the supply of large amounts of DIC and of terrestrial DOC by the Amazon tends to cause ocean outgassing, thus offsetting the biological sink. Therefore, it is the balance between this set of processes that will determine the overall balance. To account for these different processes, we use the *NoAmazon* simulation here as our reference, as only the latter does not account for the riverine input of DIC and Alk.

2.4.1 Air-sea CO_2 balance of the WTA

In the *NoAmazon* case, the WTA analysis region ($A = 9.6 \times 10^6$ km^{-2}) is a big source to the atmosphere, releasing 45.8 Tg C yr^{-1} of CO_2. Some of the coastal areas exhibit a modest uptake (< 0.5 mol C m^{-2} yr^{-1}), most likely related to the presence of the Orinoco River and small-scale upwellings stimulating primary and export production. However, the majority of the WTA in this simulation releases CO_2, except for a latitudinal band around 12° N in the western part of the region that is close to balance (Figure 2.12a).

The Amazon river in the *All* simulation reduces this CO_2 outgassing over the whole region by a factor of two to 19.3 Tg C yr^{-1}. The air-sea CO_2 fluxes also become spatially more variable, with strong source and sink regions (Figure 2.12b). The Amazon's estuary becomes a strong source of CO_2 to the atmosphere. Despite its small size, this area alone is responsible for an outgassing of 1.5 Tg C yr^{-1}. In contrast, the shelf waters become a sink of 3.7 Tg C yr^{-1}. The intensity of this sink is highest close to the estuary zone and decreases as the waters travel northwards (Figure 2.12b). The transition between the outgassing estuary and the undersaturated shelf is very sharp and corresponds to the area where the improvement of the light conditions allows for high primary production to set in (Figure 2.6). The offshore plume waters also become a sink

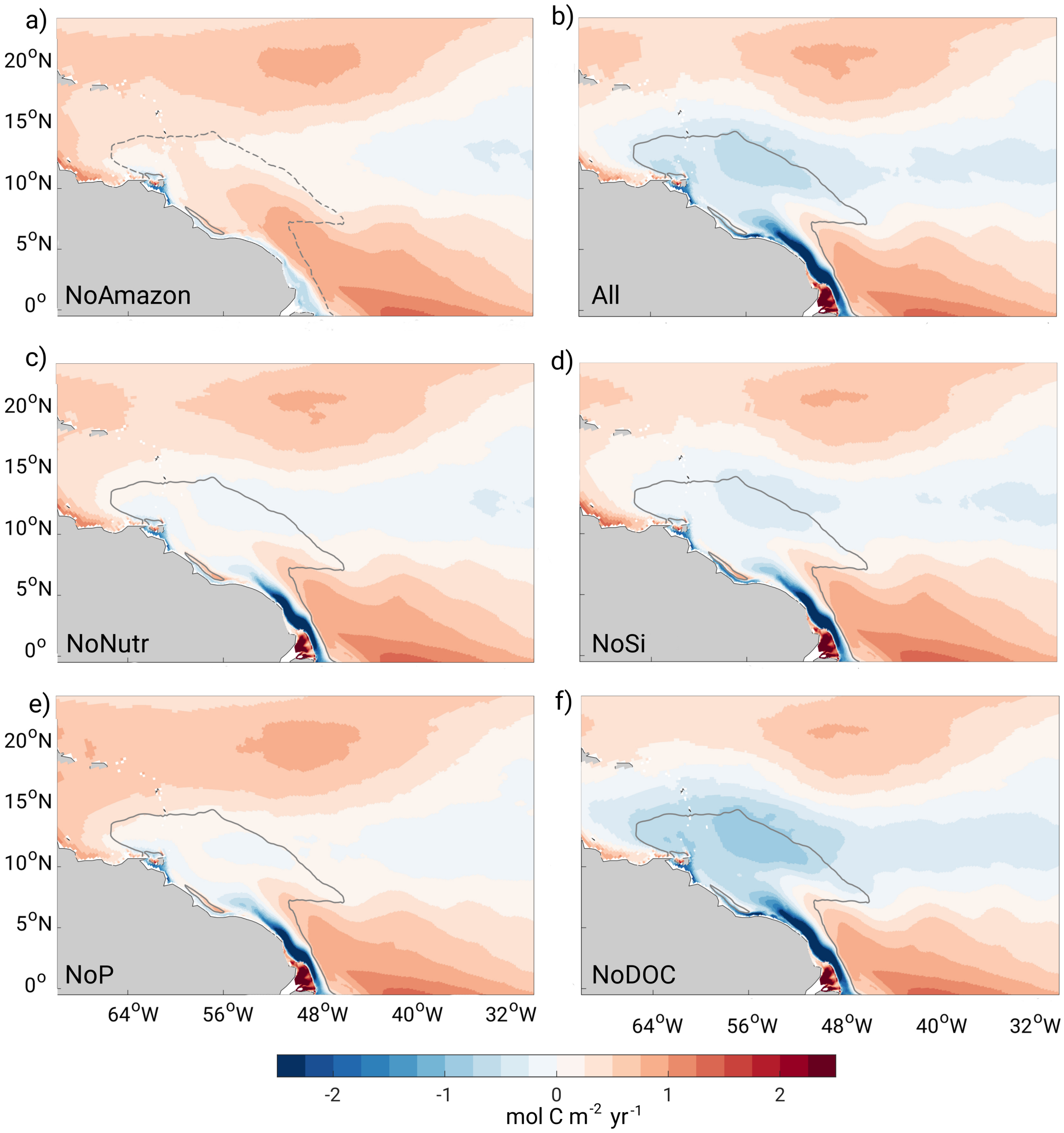

Figure 2.12 Maps of the model simulated annual average air-sea CO_2 flux density in the WTA (mol C m^{-2} yr^{-1}). Shown are the fluxes (positive outgassing) from (a) the *NoAmazon* case, (b) the *All* case, (c) the *NoNutr* case and (d) the *NoSi* case, (e) the *NoP* case, (f) the *NoDOC* case. See table 2.1 for a description of the different cases. The solid lines in each panel correspond to the average plume limits.

for atmospheric CO_2. Even though the intensity of the uptake is smaller than in the shelf waters, this region is responsible for an uptake of 4.7 Tg C yr^{-1}, representing the largest sink of our study area (Table 2.4). The non-plume waters, in contrast, are a net source of 26.2 Tg C yr^{-1}.

Table 2.4 Annually integrated CO_2 fluxes. Negative values correspond to an uptake of CO_2 by the ocean and positive values correspond to outgassing. The boundaries for the sub-regions are taken from the *All* simulation and shown in figure 2.1.

Sub-regions	*All* (Tg C yr^{-1})	*NoDOC* (Tg C yr^{-1})	*NoNutr* (Tg C yr^{-1})	*NoAmazon* (Tg C yr^{-1})	Total Effect of Amazon (Tg C yr^{-1})
Estuary	1.5	1.3	1.1	-0.2	1.7
Shelf	-3.7	-4.2	-2.3	0.7	-4.5
Offshore Plume	-4.7	-7.6	1.5	6.1	-10.8
Non-plume	26.2	18.9	34.8	39.2	-13
Total WTA	19.3	8.4	35.1	45.8	-26.5

2.4.2 Factors contributing to the air-sea CO_2 balance

The factorial simulations permit us to disentangle the different mechanisms controlling the response of the air-sea CO_2 fluxes to the input of nutrients and carbon by the Amazon River. The difference between the *All* and *NoAmazon* simulations reflects the net effect of the Amazon River (Figure 2.13). In the estuary waters, the net effect is a change of 1.7 Tg C yr^{-1} from a slight uptake in the *NoAmazon* simulation to an outgassing in the *All* simulation. In the shelf and plume waters, the presence of the Amazon River turns the slight outgassing of CO_2 in the *NoAmazon* simulation to a strong uptake, resulting in a net change of -4.5 and -10.8 Tg C yr^{-1}, respectively. In the non-plume waters, the net effect of the Amazon River comes to -13 Tg C yr^{-1}, reducing the outgassing of this vast region.

To quantify the contribution to the different factors leading to this total effect, we computed the differences between the simulations for each region as follows: (i) *All* -*NoDOC* to investigate the changes in air-sea CO_2 fluxes due to the delivery of terrestrial DOC, (ii) *NoDOC* - *NoNutr* to explore the changes due to the alteration of biology, as a response of the riverine nutrient inputs, (iii) *NoNutr* - *NoAmazon* to assess the remaining mechanisms affecting the air-sea CO_2 fluxes such as the impact of the riverine delivery of DIC and Alk, and the impact of freshwater on ocean stratification and circulation (Figure A.7). Unfortunately, we cannot disentangle these two effects in our factorial simulations. The consideration of another factorial case with only freshwater input would not solve this issue, since the addition of freshwater without any DIC or Alk would lead to an undesired strong dilution effect.

The addition of terrestrial DOC in the marine realm causes a substantial outgassing (Figure

2.13), reflecting the relatively fast breakdown of this organic matter to produce DIC that then drives a flux of CO_2 out of the ocean. The relative importance of this outgassing increases when moving from the estuary to the open ocean. In the non-plume waters, the terrestrial DOC promotes a CO_2 release of 7.3 Tg C yr^{-1}.

The effect of the river input of DIC and Alk and the physical alteration due to the input of freshwater is largest in the estuary and on the shelf. In the estuary, the river supply of waters that have almost no excess of Alk over DIC (Sarmiento and Gruber, 2006) creates a very high pCO_2 (up to nearly 700 μatm in June) leading to a strong CO_2 outgasssing (Figure 2.13). The high pCO_2 is only minimally offset by CO_2 uptake by phytoplankton growth owing to the high turbidity of the waters in this region impeding it. On the shelf, as the plume travels northward, the river waters mix with marine waters that have a relatively high excess of Alk over DIC, reducing pCO_2. As the waters clear up (around a salinity of 25), primary production sets in, lowering pCO_2 even further. In the non-plume waters, the changes are relatively small (around 4 Tg C yr^{-1}), for reasons we cannot firmly establish.

The biggest effect of the Amazon induced changes in the air-sea CO_2 balance stems from

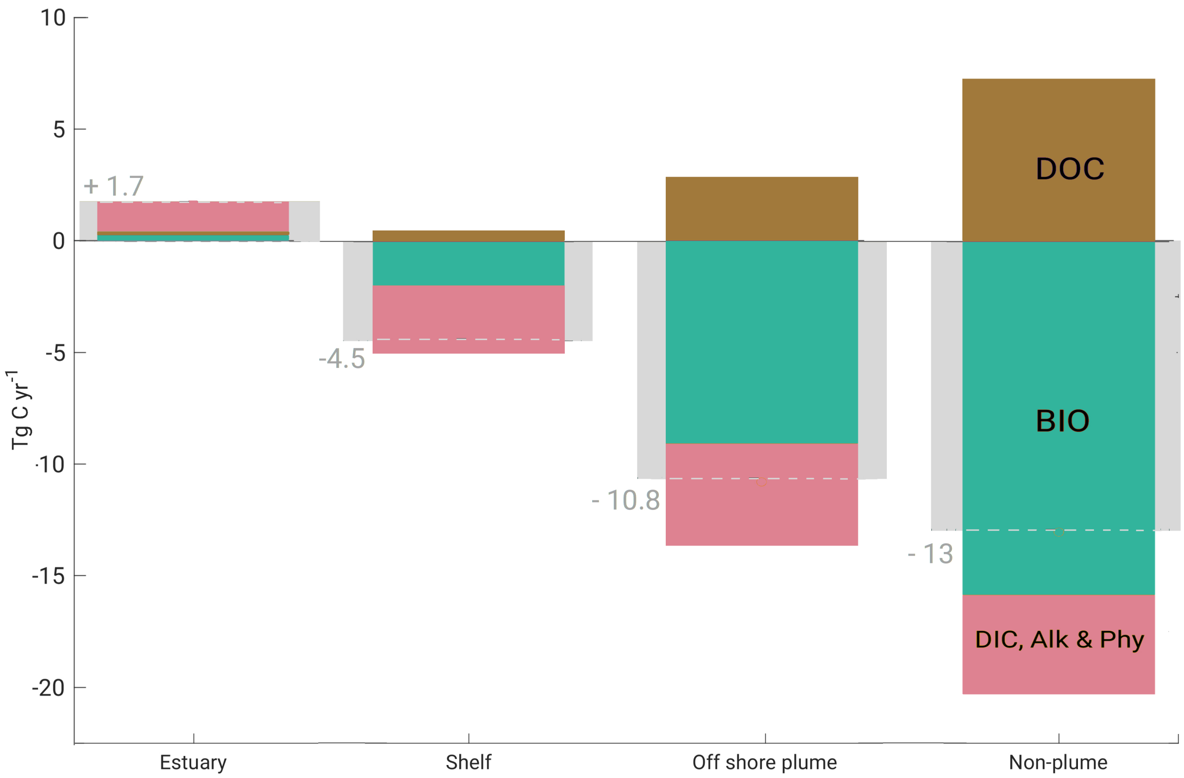

Figure 2.13 Quantification of the different factors contributing to the total effect of the Amazon River on the air-sea CO_2 fluxes in different regions. Pink corresponds to the effect of the river input of freshwater, DIC, and Alk. Green reflects the contribution of the biological pump, and brown represents the outgassing driven by the riverine input of terrestrial DOC The grey bar and associated values highlight the total net effect of the Amazon.

the biological carbon pump driving a very substantial uptake of CO_2 from the atmosphere. A key reason for this strong impact is that most of the increase of NPP and POC production occurs rather shallow in the water column (Figure 2.11), thereby increasing the fraction of CO_2 that is taken up from the atmosphere as opposed to taken from the water column (see table A.6, and e.g., Jin et al. (2008) for a discussion of this atmospheric uptake efficiency). Thus, in addition to the nutrient supply, the enhancement of stratification by the Amazon River (Pailler et al., 1999) associated with a nutrient-rich discharge makes the plume waters especially efficient in taking up atmospheric CO_2.

Overall, our results suggest that in the areas close to the mouth of the river, the riverine carbonate chemistry has the largest impact on the air-sea CO_2 balance, driving the outgasing in the estuary zone and enhancing the uptake in the shelf region. Further off shore in the plume and non-plume regions, the biological changes induced by the riverine nutrients play the leading role.

2.5 Caveat and limitations

Our modeling work comes with several limitations that are inherent to the model structure and parameters choices. Our biggest limitations are associated, perhaps, with the handling of organic matter in BEC, both particulate and dissolved. The routing of particulate organic matter through the ecosystem has been shown to differ a lot between biogeochemical models and significantly impact the magnitude of particle formation (Laufkötter et al., 2016). Particularly relevant is the role of diatoms. While we account for this in our parameterizations, we treat DDAs and normal diatoms the same way, even though DDAs have been hypothesized to be more efficient in this export (Korte et al., 2020). This means that we may tend to underestimate the contribution of DDAs to POM formation and EP. A further consideration is the treatment of grazing. With BEC having only one grazer, this provides very limited capability to implement variations in grazing pressure, with implications for the phytoplankton community structure.

Our results are also sensitive to our assumptions regarding DOM. We chose to apply a canonical Redfield stoichiometry to estimate the concentration of the terrestrial DON and DOP delivered by the Amazon. While our results are insensitive to DON, they are sensitive to our assumptions about terrestrial DOP. Using a limited number of DOP measurements, Richey et al. (1991) suggested a riverine DOP concentration of about 0.5 mmol P m^{-3}. Thus, our estimate of 4 P m^{-3} is on the high side. This would imply that we may have overestimated the DOP stimulated N_2 fixation and consequently also primary production. On the other hand, our model misses other P sources such as the desorption from particulates, which has been suggested to be significant (Berner and Rao, 1994).

Other choices likely to affect our results are the non-differentiation between terrestrial and marine DOM and the parameters driving the lifetimes of the different components of DOM. These aspects of DOM dynamics are critical in controlling where along the plume pathway regenerated nutrients and inorganic carbon are supplied back to the system. However, given the paucity of data to constrain the potential parameters, we did not implement terrestrial DOM pools in BEC to avoid adding unconstrained complexity. In this regard, more *in situ* / experimental studies unraveling the dynamics of the DOM delivered by the Amazon, especially DON and DOP would be very valuable.

The simulated nutrient dynamics and associated response to the Amazon inputs might also be affected by our decision to close the lateral boundaries in the Arctic and within the Mediterranean. Indeed, the Arctic Ocean inflow into the North Atlantic is associated with a low N:P ratio (Torres-Valdés et al., 2013) that we do not capture. But we expect this effect to be small owing to the short time-integration of our model, resulting in a smaller influence of the lateral boundary conditions in our simulations. Coles and Hood (2006) showed that the inflow of the high N:P waters from the Mediterranean has a significant effect on the basin-wide N:P stoichiometry and might lead to an overestimation of simulated N_2 fixation if this inflow was not represented in the model. But while the closed boundary within the Mediterranean implies that we do not restore the nutrients there toward observations, our model includes the Mediterranean outflow and thus includes a mechanism to carry the high N:P waters of this basin into the Atlantic. We therefore do not expect our decision to close the Mediterranean boundary to impact our results substantially.

Despite the limitations described above, our estimates of EP and air-sea CO_2 fluxes match quite well previous estimates based on observations (see section 6), giving us confidence that most of our conclusions are robust.

2.6 Comparison to previous work

Our estimate of the amount of extra NPP fueled by the input of nutrients by the Amazon is comparable in magnitude to that reported by Da Cunha and Buitenhuis (2013), especially when considering that their estimate included the enhancement from all the rivers of the region. They simulated an increase of NPP of 34% (140 Tg C yr^{-1}) in the coastal tropical Atlantic Ocean (20° S - 20° N, 70° W - 20° E), close to our value of 9% (115 Tg C yr^{-1}). In contrast, Lacroix et al. (2020) estimated a much larger increase of NPP, i.e., they found an enhancement of +166% in the Amazon shelf area (<250m deep). But they also noted that in their simulations, the sink of nutrients in coastal areas might be too large.

Our finding of the Amazon River strongly stimulating N_2 fixation in the WTA is supported by numerous observational studies (DeMaster et al., 1991; Subramaniam et al., 2008a). In fact, the region downstream of the Amazon is globally one of the regions with the highest N_2 fixation rates (Luo et al., 2012). In comparison, in their modeling study, Da Cunha and Buitenhuis (2013) found a much smaller increase of only +0.28 Tg N yr^{-1}. They considered only a single canonical diazotrophs, while the additional consideration of DDAs in our study might explain this difference. DDAs, having a higher growth rate than regular diazotrophs (Table A.1), are more prone to develop large blooms.

In line with Sohm and Capone (2010a) who highlighted an elevated turnover of PO_4 in the WTA characteristic of a P deficiency, phosphorus is the key limiting nutrient in our simulations. This situation is only reinforced by the fact that the atmospheric deposition influx is dominated by N compared to P (Chien et al., 2016). This makes the magnitude of the river supply of PO_4 and DOP the most important controls on how the Amazon impacts the WTA. Terrestrial DOP plays a special role in our model, given its direct uptake by diazotrophs and their role in stimulating further production.

Overall, the presence of the Amazon River is responsible for an increase of POC export at 100 meters of 32 Tg C yr^{-1}, which is close to the estimate of 27.6 Tg C yr^{-1} estimated by Subramaniam et al. (2008a). However, Subramaniam et al. (2008a) attributed 70% of this POC export increase to DDAs, whereas our results indicate only a 15% contribution and a much larger contribution by diatoms (70%). For their calculation, Subramaniam et al. (2008a) extrapolated their estimate of C-fixation from DDAs, thus assuming the same level of production over all the mesohaline waters (salinities of 30-35). This might have led to an overestimation of the importance of DDAs that represent 28% of the total biomass in their sampled stations. In our simulations, even if the productivity of DDAs substantially increases due to riverine inputs, their relative contribution to the total biomass is only 11% in offshore plume waters. This is in line with the simulation performed by Stukel et al. (2014), where DDAs contributed to 10% of the total biomass.

In our simulations, although DDAs play a key role in providing additional nitrogen to the system and contribute significantly to the export of carbon depths, they do not represent the main pathway for the transfer of carbon to depth. This role is taken by diatoms. This is consistent with many observations, while Korte et al. (2020) recently provided sediment trap-based evidence that suggested that DDAs might be more efficient at transferring carbon at depths than regular diatoms. If this was a general pattern, it would increase the importance of DDAs in our simulations.

Our study confirms the hypothesis put forward in several studies (Cooley et al., 2007; Subramaniam et al., 2008a; Yeung et al., 2012; Araujo et al., 2014) that the CO_2 undersaturation in the offshore plume waters is a result of an enhancement of the biological pump by the Amazon River. In the *All* simulation, the offshore plume waters constitute a sink of atmospheric CO_2 of 4.7 Tg C yr^{-1}. Our estimate is in the range of previous assessments, with earlier studies having estimated a larger sink (Körtzinger (2003): 14.5(±5) Tg C yr^{-1} , Cooley et al. (2007): 15 (±6)

Tg C yr^{-1}) than more recent ones (Lefévre et al. (2010): 5 Tg C yr^{-1}, Ibánhez et al. (2017): 7.85 ($\pm$1.02) Tg C yr^{-1}). The exact contribution of biology is rarely elucidated. Ternon et al. (2000) determined that primary production could contribute to 30% of the CO_2 undersaturation, while Cooley et al. (2007) estimated that it could enhance the undersaturation by one hundred percent. In our simulations, 60% of the net effect of the Amazon River can be attributed to changes in biology within the offshore plume waters. Our results also show that the impact goes well beyond the plume waters, with the enhanced biological pump creating an anomalous sink in the offshore non-plume waters that is less intense, but integrates to a similar net sink as that realized in the plume waters.

In all regions, the remineralization of terrestrial DOC drives an outgassing of CO_2. But the magnitude of this effect in in our model is smaller than hypothesized in a previous study (Lefèvre et al. (2017) and references herein). However, Medeiros et al. (2015) showed that a large fraction (between 50 and 76%) of the Amazon River DOM was stable in the coastal ocean. This corresponds roughly to our results, which are, of course, strongly dependent on the chosen remineralization time-scale of DOC.

2.7 Summary and Synthesis

The Amazon River has a substantial and cascading impact on marine biogeochemistry, the biological pump, and the air-sea CO_2 of the WTA, which we synthesize in figure 2.14. In the top panel, we illustrate the overall effect of the Amazon on the air-sea CO_2 fluxes and the different controlling factors. The Amazon induces an additional outgassing of 1.7 Tg C yr^{-1} in the nearshore areas, but creates an additional uptake of 28 Tg C yr^{-1} in the remaining of the WTA, as illustrated by the differences between the large yellow arrows. Most importantly, the Amazon leads to a reversal of the outgassing in the shelf regions and in the plume waters, making these regions net sinks for atmospheric CO_2. This is the combined result of the delivery of nutrients, organic and inorganic carbon, alkalinity and low salinity waters, most of them acting in concert, but not always.

Our factorial experiments permitted us to demonstrate that the Amazon-induced enhancement of the ocean's biological pump is the main driver for this enhanced uptake (green arrow in the top panel). But our study underlines the non-linearity of this causal chain and the importance of internal feedbacks. In the bottom panel of figure 2.14, we represent the distinct types and ranges of impacts that the riverine nutrients have on the different nutrients and carbon cycles. Overall, NPP increases in response to the nutrient inputs by the Amazon by 115 Tg C yr^{-1} and EP by 32 Tg C yr^{-1}. Riverine phosphorus (light green cog) plays a key role in supporting the increase in primary productivity. The ambient marine waters are highly depleted in inorganic phosphorus and any addition of riverine PO_4 is bound to translate into more productivity, in an almost proportional fashion. Even more crucial is the role of DOP whose direct use by diazotrophs is necessary to sustain their blooms. In contrast, the delivery of inorganic nitrogen does not affect the entire system very much. N_2 fixation and additional regenerated nitrogen dominate the nitrogen sources and allow NPP to increase way beyond what the total consumption of riverine DIN can support, as illustrated by the rapidly decreasing fraction of riverine N in figure 2.14. Riverine $Si(OH)_4$, on the other hand, is not completely consumed within the WTA and part of it escapes our region of study. Predominantly, $Si(OH)_4$ modulates the NPP to export relationship. Its presence results in a shift in the phytoplankton community from a small phytoplankton dominated community to a diatom-dominated community, enhancing the efficiency of the biological pump. By sending more carbon and nutrient to depths, the presence of riverine $Si(OH)_4$ also reduces the recycling of nutrients in the euphotic zone and ultimately tempers the enhancement of primary productivity.

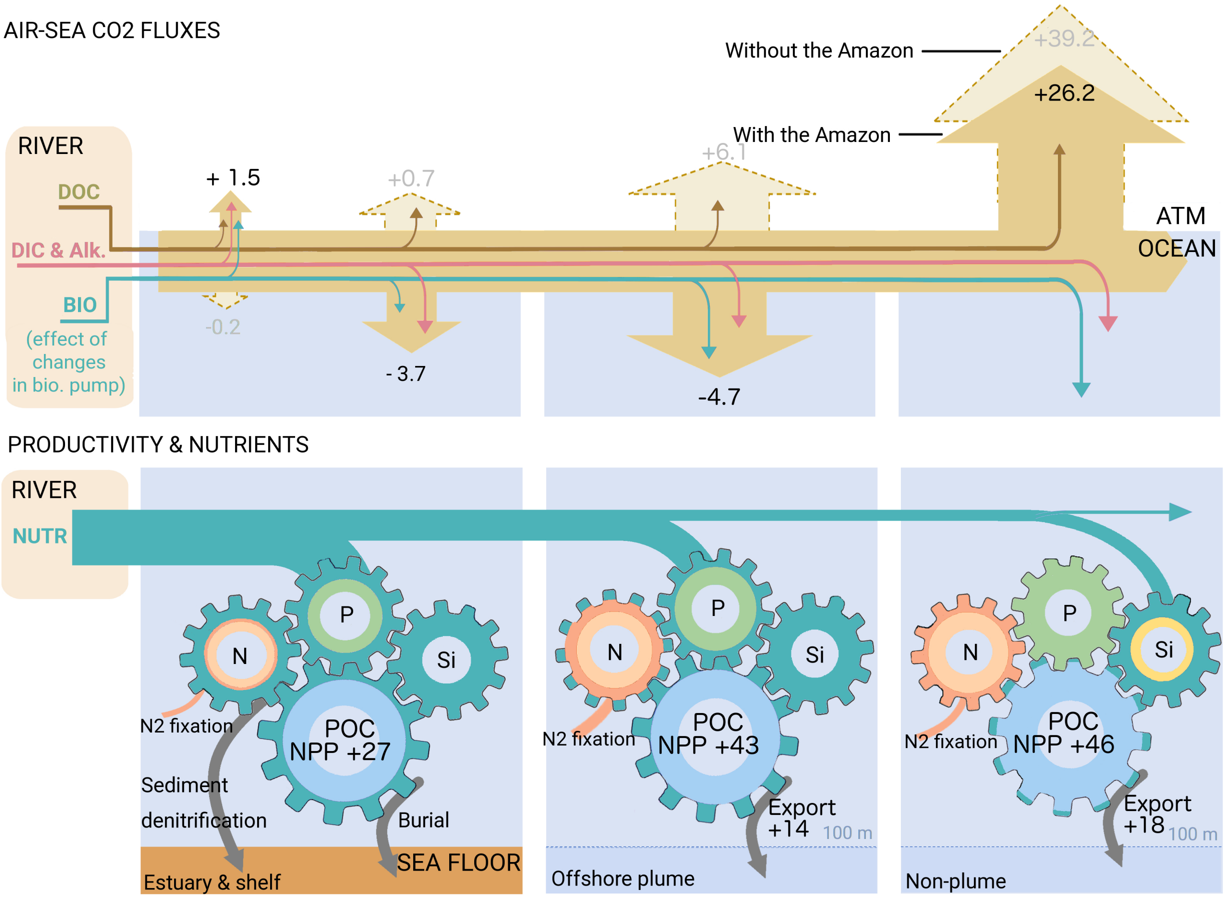
AIR-SEA CO2 FLUXES
Without the Amazon
+39.2
+26.2
With the Amazon
+6.1
RIVER
DOC
DIC & Alk.
BIO
(effect of changes in bio. pump)
+ 1.5
+0.7
-0.2
- 3.7
-4.7
ATM
OCEAN
PRODUCTIVITY & NUTRIENTS
RIVER
NUTR
N
P
Si
POC
NPP +27
N2 fixation
Sediment denitrification
Burial
Estuary & shelf
SEA FLOOR
N
P
Si
POC
NPP +43
N2 fixation
Export
+14
100 m
Offshore plume
N
P
Si
POC
NPP +46
N2 fixation
Export
+18
100 m
Non-plume

Figure 2.14 Schematic summarizing the impacts of the Amazon on the biological pump, the cycling of nutrients, and the air-sea CO_2 balance. The top yellow arrows represent the air-sea CO_2 fluxes. The solid one corresponds to the *All* simulation while the dashed one represents the *NoAmazon* case. The smaller arrows inside illustrate the effect of the different riverine inputs on the air-sea CO_2 exchange. The cogs represent the cycling of different nutrients with their riverine fraction indicated in green and the marine fraction in a different color: orange for NO_3, light green for PO_4, blue for POC and yellow for $Si(OH)_4$. All values are the climatological annual mean fluxes in Tg C yr^{-1}.

The DIC and Alk concentration of the river waters (pink arrows in figure 2.14) and the delivery of terrestrial DOC (brown arrows) are mostly affecting the regions close to the mouth of the river (estuary and shelf waters). More than the absolute amounts of DIC and alkalinity, it is the ratio between the two that affects the air-sea CO_2 balance the most, pushing the system towards oversaturated or undersaturated conditions. Regarding terrestrial DOC, our results are sensitive to its lability that will determine where it will be remineralised, counteracting the effect of the biological pump. In our simulations, the contribution of DIC, alkalinity and terrestrial DOC to the changes in air-sea CO_2 fluxes remains significant further offshore, with a clear downstream effect (Figure 2.14). The effect of the Amazon beyond the physical structure of its plume is small in relative terms but our results show that the impact can be substantial when integrated over such a large area.

Acknowledgements

This study was part of the C-CASCADES project (https://c-cascades.ulb.ac.be/) funded by the European Union's Horizon 2020 research and innovation programme under the Marie Sklodowska-Curie grant agreement No. 643052. We are grateful to Pierre Regnier for leading this effort. Financial support was provided by the Swiss Government (Staatsskretariat für Bildung, Forschung und Innovation - SBFI) and ETH Zürich. We would also like to thank Cara Nissen for her valuable insight on the BEC model and Damian Loher for technical support. Model output data are available online in the ETH library archive (doi:10.3929/ethz-b-000437973) and may alternatively be obtained upon request (domitille.louchard@usys.ethz.ch).

Chapter 3

The intensification of N_2 fixation driven by the Amazon river: the role of phytoplankton competition

D. Louchard, M. Münnich, N. Gruber

Environmental Physics, Institute of Biogeochemistry and Pollutant Dynamics, ETH Zurich, Universitätstrasse 16, 8092 Zürich, Switzerland.

This manuscript is in preparation

Abstract

The high rates of N_2 fixation observed in the Western Tropical Atlantic Ocean (WTA) are powered by the large influx of nutrients from the Amazon river. To disentangle the impact of the Amazon on the different factors controlling N_2 fixation in the region, we use a high resolution regional model (ROMS-BEC) that includes 2 diazotrophic phytoplankton classes (*Trichodesmium* and Diatom-Diazotroph-Assemblages, DDAs). In our simulations, the Amazon is responsible for an enhancement of N_2 fixation of 3.8 Tg N yr^{-1}, being an increase of 74%. This large increase is supported for the most part by DDAs that represent 90% of the diazotrophic community in the plume waters. To determine how the Amazon creates the conditions in which DDAs thrive, we analyzed the bottom up and top down controls on phytoplankton along the plume pathway and how the phytoplankton competition is disrupted by the delivery of nutrients by the river. Throughout the plume pathway, DDAs completely out-compete *Trichodesmium* as their higher maximum growth makes them more efficient in building biomass. Nevertheless, DDAs never accounts for more than 25% of the total phytoplankton biomass as they face the competition of other non-diazotrophic phytoplankton types in the use of the riverine nutrients. Overall, DDAs thrive in the offshore plume region where their nutrient uptake advantages (N-fixation, DOP uptake) is concomitant with a relaxed grazing pressure.

3.1 Introduction

The Western Tropical Atlantic Ocean (WTA) is a hotspot of N_2 fixation i.e. the reduction of dinitrogen to ammonia performed by diazotrophic plankton. Despite a spatial heterogeneity associated with the complex hydrological and biogeochemical dynamics of the WTA, among the highest reported rates of marine N_2 fixation have been measured with constancy throughout the years (Luo et al., 2012), with average N_2 fixation rate as high as 3200 μmol N m^{-2} d^{-1} within DDAs blooms (Carpenter et al., 1999). Louchard et al. (2021) predicted that around 8.9 Tg N yr^{-1} was fixed by diazotrophs in the WTA, which represents 7 to 13 % of the N_2 fixed in the global ocean depending on the global estimate (Landolfi et al., 2015; Paulsen et al., 2017; Tang et al., 2019a). By reducing N_2 and releasing it as biologically available nitrogen through excretion or upon death, diazotrophs significantly contribute to the nitrogen budget, participating in the sustainment of the local phytoplankton production. Capone et al. (2005) calculated that the nitrogen fixed by *Trichodesmium* in the tropical and subtropical North Atlantic Ocean represents 50 to 180% of the diapycnal fluxes of nitrate. N_2 fixation also affects the carbon cycle, especially in the WTA. Diatom-Diazotroph-Assemblages (DDAs), that correspond to the symbiotic association of a diatom and a diazotroph *Richelia intracellularis* (Carpenter et al., 1999; Foster et al., 2011), have been shown to drive a significant carbon export that results in negative anomalies in the air-sea CO_2 fluxes (Subramaniam et al., 2008a; Yeung et al., 2012; Louchard et al., 2021).

Despite their generally lower maximum growth rate compared to non-diazotroph phytoplankton species, N_2 fixers have been traditionally seen as particularly competitive in warm P-rich N-depleted environment (Benavides and Voss, 2015). Recent studies have nevertheless highlighted a higher variety of environmental niches for diazotrophs along with a larger diversity of species whose responses to nutrient concentration, light level and temperature differ (Pierella Karlusich et al., 2021). In the WTA, the environmental conditions are highly variable, mostly due to the large inflow of the Amazon River progressively mixing with oceanic waters. The Amazon delivers large amount of nutrients to the coastal region and adjacent offshore waters of the WTA (Araujo et al., 2014; Lacroix et al., 2020), changing the absolute concentration of marine nutrients but also their stoichiometry. Subramaniam et al. (2008a) and others after them (Goes et al., 2014; Weber et al., 2017) defined 3 sub-regions in the WTA based on salinity. The low salinity sub-region is where non-diazotroph species, especially diatoms, thrive thanks to the high nutrient load from the Amazon, leaving little room for N_2 fixers to develop. In the mesohaline sub-region (salinity between 30 and 35), high rates of N_2 fixation are supported by DDAs, taking advantage of an excess of P and $Si(OH)_4$ to N compared to the Redfieldien standard. In the oceanic type of waters (salinity above 35), DDAs are progressively replaced by *Trichodesmium* as $Si(OH)_4$ becomes limiting for them. While this explanation is persuasive, it solely focuses on the bottom up factors, ignoring the grazing pressure that constrains the accumulation of biomass.

The role of top down factors in shaping the N_2 fixation patterns has been long overlooked. The main reason is that *Trichodesmium*, historically the most studied diazotroph, has been shown to be unpalatable or even toxic for numerous zooplankton (Guo and Tester, 1994; Layton et al., 2008). However, there is mounting evidence that diazotrophs are actively preyed upon by zooplankton (Conroy et al., 2016, 2017), that grazing can be an important determinant to the fate of the N fixed by diazotrophs (Hunt et al., 2016) and that it might be a key mechanism in governing the biogeography of N_2 fixers (Stukel et al., 2014; Wang et al., 2019).

In this study, we aim at providing a better comprehension of the balance between bottom up and top down controls and how they determine the ecological success of N_2 fixers in the WTA. We use factorial simulations, i.e. simulations in which one or more riverine nutrients are suppressed from the Amazon inflow, to evaluate in which way(s) these factors are impacted by the Amazon River.

3.2 Methods

3.2.1 ROMS-BEC

This study relies on the coupling of the UCLA-ETH version of the Regional Oceanic Modeling System (ROMS; Shchepetkin and McWilliams (2005)) and the Biogeochemical Elemental Cycling (BEC, Moore et al. (2013c)). The configuration is the same as the one described in Louchard et al. (2021).

ROMS is a widely used ocean circulation model that solves the hydrostatic, incompressible, primitive equations of flow. The model runs on a telescopic grid that provides a strong horizontal refinement in our region of interest (down to <4 km) while covering the entire Atlantic basin. In the vertical, 42 terrain-following σ-coordinates are applied, which results in a high vertical resolution in shelf areas.

The biogeochemical component, BEC, is a plankton functional type model that includes 4 phytoplankton functional types (PFT). On top of carbon and oxygen, the model resolves the cycling of 3 macronutrients (N, P and Si) and one micronutrient (Fe). The phytoplankton growth depends on temperature, light availability and nutrient concentrations. The nutrient requirements are governed by the half-saturation constant (K_i, i being the nutrient) that differs depending on the phytoplankton type. 4 nutrients are considered limiting in BEC: P, N, Fe and $Si(OH)_4$. All PFTs are limited by P and Fe. For their P requirements, they can utilize both PO_4 and DOP, although with distinct efficiencies. Thus, diatoms generally do not take up DOP due to their very high K_{DOP}. In contrast, *Trichodesmium* and DDAs have the same low value for their K_{DOP} and K_{PO4}, i.e they can use as easily both forms of P as suggested by recent studies (Orchard et al., 2010; Watkins-Brandt et al., 2011; Meyer et al., 2016). The growth of small phytoplankton (SP) and diatoms is additionally limited by N, and $Si(OH)_4$ in the case of diatoms. Their higher growth rate and K_i constants make diatoms especially competitive in nutrient-rich environment while SP thrive under low-nutrient conditions.

DDAs are modeled to represent the symbiotic consortia of a diatom and its *Richelia intracellularis* endosymbiont. In the WTA, the most common type of DDA partnership includes a diatom of species *Hemiaulus hauckii* or *Rhizosolenia clevei* although we do not differentiate between the 2 species in our simulations. The host of the symbiosis being a diatom, DDAs are limited by $Si(OH)_4$. Furthermore, DDAs are modeled in 2 states: with or without a symbiont depending on the ambient NO_3 concentration. Based on *in situ* measurements and enrichment experiments, Tuo et al. (2017) demonstrated that the fraction of free living *Richelia intracellulis* decreases when levels of nitrate decrease. In BEC, only when local NO_3 is below 0.5 mmol N m^{-3}, DDAs are considered in symbiosis and performing N_2 fixation to meet their N requirements; above that threshold, they are considered as free-living. When they are free-living, DDAs use inorganic N like a regular diatom. When they are in symbiosis, N_2 fixation is their only source of N, in agreement with Pyle et al. (2020). This is in contrast with *Trichodesmium* that can use concurrently NO_3 and NH_4. The maximum growth rate of DDAs is also different depending on their state: it is lower when in symbiosis. This differentiation with maximum growth rates is also the approach taken by Stukel et al. (2014) and accounts for the fact that even if the growth rate of *Richelia* is enhanced when in symbiosis (Foster et al., 2011), the diatom host needs to have a lower growth rate to accommodate its endosymbiont. A more detailed description of the DDAs formulation can be found in Louchard et al. (2021) and relevant parameters in table A.1.

BEC has one class of zooplankton grazes on all PFTs following a Holling type II ingestion function (Holling, 1959). The specific grazing rate (γ_g^i) of the zooplankton class preying on the PFT *i* is defined as:

$$\gamma_g^i = \gamma_{max}^i \times f^Z(T) \times Z \times \frac{P^i}{z_{grz}^i + P^i} \tag{3.1}$$

where γ_{max}^i represents the maximum growth rate of the zooplankton grazing on PFT *i*, $f^Z(T)$ the temperature scaling function, z_{grz}^i the half-saturation constant for ingestion of PFT *i* and P^i the phytoplankton biomass. We assigned the lowest γ_{max} to *Trichodesmium*, accounting for their inedibility for most zooplankton (table S1). The γ_{max} of DDAs is higher than the one of *Trichodesmium* but lower than the one of diatoms i.e. if equally abundant, the grazing pressure experienced by DDAs would be higher than that of *Trichodesmium* and lower than that of diatoms. In the absence of strong evidence, this choice remains unfortunately conjectural. Until now, no grazing rate of zooplankton preying on DDAs have been estimated. Conroy et al. (2017) presented the first evidence of DDAs and *Trichodesmium* in the guts of calanoid copepods, both at mesohaline and oceanic stations. The methods used in this study did not permit to distinguish between direct grazing and secondary pathway as feeding on aggregates, although they did conclude that direct grazing was likely. We assume in our modeling that DDAs are actively grazed upon but to a lesser extent than our generic diatom PFT. This difference in γ_{max} between DDAs and diatoms is motivated by the fact that higher grazing rates in the region were always reported in the presence of asymbiotic coastal diatoms (Conroy et al., 2016). Furthermore, Bergkvist et al. (2012) suggested that the chain formation in diatoms such as *Hemiaulus hauckii* or *Rhizosolenia clevei* might tamper the risk of being preyed on. This parameter choice has implications for our results which we further discuss in section 3.4.5.

3.2.2 Simulations

For the purpose of this study, we used 4 of the factorial simulations described in Louchard et al. (2021): the *All*, *NoNutr*, *NoP* and *NoSi* simulations. For clarity, the *All* simulation is hereafter refered as the *AllNutr* simulation. The only difference between these simulations is the content of the Amazon inflow. The *AllNutr* simulation corresponds to the most realistic simulation and includes the delivery by the Amazon of the whole suite of nutrients. In the *NoP* simulation, the Amazon delivers all the nutrients except PO_4 and DOP. Similarly, in the *NoSi* simulation, the Amazon delivers all the nutrients except $Si(OH)_4$. In the *NoNutr* simulation, the Amazon delivers solely alkalinity and DIC but no inorganic nutrient or dissolved organic matter. All simulations were ran in climatological conditions following the procedure detailed in Louchard et al. (2021).

3.2.3 Masks and pathways

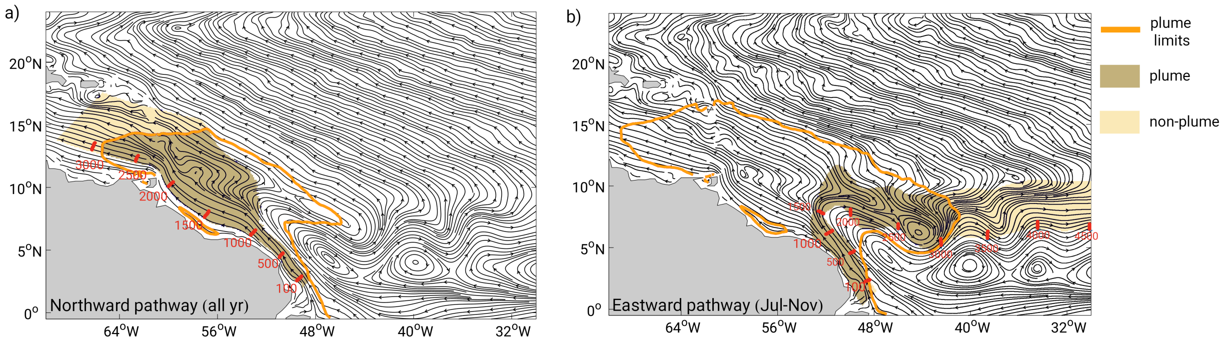

Figure 3.1 (a) Northward pathway with the annual average streamline field and annual average limit of the plume (salinity below 35.25). (b) Eastward pathway with the average streamline field and average limit of the plume (salinity below 35.25) during the retroflection (July to November). In both panels, the values in red display the distance in km from the starting point of the pathway as used in the subsequent figures.

Similar to previous studies (Subramaniam et al., 2008a; Stukel et al., 2014; Weber et al., 2017), we use salinity as a proxy of the degree of mixing between the river and oceanic waters. We adopt the threshold to 35.25 PSU to differentiate between areas under the high influence of the Amazon (plume waters) and areas with low influence from the Amazon (non-plume waters). This distinction is employed for all the spatially integrated calculation.

The dispersion of the plume waters is mostly driven by ocean dynamics and follows different pathways throughout the year (Masson and Delecluse, 2001; Coles et al., 2013). The circulation in the region is dominated by the North Brazilian Current, a western boundary current transporting the plume northward throughout the year (Hu et al., 2004). In summer, the annual migration of the Intertropical Convergence Zone (ITCZ) leads to the diversion of parts of the plume waters eastwards following the North Equatorial Counter Current (NECC). In the streamline and salinity fields of our simulation outputs, we found evidence of these 2 main pathways of the plume and used these fields to define 2 masks that permit us to analyze the gradient of environmental conditions and phytoplankton dynamics as the plume meanders and mixes with ocean waters (figure 3.1). Both pathway masks start as a quite narrow channel as the plume waters stay very close to the coast in the first 1000 km or so. In a second part, the masks get thicker, around 1100 km and 850 km for the northward and eastward pathway respectively. The distance from the beginning of the pathway was computed and in the subsequent analysis, conditions were averaged following the increasing distance regardless of the thickness of the pathway. For the northward pathway, we compute the annual average while for the eastward pathway, we average the conditions from July to November, taking only the months when the plume waters are diverted in this direction.

3.2.4 Analysis framework: growth and grazing ratios

In sections 3.2 to 3.5, we explore the impact of bottom up and top down controls on the competitiveness of DDAs over the 3 other PFTs. To do so, we computed the relative growth and grazing ratios as defined and used by Hashioka et al. (2013) and Nissen et al. (2018). For clarity, we reproduce here the main equations used for this calculation. Additional information can be found in Nissen et al. (2018).

The relative growth ratio is based on the specific growth rate of 2 PFTs i.e. DDAs on one hand and diatoms, SP or *Trichodesmium* on the other hand. In BEC, the specific growth rate μ^i of a PFT *i* can be defined as followed:

$$\mu^i = \mu^i_{max} \times f^i(T) \times g^i(N) \times h^i(I) \tag{3.2}$$

where μ^i_{max} the maximum growth rate, $f^i(T)$ the temperature dependence, $g^i(N)$ the nutrient limitation and $h^i(I)$ the light limitation of PFT *i*. The relative growth ratio μ^{ij}_{rel} is the log of the ratio of the specific growth rates of PFT *i* and *j* and can thus be described as the sum of the log-transformed differences of each growth rate component:

$$\mu^{ij}_{rel} = log\frac{\mu^i_{max}}{\mu^j_{max}} + log\frac{f^i(T)}{f^j(T)} + log\frac{g^i(N)}{g^j(N)} + log\frac{h^i(I)}{h^j(I)} \tag{3.3}$$

The relative growth ratio μ^{ij}_{rel} is nondimensionnal. When the ratio is positive, the realized growth rate of PFT *i* is larger than that of PFT *j*, meaning that overall the bottom up factors give a competitive growth advantage to PFT *i* over PFT *j*. A negative ratio is evidential of the inverse situation. Although each component was calculated, we removed from our subsequent figures and analysis the effect of temperature and light. Both have a negligible impact on the relative growth ratio as it could be expected in a warm and high lit tropical ocean.

The biomass accumulation of phytoplankton is also controlled by the grazing pressure applied by zooplankton. In analogy to the relative growth ratio, we define a relative grazing ratio to compare the grazing rate of different PFTs. To do so, we first compute the biomass-normalized specific grazing rate c^i of PFT *i*:

$$c^i = \frac{\gamma^i_g}{P^i} \tag{3.4}$$

with γ^i_g being the grazing rate of the zooplankton preying on PFT *i* and P^i the biomass of the respective phytoplankton. The relative grazing ratio is then defined as follows:

$$\gamma^{ji}_{g,rel} = log\frac{c^j}{c^i} \tag{3.5}$$

$\gamma_{g,rel}^{ji}$ is positive when the grazing rate on PFT i is smaller than the one on PFT j and vice versa. This ratio is driven by the differences in terms of maximum zooplankton growth rate and in terms of local phytoplankton biomass.

Eventually, the balance between the relative growth ratio and the relative grazing ratio gives us an indication of which PFT is more able to accumulate biomass.

3.2.5 Model evaluation

A thorough model validation has already been conducted and reported in Louchard et al. (2021). The comparison to observations demonstrated the model's capability to reproduce the main physical and biogeochemical features of the domain, including the primary production, the general N_2 fixation patterns and the nutrient dynamics. We will thus here focus more specifically on the N_2-fixers and their relative abundance.

The general characteristics of N_2-fixation in the WTA appear to be properly captured by the model. Overall, N_2-fixation is the highest in the mesohaline waters i.e. where salinity is between 30 and 35 (table 3.1). These large rates of N_2-fixation are mainly supported by *Trichodesmium* and DDAs, the latter being responsible for the highest rates in agreement with the *in situ* measurements (figure 3.2). UCYN, that are not modeled in our setup, are also sampled in the WTA although their contribution to the total N fixed remains minimal. Despite dominating the diazotrophic community, DDAs never prevail in the overall phytoplankton community. With a C-fixation in the mesohaline waters of 6.3 mmol C m^{-2} d^{-1}, they represent on average 10% of the primary production in our model. This is very close to the estimates made by Subramaniam et al. (2008a) who calculated an average C-fixation of 6.5 ± 2.5 mmol C m^{-2} d^{-1}, representing 11% of the primary production.

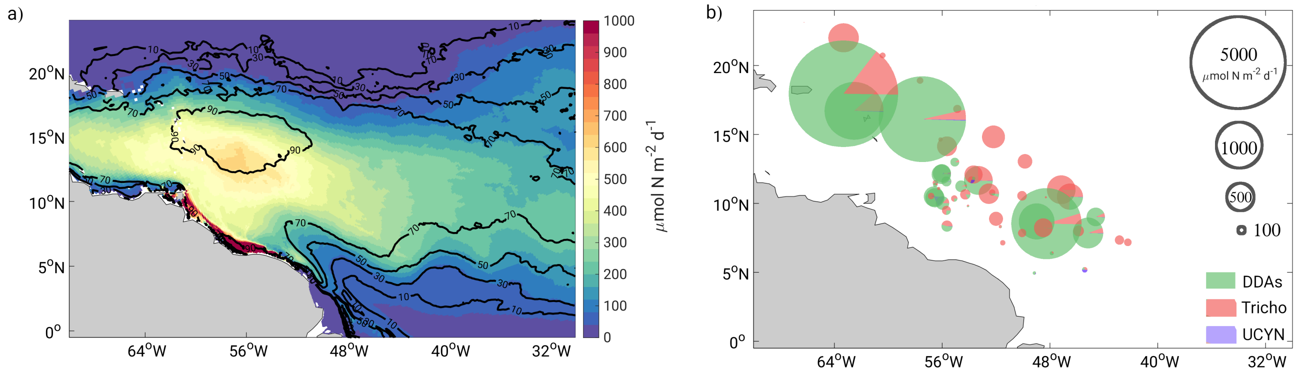

Figure 3.2 (a) Annual mean of the depth-integrated N_2 fixation in the *AllNutr* simulation and contour lines of the percentage that is supported by DDAs. (b) Measurements of depth-integrated N_2 fixation compiled in the MAREDAT database (Luo et al., 2012). We selected only the data where both DDAs and *Trichodesmium* were measured.

If the overall patterns are well reproduced by ROMS-BEC, our simulations miss some of the highest rates and the spatial patchiness of N_2-fixation (figure 3.2). However, reproducing the flickering spatial and temporal variability in N_2-fixation remains a recurrent challenge for most models (Stukel et al., 2014). In our simulations, it is especially true for *Trichodesmium* whose low maximum growth rate prevents from reaching the high rates that are sometimes observed in the region. Furthermore, *Trichodesmium* is on average not prevalent in the oceanic waters, in contrast to the results from Subramaniam et al. (2008a) which estimated that *Trichodesmium* contribute to 48% of the total N_2-fixation in this type of waters. This bias emerges from the fact that DDAs in our configuration might be a bit too competitive even in the non-plume waters compared to *Trichodesmium*. We discuss in more details this aspect in section 4.4 and 4.5.

3.3 Results

3.3.1 N_2 fixation and the importance of DDAs in the WTA

The comparison between our factorial simulations demonstrates that the delivery of riverine nutrients is directly responsible for a substantial increase of N_2 fixation in the WTA. In the *NoNutr* simulation, the annual average N_2 fixation rate is 105 μmol N m^{-2} d^{-1}, which results in the total fixation of 5.1 Tg N yr^{-1}, 0.8 of which is excreted and feeds instantaneously the NH_4 pool. In comparison, the N_2 fixation in the *AllNutr* simulation is enhanced with an annual average N_2 fixation rate of 183 μmol N m^{-2} d^{-1} and a total N_2 fixation of 8.9 Tg N yr^{-1}, being an increase of 3.8 Tg N yr^{-1}. The total N excreted remains the same in the *AllNutr* simulation. The average rate of N_2 fixation hides a large spatial heterogeneity, with higher rates around 10°N in the offshore plume

Table 3.1 Comparison between the model and observations in terms of Primary Production (PP) and N_2-fixation rates in different types of waters

	Low salinity (<30)		Mesohaline (>30,<35)		Oceanic (>35)	
	This study	Obs.	This study	Obs.	This study	Obs.
Avg PP (mmol C m^{-2} d^{-1}) [1]	31	35 ±5	63	57 ±7	30	59±3
% supported by DDAs[1]	6%	0.5%	10%	11%	9%	2%
Avg N_2 fixation by DDAs[2] (μmol N m^{-3} d^{-1})	0.54	0.8	5.0	7.5	1.18	1.1
Avg N_2 fixation by *Trichodesmium*[2] (μmol N m^{-3} d^{-1})	0.06	nr	0.47	0.026	0.34	0.074
% of total N_2-fixation supported by DDAs [2]	90	100	90	99	78	86-88
Depth-integrated N_2 fixation[1] (μmol N m^{-2} d^{-1})	59	35 ± 5	503	986 ± 373	152	157 ± 32

[1] *Observations as reported by Subramaniam et al. (2008a)*

[2] *Observations as reported by Foster et al. (2007)*

waters (figure 3.3-b) and lower rates in the non-plume waters. The areas exhibiting high rates are also the locations of the largest increase of N_2 fixation in the *AllNutr* simulation compared to the *NoNutr* simulation, even though significant increase also occurs in the non-plume waters (figure

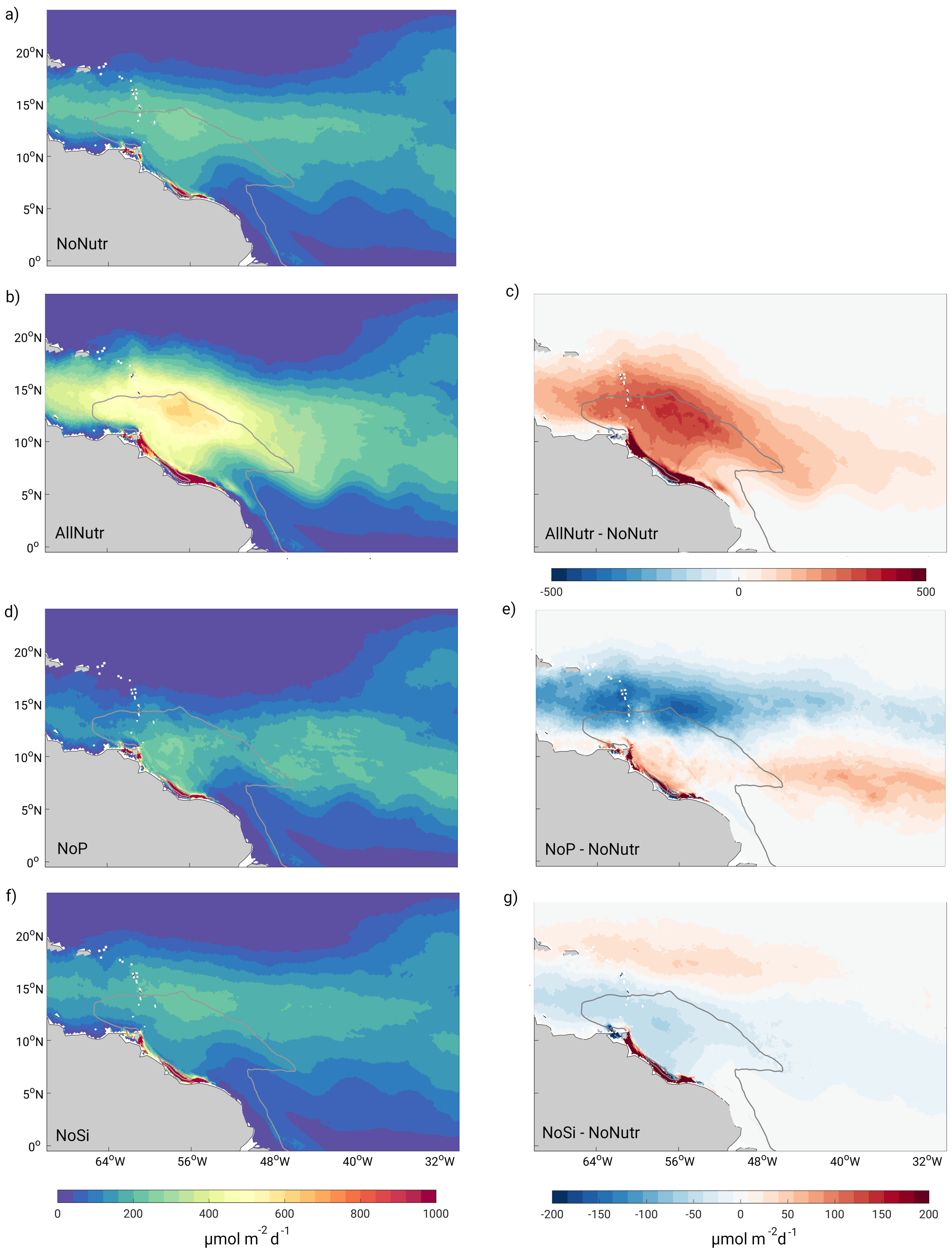
a)
20°N
15°N
10°N
5°N
0°
NoNutr
b)
AllNutr
c)
AllNutr - NoNutr
-500
0
500
d)
NoP
e)
NoP - NoNutr
f)
NoSi
g)
NoSi - NoNutr
64°W
56°W
48°W
40°W
32°W
0
200
400
600
800
1000
µmol m^{-2} d^{-1}
-200
-150
-100
-50
0
50
100
150
200
µmol m^{-2} d^{-1}

Figure 3.3 Annual mean N_2 fixation integrated in the first 100 meters (a) in the *NoNutr* simulation, (b) in the *AllNutr* simulation, (d) in the *NoP* simulation and (f) in the *NoSi* simulation. (c),(e) and (g) display the difference in annual mean N_2 fixation between each factorial simulation and the *NoNutr* simulation. The grey line in all the maps display the average limits of the plume (salinity below 35.25)

3.3-c). In contrast, the *NoP* simulation exhibits a strong decrease in N_2 fixation in the northern half of the domain and some increase in the first half of the northward pathway and along the eastward pathway (figure 3.4). In the *NoSi* simulation, the differences are smaller with a slight decrease within the plume and a slight increase north of the plume (figure 3.3-g).

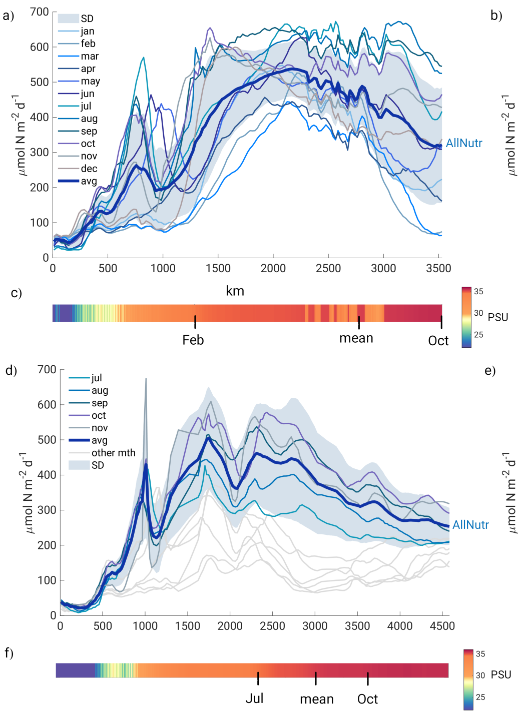

Figure 3.4 Annual average depth-integrated N_2 fixation in the *AllNutr* simulation (thick solid line) and monthly average (fine lines) along (a) the northward pathway and (d) the eastward pathway. The shaded area corresponds to the temporal standard deviation. Annual average depth-integrated N_2 fixation in the *NoNutr*, *NoP* and *NoSi* simulations (thick solid line) and corresponding temporal standard deviation along (b) the northward pathway and (e) the eastward pathway. Average salinity and mean, minimum and maximum limit of plume (salinity below 35.25) along (c) the northward pathway and (f) the eastward pathway.

Table 3.2 Total N_2 fixation integrated over the first 100 meters

Simulation(s)	Plume region (Tg N yr^{-1})	Non-Plume region (Tg N yr^{-1})	All WTA (Tg N yr^{-1})
NoNutr	1.36	3.77	5.13
AllNutr - *NoNutr*	2.06 (+152%)	1.72 (+46%)	3.78 (+74%)
NoP - *NoNutr*	-0.23 (-17%)	-0.46 (-12%)	-0.69 (-13%)
NoSi - *NoNutr*	-0.09 (-6%)	-0.02 (-0.5%)	-0.11 (-2%)

Along both the northward and eastward pathways, in the *NoNutr* simulation, N_2 fixation is at its lowest (less than 50 μmol N m^{-2} d^{-1}) in the first 1000 km while the *AllNutr* simulation exhibits a progressive increase of N_2 fixation (figure 3.4). In the rest of the two pathways, N_2 fixation stabilizes around 150 μmol N m^{-2} d^{-1} in the *NoNutr* simulation and reaches an average rate of 500 μmol N m^{-2} in the *AllNutr* simulation before slowly decreasing. This decrease is sharper along the eastward pathway as the end of this pathway is never reached by the plume waters in contrast to the northward pathway (figure 3.4-c-f). Overall, the N_2 fixation rates in the *AllNutr* simulations appear to be quite sensitive to the seasonal variation of the Amazon inputs. Thus the temporal variability is much larger in the *AllNutr* compared to the *NoNutr* simulation as evidenced by the standard deviation in figure 3.4. Along the eastward pathway, the N_2 fixation rates in the month when the plume waters are not diverted are close to those observed in the *NoNutr* simulation. While we recognize that the seasonality of the Amazon discharge plays a role in driving the high rates of N_2 fixation, we will use the average conditions in the subsequent analysis as it is sufficient to capture the main spatial patterns and the mechanisms behind them.

When spatially integrated, the plume sub-region exhibits the largest increase of N_2 fixation, both in absolute and relative terms (table 3.2). Nevertheless, the non-plume waters still contribute to an increase of 1.7 Tg N yr^{-1}. In contrast, the total N that is fixed by diazotrophs in the *NoP* and *NoSi* simulations slightly decreases compared to the *NoNutr* simulation, highlighting the fact that both nutrients are essential to support the high rates of N_2 fixation present in the *AllNutr* simulation. The increase in the *AllNutr* simulation is associated with a change in the structure of the diazotrophic community. DDAs are benefiting the most of the riverine nutrients inputs. They support 90 % of the total N_2 fixation in the plume waters, against 73 % in the *NoNutr* simulation and 75 % of the total N_2 fixation in the non-plume waters, against 64 % in the *NoNutr* simulation. In contrast, in the *NoSi* simulation, *Trichodesmium* are favored, increasing their share to 35% and 41 % in the plume and non-plume waters respectively.

In summary, more than 40% of the total N_2 fixation that we simulate in the WTA can be directly linked to the presence of the Amazon. DDAs support the majority of this river induced enhancement of N_2 fixation to the detriment of *Trichodesmium*. However, in the use of the new riverine nutrients, DDAs are also facing the competition of non-diazotrophs. Thus, to investigate the determinants of the ecological success of DDAs, we first examine their share in the whole phytoplankton community and how the community structure is affected by the Amazon (section 3.2) and then we disentangled the different controlling factors driving the competition of DDAs against both diazotrophic and non-diazotrophic PFTs (sections 3.3 to 3.5).

3.3.2 The impact of the Amazon on the phytoplankton community structure and the relative contribution of DDAs

Although in most of the WTA, the 4 PFTs co-exist, the areas where each PFT reaches its peak biomass are spatially distinct (figure 3.5). Diatoms are most abundant along the shelf, in the upstream part of the plume and in the equatorial upwelling band. SP exhibit their highest biomass in a large portion of the oceanic waters, in particular in the eastern part of the WTA. The blooms of DDAs are mostly located within the off shore plume waters, in the North-west part of the WTA. *Trichodesmium* are quite ubiquitous at a low biomass level, although their abundance is higher in a latitudinal band around 15°N.

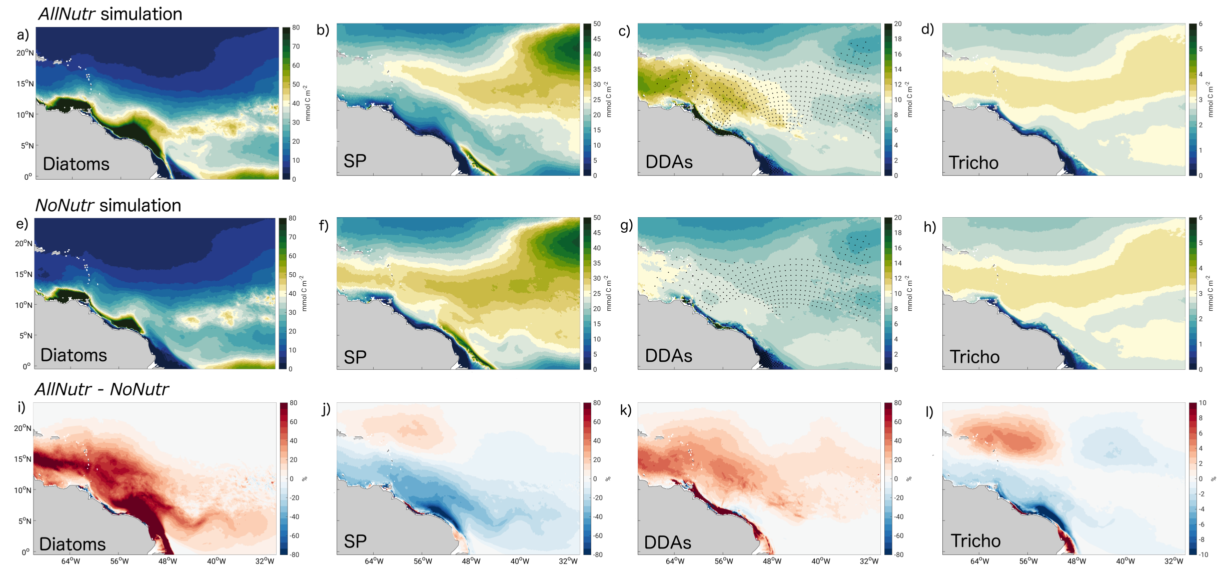

Figure 3.5 Annual average biomass of each PFT in (a-d) the *AllNutr* simulation and (e-h) the *NoNutr* simulation. (i-l) Differences between the 2 simulations in percentage. Note that the color scales differ for each PFT to better visualize the areas of highest biomass. The stippled regions on the maps of DDAs locates where DDAs are mostly fixing N_2 (fixing DDAs representing more than 20 % of the biomass).

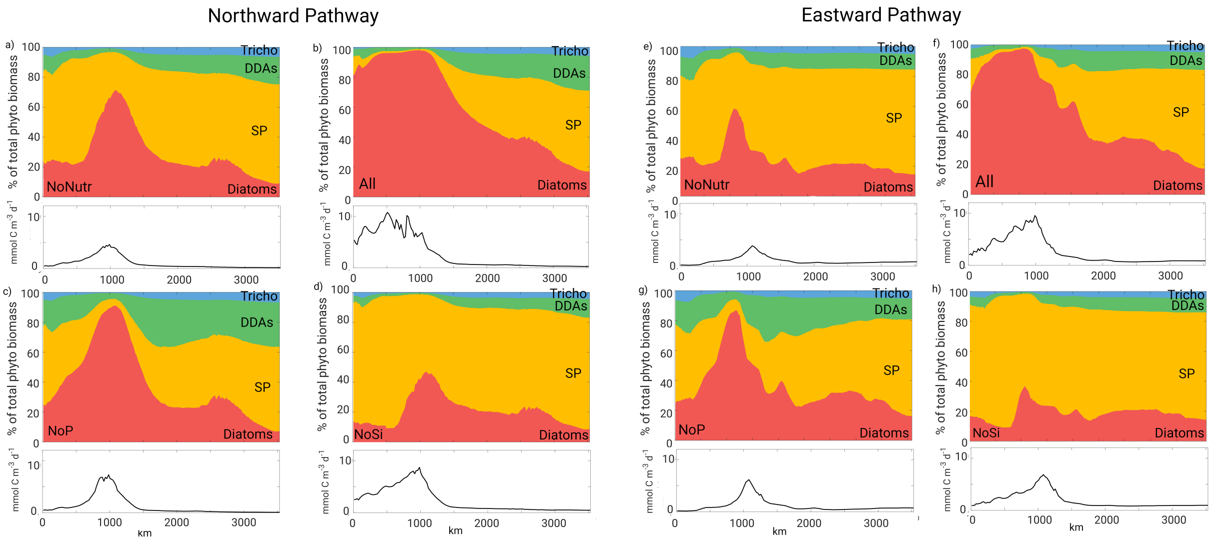

Figure 3.6 Phytoplankton community structure defined as the percentage of total biomass annually averaged along the northward pathway in (a) the *NoNutr* simulation, (b) in the *AllNutr* simulation, (c) in the *NoP* simulation and (d) in the *NoSi* simulation. Below the fraction is displayed the average total NPP for each simulation. All computations have been made for the surface conditions.

The presence/absence of the riverine nutrients does not change these overall patterns (figure 3.5). Nevertheless, diatoms and DDAs clearly benefit from the Amazon inputs, expanding their presence in the plume region, with an average increase of biomass of 173% and 94% for diatoms and DDAs respectively. In contrast, SP exhibit a decrease of biomass of 36% on average in the plume waters. Overall, the biomass of *Trichodesmium* is not heavily affected by the Amazon inputs. Our results mostly reveal a displacement of *Trichodesmium*, with slightly lower biomass in the plume waters and slightly higher biomass dowstream from the plume.

Along the plume pathways, in the *AllNutr* simulation, diatoms establish its dominance in the first 1300 km. This is also the most productive part of the plume pathway. In the rest of the pathway, the relative contribution of diatoms to total biomass decreases while DDAs progressively increase their share compared to the *NoNutr* simulation. In contrast, in the *NoSi* simulation, both diatoms and DDAs exhibit a reduction of their share in the phytoplankton community, while SP prevail. In the *NoP* simulation, DDAs expand their share in the community, illustrating their competitiveness in P-starved environment, although in absolute terms their biomass is reduced.

We will see in the subsequent analysis how DDAs, while facing the competition of 3 other PFTs in the utilization of the new nutrients delivered by the Amazon, manage to maintain and even expand their share in the phytoplankton community. To do so, we use the relative growth and grazing ratios (see methods). These ratios are very sensitive to the environmental conditions such as light or nutrient concentrations, conditions that change a lot with depth. We thus base our analysis on surface conditions only, compared to the previous results that integrated the first 100 meters. Though the community structure at the surface is very similar to the community structure we obtain when we integrate the biomass in the first 100 meters (figure S1). The main difference is a larger contribution of diatoms in the eastward pathway when we integrate with depths. This is due to a deep maximum of diatoms in this part of the region, a deep maximum that is mostly not affected by the surface lens of the Amazon plume.

To investigate the impact of the Amazon on the phytoplankton competition and eventually the structure of the phytoplankton community, we divide the northward plume pathway into an upstream section (0-1300 km) and a downstream section (1300-3500 km). The upstream section is characterized by the dominance of diatoms (figure 3.6) and the largest changes in terms of bottom up and top down controls (figure 3.7). In the downstream section, changes are smaller and less abrupt and the phytoplankton community is more mixed with a growing importance of DDAS. The same patterns and underlying mechanisms can be found along the eastward pathway although with a few nuances that we explore in section 3.5.

3.3.3 Changing competition in the northward upstream plume pathway (0-1300km)

3.3.3.1 Bottom up controls

The relative growth ratio used in this section is a metric that quantifies the competition between 2 PFTs to make use of the different resources and grow. On figure 3.7, the relative growth ratio (black solid line) is further decomposed to disentangle its different controlling factors (shaded areas). In the *AllNutr* simulation, the relative growth ratio is almost always positive, meaning that DDAs benefit from a growth advantage over diatoms, SP and *Trichodesmium*. In the case of the competition against diatoms and SP, this growth advantage is driven by the nutrients while the difference in maximum growth rates has a counterbalancing (negative) effect. In the case of *Trichodesmium*, the positive growth ratio is almost exclusively the result of the higher maximum growth rate of DDAs.

In the absence of the riverine nutrients, in the *NoNutr* simulation, the nutrient advantage of DDAs disappears in the competition with diatoms and even turns negative in the competition against SP and *Trichodesmium*. In the nutrient-depleted waters of the *NoNutr* simulation, SP and *Trichodesmium* have a strong advantage over DDAs in terms of nutrient uptake due to their lower half-saturation constants and the fact that they do not require $Si(OH)_4$. The relative growth ratio is thus negative in the competition of DDAs versus SP and substantially less positive in the competition of DDAs versus *Trichodesmium* than it is in the *AllNutr* simulation.

If we compare the realized growth rates of each PFT between the 2 simulations, we can see that the delivery of riverine nutrients leads first to a strong increase of the growth rates of all PFTs (figure 3.8). However, after a few hundreds of km, the growth rates of both diatoms and SP decreases sharply while the decline of DDAs and *Trichodesmium*'s growth rates is less steep. The difference comes from the strong N limitation experienced by SP and diatoms and not by DDAs nor *Trichodesmium* (figure 3.9).

Overall, the Amazon inputs significantly reduces the Si limitation experienced by DDAs and allow them to be the most competitive PFT in terms of growth. Yet, diatoms appear to dominate the phytoplankton community, not DDAs (figure 3.6).

3.3.3.2 Growth versus grazing

Despite their growth advantage, DDAs do not manage to accumulate more biomass than the other PFT. In fact, they are completely out-competed by diatoms. This situation arises from the different grazing pressure the 2 PFTs experience. The relative grazing ratio in the competition of DDAs versus diatoms is negative in the *AllNutr* simulation. This large grazing disadvantage for DDAs does not exist in the *NoNutr* simulation, even though the relative grazing ratio does become slightly negative between 770 and 1100km (figure 3.7-a&b). Between the *NoNutr* and *AllNutr* simulations, the grazing rate increases significantly on DDAs, +20% while it decreases on diatoms -35% (figure 3.8). In response to the increased primary production in the *AllNutr* simulation, the zooplankton is more abundant and increases its grazing pressure. But because diatoms built up so much more biomass than the other PFT, the biomass normalized grazing rate on diatoms is lower despite the lower μ_{max} of zooplankton grazing on DDAs.

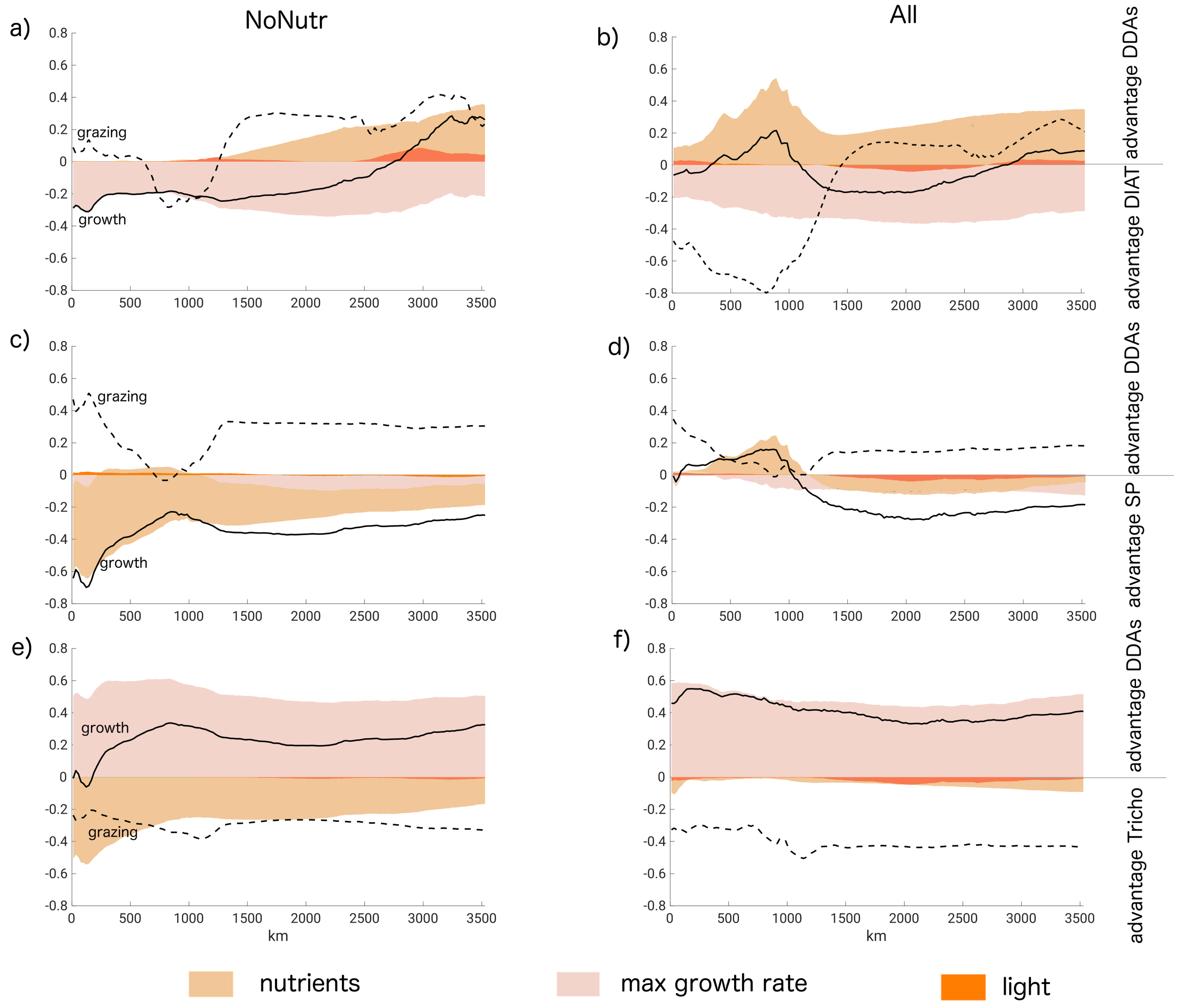

Figure 3.7 Relative growth and grazing ratios along the northward pathway between DDAs and (a-b) diatoms, (c-d) small phytoplankton and (e-f) *Trichodesmium*. The left panels correspond to the *NoNutr* simulation and the right panels to the *AllNutr* simulation

In the competition with SP, the grazing ratio is positive all along the pathway, both in the *NoNutr* and *AllNutr* simulations. Thus, DDAs benefit from a lower grazing pressure than SP although this advantage is reduced in the *AllNutr* simulation compared to the *NoNutr* simulation. In contrast, *Trichodesmium* experience a lower grazing pressure than DDAs and this advantage for *Trichodesmium* is even slightly increased in the *AllNutr* simulation (figure 3.7-e&f).

The relative grazing ratio is in the same magnitude as the relative growth ratio which highlights its importance in the phytoplankton competition. Overall, the top down factors modulate strongly the realized competition between PFTs and prevent DDAs from dominating the phytoplankton community in the part of the pathway.

3.3.4 Changing competition in the northward downstream plume pathway (1300-3500km)

The changes between the *NoNutr* and *AllNutr* simulations on the bottom up and top down controls are more subtle in the downstream plume pathway than in the upstream section. Nevertheless, it is in the downstream plume pathway that DDAs increase the most their share in the phytoplankton community (figure 3.6) and that the highest N_2 fixation rates occur (figure 3.4). We investigate in the following subsections the conditions favoring the DDAs.

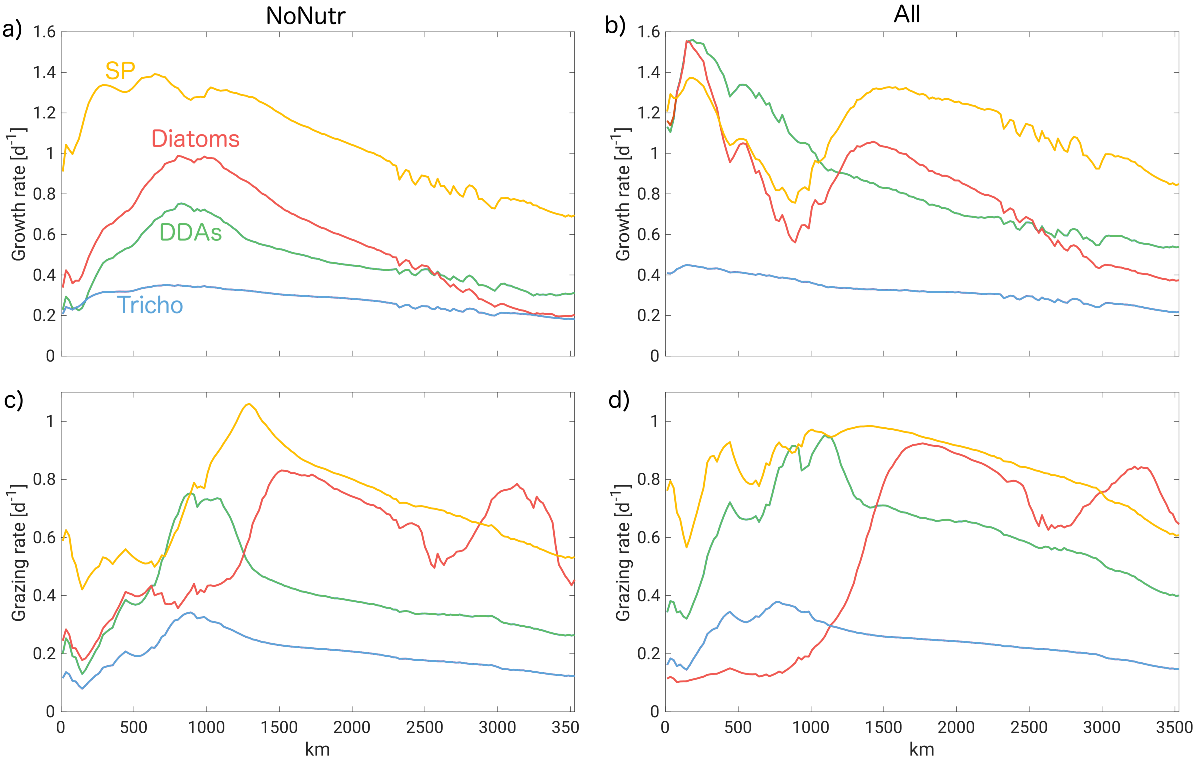

Figure 3.8 Growth rates of each PFT and biomass-normalized grazing rates on each PFT in (a & c) the *NoNutr* simulation and in (b & d) the *AllNutr* simulation

3.3.4.1 Bottom up controls

DDAs remains more competitive in terms of nutrient uptake than diatoms. In this part of the plume pathway, it is P rather than N that plays a central role. DDAs benefit from their ability to efficiently use DOP as a source of phosphorus. In a large portion of the plume, the main limiting nutrient for DDAs remains $Si(OH)_4$ when diatoms are already strongly limited by P (figure 3.9). But the lower μ_{max} of DDAs counterbalances this advantage and their realized specific growth rate is lower or only slightly higher than the one of diatoms (figure 3.8).

The realized growth rate of DDAs is also lower than the one of SP but the difference between the two is reduced compared to the *NoNutr* simulation, resulting in a less negative relative growth rate ratio the *AllNutr* simulation (figure 3.7). This diminished growth advantage of SP can be explained by the decrease of their advantage in terms of nutrient uptake. The same mechanism is at play in the competition of DDAs versus *Trichodesmium*. The advantage in terms of nutrient uptake that *Trichodesmium* experience in the *NoNutr* simulation disappears almost completely in the *AllNutr* simulation. This leads to an increase relative growth ratio, from an average of 0.25 to 0.4, meaning that the growth advantage of DDAs over *Trichodesmium* is reinforced in the *AllNutr* simulation.

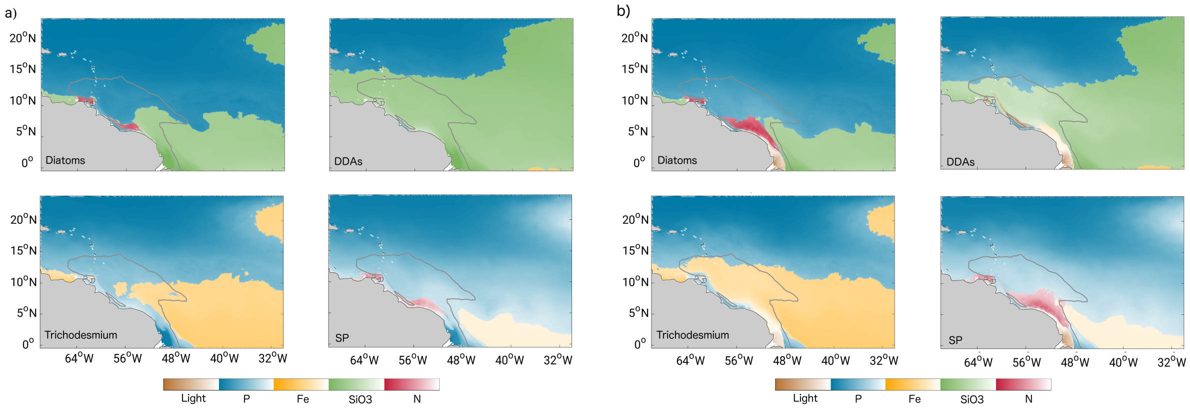

Figure 3.9 Map of the most limiting nutrient for each PFT in (a) *NoNutr* simulation and (b) in the *AllNutr* simulation

3.3.4.2 Growth versus grazing

The downstream plume pathway is characterized by a lower total biomass and lower zooplankton abundance, due to a dilution of the plume waters and a reduction of primary productivity. The difference in zooplankton μ_{max} grazing on each PFT becomes the driving factor and results in a lower grazing pressure on DDAs compared to diatoms and SP (figure 3.8). This leads to a positive relative grazing ratio, that is concomitant with an increasing relative growth ratio in the case of the competition of DDAs versus diatoms. This explains, in part, why the contribution of diatoms to the total biomass decreases throughout this section of the pathway while the share of DDAs increases (figure 3.6).

In the cases of DDAs versus SP and DDAs versus *Trichodesmium*, the grazing relative ratio is mirroring the relative growth ratio in most of the pathway, making the balance between the 2 the determining factor of the competition.

3.4 Discussion

3.4.1 The Amazon, boosting N_2 fixation in the WTA

The Amazon River has been hypothesized to drive the observed high rates of N_2 fixation in the WTA (Foster et al., 2007; Goes et al., 2014). Our simulations, and more specifically the difference between the *NoNutr* and *AllNutr* simulations, demonstrate that while N_2 fixation rates are not negligible even in the absence of the Amazon inputs (around 200 μmol N m^{-2} d^{-1} in the offshore plume waters), the delivery of riverine nutrients does result in a substantial increasing of the total N_2 fixation. The plume areas exhibit more than a doubling of N fixed (+ 2.1 Tg N yr^{-1} being an increase of 152% compared to the *NoNutr* case) and still a substantial increase in the non-plume waters (+ 1.7 Tg N yr^{-1} being an increase of 46%).

This large increase of N_2 fixation is primarily led by DDAs. In line with observations (table 3.1), the largest rates of N_2 fixation by DDAs in the *AllNutr* simulation are found in the outer plume waters (salinity $>$30) where they represent on average 90% of the total N_2 fixation. *Trichodesmium* on the other hand suffer from the delivery of riverine nutrients and see its biomass decrease in the plume areas. Only in the non-plume waters, downstream from the northward plume pathway, do *Trichodesmium* exhibit a slight increase of their biomass (+2-7%).

The delivery of P and $Si(OH)_4$ appears to be crucial to sustain the high N_2 fixation rates of DDAs. In their absence (simulations *NoP* and *NoSi*), the spatial patterns of N_2 fixation change but there is no increase in terms of total N fixed in the WTA, even overall a slight decrease, especially in the absence of P. As predicted by several field studies (Subramaniam et al., 2008b; Weber et al., 2017), the blooms of DDAs are highly dependant to the delivery of P and $Si(OH)_4$ by the Amazon. However, to make use of these ”new” nutrients, DDAs are competing against other non-diazotrophic and diazotrophic phytoplankton, a competition that we disentangled using the relative growth and grazing ratios framework.

3.4.2 DDAs versus Non-Diazotrophs: bottom up controls

Past modeling studies investigating the competition between diazotrophs and non-diazotrophs have been focusing on the P:N and Fe:N supply ratio as a main control of the ecological success of N_2 fixers (Ward et al., 2013b; Dutkiewicz et al., 2014). Based on the resource-ratio theory (Tilman, 1982), this conceptual framework predicts that diazotrophs coexist with non-diazotrophs only when the N supply is lower than the supply of inorganic P and dissolved Fe with respect to the cellular N:P and N:Fe needs of non-diazotrophs. Dutkiewicz et al. (2014) estimated that in the North Atlantic, it is rather the P:N supply than the Fe:N controlling the success of diazotrophs, the supply of Fe in the region exceeding the diazotroph demands. While this simplified framework successfully reproduces and explains the main global patterns of N_2 fixation, it fells short in the comprehension of more complex regions such as the WTA.

First, the high rates of N_2 fixation being supported primarily by DDAs, the role of $Si(OH)_4$ has to be also evaluated in the context of the WTA. Subramaniam et al. (2008b) estimated that the blooms of DDAs were partly driven by the excess of $Si(OH)_4$ over NO_3, giving DDAs an advantage over regular diatoms. Our simulations agree with that conclusion at least in the upstream part of the plume (0-1300 km) where the input of exogenous N is quickly exhausted (within the first 300 km) and strongly limits the growth of diatoms and SP, resulting in a substantial growth advantage for DDAs (positive relative growth ratio). Our factorial simulations, i.e. the *NoNutr* and *NoSi* simulations, demonstrate that this excess of $Si(OH)_4$ over NO_3 is a direct result of the delivery of $Si(OH)_4$ by the Amazon. Our results thus point out the crucial role of riverine $Si(OH)_4$ in driving the high rates of N_2 fixation although when $Si(OH)_4$ is indeed delivered by the river, it is P that exerts the strongest limitations in the rest of the plume pathways and in the non-plume region, both for the diazotrophs and non-diazotrophs.

In the downstream plume pathway (1300-3500/4500 km), it is the ability of DDAs to compete for non-N nutrients and especially P that determines its growth advantage over diatoms. There DDAs benefit from the possibility to break down DOP and use it to fulfill its P needs. This capacity is supported by multiple lines of evidence (see methods section) and appears to be decisive to sustain the large amount of N_2 fixation in our simulations. Landolfi et al. (2015) demonstrated that the DOP utilization by diazotrophs was the most likely mechanism to explain the high rates of N_2 fixation in the P-starved North Atlantic, giving a competitive advantage to N_2 fixers to thrive even in high N:P waters. However, DOP is composed of different phosphorus forms, mainly phosphorus esters, polyphosphate and phosphonates whose utilization can vary widely depending on the species (Claudia Benitez-Nelson, 2015). Both the complexity of the DOP composition and associate rates of consumption by micro-organisms are not represented in BEC. Furthermore, our results suggest a linear decrease of PO_4 along the plume pathways. Yet, *in situ* measurements showed positive deviations from the conservative mixing line North of 9°N that our model does not really capture (Weber et al., 2017). Both the simplicity of DOP in BEC and this bias in PO_4 might lead to an overestimate of the importance of DOP. Nevertheless, its is reasonable to assume that DOP utilization by DDAs affects the competition. A closer investigation of the P cycling in the WTA would give us more insight on this mechanism.

3.4.3 DDAs versus Non-Diazotrophs: top down controls

The biomass accumulation of phytoplankton is always constrained by the loss terms, especially the grazing by zooplankton. Our results reveal that the differences in grazing pressure experienced by one PFT compared to another one strongly modulate the resulting phytoplankton competition, with the relative grazing ratio being of the same magnitude as the relative growth ratio. In the *AllNutr* simulation, the environmental conditions in the upstream plume pathway support close to maximal growth rates for DDAs but top down controls prevent them from dominating the phytoplankton community. The high zooplankton biomass consequential of the high primary production in the upstream plume pathway results in a strong disadvantage for the slower growing DDAs. Along the rest of the plume pathway, as the zooplankton biomass decreases, the grazing disadvantage of DDAs tapers off and this explains the increase of DDAs relative contribution to total biomass and the overall increase in N_2 fixation.

While the top down controls on N_2 fixers remain widely under-studied, our modeling work is not the only one to emphasize its importance on the emergence of DDAs blooms. Stukel et al. (2014) reached similar conclusions and showed that in their simulation, the blooms of DDAs occur because the grazing on DDAs is linearly decreasing due to physically driven dilution of zooplankton concentration while the decrease of DDAs growth rate is slower. But this is not limited to the WTA. Wang et al. (2019) also promote grazing as a crucial mechanism that shapes the global patterns of N_2 fixation. However as underlined in the recent review on N_2 fixation by Zehr and Capone (2020), a lot is still unknown in the loss terms of N_2 fixers and awaits a more in-depth understanding. Identifying the grazers on the different N_2 fixers, estimating grazing rates along with uncovering other mortality such as viral lysis would be incredibly valuable to close this knowledge gap and support the design of better models.

3.4.4 DDAs versus *Trichodesmium*

The North Atlantic is often seen as the realm of *Trichodesmium*, heightened by the large input of iron from the Sahara dust (Sohm et al., 2011). However in the waters under the influence of the Amazon River, *Trichodesmium* appear to be out-competed by DDAs. In our simulations, DDAs benefit from a strong growth advantage resulting from their higher growth rate and the fact that the delivery of riverine nutrients completely eliminates the advantage of *Trichodesmium* in terms of nutrient uptake. The growth advantage of DDAs is counterbalanced by the large grazing advantage of *Trichodesmium* experiencing a lower grazing pressure even when zooplankton biomass is at its highest. But this grazing advantage is never large enough to allow *Trichodesmium* to dominate the diazotrophic community in most of our region of study. In our simulations, only in the highly oligotrophic oceanic waters of the northern part of our region do *Trichodesmium* dominate.

DDAs in our simulations might be a bit too competitive compared to *Trichodesmium* as we do not reproduce the rapid shift from DDAs dominance to *Trichodesmium* documented by Subramaniam et al. (2008b). This might be due to the parameters choice (see section 4.4) or to the absence of more complex processes in BEC. For instance, Tuo et al. (2017) demonstrated that the fraction of free living *Richelia intracellulis* increases when phosphate is depleted regardless of the nitrate scarcity i.e they hypothesize that the P stress on DDAs might lead to a dissociation of the partnership. This response to P shortage is not included in our model because it was only evidenced for the symbiosis between *Richelia* and *Calothrix rhizosoleniae* which are not the species we model here. Nevertheless, if this dynamic was confirmed also for *Hemiaulus hauckii* or *Rhizosolenia clevei* and included in BEC, this would give more room for *Trichodesmium* to grow in low-P oceanic waters.

3.4.5 Limits and caveat

Our study presents plausible mechanisms that explain the ecological competitiveness of DDAs within the Amazon plume. However, some of these results might be impacted by our parameter choices. Our relative growth ratio analysis highlighted the importance of the difference in maximum growth rate in driving the growth advantage of a PFT over another one. Although the hierarchy of growth rates we chose in BEC is based on decades of research, the exact ratio of maximum growth rates between 2 PFTs remains conjectural. Nevertheless, slight changes in this ratio would impact the exact resulting biomass of each PFT but would not change the overall competition and certainly would not change our conclusions regarding the impact of the Amazon that is affecting the nutrient uptake advantage.

Other limitations come from the reduced complexity of certain ecological processes in BEC. Thus, Sailley et al. (2013) showed that in ecological models with a single adaptive zooplankton PFT such as BEC, the top down controls are stronger than in models with multiple zooplankton PFTs, with implications for the phytoplankton biogeography. They also demonstrated that in BEC, the biomass of phytoplankton and zooplankton were highly coupled i.e an increase in phytoplankton biomass will result in a subsequent increase in zooplankton biomass, preventing the phytoplankton from escaping the grazing pressure. The progressive decrease of zooplankton biomass along the plume pathway is a characteristic that has been documented (Conroy et al., 2017; Araujo et al., 2017) and is well represented in our simulations but the importance of this top-down control might be slightly overestimated. Although, it is important to note that Stukel et al. (2014) reached the same conclusion regarding the importance of grazing using an ecological model that includes 2 zooplankton PFTs.

The model only represents 2 diazotrophic PFT i.e DDAs and *Trichodesmium*, which are arguably the most important diazotroph in the region. However, multiple lines of evidence suggest that unicellular cyanobacteria, especially UCYN-A (*Candidatus* Atelocyanobacterium thalassa) and UCYN-B (*Crocosphera*), might be important contributors to N_2 fixation globally and more specifically in the tropical Atlantic (Martínez-Pérez et al., 2016; Caputo et al., 2018). Including them in BEC would most likely not change our conclusions especially in the plume waters. Nevertheless, in the oceanic type of waters where UCYN have been shown to thrive (Goebel et al., 2010; Stukel et al., 2014), having an explicit representation of UCYN in BEC would result in a more refined understanding of the diazotroph dynamic and the co-existence between the different groups.

3.5 Conclusion

The large amounts of P and $Si(OH)_4$ delivered by the river fuels the intense N_2 fixation observed in the WTA. Our simulations suggest an increase of 3.8 Tg N yr^{-1} (+74%) in N_2 fixation, directly attributable to the presence of the Amazon. By modifying both the absolute concentration and the stoichiometry of nutrients, the Amazon River also reshapes the phytoplankton competition, giving more space for N_2-fixers, and notably DDAs, to develop. In the competition between phytoplankton, the Amazon River does not only alter the nutrient availability (bottom up controls) but also modifies the grazing pressure (top down controls). Both factors appear equally important. More specifically, our analysis reveals that while the excess of $Si(OH)_4$ over NO_3 favors DDAs over non-diazotrophic PFTs in the upstream plume pathway (0-1300 km), the high grazing pressure prevents them from accumulating biomass and becoming dominant in the phytoplankton community. In contrast, in the rest of the plume pathway, DDAs thrive, benefiting from a decreased grazing pressure and the slight growth advantage associated with their ability to use directly DOP. Compared to DDAs, *Trichodesmium* experience a lower grazing pressure and is more competitive in taking up nutrients at low concentration. But throughout the plume, their slow growth prevents them from outcompeting DDAs. The main findings of this work highlight the central role of P in driving the competition in a large fraction of the plume and the importance of top down controls that are often ignored in the study of N_2 fixation biogeography.

Acknowledgements

This study was part of the C-CASCADES project (https://c-cascades.ulb.ac.be/) and the NOTION project. C-CASCADES was funded by the European Union's Horizon 2020 research and innovation programme under the Marie Sklodowska-Curie grant agreement No. 643052. Financial support was provided by the Swiss Government (Staatsskretariat für Bildung, Forschung und

Innovation - SBFI) and ETH Zürich. NOTION is funded by the Fondation BNP Paribas grant agreement. We thank Pierre Regnier for leading the C-CASCADES project and Mar Benavides for leading the NOTION project.

Chapter 4

The Interannual Variability in Marine N_2 Fixation and its Drivers in the Western Tropical Atlantic

J. Härri, D. Louchard, M. Münnich, N. Gruber

Environmental Physics, Institute of Biogeochemistry and Pollutant Dynamics, ETH Zurich, Universitätstrasse 16, 8092 Zürich, Switzerland.

This study is based on the Master's thesis of Jana Härri which was co-supervised by Domitille Louchard. Domitille Louchard prepared the hindcast simulations and provided guidance for the analysis of the results. Jana Härri created the figures and lead the writing, with substantial contributions by Domitille Louchard.

Abstract

Marine N_2 fixation, the biologically mediated reduction of atmospheric N_2 to NH_3, is prevalent in the Western Tropical Atlantic ocean (WTA), fuelled by nutrient input of the Amazon River (Marconi et al., 2017; Subramaniam et al., 2008a). Despite N_2 fixation being an important component of the N cycle, little is known about interannual N_2 fixation rate variability. To quantify the magnitude and identify drivers of interannual N_2 fixation rate variability in the WTA, we use hindcast simulations, which are based on the Regional Oceanic Modelling System (ROMS) coupled to the Biogeochemical Elemental Cycling (BEC) model and range from 1983 to 2019. We show that interannual N_2 fixation rate variability is linked to variable Amazon River discharge, the Atlantic Meridional Mode (AMM), and the El Niño-Southern Oscillation (ENSO). The discharge impacts the N_2 fixation rate via the nutrient input - anomalously high (low) discharge delives more (less) nutrients to the WTA, which enhances (reduces) the N_2 fixation rate. The discharge variability can alter the N_2 fixation rate by up to 15% in the offshore plume region of the Amazon River. Positive AMM events and El Niño events (negative AMM events and La Niña events) are shown to enhance (reduce) the N_2 fixation rate by altering the nutrient availability through changes in the Mixed Layer Depth (MLD) and upwelling strength. Particularly variability in the P concentration is decisive for the N_2 fixation rate, but competition dynamics result in a non-linear relation between P concentration variability and N_2 fixation rate variability. The interannual N_2 fixation rate variability has implications for the extrapolation of field measurements, the marine N cycle, primary productivity and carbon export.

4.1 Introduction

N_2 fixation is a crucial process that introduces “new” N in the ocean, fuelling phytoplankton growth and controlling the export of organic matter into the deep ocean in many regions (Dugdale and Goering, 1967). Except for atmospheric N deposition, N provided via N_2 fixation is the only N input that leads to a net sequestration of atmospheric CO_2 in the deep ocean, because upwelling and diffusion of dissolved inorganic nitrogen (DIN) are tied to an approximately stoichiometric amount of CO_2 (Sohm et al., 2011).

Past research on N_2 fixation has been primarily focusing on understanding the environmental conditions favouring N_2-fixers and the global spatial patterns of N_2 fixation (Sohm et al., 2011). In contrast, the temporal evolution of N_2 fixation, especially on interannual timescales, is largely unstudied, mainly due to the paucity of regular measurements. The identification of regions where the N_2 fixation rate varies on interannual timescales as well as constraining the magnitude of interannual variability in the N_2 fixation rate are crucial building blocks towards a more comprehensive understanding of marine N_2 fixation. It would participate in discerning factors that control N_2 fixation (Deutsch et al., 2007), which would facilitate reliable predictions of changes in N_2 fixation in response to future environmental changes (Wang et al., 2019). Insights into the temporal and spatial variability in the N_2 fixation rate are also extremely valuable to extrapolate field measurements more precisely (Wang et al., 2019).

The Western Tropical Atlantic ocean (WTA) exhibits amongst the highest rates of N_2 fixation in the world ocean and hosts a significant fraction of the global N_2 fixation (Luo et al., 2012; Marconi et al., 2017; Louchard et al., prep). It is also a region whose physical and biogeochemical properties are bound to vary significantly on different interannual timescales (Foltz et al., 2019). We identified two main factors that could impact the N_2 fixation rate in the WTA on interannual timescales: (1) variability in the Amazon River discharge and (2) climate variability, such as the Atlantic Meridional Mode (AMM) and El Niño-Southern Oscillation (ENSO). The Amazon River is highly enriched in nutrients and suspended material, hence seasonal and interannual fluctuations strongly impact the nutrient availability in the WTA (Drake et al., 2021). The large inputs of $Si(OH)_4$ and P by the river have been shown to drive the high rates of N_2 fixation, notably favouring Diatom-Diazotroph Assemblages (DDAs) (Subramaniam et al., 2008a; Weber et al., 2017; Louchard et al., prep). Via changes in the atmospheric circulation, AMM and ENSO have an impact on the sea surface temperature (SST), stratification, and oceanic circulation (Enfield and Mayer, 1997; Chiang and Vimont, 2004; Lohmann and Latif, 2007; Yoon and Zeng, 2010; Foltz et al., 2012). Alterations of the stratification and oceanic circulation are expected to have an impact on the nutrient availability in the WTA and subsequently the ecological competitiveness of N_2-fixers.

These two factors plausibly driving the interannual variability of N_2 fixation in the region are not easy to disentangle as the main drivers of interannual Amazon River discharge variability are ENSO and AMM - both seasonally locked modes of climate variability that fully develop in winter and spring, respectively (Richey et al., 1989; Chiang and Vimont, 2004; Marengo and Espinoza, 2016). El Niño conditions result in below-average discharge due to the convection center that is located over South America being shifted eastwards over the Pacific, whereas La Niña conditions lead to above-average discharge due to an intensification of this convection center (Foley et al., 2002). Positive (negative) AMM events, which are characterized by an anomalously warm (cold) tropical North Atlantic and anomalously cold (warm) tropical South Atlantic, are associated with less (more) precipitation in the Amazon basin due to a northerly (southerly) displacement of the Intertropical Convergence Zone (ITCZ) (Yoon and Zeng, 2010).

To disentangle the different factors of the interannual variability in N_2 fixation, we use a high resolution coupled model, the Regional Ocean Modeling System (ROMS) coupled to the Biogeochemical Elemental Cycling (BEC) model, and perform four hindcast simulations that span from 1979 to 2019, including or excluding some forms of variability in the forcing fields. To isolate the impact of the interannual variability of the Amazon River runoff, we analyse and compare the simulations with different discharge scenarios, one including and the other one excluding interannual discharge variability. To disentangle the impact of AMM and ENSO, we analyse the simulation forced with interannually varying atmospheric forcing, neglecting variation in the discharge. We thus identify regions where N_2 fixation is impacted by the interannual discharge variability, AMM and ENSO and determine the magnitude of these N_2 fixation anomalies. In addition, we determine the processes driving N_2 fixation anomalies, taking into account both bottom-up and top-down controls.

4.2 Methods

4.2.1 Model

The UCLA-ETH version of ROMS (Shchepetkin and McWilliams, 2005) coupled to BEC (Moore et al., 2013d) is employed to investigate interannual N_2 fixation rate variability and its drivers. The model simulates the entire Atlantic Ocean (Figure 4.2). The model configuration is the same as used in Louchard et al. (2021). We will thus here only highlight the main features of the model that are relevant for the present study.

The model simulates four phytoplankton groups and one zooplankton class. Phytoplankton growth is controlled by nutrient availability, irradiance, and temperature. In the model, no nutrient co-limitation occurs, i.e., only the most limiting nutrient controls phytoplankton growth. The two non-diazotrophic phytoplankton groups comprise diatoms and a generic small phytoplankton group. Diazotrophic phytoplankton are represented by non-symbiotic diazotrophs whose traits are based on those of *Trichodesmium* spp., and DDAs, which are symbioses between diatoms and diazotrophs. DDAs have been implemented into the standard BEC by Louchard et al. (2021) and are modelled to combine traits of diatoms and non-symbiotic diazotrophs. Similar to non-symbiotic diazotrophs, DDAs assimilate dissolved organic phosphorus (DOP) with the same efficiency as PO_4 and require more Fe to synthesize the enzyme essential for N_2 fixation. Additionally, DDAs require $Si(OH)_4$ to build their frustules. Both diazotrophic groups can satisfy their N requirement by fixing N_2 but are also able to assimilate NO_3 and NH_4. DDAs switch to a non-symbiotic state if the NO_3 concentration exceeds a threshold value of 0.5 mMol N m^{-3} and lose their ability to fix N_2 (see Louchard et al. (prep) for more details). Non-symbiotic DDAs resort to a DIN uptake similar to that of diatoms. The uptake of DIN reduces the N_2 fixation rate of non-symbiotic diazotrophs proportionally. However, the DIN half-saturation constant of non-symbiotic diazotrophs is set high relative to non-diazotrophic phytoplankton, hence non-symbiotic diazotrophs are not strongly competing for DIN.

The C:N:P ratio of phytoplankton is fixed in BEC. The stoichiometry is close to the Redfield ratio for diatoms, small phytoplankton and DDAs, amounting to 117:16:1 (Anderson and Sarmiento, 1994). The C:N:P ratio of non-symbiotic diazotrophs is 117:45:1 (Letelier and Karl, 1998). The Si:C and Fe:C ratios are not fixed and vary depending on the ambient nutrient concentration. Si:C ratios range from 0.0457 to 0.685, whereas Fe:C ratios range from $12 \cdot 10^{-6}$ to $60 \cdot 10^{-6}$ for diazotrophs and $3 \cdot 10^{-6}$ to $20 \cdot 10^{-6}$ for non-diazotrophic phytoplankton. In Fe-depleted conditions, the silicification of diatoms and DDAs is increased compared to Fe-rich conditions. Contrarily, silicification decreases below a threshold value of 2 mMol Si m^{-3}.

4.2.2 Model Forcing

The physical core of the model was run and forced with mean conditions for 30 years as a spin up, following the procedure described in Louchard et al. (2021). The coupled ROMS-BEC was then run for ten years, producing eventually the initial conditions used for the hindcast. The hindcast itself spans 41 years (1979 - 2019) of which the first four are again considered a spin up and will not be analyzed here. At the surface, ROMS is forced with daily reanalysis data of wind stress, solar shortwave radiation, and fluxes of heat and freshwater, which are derived from ERA5: Fifth generation of ECMWF atmospheric reanalyses of the global climate, Copernicus Climate Change Service (C3S), Climate Data Store (date of access: 29/08/2020) (Hersbach et al., 2020).

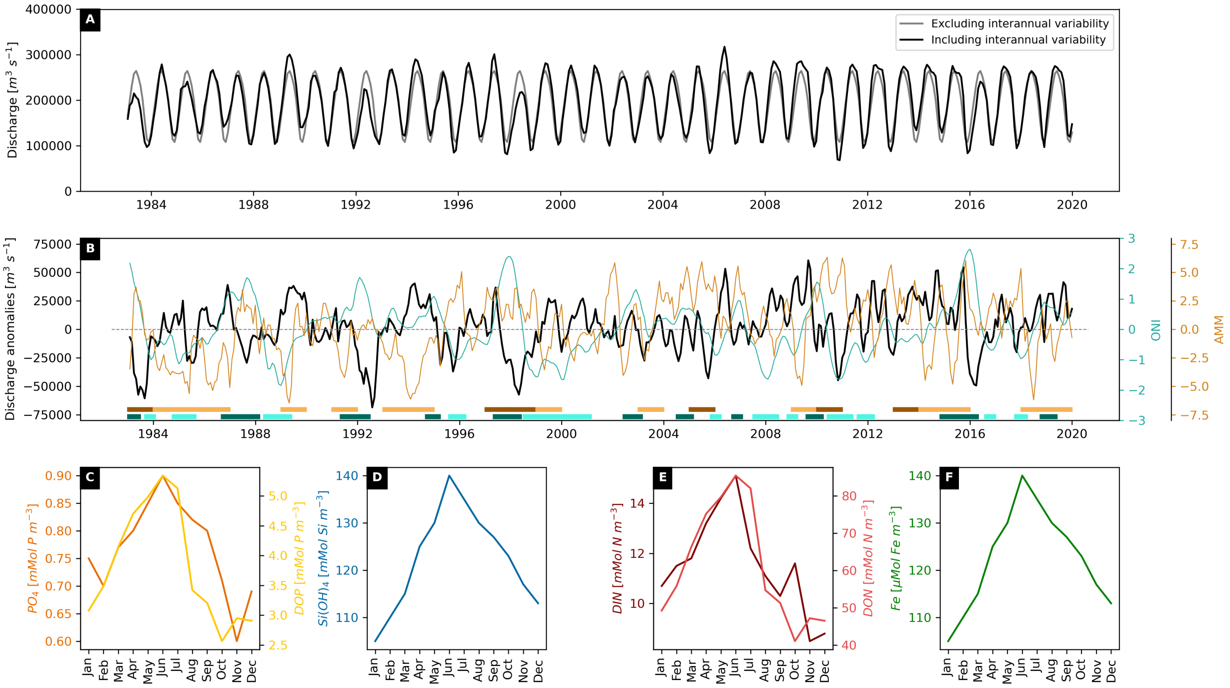

Figure 4.1 The measured discharge (black) and the discharge scenario excluding interannual variability (gray) (A). The discharge anomalies, computed as the difference between the measured discharge and the discharge scenario excluding interannual variability, the Oceanic Niño Index (ONI) (turquoise) and the Atlantic Meridional Mode (AMM) Index (brown) (B). Brown colorbars represent positive AMM events (dark) and negative AMM events (light), turquoise colorbars depict El Niño phases (dark) and La Niña phases (light). Monthly mean concentration of PO_4 and Dissolved Organic Phosphorus (DOP) (C), $Si(OH)_4$ (D), Dissolved Inorganic Nitrogen (DIN) and Dissolved Organic Nitrogen (DON) (E), and Fe (F) characterizing the Amazon River discharge based on (Araujo et al., 2014).

The Amazon discharge is implemented into the model as a 3D influx boundary condition placed within the Amazon estuary. The discharge volume was retrieved from SO-HYBAM and was completed with data from the Global Data Runoff Center (GDRC) if no data was available for an entire month. To estimate the total Amazon River discharge, the discharge measurements taken at Óbidos, which is located 800 km away from the mouth of the Amazon River, and the discharge measurements of the two main tributaries joining the Amazon River in between, measured at Itaituba and Altamira (Figure 4.2), were added, resulting in the discharge record presented in Figure 4.1A. No data was available for the measurement station at Altamira from 2017 onwards. We completed the measurement record with monthly mean discharge volume, thereby forfeiting the interannual variability of this tributary.

The Amazon River transports brackish water, alkalinity, carbon, and nutrients into the Atlantic Ocean. Most of the monthly varying nutrient concentrations were obtained from a climatology compiled from model estimates and observations (Figure 4.1C-F and Table A.3) (Araujo et al., 2014). Concentrations of NO_3, NH_4, and organic nutrients are identical to those presented in Louchard et al. (2021).

Large rivers entering the Atlantic Ocean and atmospheric forcing fields are implemented in the model as described by Louchard et al. (2021). Neither rivers, except for the Amazon River, nor atmospheric nutrient input experience year-to-year variability.

4.2.3 Simulations and Analyses

The study region comprises the fraction of the WTA that is most impacted by Amazon River water, extending from 0.5° S to 25° N and from 30° W to 80° W (Figure 4.2). The nutrient-rich Amazon freshwater is transported mostly along the Brazilian coast towards the Caribbean Sea by the strong North Brazil Current (NBC), while some water is retroflected between 5° N and 10° N in autumn, feeding the eastwards flowing North Equatorial Countercurrent (NECC) (Stramma and Schott, 1999; Schlosser et al., 2014). The equatorial region is characterized by upwelling of nutrient-rich water, while the more northern parts of the study region receive large amount of iron-rich atmospheric dust but suffer from P scarcity (Stramma and Schott, 1999; Moore et al., 2013a). To account for differing biogeochemical conditions, we divided the study region into a southern and northern part at 13° N, which roughly coincides with the northernmost position of the ITCZ (Grodsky and Carton, 2003).

To evaluate the impact of discharge variability and climate variability on the N_2 fixation rate, we performed a series of four factorial simulations, in which we systematically included or excluded interannual variability in the forcing (Table 4.1). The *Baseline* simulation establishes the mean conditions in terms of physical and biogeochemical properties of the Atlantic Ocean. The atmospheric forcing and the discharge experience monthly variation but no year-to-year variability, with the exception of the pCO_2 forcing. This constant atmospheric forcing and discharge represent the average conditions as derived from ERA5 and the discharge record, considering the years 1979 - 2016. The *VarAmz* simulation is forced with interannually varying discharge, but interannually constant atmospheric forcing. The difference between the *Baseline* simulation and *VarAmz* simulation reveals the impact of interannual discharge variability on N_2 fixation and its drivers. The atmospheric forcing of the *VarAtm* simulation includes interannual variability, whereas interannual variability is excluded for the discharge. The *VarAtm* simulation is used to isolate the effect of climate variability. The *VarAll* simulation, which includes interannual variability in the atmospheric forcing and the discharge, reveals the combined impact of discharge variability and climate variability. An overview of the four simulations and their main aims is given in Table 4.1.

Table 4.1 Overview of the ROMS-BEC simulations performed for this study.

Name	Interannual Variability in Forcing		Objective
	Atmosphere	Discharge	
Baseline	×	×	Control
VarAmz	×		VarAmz - Baseline → Impact of discharge variability
VarAtm		×	Anomalies of VarAtm → Impact of climate variability
VarAll			Anomalies of VarAll → Impact of discharge variability & climate variability

To quantify the magnitude of interannual variability in the N_2 fixation rate, we use the Mean Absolute Deviation (MAD), defined as:

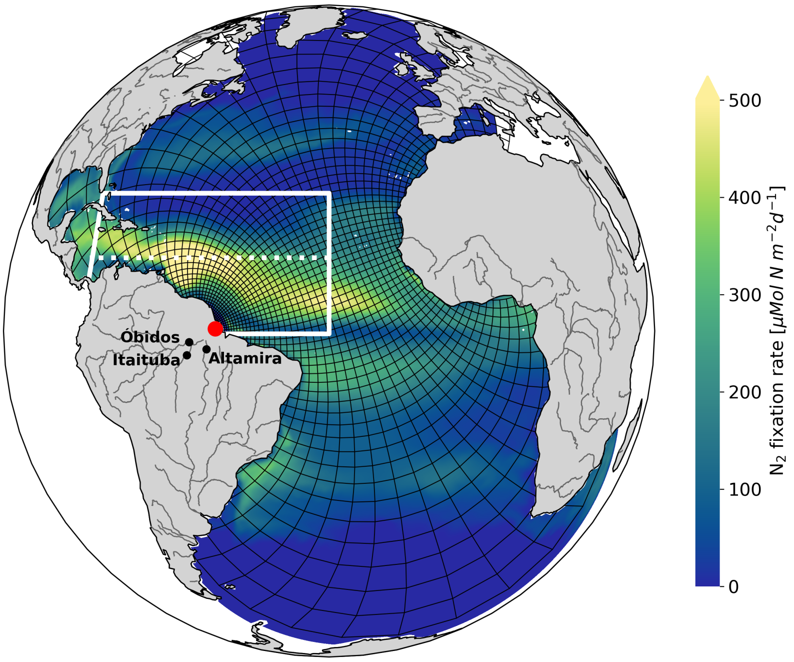

Figure 4.2 Map of the model domain with the averaged N_2 fixation rate in color, and with the telescopic grid depicted by every 10^{th} grid point. The white frame encloses the study region (0.5° S - 25° N; 30° W - 80° W) with the dashed line dividing the study region in a southern and northern part at 13° N. The red dot indicates the Amazon River outflow and the black dots indicate the location of the discharge measurement stations.

$$MAD = \frac{1}{n}\sum_{i=1}^{n} |x_{\mathrm{i}} - m(X)|$$

where n equals to the number of observations, x_i corresponds to the i^{th} observation and m(X) is the mean of all observations.

In our case, x_i - m(X) corresponds to the N_2 fixation rate difference between the *VarAmz* and *Baseline* simulation or N_2 fixation rate anomalies of the *VarAtm* or *VarAll* simulation, computed as the N_2 fixation rate deviations of the grid cell specific monthly climatological mean. To quantify the magnitude of N_2 fixation rate variability in the WTA, we average x_i - m(X) over the study region before computing the MAD. To identify regions where discharge variability and/or climate variability have a strong impact on the N_2 fixation rate, we computed the MAD without spatial averaging. Regions characterized by a large MAD are strongly impacted by discharge variability and/or climate variability. It is important to note that as a measure of the absolute deviation, this metric will always be positive.

To establish how variable discharge impacts the N_2 fixation rate, we fitted a linear regression for each grid point between the yearly averaged N_2 fixation rate anomalies associated with discharge variability and the yearly averaged discharge anomalies. The N_2 fixation rate anomalies attributed to discharge variability are defined as the difference between the *VarAmz* and *Baseline* simulation. The same analysis was conducted for the drivers of the N_2 fixation rate to assess which drivers of N_2 fixation rate variability are impacted by the discharge variability.

To evaluate how climate variability impacts the N_2 fixation rate, we analysed composites of the N_2 fixation rate anomaly fields of ENSO and AMM events. The composite analysis is based on the *VarAtm* simulation, considering only the impact of climate variability. To qualify as an AMM event, the mean of the AMM index during spring has to exceed a threshold value of $\pm 2°$ C. The AMM index is based on Atlantic SST anomalies and was provided by https://www.aos.wisc.edu/ dvimont/MModes/Data.html (date of access: 25/05/2021). ENSO events are identified based on SST anomalies in the Niño 3.4 region (Oceanic Niño Index (ONI), date of access: 25/05/2021). To qualify as an ENSO event, SST anomalies have to exceed a threshold value of $\pm 0.5°$ C, lasting at least five consecutive months. Because AMM and ENSO events are phenomena that are seasonally locked, we investigated their impact on the N_2 fixation rate on a seasonal resolution. The same analysis was applied to drivers of the N_2 fixation rate. For visualisation, we reversed the sign of anomalies of negative AMM events and La Niña events. Thus, all responses are reported relative to positive AMM events and El Niño events. This is possible due to the symmetry of anomalies.

Some nutrient concentrations, most notably $Si(OH)_4$, and the biomass and productivity of phytoplankton are affected by a model drift, therefore, data was detrended prior to analysis, using a 5^{th} degree polynomial spline. Physical parameters and phytoplankton growth limitations were not detrended. Additionally, the N_2 fixation rate and phytoplankton productivity were integrated over the top 100 m, whereas only the surface nutrient concentrations were analysed. While phytoplankton decrease with depth, nutrient concentrations increase with depth. Hence, the majority of phytoplankton is affected by variability in the surface nutrient concentration.

4.2.4 Model Evaluation

4.2.4.1 Sea Surface Temperature

The model reproduces the SST (Figure 4.3A) and interannual variability in SST (Figure 4.3B) accurately with a correlation coefficient of 0.98 and 0.84, respectively. With the forcing applied to ROMS-BEC, the warming trend is underestimated by the model towards the end of the modelled time period. Because the SST timeseries was not detrended prior to the SST anomaly computation, a negative and positive offset of model-derived SST anomalies in the beginning and end of investigated time period are observed, respectively. Nonetheless, the magnitude of the SST anomalies is comparable.

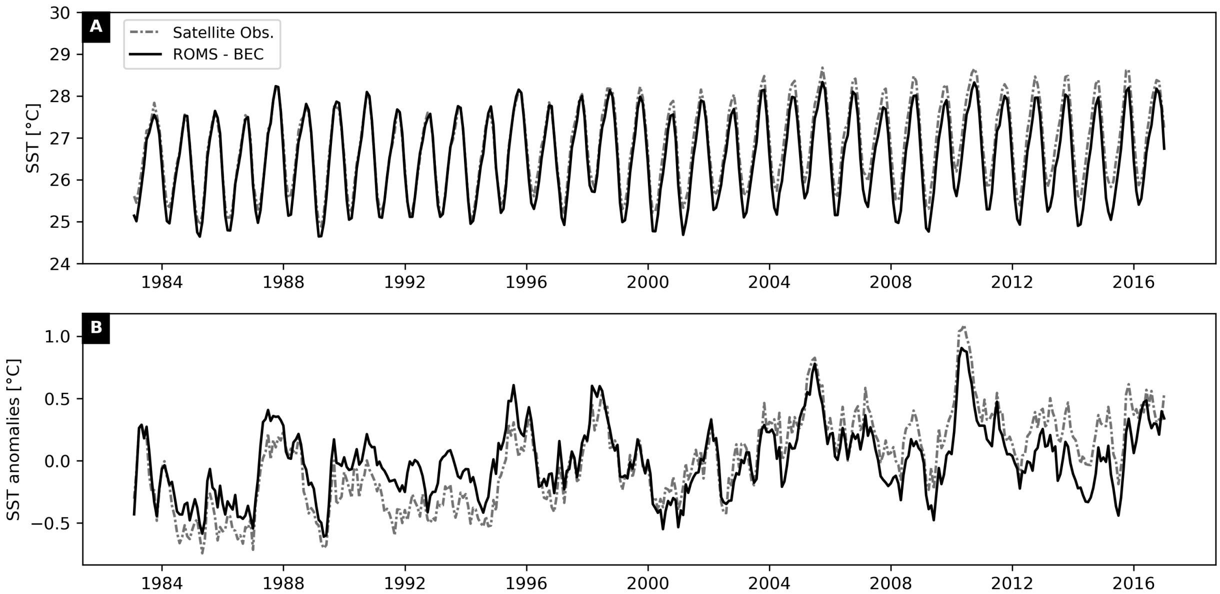

Figure 4.3 The spatially averaged SST in the study region of ROMS-BEC compared to satellite observations (A). In panel B, interannual SST anomalies are compared, which were computed by removing the modelled and observational climatology of the modelled and observational data, respectively. The satellite data was provided by the National Oceanic and Atmospheric Administration (NOAA SST V2 High Resolution) and was bilinearly interpolated to the model grid for comparison.

4.2.4.2 Sea Surface Salinity and Plume Size

Compared to the PIRATA measurement, our model generally succeeds in simulating interannual variability in the sea surface salinity (SSS) (Figure 4.4). Unfortunately, there are no PIRATA buoys that are continuously impacted by the Amazon River, which hinders a verification of the model capturing the impact of discharge fluctuations correctly. However, some of the buoy sites occasionally experience SSS values below 35.25, which is likely due to Amazon River discharge reaching the buoy site, especially for the two northernmost buoys. These drops in SSS are mostly reproduced by the model, but their magnitude is usually underestimated. However, the impact of precipitation and discharge is difficult to separate, hence these drops could also be triggered by strong rainfall.

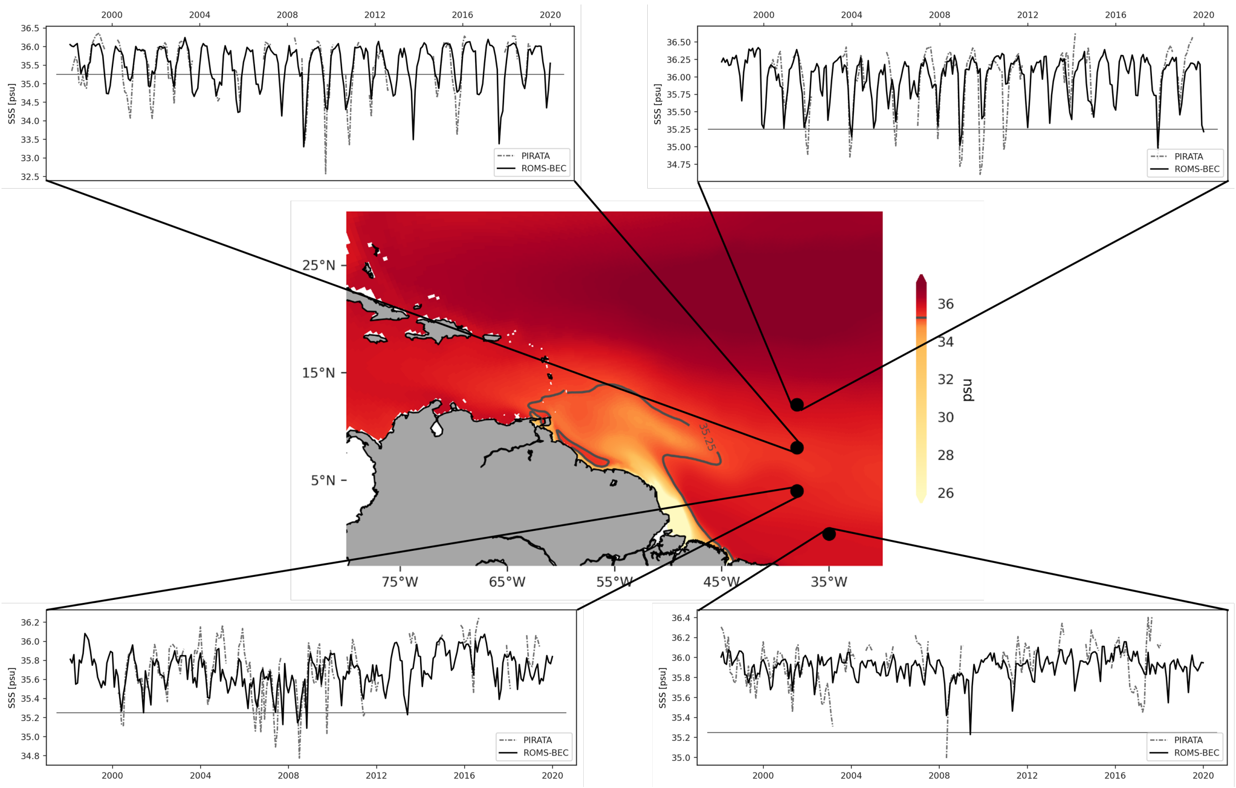

Figure 4.4 The mean SSS between 1983 and 2019 in colour and the modelled (black) and measured (gray) SSS at four PIRATA buoy sites. The contour line depicts the plume extent based on a SSS threshold of 35.25 psu.

In addition to the SSS evaluation, an evaluation of the plume size was conducted to indirectly assess if the model captures the impact of variable discharge, circulation, and stratification in the WTA. The model is mostly able to reproduce the combination of the seasonal and interannual variability in the plume size, with a correlation coefficient of 0.83 (Figure 4.5A). However, the model underestimates the plume size in general, which is due to the model overestimating the SSS in the offshore plume (Figure C.1). Notable differences exist in the interannual variability of the plume size between the model and the reanalysis (R-value = 0.40, Figure 4.5B). The inaccurate reproduction of interannual SSS variability of the model certainly plays a role (Figure C.2).

Moreover, slight deviations in the currents or the stratification could lessen the ability of the model to capture interannual variability in the plume size. Additionally, precipitation might also lead to SSS below 35.25 psu, confounding our plume size estimate. Lastly, interannual variability in the plume size based on satellite measurements and the reanalysis also varies considerably, hence the reanalysis might also suffer from some biases.

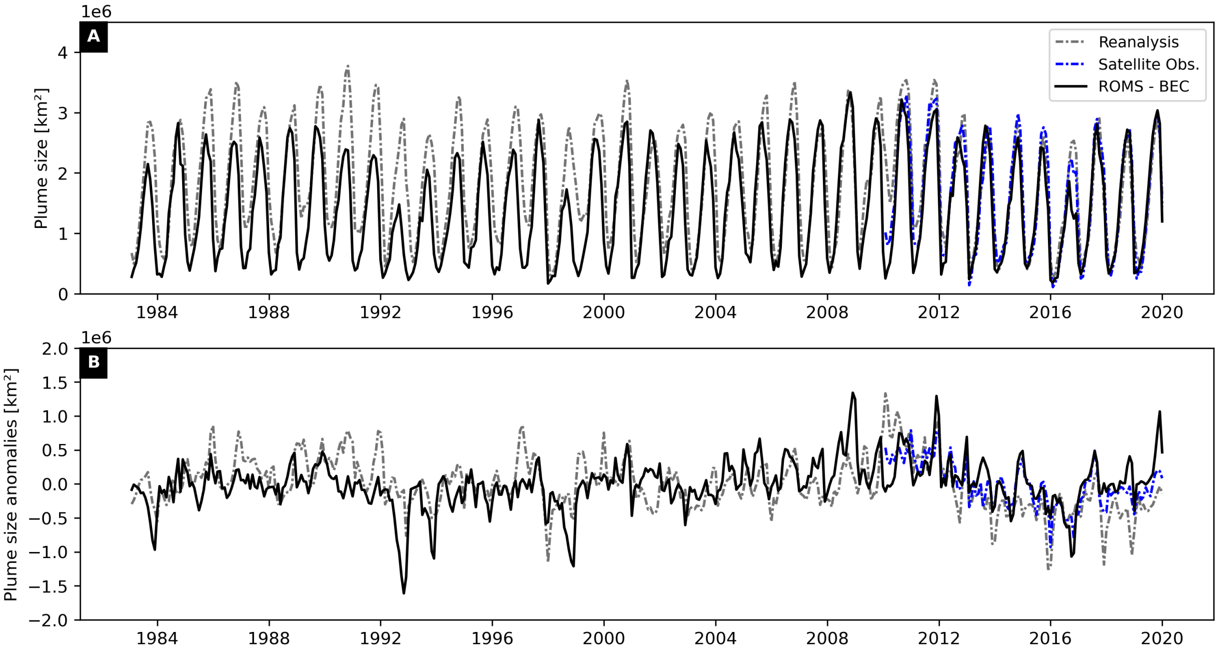

Figure 4.5 The plume size determined based on a SSS threshold value of 35.25 psu is shown in panel A. In panel B, the interannual plume size anomalies are compared, which were computed by removing the the modelled and observational monthly mean plume size. The reanalysis data was taken from the Simple Ocean Data Assimilation (SODA 3.4.2). The satellite data, available from 2010 onwards, was taken from ESA CCI V2.31. Both datasets were bilinearly interpolated to the model grid to determine the plume size.

4.2.4.3 N_2 Fixation

In the whole model domain, 41.1 Tg N y^{-1} are fixed in the upper 100 m by DDAs and non-symbiotic diazotrophs of which 13.8 Tg N y^{-1} are fixed within the study region. This is comparable to other estimates: Luo et al. (2012) have estimated that 32 Tg N and 1.8 Tg N are annually fixed in the North and South Atlantic, respectively. Wang et al. (2019) have estimated that 24 to 49.5 Tg N y^{-1} are fixed in the Atlantic, whereas Landolfi et al. (2018) have computed that 46 Tg N y^{-1} are fixed in the Atlantic based on the model output of Moore et al. (2013d).

In the WTA, the modelled average N_2 fixation rate amounts to 232 μmol N m^{-2} d^{-1} in the top 100 m. Subramaniam et al. (2008a) have divided the WTA into three sub-regions: low-salinity (<30 psu), mesohaline (between 30 and 35 psu) and oceanic (>35 psu) and have observed highest N_2 fixation rates in mesohaline waters (986 ± 373 μmol N m^{-2} d^{-1}), lowest rates in low-salinity waters (25 ± 17 μmol N m^{-2} d^{-1}), and average rates in oceanic condition (157 ± 32 μmol N

$m^{-2}\ d^{-1}$). A similar pattern is reproduced by the model with average N_2 fixation rates of 348 μmol N $m^{-2}\ d^{-1}$ in mesohaline water, 42 μmol N $m^{-2}\ d^{-1}$ in low salinity water, and 229 μmol N $m^{-2}\ d^{-1}$ in oceanic conditions.

In agreement with the spatial pattern of the mean N_2 fixation rate of the model depicted in Figure 4.6, Moore et al. (2009) measured highest N_2 fixation rates ($\sim$200 μmol N $m^{-2}\ d^{-1}$) between 0° N and 20° N, but rates lower than 40 μmol N $m^{-2}\ d^{-1}$ north of 20° N on a north-south transect. Corresponding to our results, Stukel et al. (2014) observed a slight decrease of N_2 fixation from west to east in their model, which is also supported by observations (Montoya et al., 2007).

The *in situ* rates of N_2 fixation compiled by Luo et al. (2012) exhibit greater spatial variability than the seasonally averaged N_2 fixation rates of the model. This suggests that the model is underestimating the spatial variability in N_2 fixation. However, the difference between the observational data and the averaged N_2 fixation rates of the model may partly be explained by variability being smoothed in the model output due to averaging. Moreover, the observational data has been obtained by two different measuring methods, which might also lead to additional variability in the observational data. Unfortunately, there exists no continuous measurement record of the N_2 fixation rate in the WTA, which prevents a comparison of the measured and modelled interannual variability in the N_2 fixation rate.

On average, 85% of the N is fixed by DDAs and only 15% by non-symbiotic diazotrophs in the WTA. There is large spatial variability in the relative contribution of DDAs and non-symbiotic diazotrophs to N_2 fixation. DDAs contribute predominantly to N_2 fixation in the southern part of the WTA, whereas in the northern part of the study region, the relative importance of non-symbiotic diazotrophic N_2 fixation increases, coinciding with lower N_2 fixation rates. Thus, DDAs thrive in waters that are generally nutrient-rich but DIN-depleted, whereas non-symbiotic diazotrophs predominate in oligotrophic waters. Consistent with the model simulation, Carpenter et al. (1999) found that most of the N_2 fixation can be attributed to DDAs northeast of the South American continent, at least during DDA blooms. However, compared to the results of Subramaniam et al. (2008a), the model may overestimate the contribution of DDA-fixed N in mesohaline waters. In addition, the DDA-dominated N_2 fixation is not limited to the Amazon plume area in the model, but characterizes the whole southern part of the WTA, contradicting the observations of Subramaniam et al. (2008a). However, Foster et al. (2007) found that DDAs contribute up to 88% to the total N_2 fixation in the high salinity waters of the WTA, thus our model may attribute a high fraction of N_2 fixation to DDAs but is still comparable to observations. The N_2-fixing biome accounts for 17% (13% DDAs and 4% non-symbiotic diazotrophs) of the total phytoplankton biomass, which is comparable to the results of Subramaniam et al. (2008a).

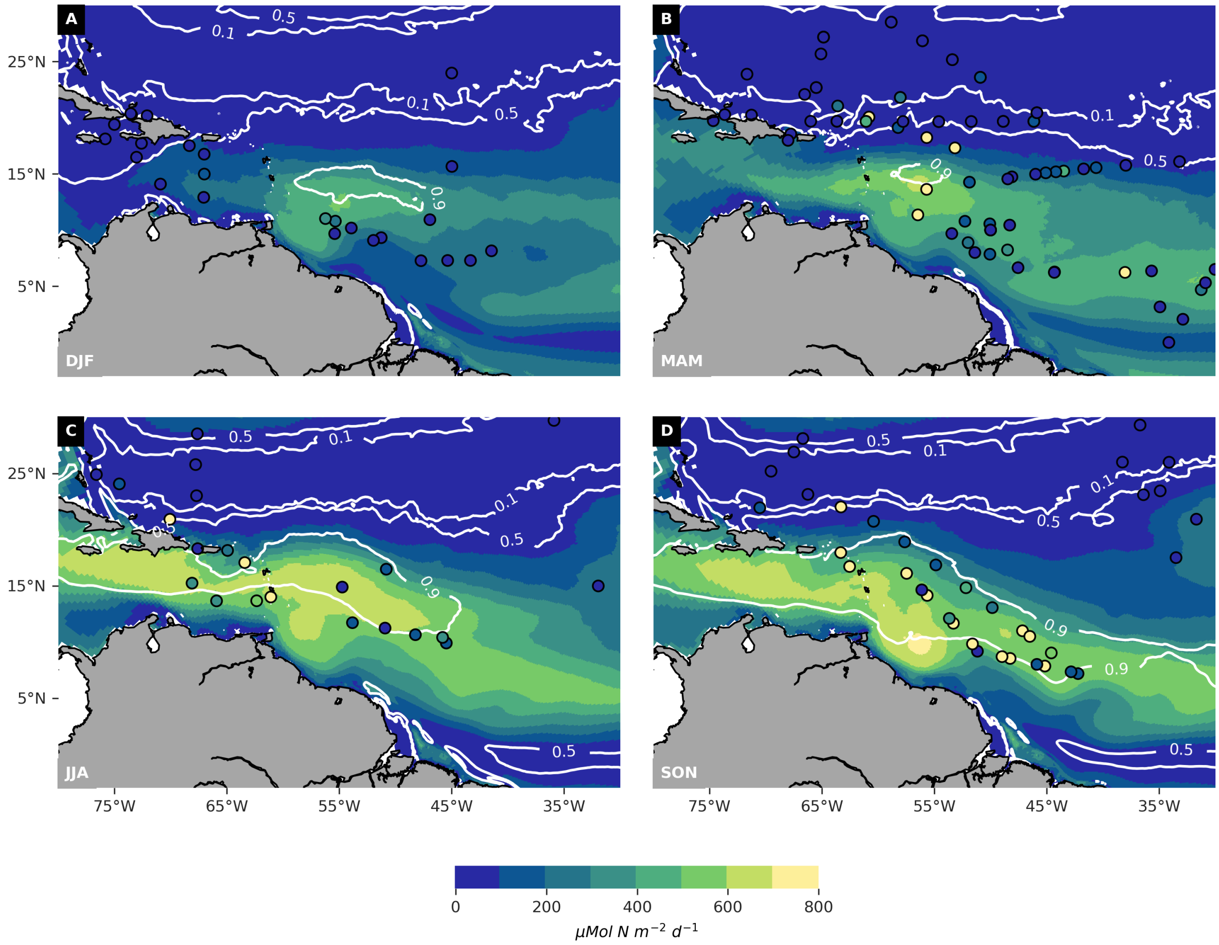

Figure 4.6 The mean of the depth-integrated N_2 fixation rate for the time period between 1983 and 2019 is shown in colors, the filled circles correspond to integrated *in situ* measurements (depth $>$ 80m) (Luo et al., 2012) and the contour lines depict the fraction of N fixed by DDAs, whereas the remaining fraction is fixed by non-symbiotic diazotrophs.

4.3 Results and discussion

4.3.1 Variability in N_2 Fixation

Our results demonstrate that N_2 fixation rates in the WTA vary substantially on interannual timescales. The magnitude of the N_2 fixation rate variability in the WTA, computed as the MAD of the spatially averaged N_2 fixation rate, amounts to 16 μmol N m^{-2} s^{-1} (Table 4.2). Largest variations in the N_2 fixation rate occur in the southern part of the study region, where diazotrophs are abundant. The N_2 fixation rate deviates most strongly from the climatological mean in spring, suggesting that a phenomenon that is seasonally locked to spring is an important driver of N_2 fixation rate variability. Because the majority of the N_2 fixation rate variability is attributed to climate variability (16 μmol N m^{-2} s^{-1}), it is likely that a climate mode causes most of the N_2 fixation rate variability in spring. However, independent of the season, variability in the Amazon

River discharge also results in considerable N_2 fixation rate variability (9 μmol N m^{-2} s^{-1}).

Table 4.2 The MAD of the spatially averaged N_2 fixation rate variability. The MAD of the N_2 fixation rate variability was computed for the whole study region and the southern and northern part separately denoted in italics.

	Total N_2 fixation rate variability (*south; north*) [μmol N m^{-2} d^{-1}]	**N_2 fixation rate variability attributed to discharge variability (*south; north*)** [μmol N m^{-2} d^{-1}]	**N_2 fixation rate variability attributed to climate variability (*south; north*)** [μmol N m^{-2} d^{-1}]
Simulation	Anomalies of VarAll	VarAmz - Baseline	Anomalies of VarAtm
Winter (DJF)	16 (*33; 16*)	9 (*15; 8*)	17 (*35; 15*)
Spring (MAM)	21 (*37; 15*)	10 (*15; 13*)	21 (*36; 16*)
Summer (JJA)	11 (*19; 13*)	8 (*14; 11*)	12 (*19; 13*)
Autumn (SON)	15 (*17; 22*)	8 (*13; 10*)	14 (*19; 21*)
Total	16 (*26; 16*)	9 (*14; 11*)	16 (*27; 16*)

The spatially averaged variability in the N_2 fixation rate experiences prominent peaks, most of which are prompted by strong AMM and ENSO events (Figure 4.7). Generally, positive AMM events and El Niño events augment the N_2 fixation rates, whereas negative AMM events and La Niña events reduce the N_2 fixation rate. Furthermore, the N_2 fixation rate is also affected by discharge variability. The fraction of the N_2 fixation rate variability attributed to discharge variability is significantly correlated to the Amazon River discharge anomalies (R-value = 0.40 including a time lag of 5 months, $p\text{-value} < 0.05$), but also the total N_2 fixation rate variability is correlated to discharge anomalies because AMM and ENSO events are major drivers of the discharge variability (Richey et al., 1989; Marengo and Espinoza, 2016). Elevated discharge enhances the N_2 fixation rate, whereas reduced discharge quenches the N_2 fixation rate. During periods when the N_2 fixation rate is only moderately impacted by climate variability, the N_2 fixation rate variability attributed to discharge variability does not strictly counteract or reinforce N_2 fixation rate variability attributed to climate variability. However, during strong AMM or ENSO events, the N_2 fixation rate variability attributed to discharge variability usually counteracts the N_2 fixation rate variability attributed to climate variability, resulting in the total N_2 fixation rate variability being slightly smaller than the N_2 fixation rate variability attributed to climate variability. Our simulations indicate that climate variability and discharge variability have a non-linear impact on the N_2 fixation rate, with the climate variability slightly suppressing the impact of the discharge variability on the N_2 fixation rate.

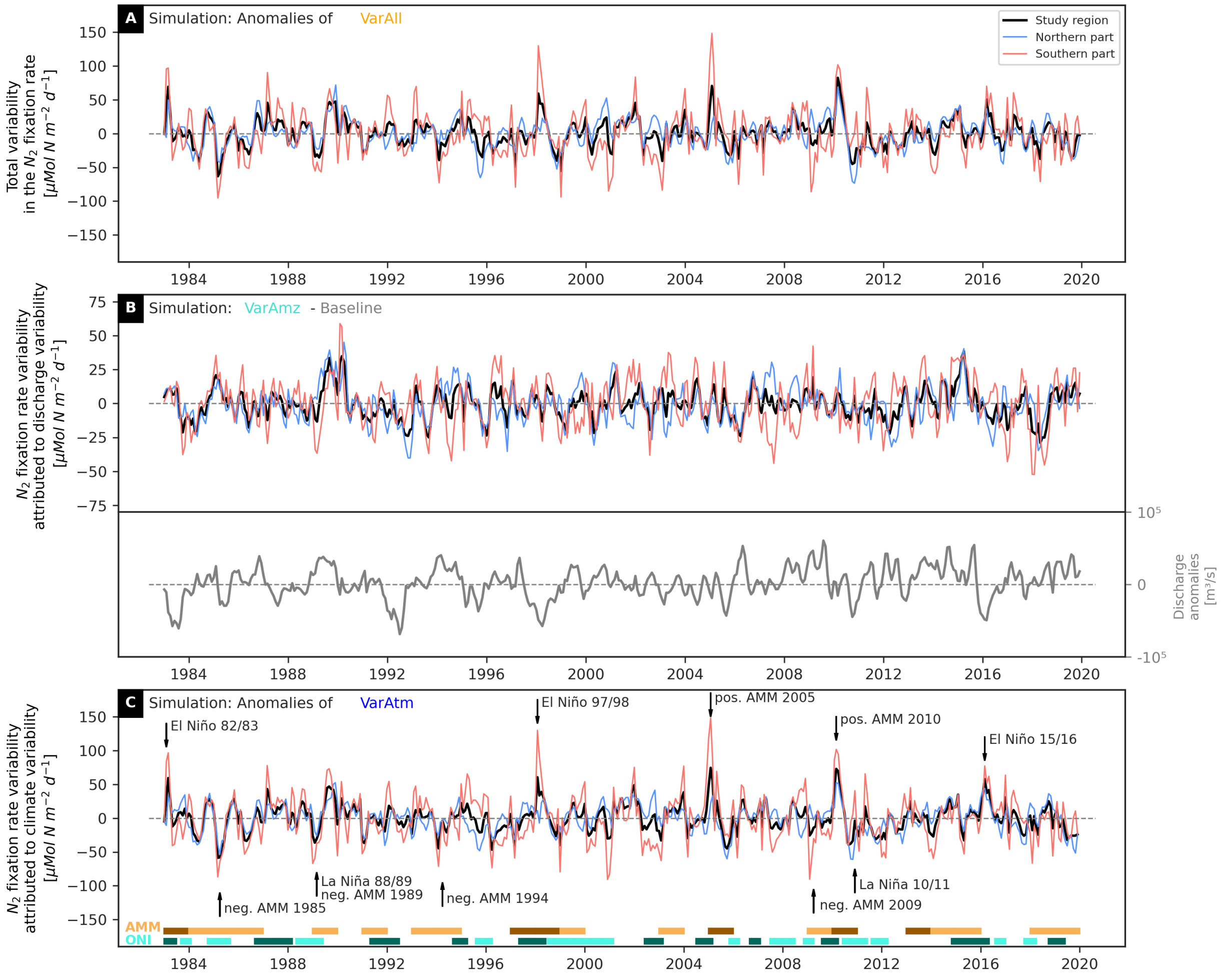

Figure 4.7 The total (A), discharge variability induced (B), and climate variability induced (C) spatially averaged N_2 fixation rate variability. The gray line in panel B depicts discharge anomalies. In panel C, brown bars depict positive (dark) and negative (light) AMM events, whereas turquoise bars depict El Niño (dark) and La Niña (light) events.

Spatially, the N_2 fixation rate variability generally scales with the N_2 fixation rate (Figure 4.8). The total and climate variability induced N_2 fixation rate variability deviate from this general observation in the latitudinal band between 15° N and 20° N, where the N_2 fixation rate variability is large relative to the N_2 fixation rate. N_2 fixation rate variability attributed to discharge variability tends to be larger in the western part of the basin than in the eastern part relative to the N_2 fixation rate, coinciding with the offshore plume region of the Amazon River. Additionally, the discharge variability derived N_2 fixation rate variability is larger than the total and climate variability induced N_2 fixation rate variability, which has two causes. Firstly, the two disparate discharge forcings lead to subtle differences in the physics of the model, which can lead to slight differences in the N_2 fixation rate. However, averaged over the study region, the resulting differences in the N_2 fixation rate tend to cancel out. Nonetheless, slight differences in the physical parameters triggered by disparate discharge forcing might lead to a slight overestimation of the N_2 fixation rate variability attributed to discharge variability in Table 4.2. Secondly, variability in the Amazon River discharge results mainly in a displacement of the N_2 fixation rate, which leads to large spatial variability that becomes significantly smaller if averaged over the study region.

To visualize how the discharge variability affects the N_2 fixation rate, we fitted a linear regression between the yearly averaged N_2 fixation rate anomalies attributed to discharge variability and the discharge anomalies. The slope of this linear regression indicates that the discharge variability impacts the N_2 fixation rate strongest in the area between 10° N - 20° N and 45° W - 70° W (Figure 4.9), which coincides with the region of largest N_2 fixation rate variability associated with discharge variability identified in Figure 4.8. The positive slope indicates that anomalously high discharge results in an elevated N_2 fixation rate, whereas anomalously low discharge results in a lowered N_2 fixation rate. In the surrounding areas, a predominantly negative relationship is observed, which is however rarely significant. Hence, the increase (decrease) in the N_2 fixation rate following anomalously high (low) discharge is focused and long-lived, whereas the partial compensation of this increase (decrease) is either more short-lived or less focused. The discharge variability can increase (decrease) the N_2 fixation rate in the offshore plume region depicted in Figure 4.9 by the contour line by up to 35 μmol N m^{-2} d^{-1} (24 μmol N m^{-2} d^{-1}) throughout a year. An important driver of the discharge variability induced N_2 fixation rate variability is variation in the riverine nutrient input, which will be discussed in more detail in Section 4.3.3.

The composites of N_2 fixation rate anomalies based on AMM and ENSO reveal that these two climate modes impact the N_2 fixation rate in a similar way (Figure 4.10). In winter and spring, positive AMM events and El Niño conditions mostly enhance the N_2 fixation rate, whereas negative AMM events and La Niña conditions mostly decrease the N_2 fixation rate, with the equatorial upwelling region posing an exception. The N_2 fixation rate anomalies are most pronounced in spring, when the AMM is fully developed. Although ENSO reaches its full intensity already in winter, the impact on the N_2 fixation rate in the WTA is strongest in spring. This is in agreement with the magnitude of the total N_2 fixation rate variability being largest in spring, indicating that the seasonally locked AMM and ENSO are important drivers of the N_2 fixation rate variability. In summer, N_2 fixation rate anomalies become more heterogeneous, expressing a zonal pattern. In autumn, positive AMM events and El Niño phases mainly decrease the N_2 fixation rate, whereas negative AMM events and La Niña phases slightly increase the N_2 fixation rate.

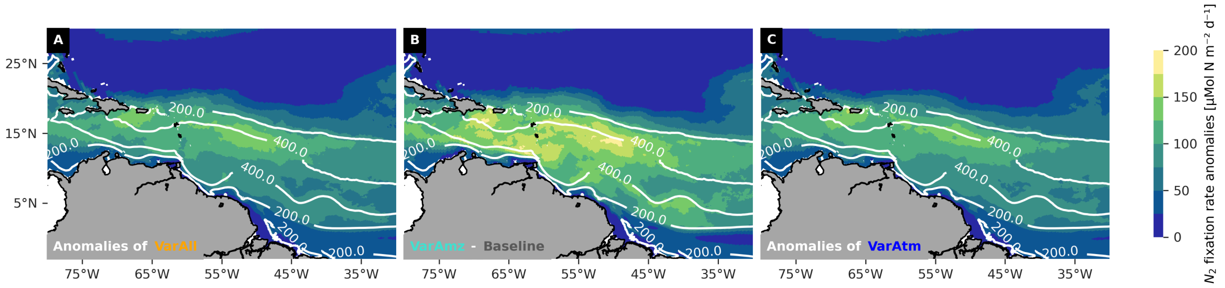

Figure 4.8 The mean absolute deviation of the total (A), discharge variability induced (B), and climate variability induced (C) variability in theN_2 fixation rate. Contour lines depict the average N_2 fixation rate.

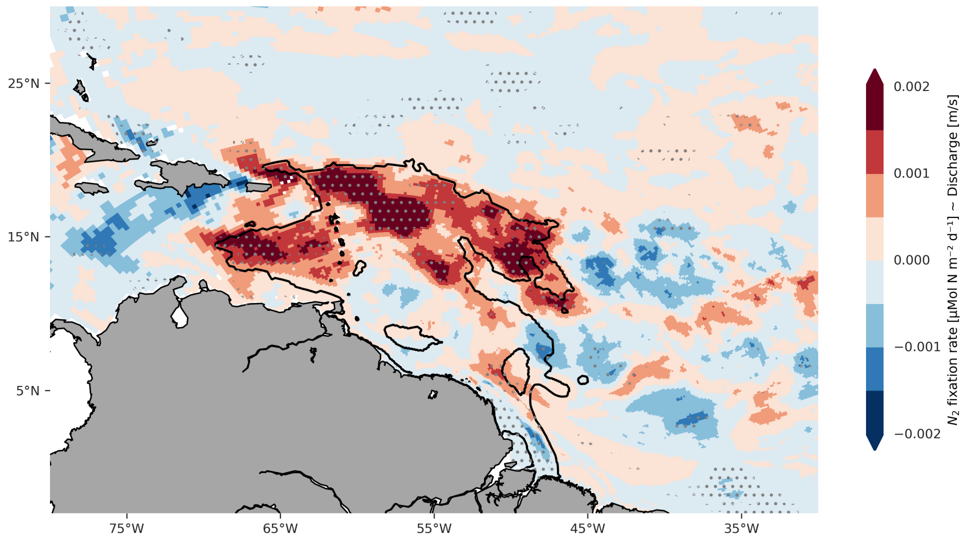

Figure 4.9 The slope between the yearly averaged N_2 fixation rate anomalies attributed to the discharge variability and the yearly averaged discharge anomalies. Stippled area represents the region exceeding the 95% confidence level. The contour line depicts the area where the SSS is influenced by discharge variability (compare to Figure 4.13D). It is defined as the area where the slope between SSS variability associated with discharge variability and discharge anomalies is smaller than $-1.5 \cdot 10^{-6}$ and significant on a 95% confidence level, including data south of 20° N and west of 45° W.

Drivers of these climate variability related N_2 fixation rate anomalies are wind-induced changes in the Mixed Layer Depth (MLD) and upwelling strength in the equatorial upwelling system, which result in varying nutrient concentration. Drivers of N_2 fixation rate variability attributed to AMM and ENSO will be discussed in more detail in Section 4.3.4.

Despite the discharge variability being partly driven by climate variability, the areas where N_2 fixation is impacted by discharge variability and climate variability differ greatly. Discharge variability derived N_2 fixation rate anomalies occur at the fringes of the Amazon offshore plume. A possible mechanism might be the improvement (destruction) of an ecological niche for diazotrophs at the fringe of the offshore plume during anomalously high (low) discharge. In contrast, climate variability results in N_2 fixation rate variability in the southeastern part of the study region. Alterations of the wind pattern that result in differing oceanic conditions are a mechanism to could explain N_2 fixation rate anomalies attributed to climate variability. To identify the mechanisms through which discharge variability and climate variability impact the N_2 fixation rate, we have to discern the drivers of N_2 fixation rate variability, before assessing how discharge variability and climate variability impact those drivers.

4.3.2 Bottom-up Controls Drive Variability in N_2 Fixation

For nutrients to impact the N_2 fixation rate, they need to either limit diazotrophic growth or affect the competitive pressure. P variability is expected to be an important driver of N_2 fixation rate variability because P availability limits the growth of all phytoplankton groups in the northern

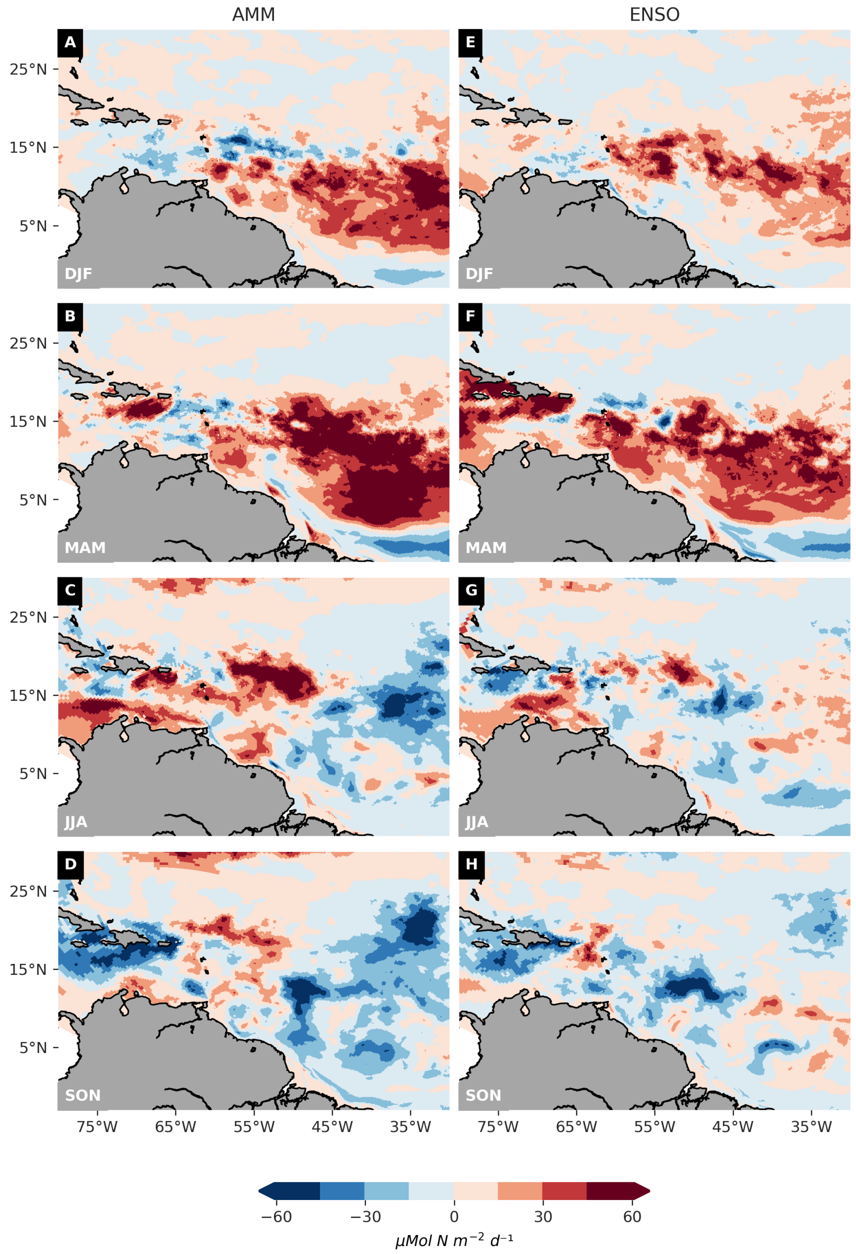

Figure 4.10 The N_2 fixation rate anomalies following AMM events (left column) and ENSO events (right column). The pattern is shown for positive AMM events and El Niño phases, respectively. The pattern for negative AMM events and La Niña phases corresponds to the inverse of the displayed pattern. The impact of the discharge variability is excluded, i.e., anomalies of the *VarAtm* were binned.

part of the study region (Figure 4.11). Additionally, P availability curbs non-diazotrophic growth in the majority of the southern part of the study region, where competition dynamics play an important role. Variable Fe and $Si(OH)_4$ concentrations could impact the N_2 fixation rate in the southern part, but subsequent analysis reveals that Fe and $Si(OH)_4$ variability have a small influence on the N_2 fixation rate, due to competitive pressure mostly controlling the N_2 fixation rate in the southern part of the study region. However, it should be noted that the $Si(OH)_4$ limitation might be underestimated in our model, due to a drift in the $Si(OH)_4$ concentration. Along the coast, where non-diazotrophic growth is limited by N availability, the N_2 fixation rate and variability therein is low. Hence, N variability in this region is unlikely to trigger considerable N_2 fixation rate variability.

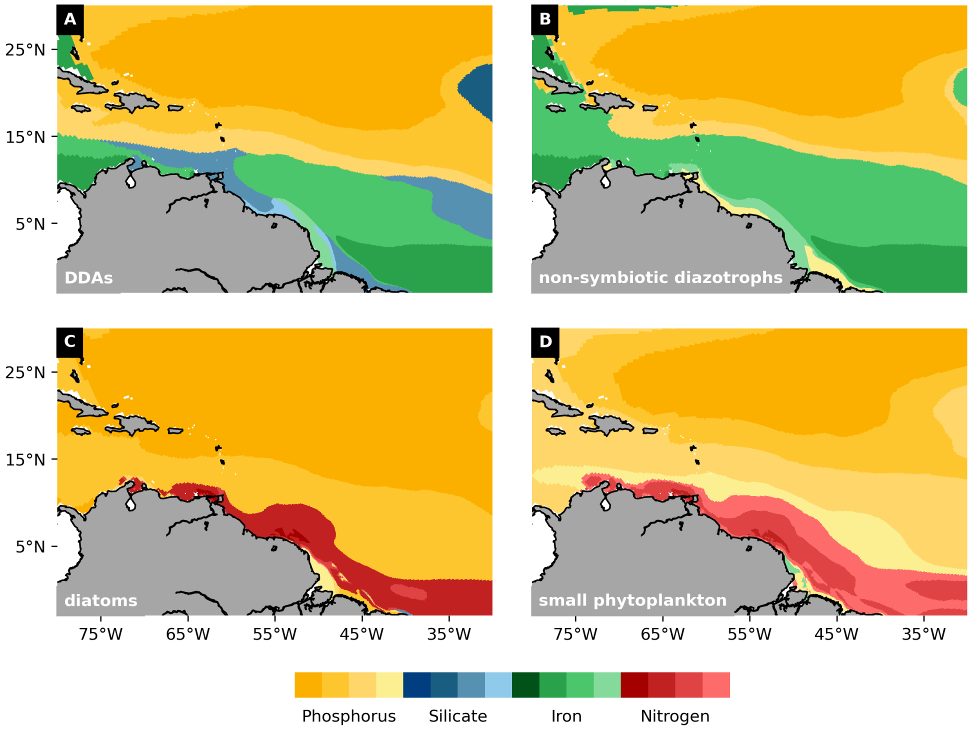

Figure 4.11 The most limiting nutrient for DDAs (A), non-symbiotic diazotrophs (B), diatoms (C), and small phytoplankton (D).

The spatial linear regression between N_2 fixation rate variability and nutrient variability confirms our expectation that P variability has a strong impact on the N_2 fixation rate (Figure 4.12). The slope of the linear regression between N_2 fixation rate variability and PO_4 variability indicates that the N_2 fixation rate is very sensitive to PO_4 variability between 15° N - 20° N and 45° N - 65° N. In this region, PO_4 is scarce and an increase (decrease) leads to an increase (decrease) in the N_2 fixation rate. In the southern part of the study region, N_2 fixation rate variability and PO_4 variability are negatively related. This is due to non-diazotrophic growth being controlled by PO_4 availability, whereas diazotrophs are only indirectly affected by PO_4 variability via changes in the competitive pressure. DOP variability has a similar impact on the N_2 fixation rate as PO_4 variability, but the slope is smaller. The area where diazotrophs profit from increases in the DOP concentration extends slightly more to the south in comparison to PO_4, which reflects the advantage of diazotrophs in assimilating DOP. Landolfi et al. (2015) highlight that this advantage allows diazotrophs to thrive in regions that are characterized by a high N:P ratio. In our model, the quantitative importance of DOP variability on the N_2 fixation rate is likely underestimated, because we did not account for the fact that only a fraction of the DOP is assimilated. Overall, our finding that variations in P availability trigger interannual N_2 fixation rate variability is supported by other studies that found P availability to limit the growth of N_2-fixers in the WTA (Sañudo-Wilhelmy et al., 2001; Webb et al., 2007; Sohm et al., 2008; Sohm and Capone, 2010b).

The N_2 fixation rate variability and the NO_3 variability are mostly negatively related, which has three causes. Firstly, non-symbiotic diazotrophs reduce their N_2 fixation rate proportionally if they assimilate DIN. Hence, a higher NO_3 concentration reduces the N_2 fixation rate, because N_2-fixers assimilate more DIN. Secondly, NO_3 availability affects the competitive pressure that diazotrophs are exposed to. N_2-fixers profit when NO_3 is scarce, because N scarcity limits non-diazotrophic growth, whereas diazotrophs can overcome N limitation by fixing N_2. Lastly, in the region where NO_3 variability has a strong impact on the N_2 fixation rate, the NO_3 concentration in the mean state is close to 0.5 mMol N m^{-3}. Because DDAs only contribute to N_2 fixation if the NO_3 concentration is below 0.5 mMol N m^{-3}, small variability in the NO_3 concentration has a large impact on the N_2 fixation rate in this region.

To assess the impact of $Si(OH)_4$ and Fe variability on the N_2 fixation rate, we depict the

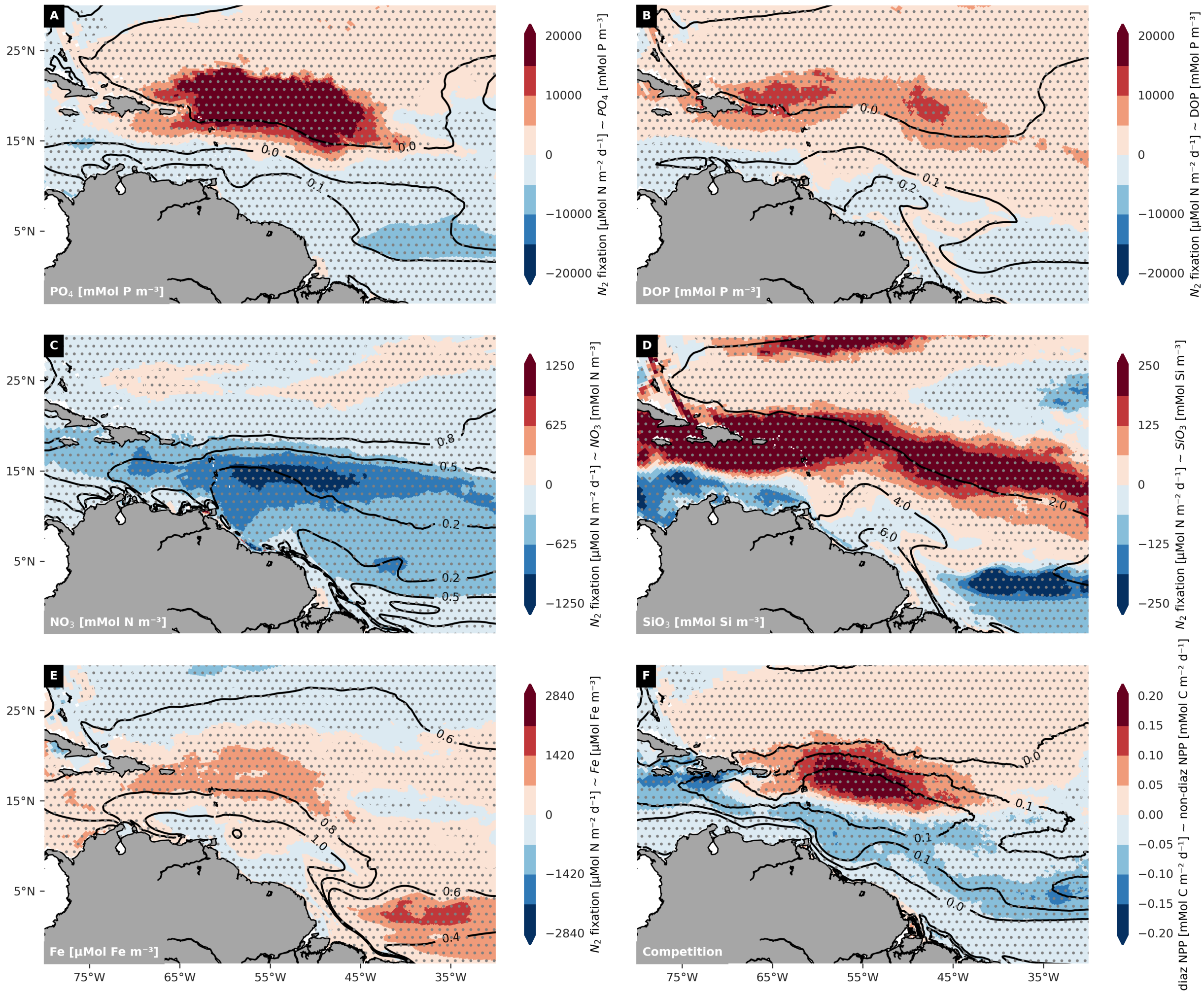
A
B
C
D
E
F
25°N
15°N
5°N
75°W
65°W
55°W
45°W
35°W
PO₄ [mMol P m⁻³]
DOP [mMol P m⁻³]
NO₃ [mMol N m⁻³]
SiO₃ [mMol Si m⁻³]
Fe [µMol Fe m⁻³]
Competition
N₂ fixation [µMol N m⁻² d⁻¹] ~ PO₄ [mMol P m⁻³]
N₂ fixation [µMol N m⁻² d⁻¹] ~ DOP [mMol P m⁻³]
N₂ fixation [µMol N m⁻² d⁻¹] ~ NO₃ [mMol N m⁻³]
N₂ fixation [µMol N m⁻² d⁻¹] ~ SiO₃ [mMol Si m⁻³]
N₂ fixation [µMol N m⁻² d⁻¹] ~ Fe [µMol Fe m⁻³]
diaz NPP [mMol C m⁻² d⁻¹] ~ non-diaz NPP [mMol C m⁻² d⁻¹]
20000
10000
0
−10000
−20000
1250
625
−625
−1250
250
125
−125
−250
2840
1420
−1420
−2840
0.20
0.15
0.10
0.05
0.00
−0.05
−0.10
−0.15
−0.20
0.0
0.1
0.2
0.5
0.8
2.0
4.0
6.0
0.4
0.6
1.0

Figure 4.12 The slope of the linear regression fitted between N_2 fixation rate anomalies and surface nutrient anomalies (A-E) and the diazotrophic NPP anomalies and non-diazotrophic NPP anomalies. Anomalies are derived from the *VarAll* simulation. The slopes of the linear regression are scales according to an extended Si:N:P:Fe Redfield ratio amounting to 80:16:1:0.007. The contour lines depict the surface nutrient concentration in the mean state (A-E) and the fraction of NPP attributed to diazotrophs in the mean state (F). Stippled area represents the region exceeding the 95% confidence level.

theoretical maximum impact of variability in these nutrients on the N_2 fixation rate. The results indicate that especially $Si(OH)_4$ variability could potentially impact the N_2 fixation rate greatly. However, due to variable Si:C and Fe:C ratios, the realized impact is likely significantly smaller. Indeed, subsequent analysis revealed $Si(OH)_4$ and Fe variability to be insignificant drivers of N_2 fixation rate variability, indicating that the Si:C and Fe:c ratio is generally smaller than the maximum ratio of 80:117 and 0.007:117, respectively. In agreement with our results, other studies have found that Fe availability is only moderately coupled to the N_2 fixation rate (Sañudo-Wilhelmy et al., 2001; Webb et al., 2007). Nonetheless, diazotrophs are Fe-limited in the southern part of the study region in our model. Thus, Fe variability would likely drive N_2 fixation rate variability if variability in the Fe supply were more pronounced, which might be the case if the model was forced with interannually varying iron-containing dust deposition.

In addition to nutrient limitation, also variability in physical parameters, such as temperature and light, could potentially induce variability in the N_2 fixation rate. Our model indicates that neither light variability nor temperature variability impacts the N_2 fixation rate greatly. However, both temperature and light availability are closely related to the MLD variability, which also controls the vertical nutrient supply, which will be discussed in more detail in Section 4.3.4. Therefore, the impact of variability in temperature, light availability and nutrient availability on the N_2 fixation rate cannot be disentangled completely.

Lastly, variability in top-down controls, such as variability in the grazing pressure, have a minor impact on the N_2 fixation rate. Variability in the biomass normalized grazing is generally positively related to the variability in diazotrophic Net Primary Productivity (NPP), which suppresses N_2 fixation rate variability (Figure C.5). One exception occurs along the coast, where the relation between variability in the diazotrophic biomass normalized grazing pressure and diazotrophic NPP variability is weak. In this region, diatom blooms dictate when grazing pressure peaks. Overall, grazing dynamics counteract N_2 fixation rate anomalies but are unlikely to drive the distinct pattern of N_2 fixation rate anomalies triggered by discharge variability or climate variability. This finding contrasts the result of Louchard et al. (*in prep.*), who found that top-down controls govern the distribution of diazotrophs in the mean state. This may be due to variability in grazing being small compared to nutrient variability or grazing acting on longer timescales than the impact of interannual phenomena lasts, which would explain why grazing shapes diazotrophic distribution in the mean state but does not contribute to interannual variability in the N_2 fixation rate.

In conclusion, our results suggest that bottom-up controls, in particular variable P and NO_3 availability coupled to competition, drive interannual N_2 fixation rate variability. In contrast, physical conditions, such as light availability and temperature, and top-down controls play a minor role. However, the question remains how discharge variability and climate variability impacts drivers of N_2 fixation rate variability.

4.3.3 The Amazon River as a Source of Variable Nutrient Input

In our model, the nutrient input of the Amazon River varies on interannual timescales and scales linearly with the discharge. If variable input of either of the nutrients identified to drive N_2 fixation rate variability impacts the nutrient concentration in the region where we observe large N_2 fixation rate variability associated with discharge variability, input variability of this nutrient can be considered a driver of N_2 fixation rate variability associated with discharge variability. While DOP, NO_3 and $Si(OH)_4$ concentrations are impacted by discharge variability in the region where the N_2 fixation rate is impacted by discharge variability (Figure 4.13), variable PO_4 and Fe input do not reach this region and are neglected in the following discussion. The region where the SSS is impacted by discharge variability establishes the boundaries where nutrient input variability can affect the nutrient concentration.

The DOP concentration is greatly impacted by discharge variability in a sizeable fraction of the WTA and DOP input variability reaches the region where we observe large variability in the N_2 fixation rate associated with discharge variability. Therefore, variable DOP input by the Amazon River is an important driver of N_2 fixation rate variability that is associated with discharge variability. DOP is transported further distances than PO_4, because non-diazotrophs,

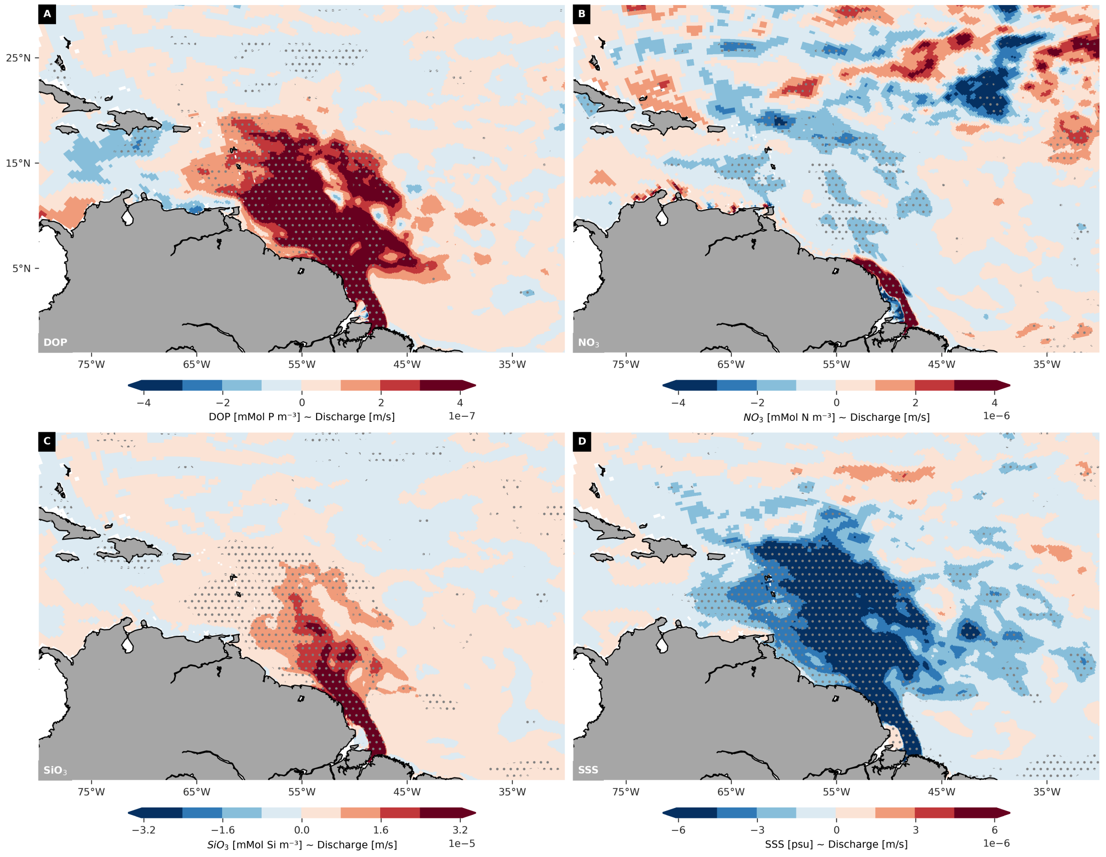
A
B
C
D
25°N
15°N
5°N
DOP
NO₃
SiO₃
SSS
75°W
65°W
55°W
45°W
35°W
−4
−2
0
2
4
DOP [mMol P m⁻³] ~ Discharge [m/s]
1e−7
NO₃ [mMol N m⁻³] ~ Discharge [m/s]
1e−6
−3.2
−1.6
0.0
1.6
3.2
SiO₃ [mMol Si m⁻³] ~ Discharge [m/s]
1e−5
−6
−3
0
3
6
SSS [psu] ~ Discharge [m/s]
1e−6

Figure 4.13 The slope of the linear regression fitted for the yearly averaged discharge anomalies as the explanatory variable and averaged P anomalies (A), NO_3 anomalies (B), $Si(OH)_4$ (C) anomalies, and SSS anomalies (D) as the dependent variable. The slope are scaled according to a Si:N:P ratio of 80:10:1. Stippled area represents the region exceeding the 95% confidence level.

especially diatoms, are less efficient in assimilating DOP relative to PO_4.

In addition to variable DOP input, also variable NO_3 input impacts the NO_3 concentration in the region where we observe large N_2 fixation rate variability associated with discharge variability. Thus, variable NO_3 is a second important driver of N_2 fixation rate variability associated to discharge variability. Although the NO_3 variability associated with discharge variability would become insignificant if scaled according to the Redfield ratio, NO_3 variability associated with discharge variability is nonetheless considered a major driver of N_2 fixation rate variability associated with discharge variability due to subtle changes in the NO_3 concentration determining if DDAs contribute to the N_2 fixation rate. The negative slope between the NO_3 variability and the discharge variability is observed due to the assimilation of NO_3 of non-diazotrophs overcompensating the variability in the NO_3 input.

Although the $Si(OH)_4$ concentration is significantly affect by variable $Si(OH)_4$ input, if scaled according to the maximum Si:C ratio, the $Si(OH)_4$ variability does hardly reach the region where we observe largest N_2 fixation rate variability associated with discharge variability. Therefore, variable $Si(OH)_4$ input has a limited impact on N_2 fixation rate variability associated with discharge variability. Nonetheless, $Si(OH)_4$ input by the Amazon River has been shown to be essential to sustain N_2 fixation rate in the WTA (Louchard et al., 2021).

In the years to come, the relevance of the Amazon River as a source of nutrients and the discharge variability as a driver of N_2 fixation rate variability might decrease. There are already more than hundred hydropower dams along the Amazon River and there are numerous proposals for additional dams (Latrubesse et al., 2017). Damming of the Amazon River will firstly decrease interannual variability in the discharge and secondly impact the nutrient load of the Amazon River (Almeida et al., 2015; Maavara et al., 2020). In hdyropower reservoirs, nutrients are eliminated via sedimentation or gaseous release to the atmosphere, which also impacts the nutrient ratio (Maavara et al., 2020). Damming of the Amazon River could thus not only decrease the magnitude of N_2 fixation rate variability, but has the potential to change the mean distribution of N_2-fixers in the WTA.

4.3.4 The Role of Climate Variability

AMM and ENSO events create distinct nutrient anomalies, having a particularly strong impact on PO_4 availability (Figure 4.14). In agreement with N_2 fixation rate anomalies, PO_4 anomalies are strongest in spring. During positive AMM events and El Niño conditions (negative AMM events and La Niña conditions), the southeastern part of the study region experiences negative (positive) PO_4 anomalies, whereas the equatorial upwelling region is characterized by PO_4 concentrations above (below) average. The mainly decreased (increased) PO_4 concentration during positive AMM events and El Niño phases (negative AMM events and La Niña phases) suppresses (enhances) non-diazotrophic NPP in all the regions where non-diazotrophs are limited by P (Figure C.7). As a result, the competitive pressure decreases (increases) and diazotrophs, which are not limited by P in the southern part of the study region, thrive (decline), thereby increasing (decreasing) the N_2 fixation rate. In contrast, DOP anomalies are mostly restricted to the offshore plume region, which is a result of the river water being transported along a different trajectory during AMM and ENSO events (Figure C.8). The DOP concentration does not vary greatly in the southeastern part of the study region. Climate variability impacts the vertical supply of nutrients, but DOP is remineralized in the deep ocean and is not supplied via vertical transport. Thus, DOP anomalies are unlikely to drive N_2 fixation rate variability associated with climate variability. While $Si(OH)_4$ and Fe anomalies are insignificant following AMM and ENSO events if scaled according to the maximum Si:C and Fe:C ratio (Figure C.9 and Figure C.10), a slight decrease (increase) in the NO_3 concentration following positive AMM events and El Niño phases (negative AMM events and La Niña phases) in winter and spring could contribute to the increase (decrease) in the N_2 fixation rate that is observed in these seasons (Figure C.11). In conclusion, it is mainly a change in the competitive pressure associated with variability in the PO_4 concentration that drives N_2 fixation rate variability associated with climate variability.

The nutrient anomalies in the southeastern part of the study region are triggered by changes in the MLD and upwelling strength. These changes are induced by modulations in the atmospheric circulation and are linked to AMM and ENSO events. Variations in the MLD and upwelling strength impact the vertical supply of inorganic nutrients from the deep ocean. A deepening of the MLD leads to entrainment of nutrients from the underlying thermocline, increasing the nutrient availability (Williams and Follows, 2003), whereas an increase in the upwelling strength transports more nutrient-rich deep water to the surface. Both positive AMM events and El Niño conditions (negative AMM events and La Niña conditions) lead to a shallower (deeper) MLD in winter and spring (Figure 4.15). An exception is the equatorial upwelling region, where a deepening (shoaling) of the MLD is observed during positive AMM events and El Niño phases (negative AMM events and La Niña phases). In summer and autumn, the MLD anomalies associated with AMM and ENSO subside. The prominent MLD anomalies in winter and spring have a clear imprint on the SST, with a shallower (deeper) MLD coinciding with positive (negative) SST anomalies. Furthermore, a shallower (deeper) MLD is usually associated with higher (lower) light availability (Sverdrup, 1953). However, given that neither diazotrophs nor non-diazotrophs gain a significant competitive advantage through changes in SST and light availability, variations in these parameters do not drive N_2 fixation rate variability. While AMM and ENSO events create distinct MLD anomalies, the impact of AMM and ENSO events on the upwelling strength is less clear (Figure C.6). However, although patchy, the upwelling strength appears to be increased (decreased) in summer in multiple areas following positive AMM events and El Niño phases (negative AMM events and La Niña phases). An increase (decrease) in the upwelling strength transports more (less) remineralized nutrients to the surface ocean. MLD anomalies and changes in the upwelling strength are expected to reinforce nutrient anomalies in summer in the equatorial

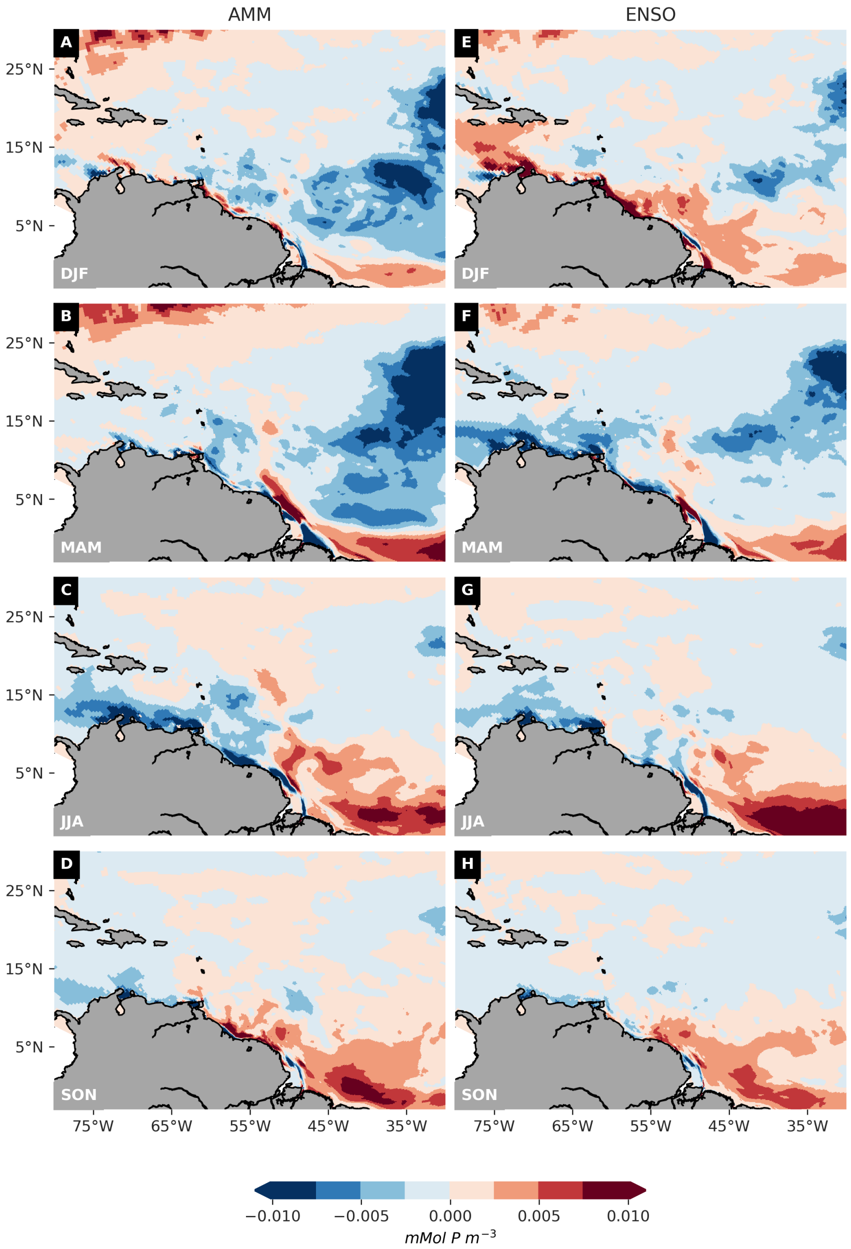

Figure 4.14 PO_4 anomalies following AMM events (left column) and ENSO events (right column). The pattern is shown for positive AMM events and El Niño events, respectively. The pattern for negative AMM events and La Niña events corresponds to the inverse of the displayed pattern. The impact of the discharge variability is excluded, i.e., anomalies of the *VarAtm* simulation were binned.

upwelling region.

Due to global warming, the surface ocean is likely to become more stratified in the future (Bindoff et al., 2019). Hence, conditions similar to those triggered by positive AMM events and El Niño conditions may become more common in the WTA. In a more stratified ocean, the importance of N_2 fixation is speculated to increase even more, because the introduction of bioavailable N via N_2 fixation could partly compensate for the reduced transport of nutrient-rich water from the deep ocean to the surface (Wrightson and Tagliabue, 2020). However, it remains questionable if stratified conditions would increase the N_2 fixation rate indefinitely because reduced vertical supply of inorganic nutrients might also limit diazotrophic growth.

4.4 Caveats

In our efforts to discern the N_2 fixation rate variability attributed to discharge variability and climate variability, we forced the model with daily reanalysis data and monthly averaged climatological data. The difference in the temporal resolution of the forcing resulted in differences in

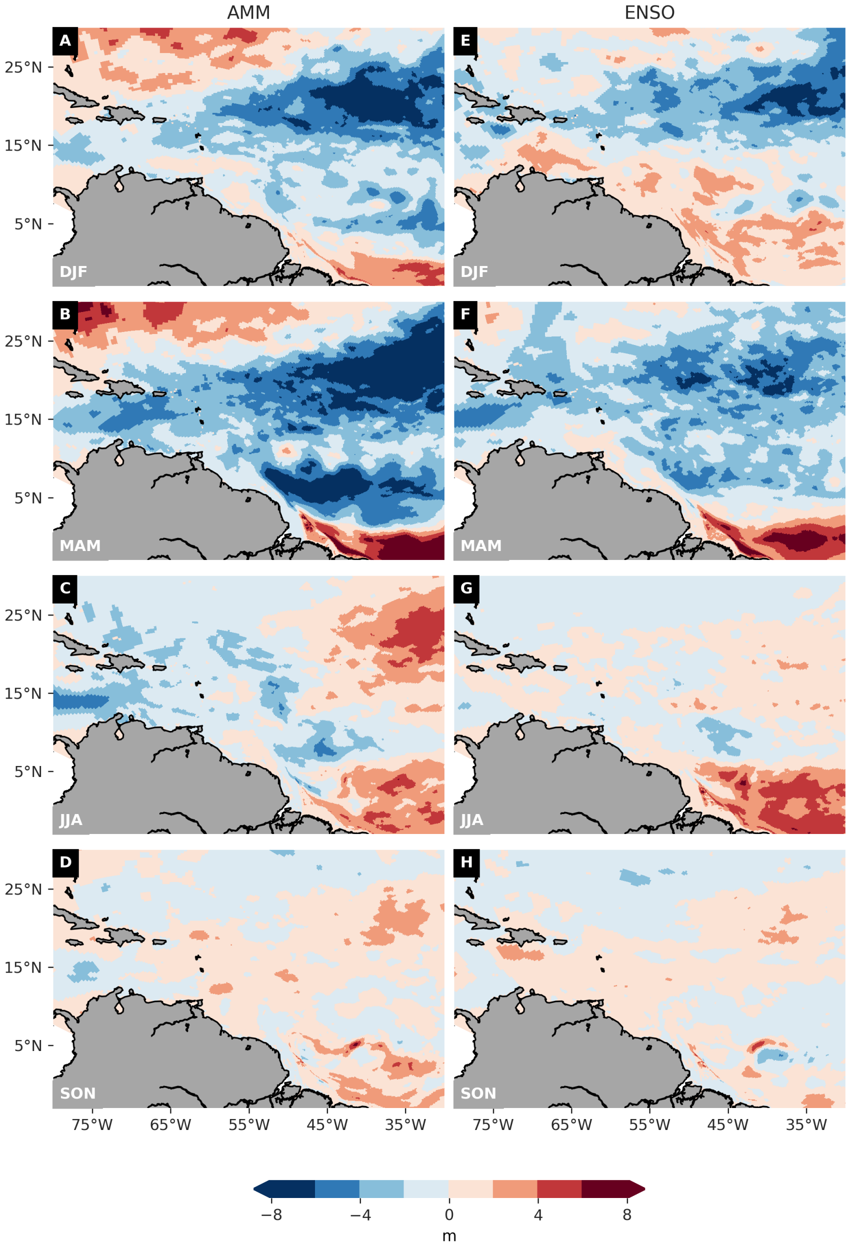

Figure 4.15 MLD anomalies following AMM events (left column) and ENSO events (right column). The pattern is shown for positive AMM events and El Niño events, respectively. The pattern for negative AMM events and La Niña events corresponds to the inverse of the displayed pattern. The impact of the discharge variability is excluded, i.e., anomalies of the *VarAtm* simulation were binned.

the model output that are not solely triggered by climate variability. It was therefore impossible to identify the impact of climate variability or combined impact of discharge variability and climate variability in the form of differences between the *VarAtm* simulation or *VarAll* simulation and the *Baseline* simulation. Instead, the impact of climate variability and combined impact of discharge variability and climate variability was assumed to correspond to the deviations from the climatological mean of the respective simulation. Although our hindcast simulation spans 37 years, which should provide a robust climatology, our assumption induces some uncertainty.

In the forcing of the model, the nutrient input of the Amazon River scales linearly with the discharge volume. Due to the lack of interannual variability in the nutrient concentrations, the nutrient ratios of the Amazon River discharge remain constant through time. The absence of interannual variability in the nutrient ratios may obscure our results because variations in the nutrient ratio may have implications for the diazotrophic niche formation. Although there is some evidence that most nutrient concentrations are elevated during periods of high Amazon River discharge and decreased during periods of low discharge (Almeida et al., 2015; Araujo et al., 2014), a recently published study found that DIN concentrations are inversely related to discharge (Drake et al., 2021). Overall, a lot of uncertainty is still associated with the nutrient concentration variability in the Amazon River on interannual timescales, which prevented the implementation of such variability in the model forcing.

The fact that nutrient concentrations are generally low in the surface due to assimilation and elevated in the deep ocean due to remineralization has made an analysis between depth-integrated N_2 fixation rate and integrated nutrient concentrations futile, which is why we compared the surface concentration of nutrients to the integrated N_2 fixation rate. This leads to some uncertainties in the importance of the different nutrient variability on the N_2 fixation rate. Nonetheless, we are confident that we have uncovered the key nutrients that drive N_2 fixation rate, but their quantitative impact should be regarded with caution.

Although we can show that P variability plays a key role in N_2 fixation rate variability, we cannot quantify the impact of dop variability on the N_2 fixation rate precisely. To be able to compare the importance of DOP variability to PO_4 variability, we would need to quantify the fraction of DOP that is assimilated, which could be achieved with a budget analysis. For the scope of our study, this is not a major drawback, because we focused on the qualitative, rather than on the quantitative impact of DOP variability.

Lastly, given the lack of long-term measurement records of nutrients and N_2 fixation in the WTA, we can neither evaluate if the simulated magnitude of N_2 fixation rate variability corresponds to reality nor if the discharge variability and climate variability have the simulated effect on nutrient concentrations and N_2 fixation.

4.5 Conclusion

We simulate pronounced interannual variability in the N_2 fixation rate in the WTA, which we can link to discharge variability and climate variability, in particular AMM and ENSO. While discharge variability impacts the N_2 fixation rate in the western part of the study region, climate variability impacts the N_2 fixation rate in the southeastern part of the study region (Figure 4.16). The discharge variability impacts the N_2 fixation rate through different mechanisms, which ultimately result in elevated (reduced) N_2 fixation rates during anomalously high (low) discharge events. As depicted by the pie chart, the Amazon River transports a lot of DOP to the WTA. During anomalously high discharge events, the P-limited N_2-fixers profit from an elevated DOP supply. Simultaneously, less NO_3 reaches the region where the discharge variability most strongly impacts the N_2 fixation rate during anomalously high discharge events, improving an ecological niche for diazotrophs and augmenting the participation of DDAs towards N_2 fixation. And the inverse is true during low discharge. Positive AMM events and El Niño conditions enhance the N_2 fixation rate via changes in the vertical supply of PO_4. AMM and ENSO events impact the vertical supply of PO_4 via changes in the MLD and upwelling strength. As illustrated by the lines, the MLD shoals during positive AMM events and El Niño phases, supplying less PO_4 to the surface. Because non-diazotrophic phytoplankton are limited by P in the southeastern part of the study region, variability in the PO_4 supply impacts the competitive pressure that diazotrophs experience. During positive AMM events and El Niño conditions, non-diazotrophic competition lessens, spurring the growth of N_2-fixers, thereby enhancing the N_2 fixation rate. In the equatorial upwelling region, the MLD deepens during positive AMM events and El Niño phases in combination with an increasein the upwelling strength. Thus, the PO_4 availability increases, which intensifies the competitive pressure experienced by diazotrophs and results in a lower N_2 fixation rate. The exact opposite is at play during negative AMM events and La Niña conditions.

The variability in the N_2 fixation rate variability has implication for the N and C cycle. Variability in the introduction of “new” N results in variable primary productivity, carbon export, and carbon sequestration (Sohm et al., 2011). Variability in the carbon sequestration has implications for the global climate, because carbon export and sequestration allows the surface ocean to take up additional atmospheric CO_2. However, some of the variation in the bioavailable DIN budget that is associated with a variable N_2 fixation rate may be offset by denitrification. Denitrification, which only occurs in the absence or near-absence of oxygen (Voss et al., 2013), is thought to be in approximate balance with N_2 fixation, ensuring the homeostasis of the marine N cycle (Gruber, 2016; Zehr and Capone, 2020). If enhanced N_2 fixation rate results in more biological carbon export, the oxygen concentration in the deep ocean is expected to drop due to more heterotrophic respiration. If heterotrophic respiration leads to oxygen depletion, denitrification can lead to a net loss of DIN. It should be noted that recent results indicate that N_2 fixation and denitrification occur spatially separated, and such a feedback, if present, is probably weak (Wang et al., 2019; Gruber, 2019).

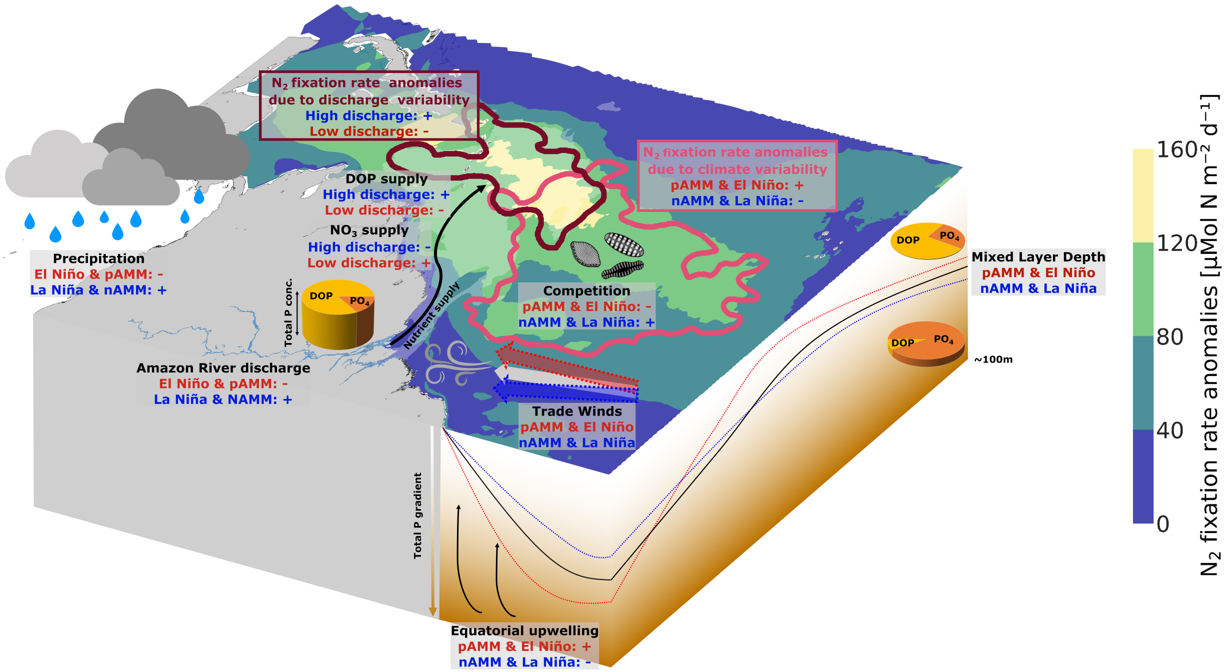
N_2 fixation rate anomalies
due to discharge variability
High discharge: +
Low discharge: -
N_2 fixation rate anomalies
due to climate variability
pAMM & El Niño: +
nAMM & La Niña: -
DOP supply
High discharge: +
Low discharge: -
NO_3 supply
High discharge: -
Low discharge: +
Precipitation
El Niño & pAMM: -
La Niña & nAMM: +
Total P conc.
DOP
PO_4
Nutrient supply
Amazon River discharge
El Niño & pAMM: -
La Niña & NAMM: +
Competition
pAMM & El Niño: -
nAMM & La Niña: +
Trade Winds
pAMM & El Niño
nAMM & La Niña
DOP
PO_4
Mixed Layer Depth
pAMM & El Niño
nAMM & La Niña
DOP
PO_4
~100m
Total P gradient
Equatorial upwelling
pAMM & El Niño: +
nAMM & La Niña: -
160
120
80
40
0
N_2 fixation rate anomalies [µMol N m^{-2} d^{-1}]

Figure 4.16 Processes resulting in interannual N_2 fixation rate variability in the WTA. In colour, the N_2 fixation rate anomalies computed as the MAD from the VarAll simulation are shown. The pie charts depict the PO_4:DOP ratio and the total P concentration in the Amazon River discharge, at the surface and at 100m depth, averaged over the whole study region.

Chapter 5

Synthesis & Outlook

From the upstream lands to the open ocean, water flows through a myriad of physically and biogeochemically diverse aquatic environments, formalised as a Land-to-Ocean Aquatic Continuum (LOAC) that bridges the terrestrial and the marine worlds (Billen et al., 1991; Bouwman et al., 2013). The LOAC was for a long time studied in a non-integrative manner i.e., each component investigated in isolation, and crudely represented, if at all, in earth system models. It has recently received increasing attention with numerous studies highlighting its importance for the regional to global carbon and nutrient cycling and pleading for a better assessment of its anthropogenic perturbations (e.g., Regnier et al. (2013); Terhaar et al. (2021); Lacroix et al. (021b)). As an ever-moving interface between land and ocean, river plumes constitute the low-end of the LOAC. The world's largest rivers such as the Amazon generate plumes that can spread in the ocean over thousands to millions of km^2, significantly altering the marine biogeochemistry and the phytoplankton dynamics (e.g., Weber et al. (2017) and references therein). Critically, the exogenous carbon and nutrients delivered by rivers have been shown to increase marine primary production (Gouveia et al., 2019), alter phytoplankton community structure (Subramaniam et al., 2008a), induce an uptake of CO_2 (Yeung et al., 2012) or inversely a release of CO_2 to the atmosphere (Lacroix et al., 2020). Due to the diversity and variability of the physical and biogeochemical processes shaping the plume properties, river plumes are highly variable environments whose average impact and full complexity are hard to capture with instantaneous field measurements and remote sensing approaches. Numerical modeling can help to unravel this complexity and provide quantitative assessments of these impacts.

In this thesis, I performed high-resolution simulations using a coupled physical-biogeochemical-ecological model to disentangle and, when possible, quantify the intertwined responses of marine biogeochemistry and ecology to the terrestrial inputs delivered by the Amazon River. This research notably sheds light on the links between the riverine nutrients, the changes in primary and export production, the mediating role of phytoplankton community and the prevalence of N_2 fixation. In this synthesis section, I intend to summarize my key findings that answer the research questions posed in the introduction (section 1.5) and highlight their implications in the context of the LOAC (section 1 & 2). I will then discuss the limitations of this work (section 3) and suggest new avenues of research ensuing from this thesis (section 4).

5.1 Major scientific findings and conclusions

Q1. What are the individual and cumulative impacts of the riverine nitrogen, phosphorus and silicic acid inputs on marine primary production? How do shifts in the phytoplankton community structure affect export production?

In Chapter 2, I aimed first at offering a comprehensive understanding of how marine primary production and the biological pump are affected by the large riverine inputs. To disentangle the effects of the different dissolved elements provided by the Amazon, I ran a set of factorial simulations where one or several nutrients are removed from the freshwater inflow. My results indicate that over the whole Western Tropical Atlantic Ocean (WTA), the Amazon is responsible for an increase of the Net Primary Production (NPP) of 115 Tg C yr^{-1} and an increase of the export production (EP) of 32 Tg C yr^{-1}. The NPP increase goes beyond a strict utilization of the nutrients delivered by the Amazon and does not proportionally match the increase in EP, which lead me to uncover internal feedbacks and non-linearities in the system.

My factorial simulations demonstrated that NPP in the WTA is impacted differently by each riverine nutrient. Phosphorus (P), inorganic and organic, determines the magnitude of the NPP increase as phytoplankton growth in the WTA is mostly limited by P. Furthermore, our results highlight the key role of dissolved organic phosphorus (DOP) in sustaining the intense N_2 fixation rates as DOP is primarily uptaken by diazotrophs. N_2 fixation is especially important as it constitutes a source of ”new” N and combined with regenerated N, it supports most of the increase of NPP, giving a minor role to riverine nitrogen in that regard. In contrast, the delivery $Si(OH)_4$ by the Amazon actually curtails the increase of NPP. Indeed riverine $Si(OH)_4$ induces a shift in the phytoplankton community towards a community dominated by non-symbiotic and symbiotic diatoms, larger phytoplankton types that are more prompt to sink out, reducing consequently the recycling of nutrients in the euphotic zone. This enhancement of the downward flux of organic matter means that a larger fraction of NPP is exported to depths, explaining the proportionally larger increase of EP compared to NPP. This change in the phytoplankton community composition thus drives the enhancement of the biological pump.

Q2. How much does the Amazon River alter the air-sea CO_2 fluxes in the WTA? What are the different factors driving the changes in the air-sea CO_2 balance?

In order to give a quantitative assessment of the CO_2 anomalies induced by the river and disentangle the driving forces involved, I ran additional factorial simulations, i.e, one without Dissolved Organic Carbon (DOC) and one where the Amazon simply does not flow, Generally, our baseline simulation agrees with the observations that indicate a moderate to strong CO_2 outgasing by the non-plume waters and an uptake of CO_2 by the regions under the Amazon plume's influence, except in the estuary zone (Lefèvre et al., 2017, 2020). In contrast, in the absence of the Amazon River (no inflow), the estuary exhibits a slight uptake of atmospheric CO_2 while the rest of the domain releases CO_2. Overall, our factorial simulations establish that the Amazon river is responsible for an additional outgasing of 1.7 Tg C yr^{-1} in the estuary and an additionnal uptake of 28 Tg C yr^{-1} in the rest of the domain.

The estuary and the shelf are primarily affected by the delivery of riverine DIC and alkalinity whose changing ratio pushes the waters to be oversaturated with respect to the atmosphere in the estuary and undersaturated in the shelf region. The terrestrial DOC delivered by the Amazon is progressively remineralized along the plume pathway and is thus driving the system toward outgasing. Finally, the changes in the biological pump associated with the shift in the phytoplankton community structure (Q1) constitute the most important factor, turning the offshore plume in to a sink of CO_2 and tempering the outgasing of the non-plume waters. Appraising the effect of the Amazon beyond the physical bounds of its plume is hard to achieve with observations as the signal is tenuous. But my results indicate that integrated over the large areal extent of the non-plume waters, the long range impact of the Amazon on the air-sea CO_2 exchanges might be sizable.

Q3. How much does the Amazon contribute to the high rates of N_2 fixation in the WTA? In what ways do the riverine inputs affect the bottom-up and top-down factors that control the phytoplankton competition and eventually determine the ecological success of Diatom-Diazotroph-Assemblages (DDAs)?

Chapter 2 highlighted the importance of N_2 fixation in providing "new" N in the system and additional pathways for carbon sequestration. Chapter 3 aimed at a better assessment of the role of the Amazon in fueling this intense N_2 fixation in the WTA. Over the whole study area, the fixation of 3.8 Tg N yr^{-1} can be directly attributed to the delivery of riverine nutrients. This represents an increase of 74% compared to the simulation without riverine inputs, with a larger contribution of the plume waters than the non-plume waters, +152% and + 46% respectively. The majority of this increase is supported by DDAs. The magnitude of the increase in N_2 fixation as well as its controlling factors vary substantially between the upstream (0-1300 km) and the downstream (1300-3500km) sections of the plume.

To uncover why and where DDAs become successful along the plume pathways, I investigated the changes in the phytoplankton competition induced by the Amazon using the growth and grazing ratio framework introduced by Hashioka et al. (2013). Although the physical properties of the ocean are altered by the river plume, changes in temperature and light availability have a negligible impact on the phytoplankton competition. Much more important is the role of nutrients. Our analysis shows that in the upstream section of the plume, the excess of $Si(OH)_4$ over NO_3 in the river waters gives DDAs a competitive advantage over non-diazotrophic phytoplankton.

This advantage does not translate in a prevalence of DDAs in the phytoplankton community as their competitiveness in growth is suppressed by a strong disadvantage in grazing. In this portion of the plume, the zooplankton biomass peaks following the enhancement of primary production, which results in a higher grazing pressure on slower-growing diazotrophs. The same situation arises in the simulations by Wang et al. (2019) where the diazotrophs exhibit high growth rates in nutrient-rich upwelling systems but do not bloom, constrained by the high grazing pressure.

In contrast, the N_2 fixation rates of DDAs increase significantly in the downstream section of the plume. Their success there is driven by a relaxed grazing pressure and the maintenance of a growth advantage over diatoms thanks to their ability to directly use DOP. In their competition against *Trichodesmium*, DDAs benefit from their higher maximum growth rate that is not counterbalanced by the grazing advantage of *Trichodesmium*. Only in really oligotrophic waters do *Trichodesmium* manage to dominate the diazotrophic community.

Overall, the analysis presented in chapter 3 confirms that the Amazon River is driving the high rates of N_2 fixation observed in the WTA. The Amazon primarily alters the concentration and stoichiometry of nutrients in the ocean but doing so, it changes both bottom-up and top-down controls that drive the phytoplankton competition. In agreement with Stukel et al. (2014), this work highlights the fact that it is the changed balance between the two that allows DDAs to thrive in the off-shore plume waters.

Q4. What is the response of N_2 fixation in the WTA to the Amazon discharge variability and the climate variability on interannual timescales? What are the mechanisms driving the negative and positive anomalies of N_2 fixation?

Chapter 4 presents evidence for a substantial amount of interannual variability of N_2 fixation in the WTA and investigates its controlling factors associated with the variability of the Amazon discharge and two climate modes, the Atlantic Meridional Mode (AMM) and the El Niño-Southern Oscillation (ENSO). This analysis is based on a set of 4 hindcast simulations that cover the 1979-2019 period. One hindcast represents the most realistic simulation and includes all modes of variability while the other hindcasts exclude at least one mode of variability i.e., using constant river discharge and/or climatological atmospheric forcing.

In my simulations, the variability of the Amazon has the largest impact in the plume waters in the northwestern part of the domain, where it can alter N_2 fixation rates by up to 15%. The anomalously high (low) discharge events are associated with positive (negative) N_2 fixation anomalies. These changes are mostly driven by the availability of nutrients: during high discharge event, more DOP is delivered in the offshore plume waters and due to an intensification of primary production in the upstream part of the plume, less NO_3 is reaching the offshore plume. Both mechanisms give a competitive advantage to N_2-fixers over non-diazotrophic phytoplankton, leading to the enhancement of N_2 fixation.

My results show that positive AMM events and El Niño conditions trigger positive anomalies in N_2 fixation and vice et versa. AMM and ENSO affect the nutrient availability through changes in the equatorial upwelling strength and in the mixed layer depths (MLD), impacting primarily the southern and eastern part of the WTA. During positive AMM events and El Niño conditions, the MLD shoals in the eastern part of the study region, reducing the supply of nutrients to the surface. In contrast, the equatorial upwelling strengthens, resulting in a larger upward flux of nutrients. During negative AMM events and La Niña conditions, the MLD in the eastern region deepens while the equatorial upwelling weakens with inverse effect on the supply of nutrients. Our results indicate that PO_4 availability is the key determinant in driving the anomalies in the N_2 fixation rates in these regions. But in contrast with the excess P observed in the Amazon plume, PO_4 supplied in response to physical changes is brought to the surface ocean in a N:P ratio close to 16:1, that is the classical Redfield stoichiometry. Thus, the increase availability of PO_4 benefits first and foremost the non-diazotrophs, increasing the competition pressure on diazotrophs and consequently reducing N_2 fixation. In contrast, when the supply of PO_4 is reduced, diazotrophs have a competitive growth advantage associated with their ability to directly use DOP as an alternative source of P.

Overall, the changes in bottom up controls play the largest role in the variability of N_2 fixation in response to the variability of both the Amazon discharge and the two climates modes investigated here. Phosphorus is mostly driving the anomalies in N_2 fixation, although with a contrasting effect depending on the N:P ratio and the P:DOP ratio of the nutrient supply. In comparison, top-down controls appear to play a minor role. My results in chapter 3 showed that a strong increase in NPP results in higher levels of zooplankton biomass, indirectly influencing the grazing pressure experienced by diazotrophs. The changes in primary production induced by the interannual variability of the Amazon discharge and climate modes are not large enough to significantly affect the grazing dynamics.

5.2 Implications

By assessing, I exposed the impacts of the Amazon River inputs on the marine biogeochemistry, exposing the intricate links and feedbacks between primary production, phytoplankton community structure, export production, N_2 fixation and air-sea CO_2 exchanges. In the context of rising anthropogenic perturbations, this work has direct implications for present and future changes, implications I will outline in this section.

Its immensity as well as its location in the very productive wet tropics make the Amazon River a crucial component in the global carbon cycle. Past studies establishing a carbon budget for the Amazon only took into account the inland portion of the LOAC, focusing primarily on the upland and central basin, neglecting the lower reach of the river from Òbidos to the mouth (Ward et al., 2017). Generally oversaturated in comparison to atmospheric levels, the Amazon fluvial network represents a source of CO_2. For the fluvial network upstream of Òbidos, Richey et al. (2002) estimated a basin-wide release of 0.5 Pg C yr^{-1}, which almost matches the estimated carbon sequestration by the Amazon terrestrial biosphere. The quantification of additional sources and/or sinks along the Amazon LOAC challenges this putative balance. The main source of uncertainty in the upscaling of individual measurements lies in the temporal and spatial variability of gas exchange coefficients (Alin et al., 2011). Using a 5-year dataset of direct measurements to better constrain the gas transfer velocity, de Fátima F. L. Rasera et al. (2013) revised upward the estimate of the CO_2 efflux to 0.8 Pg C yr^{-1}, still accounting only for the aquatic network upstream of Òbidos. To elucidate the missing portion of the river, Sawakuchi et al. (2017) made a series of measurements in the lower stretch of the Amazon basin, downstream of Òbidos and estimated a CO_2 evasion of 20 Tg C yr-1 from Òbidos to Macapà and an additional 28 Tg C yr-1 from Macapà to the mouth of the river. The last area they consider in this study overlaps the domain I simulated in this thesis. My results in this zone do not indicate a strong outgasing - only 1.7 Tg C yr^{-1} for the whole estuary - although it is important to note that the dynamics simulated in this sub-region are highly dependant of the boundary inputs, notably the saturation level of the incoming waters and the DOC both load and lability. Once in the ocean, the plume waters can cover an area of up to 2 millions of km^2 where terrestrial carbon continues to be transformed and where terrestrial nutrients alter the marine carbon cycling. To establish a truly comprehensive budget of the carbon sinks and sources along the Amazon LOAC, this further processing of carbon in the marine realm should also be accounted for. In contrast to the Amazon freshwater network, the plume waters generate a sink of atmospheric CO_2. Compared to the estimated CO_2 evasion from the inland waters, the uptake of the plume waters in my simulations is not negligible but relatively small (8.4 Tg C yr^{-1}). But my results also suggest that in the absence of the Amazon River inflow, the WTA would be overall a strong source of CO_2. Hence the total effect of the Amazon inputs on the air-sea CO_2 balance amounts to more than 15 Tg C yr^{-1} for the plume waters and 28 Tg C yr^{-1} integrated over the whole WTA. This assessment is in the same magnitude as the CO_2 evasion estimated from the lower Amazon waterways (Sawakuchi et al., 2017) which highlights the necessity to consider the Amazon LOAC to its full extent.

This thesis revealed that the CO_2 uptake observed in the plume waters is the result of a complex balance, reliant on the Amazon inputs. To some extent, the absolute concentration of riverine nutrients, especially of P, dictates the increase of the primary production. But more important is the singular stoichiometry of these nutrients that shapes the changes in the phytoplankton community structure, leading to an enhancement of the biological pump. The excess of $Si(OH)_4$ and P (PO_4 and DOP) over NO_3 favor DDAs and together with a relaxed grazing pressure, allow them to thrive in the offshore plume waters. DDAs being able to fix N_2, their presence increases the primary production beyond the local DIN capabilities and combined with regular diatoms, participates in a more efficient sequestration of carbon. Any disturbance of the riverine nutrient absolute concentration and stoichiometry might alter this equilibrium. For instance, the multiplication of dams and reservoirs in the Amazon basin might lead to an increase N:P and N:Si ratios, as P and Si appear to be more efficiently eliminated in reservoirs (Maavara et al., 2020). The factorial simulations used in chapter 2 and 3 can provide some insight on what could be the consequences of such a scenario. The changes in stoichiometry would most likely reduce the environmental niche of DDAs and the associated high rates of N_2 fixation. For instance, an excess of inorganic nitrogen has been hypothesized to suppress diazotrophy in the plume of the Yangtze River (Gomes et al., 2018). Besides, a reduction of the P load would curtail the primary production while a decrease of the Si load would shift the phytoplankton community towards the dominance of smaller phytoplankton. Such a phytoplankton community would be less efficient at exporting carbon to depths, leading to either a reduction of the atmospheric CO_2 uptake or even a release of CO_2.

To make robust predictions on future changes, ocean models should adequately represent the riverine load. My results demonstrate that riverine inputs in models should (i) include carbon but also the whole suite of essential nutrients (N, P, Si and Fe) and (ii) be seasonally resolved. As described in the paragraph above, each nutrient has a distinct effect on the system and ignoring one would vastly change the results. I want to underline the fact that although riverine Fe does not have a strong impact in my simulations due to the large inputs of dust-derived Fe in the WTA, Fe should also be included in the riverine inputs as this micronutrient limits the growth of phytoplankton in large portions of the world ocean (Moore et al., 2013b). In my simulations, Fe was indeed included but was not limiting the phytoplankton growth.

In terms of ecological complexity, my work highlights the necessity to represent N_2 fixation in an explicit manner. Although N_2 fixation rates are especially high in the WTA in response to the Amazon inputs, N_2 fixers have been found in the plumes of other large rivers such as the Mekong River (Voss et al., 2006; Grosse et al., 2010; Weber et al., 2021), the Orinoco River and the Congo River (Foster and O'Mullan, 2008) and should not be neglected in the context of the LOAC. My results suggest that representing at least 2 N_2-fixers i.e., *Trichodesmium* and DDAs, is necessary to properly capture the effect of N_2 fixation on biogeochemical cycles. Even if *Trichodesmium* and DDAs co-exist, they have different environmental niches and thus different spatial patterns. Furthermore, they have a distinct impact on the cycling of nutrients and carbon. Owing to its buoyancy and its low palatability for grazers, *Trichodesmium* is more likely to retain nutrients and carbon in the euphotic zone, favoring their recycling and their potential use for the rest of the food web (Letelier and Karl, 1998; Capone et al., 2005). In contrast, DDAs have been hypothesized to drive a stronger export to depths, resulting in a decrease of surface CO_2 levels but also causing a larger loss of nutrients (Korte et al., 2020; Follett et al., 2018). In line with Landolfi et al. (2015), I find that the competitive advantage of diazotrophs over non-diazotrophs does not rely solely on its N_2 fixation capacity. In my simulations, the direct use of DOP by diazotrophs plays a crucial role in sustaining high rates of N_2 fixation the P-starved environment of the WTA. DOP assimilation has been documented both for *Trichodesmium* (Benavides et al., 2017) and DDAs (Meyer et al., 2016) and should be represented in the explicit modeling of N_2-fixers which is still not the case in numerous models (e.g., Stukel et al. (2014); Paulsen et al. (2017); Follett et al. (2018)).

The importance of N_2 fixation in the WTA is confirmed in my simulations. In my baseline simulation, in climatological conditions, the total N fixed in the WTA (8.9 Tg N yr^-1) represents 34% of the N2 fixation simulated for the whole Atlantic. In regard to global estimates, the WTA could account for 7 to 13 % of the N_2 fixed in the global ocean (Landolfi et al., 2015; Paulsen et al., 2017; Tang et al., 2019a). Disentangling the underlying processes driving this intense N_2 fixation appears all the more crucial. In this context, chapter 4 constitutes the first assessment of interannual variability in N_2 fixation in the WTA. My results highlight the importance to consider both the effect of the discharge variability and the impact of atmospheric forcing variability. My analysis of the impacts of the discharge interannual variability provides also hints on how N_2 fixation would react to future changes in runoff. Multiple studies have suggested that the hydrological cycles over the Amazon are intensifying, resulting in an increased discharge during the high discharge regime and a lower discharge during the low discharge regime (Gloor et al., 2013; Friedman et al., 2021). My results suggest that the increased discharge, concurrent to the seasonal widest spread of the plume, would result in an enhancement of N_2 fixation in response to a larger supply of DOP to the offshore plume waters. More work is needed to evaluate the importance of this effect in the context of multiple anthropogenic perturbations.

5.3 Limits and shortcomings

Modeling frameworks are extremely useful to unravel complex systems, test hypotheses and offer quantification of highly variable processes. Nevertheless, there are inherent limitations associated with the simplified representation of natural dynamics. In this section, I will outline the main limitations of my model setup and discuss their implications.

The representation of processes on the shelf

For the first few hundreds of kilometers, the plume waters travel inshore in the shallow band of the continental shelf. A first bias in my results can stem from the simplistic representation of particulate matter dynamics and processes at the sediment-water interface. In my model setup, the sinking of particulate organic carbon (POC) follows the ballast model introduced by Armstrong et al. (2001). In such a model, POC is assumed to comprise a free fraction that is rapidly decomposed and a fraction associated with ballast mineral that is remineralized on longer timescales. These distinct dissolution length scales determine the depth at which the POC is remineralized. With the implicit sinking scheme that I use, POC is instantaneously distributed across the water column upon production. Such a parametrization provides reasonable results but neglects the lateral advection of particulate matter. The Amazon shelf is a very dynamic environment where particulate matter does not settle directly. Instead, the trajectory of this organic material is governed by the combined effect of strong trade winds, geostrophic flows, tidal forcing and northwestward background circulation (Fontes et al., 2008; Nittrouer et al., 2021). Additionally, once at the seabed, particulate matter can be resuspended and/or continue its northward migration within the fluid mud belt that tops the shelf (Nittrouer and DeMaster, 1996; Gabioux et al., 2005). Neglecting all these physical aspects has consequences for the spatial patterns of the flux to the sediments, the remineralized flux back to the water column and eventually the cross shelf export of particulate matter. To address these limitations, Zhao et al. (*in prep.*) recently used an explicit sinking scheme that allows the lateral advection of particulate matter (Frischknecht, 2018) and performed similar simulations as the one used in this thesis. The preliminary results indicate that while spatial patterns of remineralization and burial slightly change on the shelf, the integrated loss of nutrients and carbon to the sediments remains equivalent to the one in my simulations. It is important to note though that these new simulations still exclude resuspension of particles and mobile fluid sediments.

Beyond the physical transport of particles, bias can arise from the biogeochemical processes simulated at the water-sediment interface. The sediment component in my model setup constitutes a semi-reflective boundary. When the particulate matter reaches the sediments, part of it is buried and part of it remineralized and instantaneously feeds back the bottom cell of the water column. For instance, the loss of POC follows the algorithm developed by Soetaert et al. (1996) which relates the POC burial to the flux of organic carbon reaching the sediments, with a maximum efficiency of 80%. Such simplified formulations have been hypothesized to overestimate burial fluxes (Hülse et al., 2017), which could be the case as the Amazon shelf exhibits relatively high remineralization rates (Aller and Blair, 2006). Besides, this approach neglects the time delay of carbon and nutrient recycling, affecting the temporal and spatial dynamics of fluxes escaping from the sediments. Also simplified is the representation of sediment denitrification in the model, which is based on a simple transfer function established by Bohlen et al. (2012). Overall the recycling of nutrients and carbon might be somewhat underestimated in my simulations, which might translate in an underestimation of the cross shelf export of nutrients and carbon. These putative biases would enhance the primary production and expand the blooms further offshore. However, they would not fundamentally change the main conclusions of this thesis.

Modeling N_2-fixers

The standard version of BEC includes only one class of N_2 fixers, reproducing the main functional traits of *Trichodesmium* (Moore et al., 2001). I incorporated in BEC another type of N_2 fixer i.e., DDAs. Beyond the parameter choices that always come with some uncertainties, I had to make decisions on how to represent this complex symbiosis, based on available knowledge. Because their symbiotic association is fragile and easily compromised, both in field measurements and in culture experiments, physiological measures such as uptake rates or inner exchanges between the symbiont and the host are technically challenging to make and are thus limited (Foster and O'Mullan, 2008). Hence there are still quite a few open questions on the functioning of the symbiosis. One major yet unresolved question is how do DDAs exactly form their symbiotic association? For now in the model, DDAs are considered in symbiosis when the local NO_3 concentration is below 0.5 mmol N m^{-3} (see section 2.2.1), which is also the approach taken by Stukel et al. (2014). But this can lead to unrealistic oscillations between symbiotic and non-symbiotic state when the local conditions vary around the threshold. Besides other factors can also drive the formation or the parting of the symbiosis e.g., Tuo et al. (2017) suggested that the scarcity of P could result in the dissociation of the symbiosis. Foster and O'Mullan (2008) also hypothesized that free-living *Richelia* were supplied by rivers as heterocystous diazotroph thrive in brackish waters. This fluvial input would give an additional importance to rivers in supporting DDAs blooms.

Another open question is: do DDAs release excess N to the environment in the same manner as *Trichodesmium*? In BEC, *Trichodesmium* fixes 30% of N more than necessary to sustain their growth, based on their C-fixation. This surplus is directly released to the surroundings as NH_4, ready to be assimilated by any other phytoplankton. With a coarse-grained model representing the *Hemiaulus–Richelia* symbiosis, Inomura et al. (2020) showed that the symbiont already needs to fix N_2 4.5 times faster than in a free-living situation in order to meet the needs of its host, leaving maybe less room for excess N fixing and exudation. Nevertheless, using secondary ion mass spectrometry measures and simple modeling, Foster et al. (2021) recently demonstrated that DDAs comprising *Hemiaulus hauckii* and *Hemiaulus membranaceus* diatoms might be directly releasing 7.5% and 11% of their fixed N, respectively. Considering the high N_2 fixation rates in my simulations, implementing such a release of excess N would lead to an enhanced retaining of N in the surface waters.

The last major unknown in the modeling of DDAs is related to its export efficiency, influencing also the retention/loss balance of nutrients and carbon in the euphotic zone. Based on the analysis of the carbon and biogenic silica content of sediment traps, Korte et al. (2020) suggested that DDAs blooms in the WTA might be more efficient at exporting carbon at depths than regular coastal diatoms. However, the sinking velocity of DDAs is related to their radius, cell density and form resistance, which are dependent on the species of the diatom host. Form resistance is for example enhanced by chain formation which performed by the *Hemiaulus hauckii*, reducing their sinking rates. Taking into account all these factors, Foster et al. (2021) calculated sinking speeds of less than 10 m d^{-1} which is similar to that of other non-symbiotic diatoms (Miklasz and Denny, 2010). Determining the contribution of DDAs to the downward flux of particles plays an critical role in constraining the impact of DDAs blooms on biogeochemical cycles, but more investigation is needed before a more refined parametrization can be implemented in my model.

Beyond the uncertainties associated with the modeling of DDAs, some bias in the N_2 fixation patterns might arise from the absence of UCYN in my model framework. UCYN have been detected throughout the tropical Atlantic Ocean and especially in the eastern tropical Atlantic where their contribution to total N fixed can locally exceed 50% (Martínez-Pérez et al., 2016). However, the observed concentrations of UCYN in the WTA are quite low (Goebel et al., 2010) and based on the simulations by Stukel et al. (2014), it seems that UCYN are primarily found in the open ocean, with marginal contribution to total N_2 fixation in the fringes of the Amazon plume. Their absence in BEC is likely to have little impact on my main results. Nevertheless, in the factorial simulations, the presence of UCYN could have had interesting implications e.g., a shift in the diazotrophic community and an enhanced contribution of UCYN to N_2 fixation in the absence of riverine $Si(OH)_4$. This also means that in simulations exploring perturbation scenarios, UCYN is important to consider to properly capture the response of the system. And beyond the scope of this thesis, since UCYN are rarely included in models, there is a lot to investigate, in terms of competition with other diazotrophs, quantified contribution to N_2 fixation on large-scales or impact on nutrient cycling.

Modeling zooplankton

In chapter 3, my results demonstrate that the presence of the Amazon River triggers an enhancement of the zooplankton biomass and affects the relative weight of top-down controls, which has major implications for the phytoplankton competition. More specifically, the relative grazing pressure on DDAs shifts along the plume pathway from being a disadvantage compared to non-diazotrophic phytoplankton to being an advantage. And this progressive change is one of the major factors driving their blooms in the offshore plume waters. Yet the simplicity of the grazing parametrization in BEC might limit our ability to represent more complex aspects of the grazing dynamics. In the model, the generic zooplankton class comprises the representation of both microzooplankton and mesozooplankton (Moore et al., 2001) and preys indiscriminately on the 4 phytoplankton functional types (PFTs) using a Holling type II ingestion function (Holling, 1959). Emerging from this simple formulation is a tight coupling between phytoplankton biomass and zooplankton biomass and a strong dependence of the grazing pressure on the prey biomass (Sailley et al., 2013). Concretely, the zooplankton biomass increases almost linearly with the phytoplankton biomass, although Nissen (2019) demonstrated that the zooplankton biomass can reach a saturation state above which it ceases to increase, an upper limit to grazing that I also found in my simulations (figure B.3). But the initial coupling of zooplankton and phytoplankton biomass means that during strong phytoplankton blooms, that are mostly driven by the fast-growing diatoms, the zooplankton accumulates rapidly biomass and in turn, imposes a stronger grazing pressure on slower-growing PFTs such as DDAs and *Trichodesmium*. Based on simulations using BEC coupled to CESM, the same dynamic has been identified by Wang et al. (2019) in the highly productive regions such as upwelling systems. Switching to Holling Type III for the ingestion function could help temper this effect as it would create a prey refuge for the slow-growing PFT and thus reduce the strong grazing pressure on N_2 fixers.

However, introducing additional zooplankton classes in BEC could be even more critical to improve the modeling of grazing in BEC (Nissen, 2019). Indeed, having one generic zooplankton class hampers the representation of a more complex predator-prey interplay, neglecting for example the multilevel trophic organization of the food web (Steinberg and Landry, 2017). Additionally, assigning distinct particle formation efficiency to the different zooplankton groups would also help better constrain the downward C flux resulting from grazing. In the WTA, the zooplankton community structure has been shown to shift from a mesozooplankton dominated community in the coastal and low-salinity regions to a microzooplankton dominated community in the offshore plume and oceanic regions (Conroy et al., 2016). The direct consequence of this change is a transition from a ”export” type of food web, driving a strong C transfer to depths, to a ”retention” type of food web, characterized by an efficient nutrient recycling (Sarmiento and Gruber, 2006). Thus the single zooplankton approach in BEC is also a source of uncertainty in the representation of particle export and its spatio-temporal variability.

5.4 Outlook and suggestions for future research

This thesis provided a novel insight on the cascading effects of the Amazon River on the marine biogeochemistry and phytoplankton dynamics (section 1) but it also opened the door to more questions. In this section, I will briefly introduce potential research topics emerging from this work.

Interannual variability of the Amazon discharge and the marine carbon cycling

The interannual variability affecting the LOAC, especially its marine component, is quite understudied. Focusing on land processes, Hastie et al. (2019) recently showed that the C balance in the Amazon basin is strongly affected by the interannual variability of precipitation and temperature. Their model-based analysis indicates that during wet years, while the CO_2 evasion from the aquatic network is increased, the net ecosystem productivity (NEP) and carbon sequestration on land is also higher, resulting in a net reduction of the CO_2 flux from the whole system. In my hindcast simulations, the increase on the Amazon discharge, associated with wet years, induces an enhancement of N_2 fixation in the offshore plume. But I have not explored yet the response of the carbon cycling. It would be very interesting to see if wet years can also be linked to positive anomalies in the CO_2 uptake by the ocean.

Ibánhez et al. (2015) analyze the data collected by a merchant ship equipped with an automated CO_2 analyzer, making regular journeys between Le Havre (metropolitan France) and Kourou (French Guyana). Ranging from 122.9 to 438 μatm, the recorded fugacity of sea water CO_2 exhibited a high spatial and temporal variability that Ibánhez et al. (2015) attribute to the location of the Amazon River plume and the associated variable intensity of biologically-induced C drawdown. Mu et al. (2021) base their analysis of the air-sea CO_2 exchanges in the plume waters on three sampling expeditions that took place in May–June 2010, September–October 2011, and July 2012. While they aim at explaining the mean conditions, they speculate that the data collected in June 2010 is nontypical and actually influenced by ENSO. One of the conclusion of this study is the need to investigate in more depth the interannual variability of the system. My hindcast simulations could help quantify the contribution of the Amazon plume to the observed CO_2 anomalies, determine the main mechanisms involved and thus contribute to a complete assessment of the C balance along the Amazon LOAC. Such an analysis could also put these plume-driven anomalies in the context of the climate-driven anomalies. Indeed, the ENSO modes that are partly driving the precipitation over the Amazon basin and thus the discharge are also associated with changes in circulation and SST anomalies in the northern tropical Atlantic, with consequences on the sea surface CO_2 levels (Ibánhez et al., 2017). Similar to chapter 4, the analysis of the hindcasts with a carbon perspective would also give some insight on the interplay between these different modes of variability.

The fate of the nitrogen & carbon fixed by diazotrophs

Chapter 2 presented evidence that diazotrophs, especially DDAs, contribute significantly to the replenishment of the nitrogen pool and to the vertical export of carbon in the WTA. But this assessment was not refined. The fate of the N and C fixed by diazotrophs has multiple pathways (e.g., exudation, formation of Particulate Organic Matter (POM) upon death, Diazotroph Derived N (DDN) transfer to the planktonic food web etc.) and needs to be investigated in more details and better quantified. Tacking where the ”new nitrogen” fixed by diazotrophs goes is technically challenging, although advances in isotope tracing and Dissolved Organic Matter (DOM) characterization provide a way forward (Benavides and Voss, 2015). Additionally, research on the predators of N_2 fixers and other loss terms, which is especially critical to determine the impact of diazotrophs on the biological pump, is still at its infancy (Zehr and Capone, 2020). Nevertheless, past *in situ* measurements and lab experiments have already demonstrated that (i) DDN transfer to the dissolved pool and to the non-diazotrophs is significant but varies according to the type of diazotroph (e.g., Berthelot et al. (2016); Martínez-Pérez et al. (2016); Caffin et al. (2018)), (ii) diazotrophs are ingested by zooplankton either directly or via a secondary pathway (e.g., grazers feeding on DDN POM) with again differences depending on the type of diazotroph (e.g., Hunt et al. (2016); Conroy et al. (2016, 2017)) and (iii) larger N_2-fixers can drive a significant N and C export (e.g., Dore et al. (2002); Yeung et al. (2012); Karl et al. (2012)). In contrast, most modeling studies quantify how much N is fixed by diazotrophs but do not track the ”new” N beyond that point (e.g., Wang et al. (2019)). Only a handful of modeling experiments have recently investigated the effect of diazotrophs on primary production and export (e.g., Follett et al. (2018); Dutheil et al. (2018)). And yet, models could play a key role in tracking the DDN in the food web and quantifying the importance of its different pathways as well as investigating the impact on the carbon cycle. The prerequisite for such a study is to explicitly represent in the model at least three diazotrophic ecotypes i.e., *Trichodesmium*, DDAs and UCYN. Building on the main findings of lab experiments, this modeling framework could provide a more comprehensive picture of the distinct ecological consequences of the diazotrophs.

N_2-fixers in a changing world, winners or losers?

The upper ocean conditions are currently changing in response to the increasing CO_2 concentrations in the atmosphere and associated effects. Adapted to warm tropical waters and stratified conditions, one could assume that diazotrophs will suffer less or even benefit from global warming. And indeed, Trichodesmium is hypothesized to expand its geographic to higher latitudes in a future warmer ocean (Fu et al., 2014; Boatman et al., 2017). But the combined effect of the multiple physical (e.g., temperature, irradiance) and chemical (e.g., nutrient availability and stoichiometry) changes induced by climate change will surely result in a more complex response, with factors acting in concert or counteracting each other. For instance, Jiang et al. (2018) demonstrated that the optimum growth temperature of *Trichodesmium* is 5° C higher when the cells are experiencing strong Fe limitation compared to replete conditions. Projecting this result under a IPCC representative concentration pathway RCP8.5 scenario, Jiang et al. (2018) suggested a global increase of N_2 fixation of 22% by 2100. However, the acidification of the ocean could reduce the growth rate of *Trichodesmium* due to a decreased nitrogenase efficiency (Luo et al., 2019). Besides, the response to the different stressors varies according to the ecotype, the specie or even strain. For example, different strains of the unicellular *Crocosphaera* exhibit distinct temperature and CO_2 optima (Hutchins et al., 2013; Fu et al., 2014). A reshuffling of the diazotrophic flora can thus be expected at the global scale, which renders the tentative assessment of future global N_2 fixation all the more complicated.

Wrightson and Tagliabue (2020) investigated the response of N_2 fixation to RCP8.5 conditions in an ensemble of nine Earth System Models (ESM). They found overall a global decrease of N_2 fixation with some counteracting spatial responses. However, the representation of diazotrophs in these models is quite crude: two are using a restoring parametrization, four are representing N_2 fixers implicitly and three have an explicit representation of only one diazotroph i.e., *Trichodesmium*. In my view, a more complex representation of N_2-fixers is critically needed in marine ecosystem models used for future projections. In a joint effort with the observational community, a more accurate representation of the different diazotrophic ecotypes is crucial to appropriately assess the potential large-scale shift in the diazotrophic biogeography, to better quantify the changes in total N_2 fixation and to identify possible synergistic or antagonistic responses.

Appendix A

Appendix to Chapter 2

1. Figure A1 and Tables A1 to A4: additional information on the model configuration
2. Figures A2 to A7: additional figures to illustrate the evaluation section
3. Tables A5 and A6: additional quantitative results

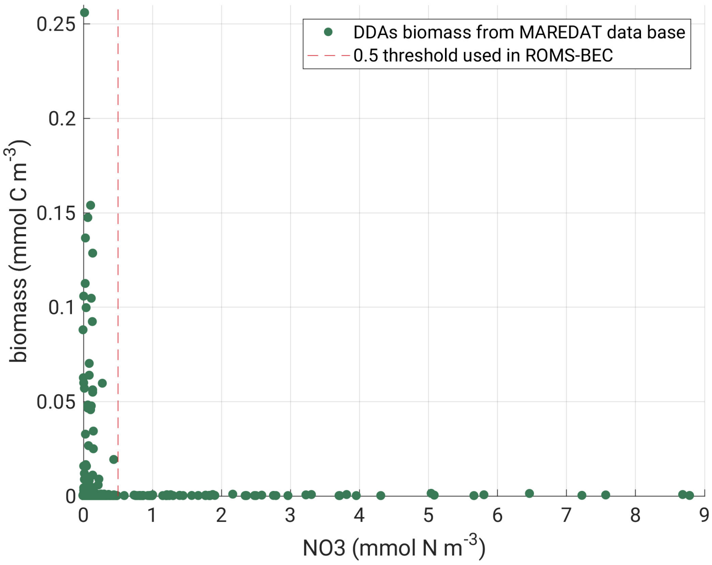

Figure A.1 DDAs biomass as a function of reported nitrate concentration. Observations come from the database established by Luo et al. (2012) (N=523)

Table A.1 List of relevant BEC parameters used for the phytoplankton uptake and losses

Parameter	Description	Unit	SP	Diatom	Tricho	DDA
μmax	Maximum Growth Rate	d^{-1}	2	3.5	0.55	1.5/2.25**
kNO3	Half Saturation Constant	mmol m^{-3}	0.5	1.2	1.0 *	1.2*
kFe	Half Saturation Constant	μmol m^{-3}	0.08	0.12	0.5	0.5
kPO4	Half Saturation Constant	mmol m^{-3}	0.01	0.06	0.04	0.06
kDOP	Half Saturation Constant	mmol m^{-3}	0.26	2.0	0.04	0.06
kSiO3	Half Saturation Constant	mmol m^{-3}	0.0	1.8	0.0	1.8
agg rate max	Maximum Aggregation Rate	d^{-1}	0.9	0.9	0.0	0.9
graze poc	Routing of grazed matter to POC	/	0.05	0.42	0.05	0.42

**constant used to calculate uptake rate but that does not limit the growth.*

***left rate is used when DDAs fix N_2, right rate is used when the diatom is assumed alone i.e. not fixing*

Table A.2 List of relevant BEC parameters used for the cycling of DOM

Parameter	Description	PAR $> 1\%$	PAR $< 1\%$
DONrefract	fraction of N routed to the refractory pool	0.08	0.08
DOPrefract	fraction of P routed to the refractory pool	0.03	0.03
DOC remin	remin. rate for semi-labile DOC	1/250 d	1/10 yr
DON remin	remin. rate for semi-labile DON	1/160 d	1/4 yr
DOP remin	remin. rate for semi-labile DOP	1/160 d	1/9 yr
DONr remin	remin. rate for refractory DON	1/2.5 yr	1/670 yr
DOPr remin	remin. rate for refractory DOP	1/2.5 yr	1/460 yr

Table A.3 Physical and biogeochemical properties of the Amazon River influx in our study. Monthly mean and weighted annual mean. All estimates originate from Araujo et al. (2014), except the values in gray (see main text for a description of how these values were determined).

Mth	Discharge $m^{-3}\,s^{-1}$	Temp °C	Salt	NO_3 mmol m^{-3}	NH_4 mmol m^{-3}	PO_4 mmol m^{-3}	SiO_3 mmol m^{-3}	Fe μmol m^{-3}	DOC mmol m^{-3}	DON mmol m^{-3}	DOP mmol m^{-3}	DIC mmol m^{-3}	Alk mmol m^{-3}	N:P:Si
1	136 053	28	5.5	10	0.5	0.7	105	13	360	49	3	571	560	14:1:150
2	152 047	29	4.5	11	0.6	0.7	110	11	408	56	3	523	513	16:1:157
3	178 252	28	4	11	0.6	0.8	115	15	485	66	4	499	489	14:1:144
4	208 275	27	3	12	0.7	0.8	125	16	550	75	5	452	441	15:1:156
5	236 903	27	2	13	0.7	0.8	130	17	583	80	5	404	386	16:1:162
6	239 302	27	1.5	14	0.7	0.9	140	17	625	85	5	380	360	15:1:155
7	217 956	27	2.2	12	0.6	0.8	135	15	600	82	5	413	393	15:1:169
8	182 621	26	4	10	0.5	0.8	130	14	400	55	3	499	489	11:1:162
9	148 355	26	5	10	0.5	0.8	127	12	375	51	3	547	536	11:1:159
10	121 729	27	5.5	11	0.6	0.7	123	10	300	41	2	570	560	16:1:176
11	113 602	27	6.2	8	0.4	0.6	117	9	345	47	3	604	593	13:1:195
12	124 857	28	6	8	0.4	0.7	113	11	340	46	3	594	584	11:1:161
mean	171 166	27	3.8	11	0.6	0.8	124	14	474	65	4	486	472	14:1:155

Table A.4 Total annual atmospheric deposition of nutrients over the WTA

Nutrient	total fallout
P (Tg P yr^{-1})	0.006
N (Tg N yr^{-1})	0.6
Bio-available Fe (Tg Fe yr^{-1})	0.07

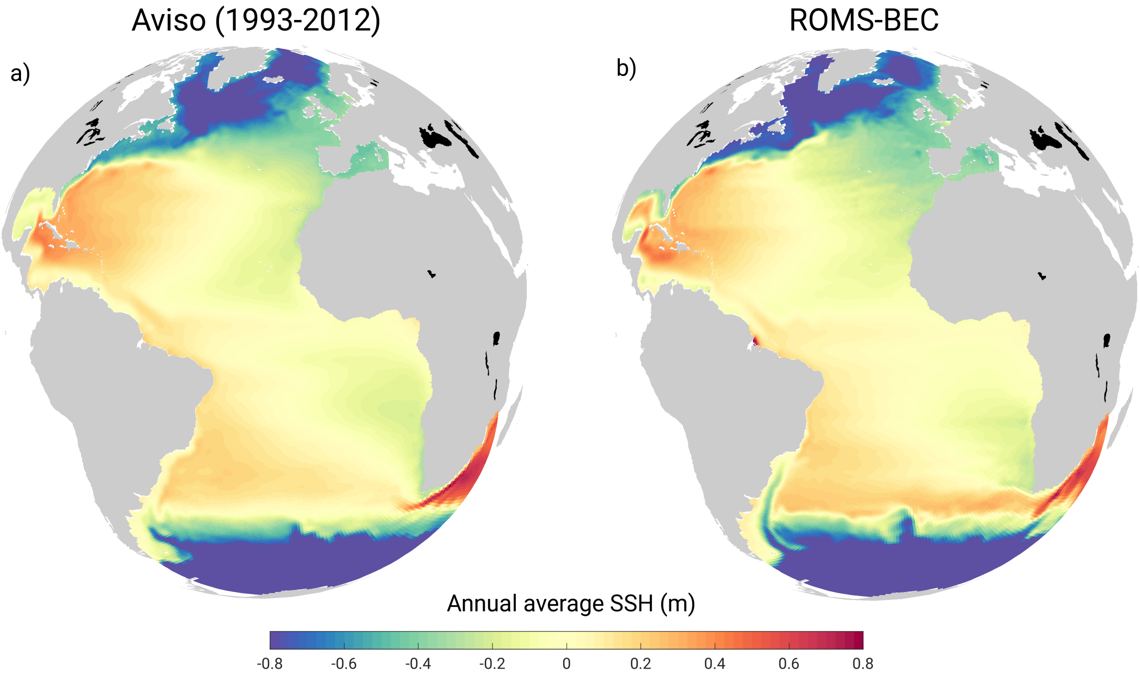
Aviso (1993-2012)
ROMS-BEC
a)
b)
Annual average SSH (m)
-0.8
-0.6
-0.4
-0.2
0
0.2
0.4
0.6
0.8

Figure A.2 Annual average sea surface height in (a) Aviso (1993-2012) and in (b) ROMS-BEC. Aviso products were processed by SSALTO/DUACS and distributed by AVISO+ (https://www.aviso.altimetry.fr) with support from CNES.

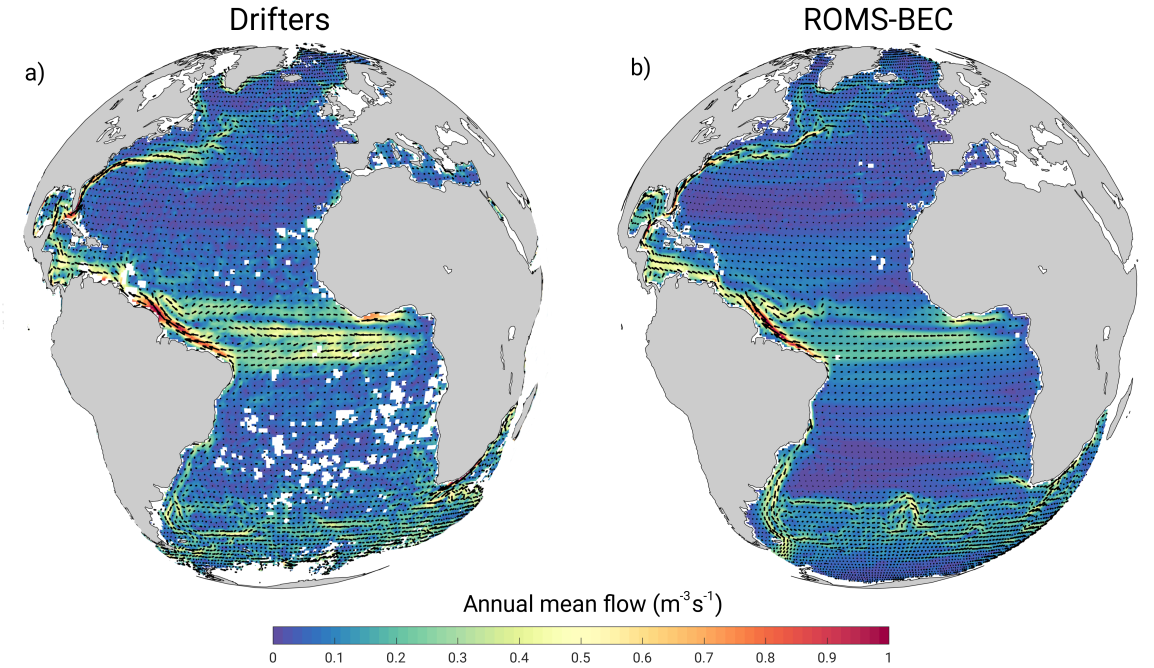
Drifters
ROMS-BEC
a)
b)
Annual mean flow (m^{3}s^{-1})
0
0.1
0.2
0.3
0.4
0.5
0.6
0.7
0.8
0.9
1

Figure A.3 Maps of the annual mean surface ocean circulation in the Atlantic Ocean. (a) Average surface flow (m s^{-1}) estimated from drifters (Lumpkin et al. 2010) and (b) in ROMS-BEC (integrated in the first 15 meters to be comparable to drifter data).

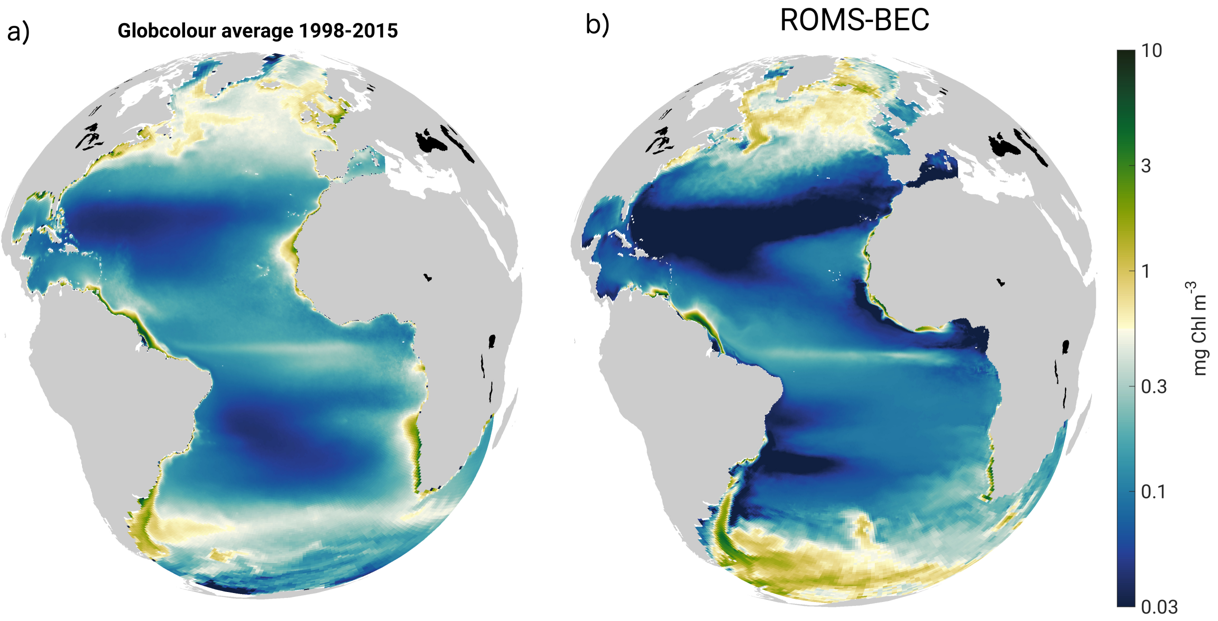

Figure A.4 annual average surface chlorophyll in (a) Globcolour 1998-2015 (Maritorena et al. 2010) and in (b) ROMS-BEC

Table A.5 NPP and EP in the offshore Plume and Non-plume sub-regions (see the Methods section for the definition of these sub-regions)

Simulation	NPP		EP	
	Off Shore Plume	Non Plume	Off Shore Plume	Non Plume
NoNutr	201.5	966.9	34	158.1
All	244.1	1012.7	176.1	224.1
NoDIN	241.2	1015.7	47.2	176.8
NoPO4	239.9	997.9	46.7	174.1
NoDOP	202.7	935.9	34.9	138.1
NoP	191.6	920.9	39	164.1
NoSi	263.1	1074.9	39.6	68.9
NoAmazon	209.2	986.6	35.4	162.7

Table A.6 Anomalous fluxes and related uptake efficiencies as defined by Jin et al. (2008), neglecting the DOC flux: $e_{uptake} = \frac{\int_A \int_t \Delta \mathrm{CO}_{2\text{air-sea}}}{\int_A \int_t \Delta EP}$ where $\Delta \mathrm{CO}_{2\text{air-sea}}$ is the change of atmosphere-ocean CO_2 exchange between the case under investigation and the *NoAmazon* case, ΔEP is the corresponding change in export production at 100 meters, and where we integrated all fluxes over the whole region of study. A positive anomaly means an anomalous uptake.

	All	NoDIN	NoPO_4	NoDOP	NoP	NoSi
$\Delta \mathrm{CO}_{2\text{air-sea}}$*	159	147	143	57	26	109
Δ EP	156	172	136	49	30	63
$\mathrm{e}_{\mathrm{upt}}$	1.02	0.94	1.05	1.18	0.87	1.74

$**$*all anomalies are in Tg C.*

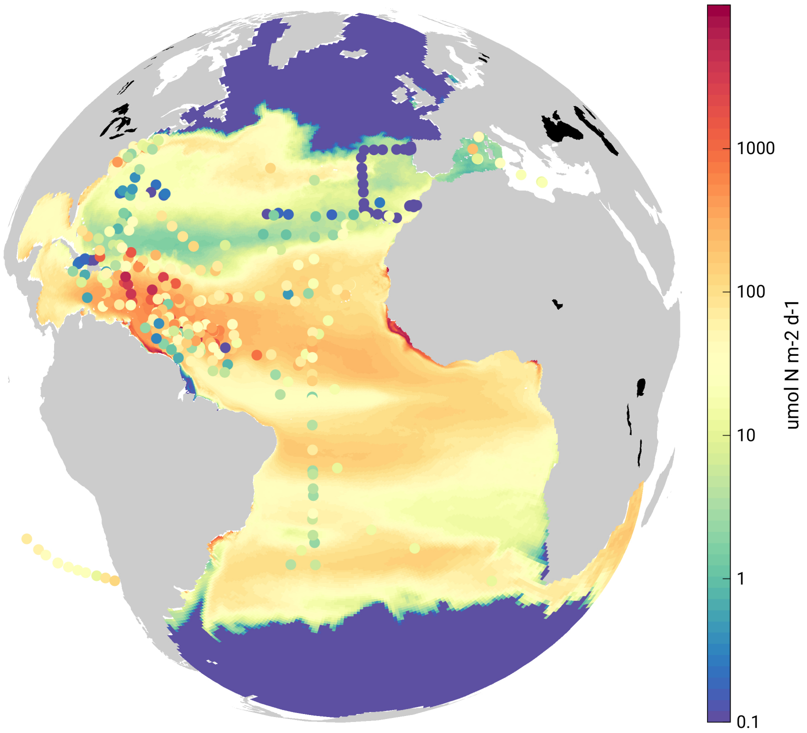
1000
100
10
1
0.1
umol N m-2 d-1

Figure A.5 Average integrated total N_2 fixation in ROMS-BEC, compared to integrated total N_2 fixation reported in Luo et al. (2012) (dots)

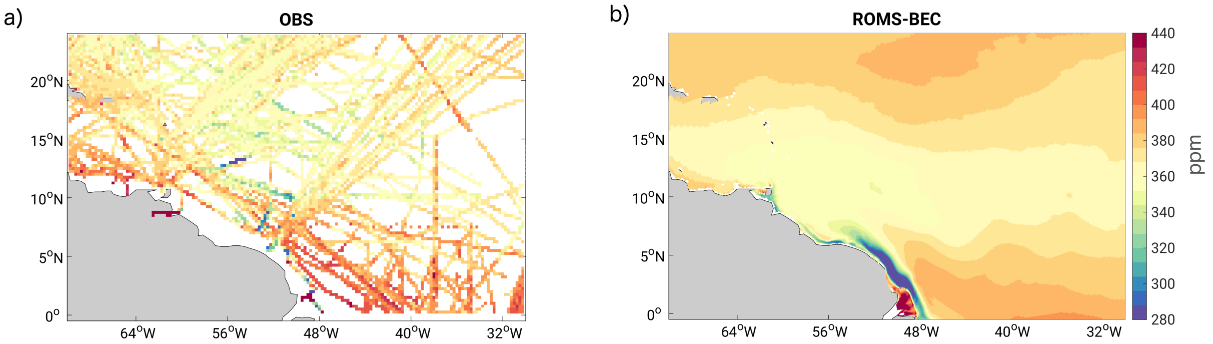
a)
OBS
20°N
15°N
10°N
5°N
0°
64°W
56°W
48°W
40°W
32°W
b)
ROMS-BEC
20°N
15°N
10°N
5°N
0°
64°W
56°W
48°W
40°W
32°W
440
420
400
380
360
340
320
300
280
ppm

Figure A.6 Annual average pCO_2 in (a) observations and in (b) ROMS-BEC. Observations are derived from the Surface Ocean CO_2 Atlas (SOCAT version 2020). All data (1970-2019) have been normalized to the year 2006.

Appendix B

Appendix to Chapter 3

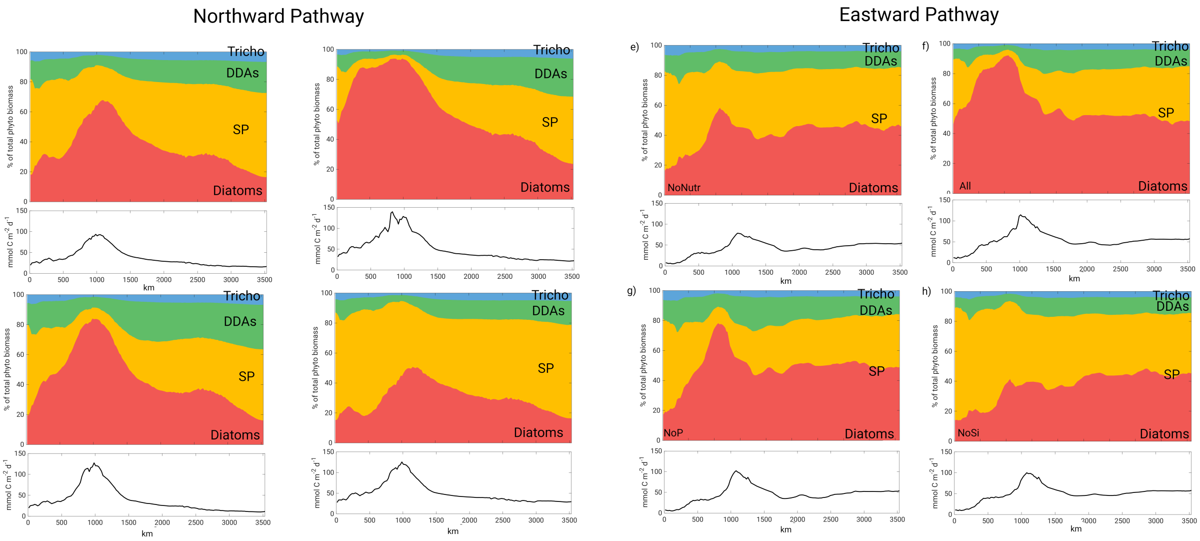

Figure B.1 Phytoplankton community structure defined as the percentage of total biomass annually averaged along the northward pathway in (a) the *NoNutr* simulation, (b) in the *AllNutr* simulation, (c) in the *NoP* simulation and (d) in the *NoSi* simulation. Below the fraction is displayed the average total NPP for each simulation. The total biomass was integrated over the first 100 meters.

Short analysis of figure B.2

The same mechanisms driving the balance between the bottom factors and top down factors along the northward pathway are displayed along the eastward pathway (figure B.2). More importantly, the changes triggered by the presence of riverine nutrients i.e the differences between the *NoNutr* and *AllNutr* are also very similar between the two pathways. Nevertheless, there are a few noteworthy differences between the pathways.

First, we observe little changes on smaller scale in the downstream plume pathway (1300-4500 km) giving the graph a more wavy aspect. This is due to the mixing with waters coming from the southern part of the domain, as evidential in the streamline fields (figure 3.1). This lateral advection brings nutrients, especially N and P, from the equatorial upwelling. The input of N results in a higher maximum growth rate for DDAs as the N concentration in the equatorial upwelling exceeds often 0.5 mmol N m^{-3} putting DDAs in a non-symbiotic state. Conversely, the additionnal N reduces the competitiveness of DDAs in terms of nutrient uptake, especially in the competition against diatoms and SP.

In the competition against *Trichodesmium* in the *AllNutr* simulation, DDAs appear to be a bit less competitive in the eastward pathway than in the northward pathway, especially towards the end, from 2500 km on (figure B.2). In this part of the pathway, the advantage of *Trichodesmium* in terms of nutrient uptake progressively increases, resulting in the decrease of the relative growth ratio. The influence of the Amazon is weaker in this very downstream part of the pathway and the more oligotrophic conditions of the open ocean are more favorable to *Trichodesmium*. Nevertheless, the higher maximum growth rate of DDAs allows them to keep a growth advantage.

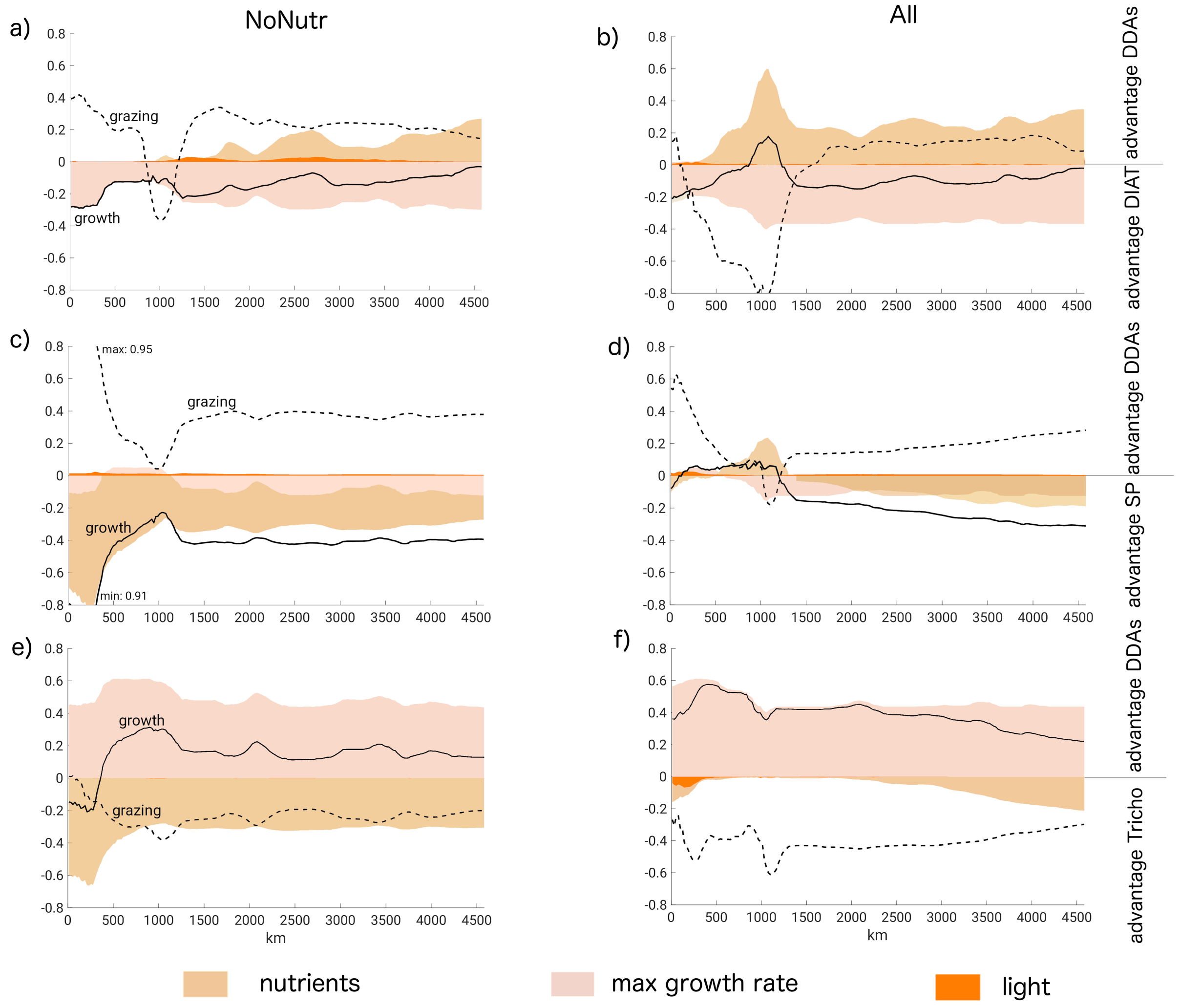

Figure B.2 Relative growth and grazing ratios along the eastward pathway between DDAs and (a-b) diatoms, (c-d) small phytoplankton and (e-f) *Trichodesmium*. The left panels correspond to the *NoNutr* simulation and the right panels to the *AllNutr* simulation

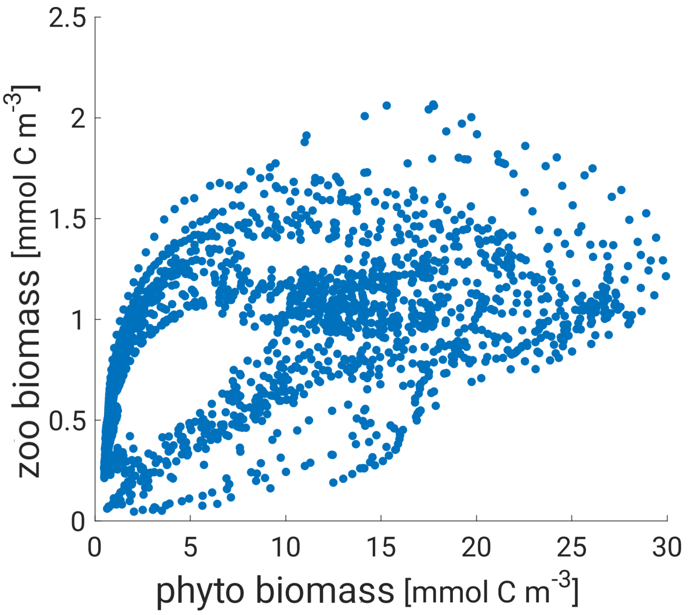

Figure B.3 Average phytoplankton biomass versus zooplankton biomass in the *AllNutr* simulation, average over the northward pathway

Appendix C

Appendix to Chapter 4

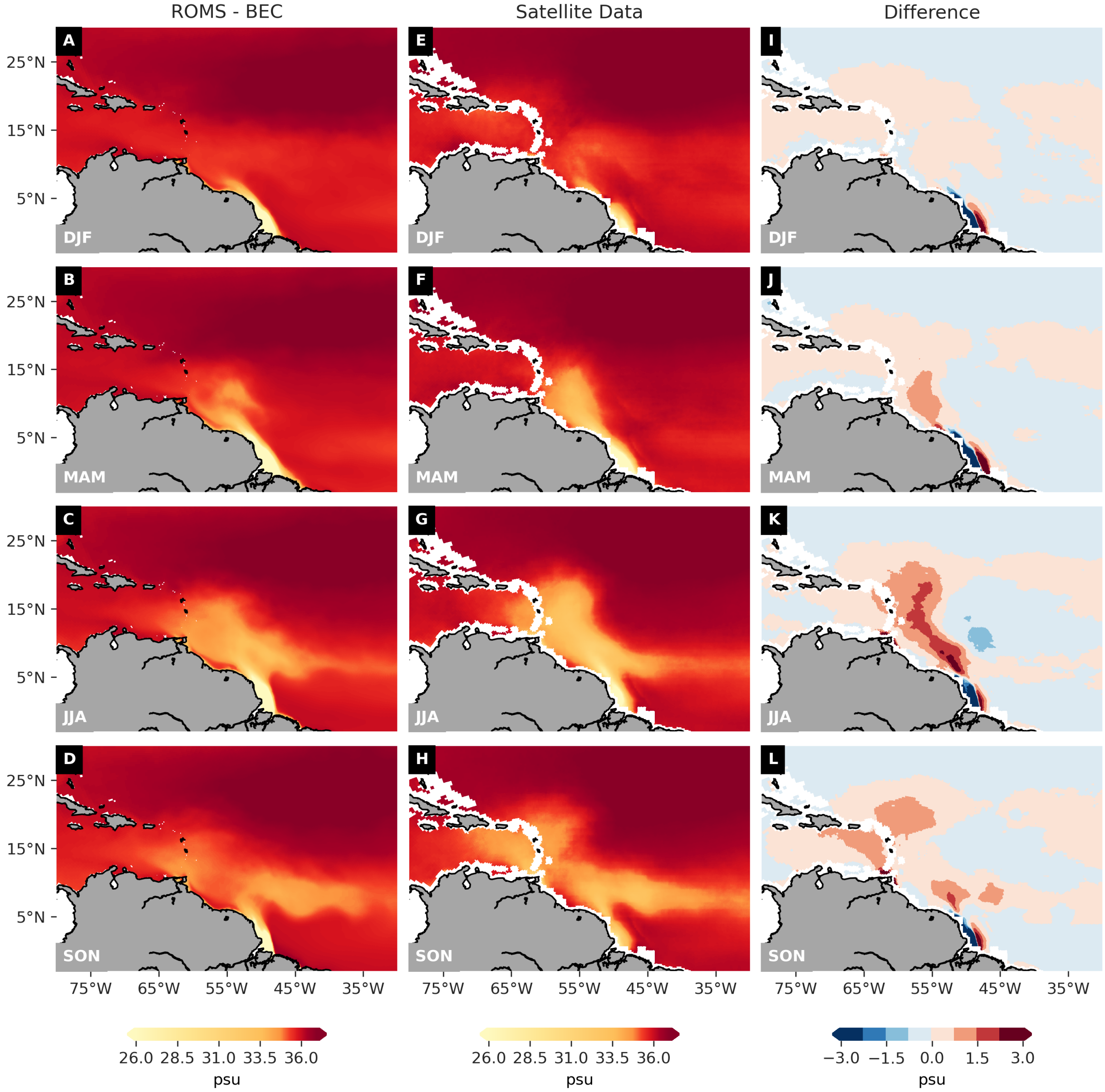
ROMS - BEC
Satellite Data
Difference
A
B
C
D
E
F
G
H
I
J
K
L
DJF
MAM
JJA
SON
25°N
15°N
5°N
75°W
65°W
55°W
45°W
35°W
26.0 28.5 31.0 33.5 36.0
psu
−3.0 −1.5 0.0 1.5 3.0
psu

Figure C.1 The seasonal mean SSS simulated by ROMS-BEC (A-D) and the seasonal mean of the ESA CCI V2.31 SSS product bilinearly interpolated to the model grid (E-H) between 2010 and 2019. The difference was computed by subtracting the seasonally averaged SSS of the satellite data from the seasonally averaged SSS of the model output (I-L). Hence, positive (negative) differences are an indication of higher (lower) SSS simulated by the model than measured by the satellite.

In the mean state, the model successfully simulates the seasonal pattern of SSS in the WTA (Figure C.1). The imprint of the low salinity water delivered by the Amazon River is most clearly observed in summer when the runoff peaks. In winter, when the discharge is lowest, the plume area is smallest. During summer and autumn, the low salinity water is transported as far as the Caribbean Sea by the NBC, which is in accordance with the observations of Froelich et al. (1978); Muller-Karger et al. (1988) and Hellweger and Gordon (2002). By late summer, the NECC retroflects between 5° N and 10° N, transporting low salinity water eastwards. In the difference plots (Figure C.1I-C.1L), the most prominent deviations in SSS are observed near the Amazon River mouth, which arise most likely due to complications of satellite measurements in low salinity areas (Fournier et al., 2015). While the model underestimates the SSS close to the river outflow, it overestimates the SSS in the remaining part of the impact region of the Amazon River. In autumn, the model underestimates the eastward transport of freshwater by the NECC, which is depicted by positive SSS differences between 5° N and 10° N.

ROMS-BEC mostly captures the SSS (Figure C.2A) and the interannual variability in SSS (Figure C.2B), with a correlation coefficient of 0.83 and 0.60, respectively. However, the model underestimates the magnitude of the seasonal cycle in SSS and is generally characterized by mean SSS lower than indicated by the reanalysis data and satellite observations. The latter is a result of the model producing SSS lower than observed in the outflow region of the Amazon River (Figure C.1). In contrast, the ROMS-BEC overestimates the SSS in the rest of the Amazon plume pathway. Compared to the reanalysis data, the model underestimates the interannual SSS anomalies, but the modelled SSS anomalies are congruent with the satellite observations.

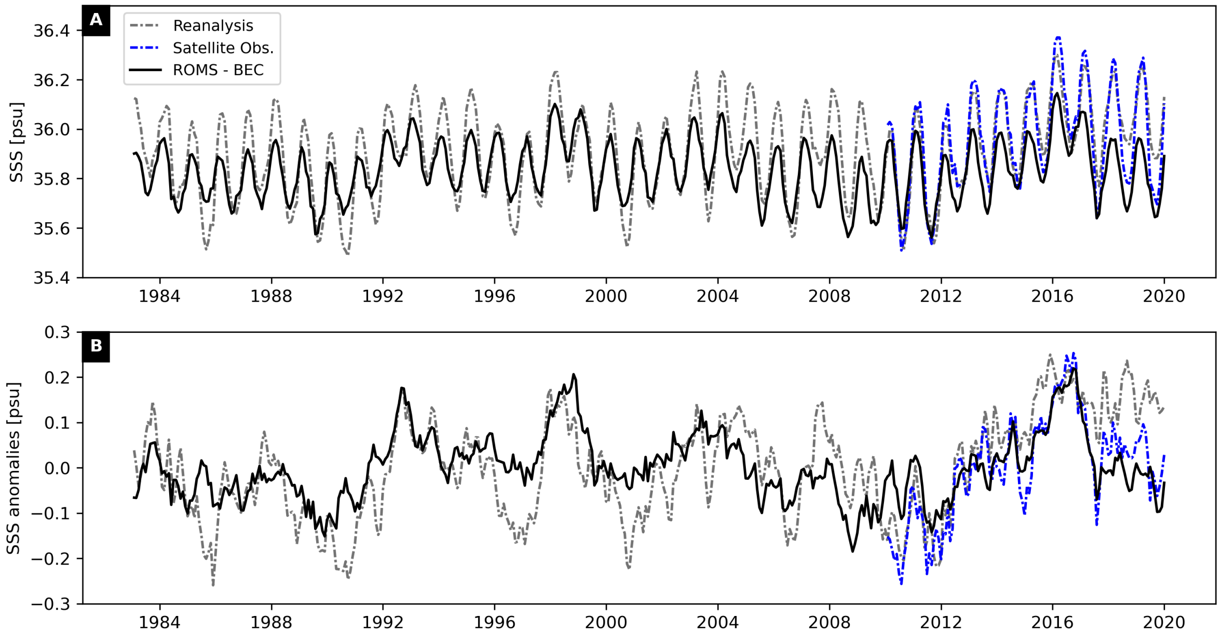

Figure C.2 The spatially averaged SSS in the study region of ROMS-BEC compared to reanalysis data and satellite observations (A). In panel B, interannual SSS anomalies are compared, which were computed by removing the grid cell specific seasonal cycle. The reanalysis data was taken from the Simple Ocean Data Assimilation (SODA 3.4.2). The satellite data available from 2010 onwards was taken from ESA CCI V2.31. Both datasets were bilinearly interpolated to the model grid.

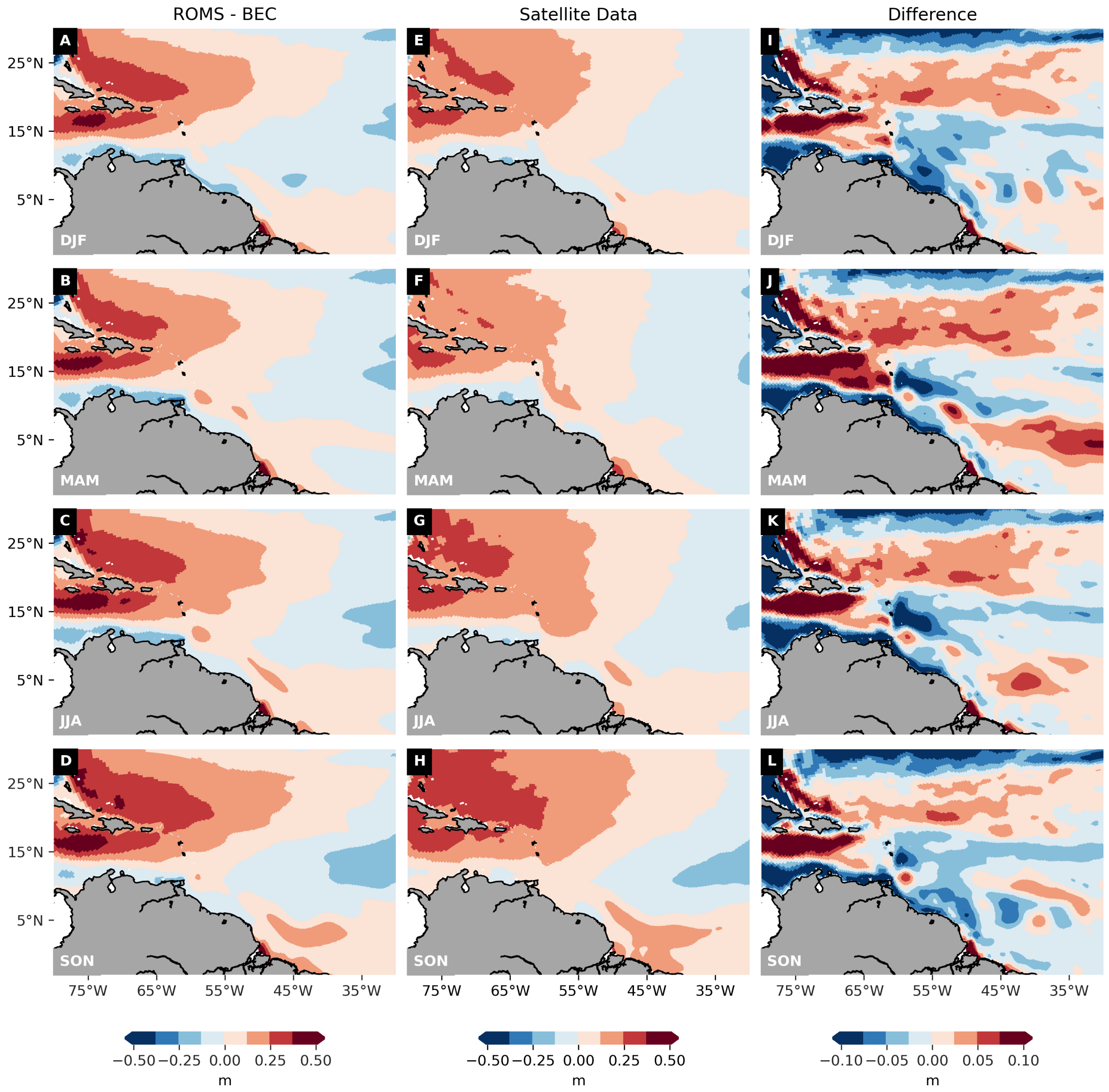

Figure C.3 The seasonal mean SSH simulated by ROMS-BEC (A-D) and the seasonal mean SSH of the monthly CMEMS product bilinearly interpolated to the ROMS-BEC grid (E-H) between 1993 and 2017, and the difference between the two (I-L). The SSH of both the model and the satellite measurements are absolute deviations of the SSH from the mean height of the tropical Atlantic (25° S - 25° N and 80° W - 0° W). Positive (negative) differences are an indication of higher (lower) SSH simulated by the model than measured by the satellites.

To validate whether the model reproduces the surface currents realistically, we compare the seasonal mean SSH of the model to that of satellite measurements. The model replicates the measured SSH well in the tropical Atlantic (Figure C.3). The simulated east-west gradient in SSH across the tropical Atlantic is concurring with observations. This implies that the model generally simulates geostrophic currents in the tropical Atlantic correctly. However, the model reproduces a too strong eastward flow between 5° N and 10° N, which is not coherent with satellite observations. Throughout all seasons, the largest differences in SSH arise in the Caribbean, where the model overestimates the SSH in the northern part and underestimates it in the southern part, caused by a too strong current and some unrealistic recirculation. This inaccuracy might be a numerical artefact, which is caused by the rapidly increasing model resolution in the Caribbean Sea (Figure 4.2). Outside of the study region, the model captures large scale circulation patterns, with the exception of the extension of the Gulf Stream. Since the Gulf Stream passes the Caribbean Sea, the inaccurate simulation of the SSH in the Caribbean Sea by ROMS-BEC might result in the extension of the Gulf Stream not being reproduced well. Moreover, there are deviations in SSH in the Southern Ocean, which may partly be explained by the coarse model resolution in this region.

The model succeeds in reproducing the mean surface fields of PO_4, Si, Fe, and NO_3, although a quantitative comparison is impeded by the sparsity of the measurements (Figure C.4). Throughout the whole year, surface PO_4 concentrations are highest around the river mouth and along the South American coast. Lowest PO_4 concentrations are modelled north of 15° N. During summer, elevated PO_4 concentrations are confined to the surroundings of the river mouth and the Brazilian shelf, whereas in winter, elevated PO_4 concentrations prevail greater distances away from the coast. The inflow of Amazon River water into the Atlantic Ocean results in a clear imprint on the surface Si concentrations in the Amazon River plume area. Generally, a negative gradient is modelled along the pathway of the Amazon River plume, with highest concentrations at the river mouth. During autumn, Si is transported eastwards by the NECC, which is in accordance with *in situ* measurements. NO_3 concentrations are low in the offshore plume of the Amazon River, which is coherent with observations (Araujo et al., 2017). Louchard et al. (2021) attributed the low NO_3 concentrations to benthic denitrification simulated to occur on the North Brazilian shelf. This NO_3 loss via denitrification leads to an excess of PO_4 and Si over NO_3, as reported by several studies (Subramaniam et al., 2008a; Goes et al., 2014; Weber et al., 2017; Araujo et al., 2017). These conditions favour N_2 fixing organisms (Subramaniam et al., 2008b). Surface NO_3 concentrations increase north of 15° N. Fe concentrations are highest around the mouth of the Amazon River and along the coast, similar to the PO_4 concentrations. During autumn, part of the Fe is transported eastwards by the NECC. However, the lack of *in situ* measurements of Fe in autumn impedes an observational verification.

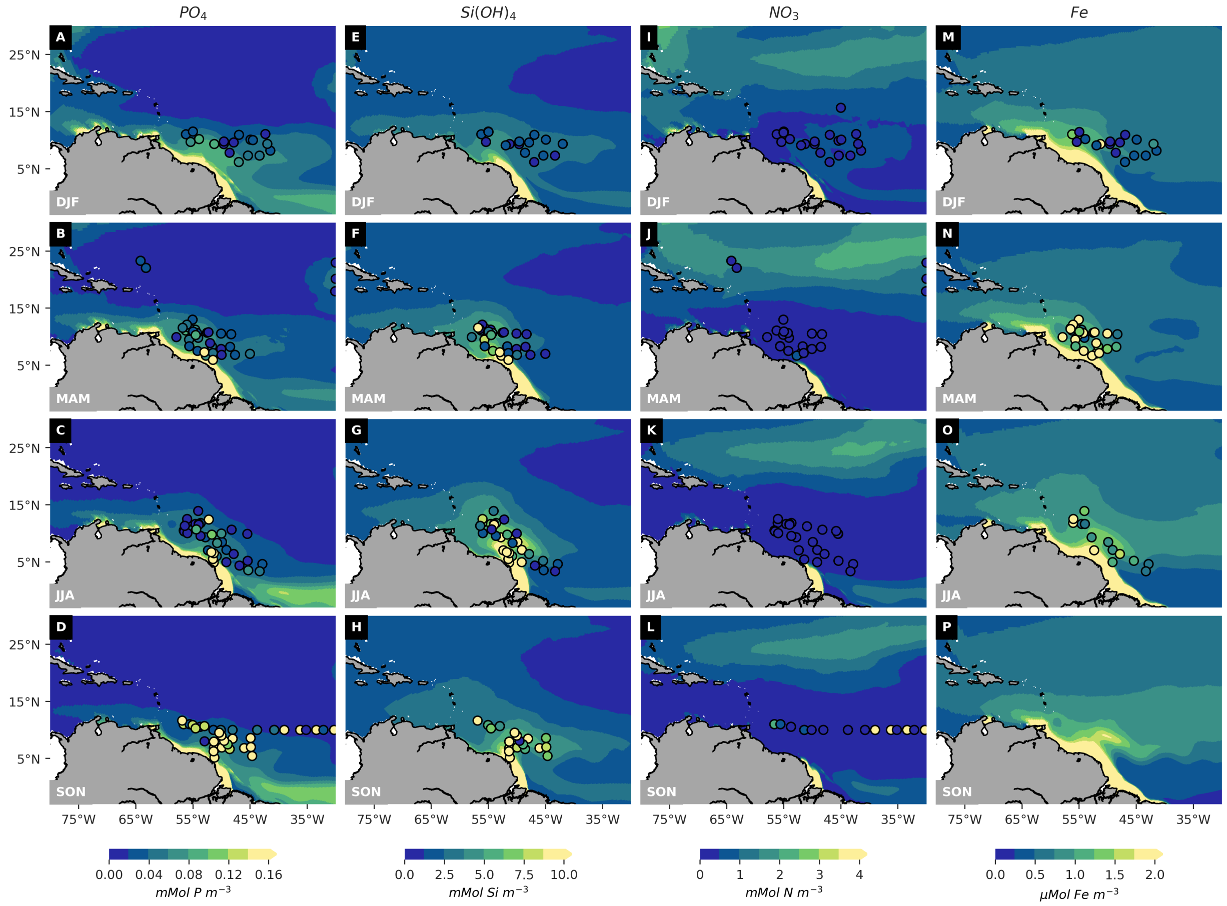
PO$_4$
Si(OH)$_4$
NO$_3$
Fe
A
E
I
M
B
F
J
N
C
G
K
O
D
H
L
P
DJF
MAM
JJA
SON
25°N
15°N
5°N
75°W
65°W
55°W
45°W
35°W
0.00
0.04
0.08
0.12
0.16
mMol P m^{-3}
0.0
2.5
5.0
7.5
10.0
mMol Si m^{-3}
0
1
2
3
4
mMol N m^{-3}
0.0
0.5
1.0
1.5
2.0
µMol Fe m^{-3}

Figure C.4 The seasonal mean of surface concentrations of PO$_4$ (A-D), Si(OH)$_4$ (E-H), NO$_3$ (I-L) and Fe (M-P) between 1983 and 2019. The filled circles correspond to *in situ* measurements collected during different cruises Langlois et al. (2008); Subramaniam et al. (2008a); Doherty et al. (2017a)

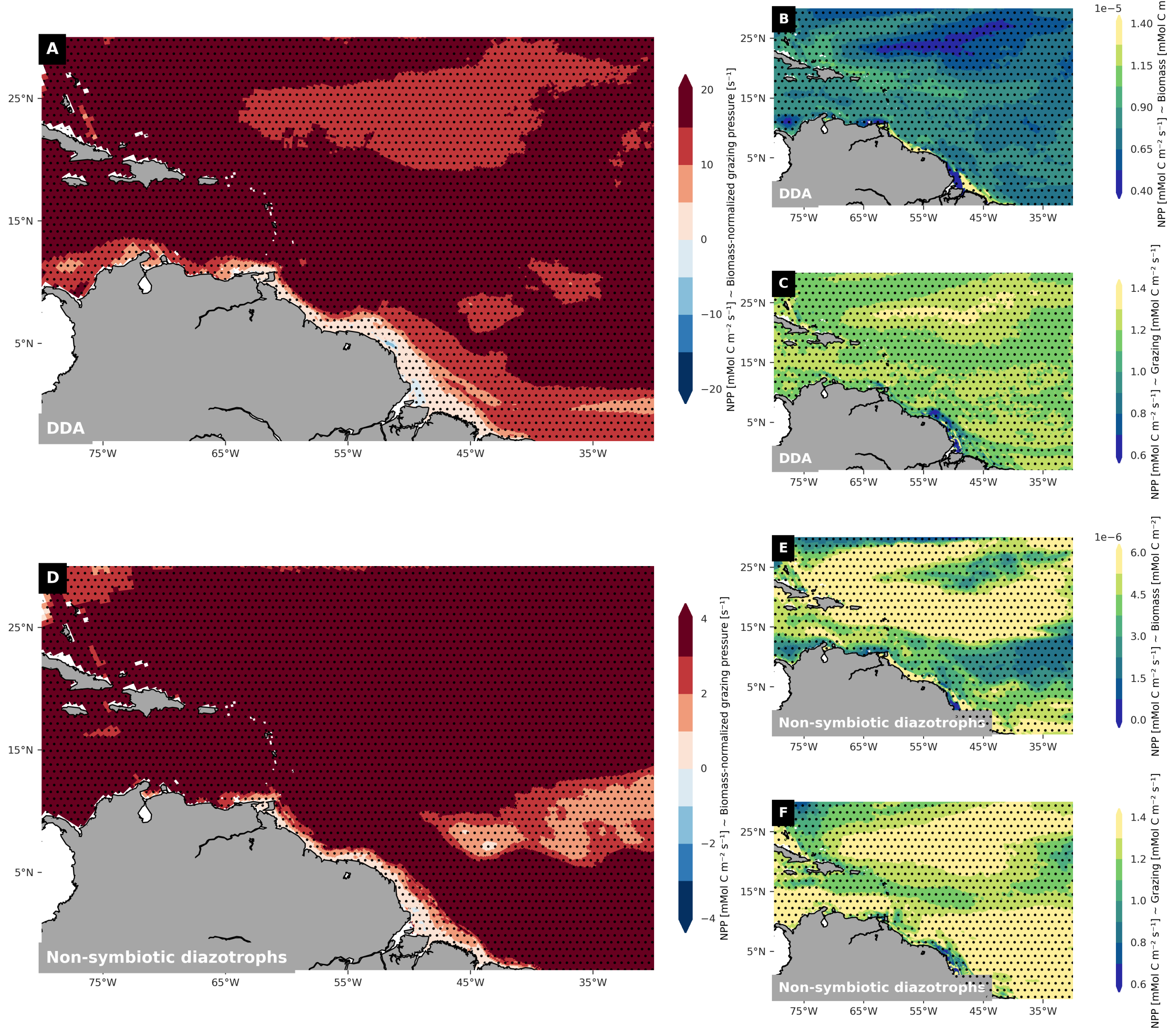
A
DDA
25°N
15°N
5°N
75°W
65°W
55°W
45°W
35°W
20
10
0
−10
−20
NPP [mMol C m⁻² s⁻¹] ~ Biomass-normalized grazing pressure [s⁻¹]
B
DDA
1e−5
1.40
1.15
0.90
0.65
0.40
NPP [mMol C m⁻² s⁻¹] ~ Biomass [mMol C m⁻²]
C
DDA
1.4
1.2
1.0
0.8
0.6
NPP [mMol C m⁻² s⁻¹] ~ Grazing [mMol C m⁻² s⁻¹]
D
Non-symbiotic diazotrophs
4
2
0
−2
−4
NPP [mMol C m⁻² s⁻¹] ~ Biomass-normalized grazing pressure [s⁻¹]
E
Non-symbiotic diazotrophs
1e−6
6.0
4.5
3.0
1.5
0.0
NPP [mMol C m⁻² s⁻¹] ~ Biomass [mMol C m⁻²]
F
Non-symbiotic diazotrophs
1.4
1.2
1.0
0.8
0.6
NPP [mMol C m⁻² s⁻¹] ~ Grazing [mMol C m⁻² s⁻¹]

Figure C.5 The slope of the linear regressions fitted for NPP anomalies as a function of biomass-normalized grazing pressure anomalies (A and D), biomass anomalies (B and E), and grazing anomalies (C and F). Panel A to C show the aforementioned slope for DDAs, without differentiating between symbiotic and non-symbiotic DDAs, panel D to F show the slope for non-symbiotic diazotrophs. Stippled area represents the region exceeding the 95% confidence level.

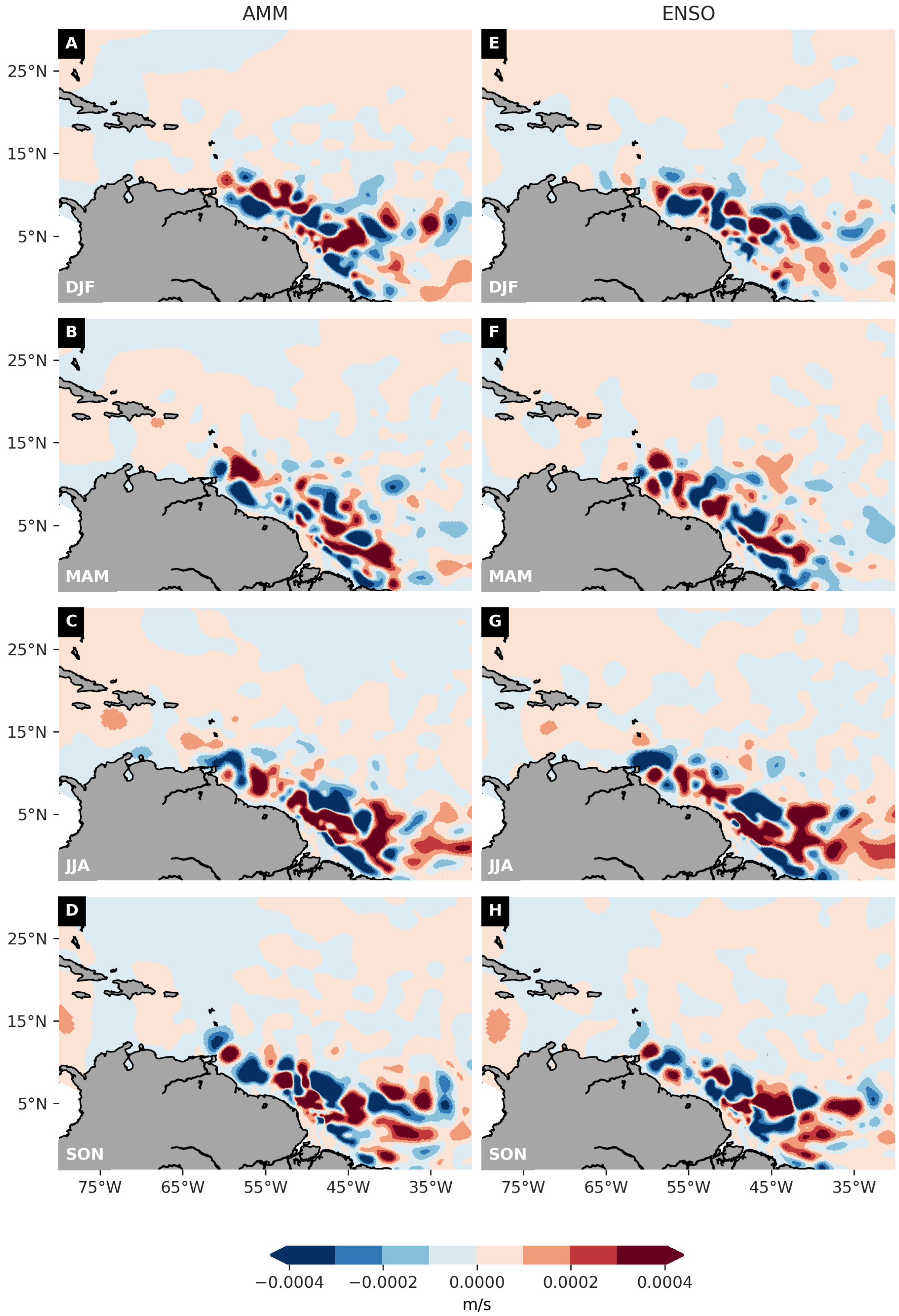
AMM
ENSO
A
B
C
D
E
F
G
H
DJF
MAM
JJA
SON
25°N
15°N
5°N
75°W
65°W
55°W
45°W
35°W
−0.0004
−0.0002
0.0000
0.0002
0.0004
m/s

Figure C.6 Vertical velocity anomalies integrated over the top 150m following AMM events (left column) and ENSO events (right column). The pattern is shown for positive AMM events and El Niño events, respectively. The pattern for negative AMM events and La Niña events corresponds to the inverse of the displayed pattern. The impact of the discharge variability is excluded, i.e., anomalies of the *VarAtm* simulation were binned.

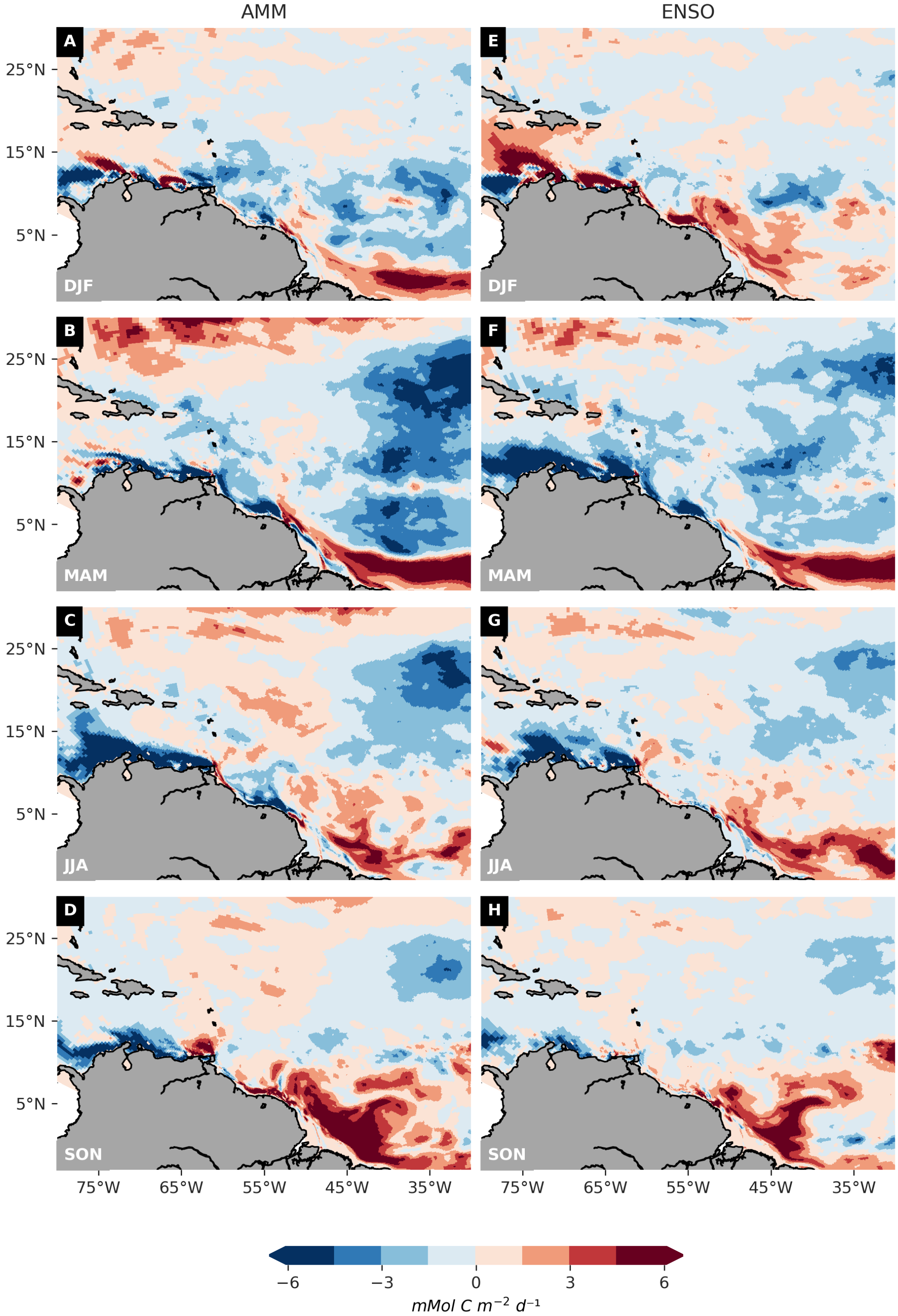
AMM
ENSO
A
B
C
D
E
F
G
H
DJF
MAM
JJA
SON
25°N
15°N
5°N
75°W
65°W
55°W
45°W
35°W
−6
−3
0
3
6
mMol C m^{-2} d^{-1}

Figure C.7 Depth-integrated non-diazotrophic NPP anomalies following AMM events (left column) and ENSO events (right column). The pattern is shown for positive AMM events and El Niño events, respectively. The pattern for negative AMM events and La Niña events corresponds to the inverse of the displayed pattern. The impact of the discharge variability is excluded, i.e., anomalies of the *VarAtm* simulation were binned.

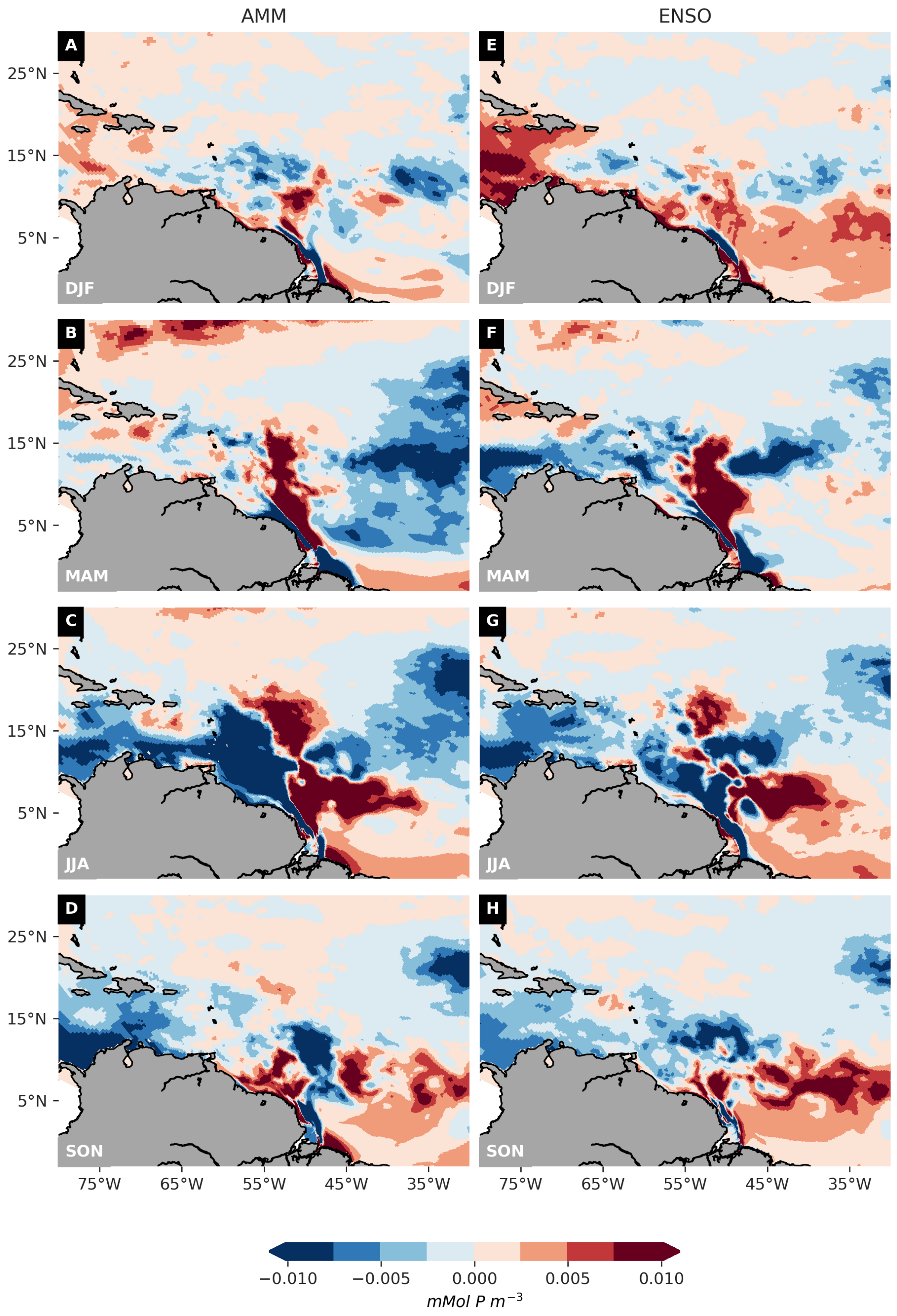
AMM
ENSO
A
B
C
D
E
F
G
H
DJF
MAM
JJA
SON
25°N
15°N
5°N
75°W
65°W
55°W
45°W
35°W
−0.010
−0.005
0.000
0.005
0.010
mMol P m^{-3}

Figure C.8 DOP anomalies following AMM events (left column) and ENSO events (right column). The pattern is shown for positive AMM events and El Niño events, respectively. The pattern for negative AMM events and La Niña events corresponds to the inverse of the displayed pattern. The impact of the discharge variability is excluded, i.e., anomalies of the *VarAtm* simulation were binned.

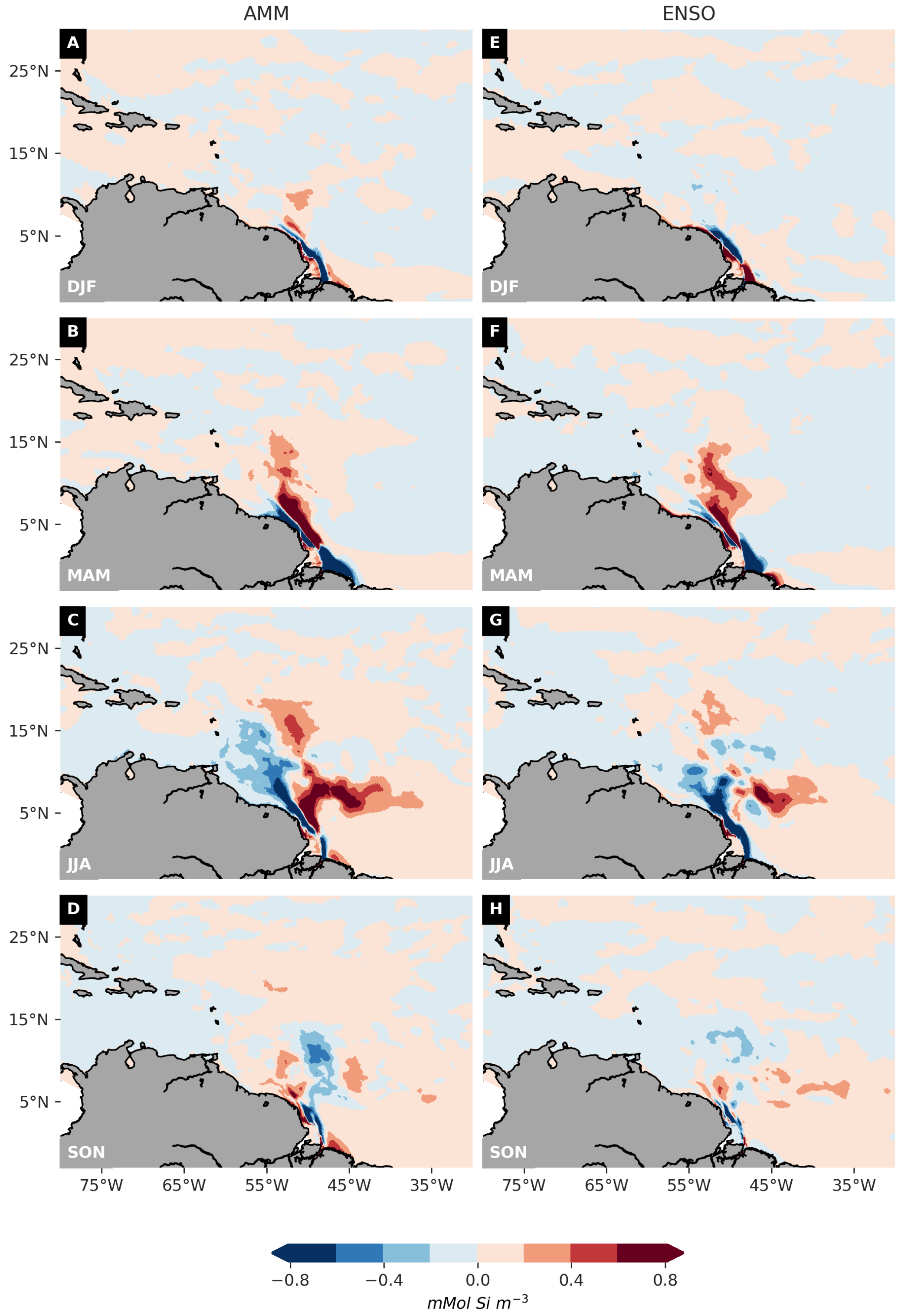
AMM
ENSO
A
B
C
D
E
F
G
H
DJF
MAM
JJA
SON
25°N
15°N
5°N
75°W
65°W
55°W
45°W
35°W
−0.8
−0.4
0.0
0.4
0.8
mMol Si m−3

Figure C.9 SiO_3 anomalies following AMM events (left column) and ENSO events (right column). The pattern is shown for positive AMM events and El Niño events, respectively. The pattern for negative AMM events and La Niña events corresponds to the inverse of the displayed pattern. The impact of the discharge variability is excluded, i.e., anomalies of the *VarAtm* simulation were binned.

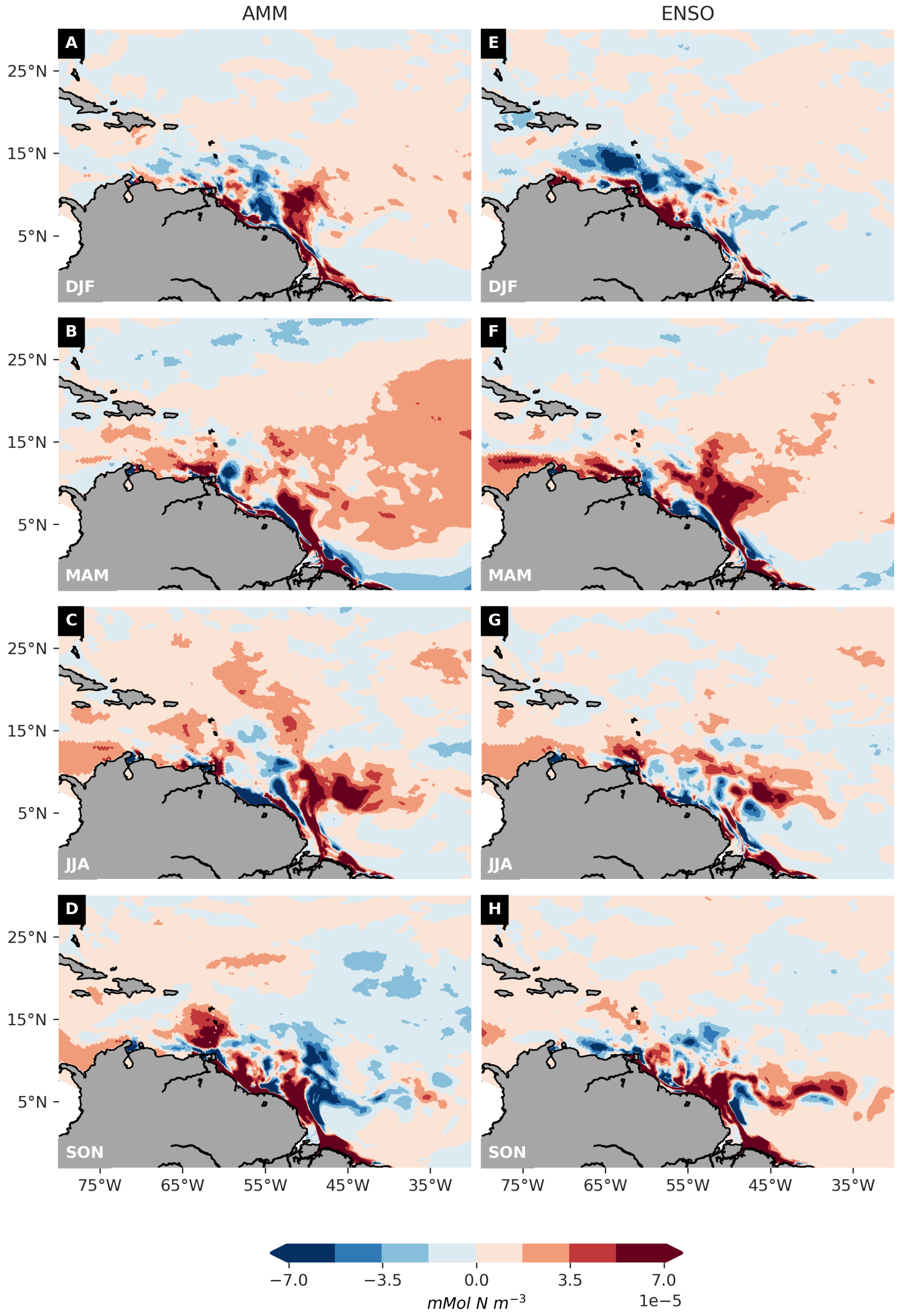
AMM
ENSO
A
B
C
D
E
F
G
H
DJF
MAM
JJA
SON
25°N
15°N
5°N
75°W
65°W
55°W
45°W
35°W
−7.0
−3.5
0.0
3.5
7.0
1e−5
mMol N m−3

Figure C.10 Fe anomalies following AMM events (left column) and ENSO events (right column). The pattern is shown for positive AMM events and El Niño events, respectively. The pattern for negative AMM events and La Niña events corresponds to the inverse of the displayed pattern. The impact of the discharge variability is excluded, i.e., anomalies of the *VarAtm* simulation were binned.

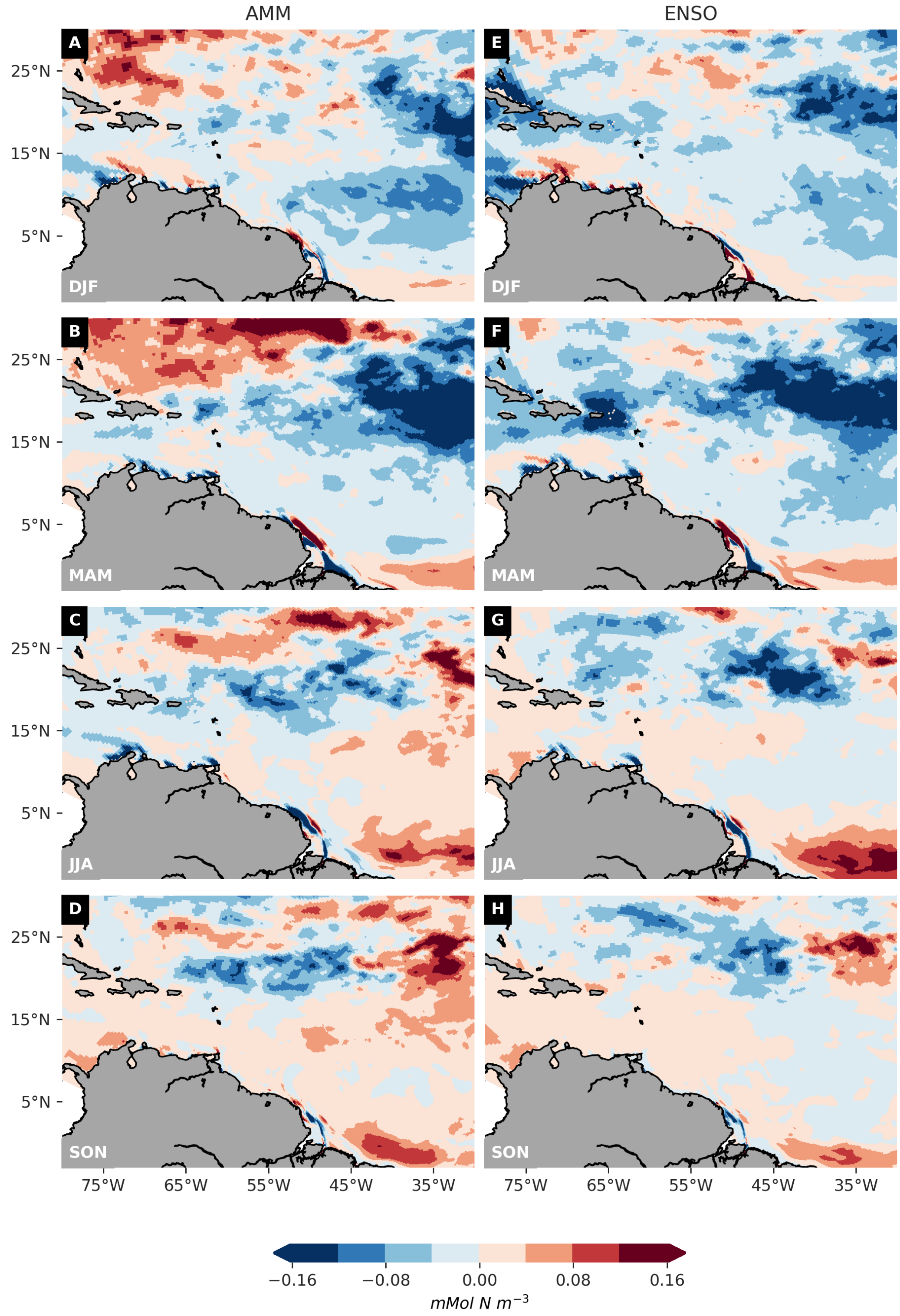
AMM
ENSO
A
B
C
D
E
F
G
H
DJF
MAM
JJA
SON
25°N
15°N
5°N
75°W
65°W
55°W
45°W
35°W
−0.16
−0.08
0.00
0.08
0.16
mMol N m−3

Figure C.11 NO_3 anomalies following AMM events (left column) and ENSO events (right column). The pattern is shown for positive AMM events and El Niño events, respectively. The pattern for negative AMM events and La Niña events corresponds to the inverse of the displayed pattern. The impact of the discharge variability is excluded, i.e., anomalies of the *VarAtm* simulation were binned.

List of Figures

1.1 Schematic of a generic river basin: its main components (rectangles) and the main processes delivering water, particulate matter and dissolved solutes to the river network (arrows). Adapted from Bouwman et al. (2013). 2

1.2 Global carbon budget for the LOAC combining both natural and human-induced emissions and uptake. Source: Global Carbon Budget (http://www.globalcarbonproject.org/). 3

1.3 Both pictures were retrieved from NASA Observatory and annoted by myself. a) Picture taken from space on August 19, 2008. The region shown here is located around 1000 km inland from the mouth of the river and is indicated by a red cross on figure 1.4. The yellowish color is the result of the setting sun glinting off the water and the smoke particles from forest fires in the air reflecting light. The sun's reflection reveals features that are normally dark and hard to see from space. Image provided by the ISS Crew Earth Observations experiment and the Image Science & Analysis Laboratory, Johnson Space Center. The arrow indicates the flow direction. b) Image of the Amazon from Lauren Dauphin, using the Moderate Resolution Imaging Spectroradiometer on Nasa's Terra satellite (July 29, 2020). 7

1.4 a) Geographical setting of the Amazon basin, major circulation features and sea surface salinity in the Western Tropical Atlantic. The Amazon stream network is the result of a topography-independent analysis method (Mayorga et al., 2012) (last access: October 14, 2021). The sea surface salinity corresponds to the annual average conditions simulated by ROMS (*All* simulation described in chapter 2). The lines locate the plume limits (salinity below 35.25) on average (solid line) and at its minimum and maximum extent (dashed line). b) Monthly average discharge of the Amazon (1979-2016) and discharge during 3 years of El Niño (1983, 1992, 1998) and La Niña (2000, 2008, 2011), data from HYBAM (last access: December 13, 2019). c) Monthly average surface of the plume with the same data as in a. d) Mean trade winds and North Brazilian Current velocity adapted from DeMaster and C. (2001) 10

1.5 Surface oceanic Chlorophyll a and land vegetation index as observed from space. Screenshot of one day conditions in spring 2006. The data originates from Sea-viewing Wide Field-of-view Sensor (SeaWiFS) Ocean Color Data and the visualization was made by NASA's Goddard Space Flight Center. 12

1.6 The climatological mean pCO_2 is reported for (a) a merged climatology based on two neural network-based pCO_2 products (Landschützer et al., 2020), (b) all available SOCATv5 data for the open ocean, covering the 1998-2015 period, and (c) all coastal SOCATv5 data. Adapted from Landschützer et al. (2020) 14

1.7 a) Field observations of depth-integrated N_2 fixation rates, map from Tang et al. (2019a). b) Simulated distribution of diazotrophs using a random forest machine learning technique, map from Tang et al. (2019b) 18

1.8 Images of *Trichodesmium* (left pannel) and *Hemiaulus inter Richelia* (right panel) retrieved during the Tara Ocean expedition using Environmental High-Content Fluorescent Microscopy (eHCFM). For both panels, each micrograph is displayed here and represents a) the cell surface, b) the cellular membranes, c) the chlorophyll autofluorescence, d) the bright field and e) the merged channels. Source: https://www.ebi.ac.uk/biostudies/S-BSST529 (last access: Oct21, 2021), compiled by Pierella Karlusich et al. (2021). 19

1.9 Schematics of 4 different types of N2-fixation modeling. In the equation, μ_{max} is maximum growth rate, K is the half saturation constant that drives the growth depending on the nutrient concentration. The red square highlights the model used in this thesis. Adapted from: Inomura et al. (2020) 22

2.1 Maps of the model domain and the analysis regions: (a) Model domain showing the modeled annual average sea surface salinity, and the telescopic grid at by every 12th grid line. The white quadrilateral indicates our region of study (0.5° S-24° N; 30°-70° W) (b) Map of the analysis region with the annual average offshore and non-plume areas colored in dark and light blue, respectively. Black arrows indicate the North Brazilian current (NBC) and the seasonally varying North Equatorial Counter Current (NECC). (c-f) Seasonal maps illustrating the evolution of the offshore plume and non-plume waters. See text for how we delineated the different areas. 31

2.2 Maps of the seasonal mean surface ocean circulation in the Western Tropical Atlantic. (a-b) Average surface flow (m s^{-1}) in spring and fall estimated from drifters (Lumpkin and Johnson, 2013) and (c-d) in ROMS-BEC (integrated in the first 15 meters to be comparable to drifter data). Solid and dashed lines mark the boundaries of the plume waters ($S<35.25$) in ROMS-BEC and in the satellite estimates (SMAP 2015-2017), respectively. The North Brazilian Current (NBC) and the North Equatorial Counter Current (NECC) are indicated in (b). 37

2.3 Maps of the seasonal mean surface chlorophyll concentration. (a-d) Average chlorophyll simulated by ROMS-BEC and (e-h) estimated from Sea-viewing Wide Field-of-view Sensor (SeaWiFS) Ocean Color Data (https://oceandata.sci.gsfc.nasa.gov/SeaWiFS/ data accessed and compiled in October 2012). (i-l) Difference between the two: SeaWiFs - ROMS-BEC. Winter is the mean of the months December through February, spring is March through May, summer is June through Augus and fall is September through November. 38

2.4 Maps of the seasonal mean surface concentrations of (a-d) NO_3, (e-h) PO_4 and (i-l) $Si(OH)_4$. The filled circles correspond to *in-situ* measurements collected during several different cruises (Langlois et al., 2008; Subramaniam et al., 2008a; Doherty et al., 2017a). Only surface measurements are plotted (depth $<$ 15 m). The seasons are defined as in Fig. 3. 39

2.5 Evaluation of the surface ocean pCO_2: Depicted in this violin plot are the observations (yellow) and the results from ROMS-BEC (green) for every season (a) over the shelf area (b) in the offshore plume waters and (c) in the non-plume waters. The shape of the plots corresponds to the kernel density, the solid line to the mean and the dashed line to the median. The dotted line is the mean atmospheric pCO_2 within the domain. Observations are derived from the ungridded Surface Ocean CO_2 Atlas (SOCAT version 2020). All data (1970-2019) have been normalized to the year 2006 and concatenated by region and seasons. The model was sampled at the same locations as the observations. The seasons are defined as in Fig. 3. 40

2.6 Maps illustrating the changes in annual mean net primary production (NPP) and export production (EP) in the western tropical Atlantic in response to the Amazon river input. (a) and (b) Differences between *All* and *NoNutr* simulations showing the overall impact of the Amazon on the ocean's biological pump. (c) and (d) Differences between the *NoSi* and *NoNutr* simulations showing the impact of all nutrients but $Si(OH)_4$. (e) and (f) Differences between *NoPO4* and *NoNutr* simulations showing the impact of all nutrients but PO_4. Gray lines mark the boundaries of the plume region (salinity < 35.25). 43

2.7 Relationship between the Amazon-river induced changes in NPP (integrated in the first 100 meters)(ΔNPP) and the changes in export production (at 100 m) (ΔEP) for (a) the entire WTA analysis region and (b) for the individual subregions. The regionally integrated changes in production and export were computed relative to the *NoNutr* case. Shown as crosses in (a) are the potential changes in NPP and export ($\Delta\text{NPP}^{i,pot}$ and $\Delta\text{EP}^{i,pot}$), estimated based on the nutrient delivery by the Amazon (see text for further details). The line corresponds to the average e-ratio of 0.16 across the whole WTA region in the *NoNutr* simulation. In (b) the shapes represent different zones in the region (see figure 2.1). The solid line and the dashed line indicate the e-ratio in the plume and non-plume regions, respectively, taken from the *All* simulation. In both (a) and (b), the colors correspond to the different simulations and will be used in subsequent figures. . . 45

2.8 Amazon-river induced relative changes in the *e*-ratio and in its multiplicative factors, i.e., the *p*- and *s*-ratios. Shown are the changes simulated for the *All* case and the factorial experiments relative to the *NoNutr* simulation. (a) Changes in the offshore plume waters. (b) Changes in the non-plume waters. (c) Average *p*-ratio in the plume waters as a function of the percentage of diatoms in the total phytoplankton biomass. See figure 2.1 for the region boundaries. 48

2.9 Phytoplankton community structure and pathways for the formation of detrital POC in the *NoNutr* simulation (top panel) and the *All* simulation (bottom panel). Indicated within each circle is the relative contribution in % of each PFT to the total phytoplankton biomass. Indicated by the arrows is the relative contribution of the different POC formation pathways associated with each PFT, given as % of total NPP in the top 100 m. The integrated POC fluxes are given separately for the plume and non-plume waters for the *NoNutr* and *All* simulations. 49

2.10 Maps of the changes in NPP integrated over the top 100 m in response to the nutrient addition by the Amazon river for the different Phytoplankton Functional Types, i.e., (a) the diatoms, (b) the diatom-diazotroph assemblage (DDA), (c) the small phytoplankton, and (d) the Trichodesmium groups. Shown are the differences between the *All* and the *NoNutr* simulations. 50

2.11 Annual mean rate of detrital POC production in the plume waters as a function of depth (a) in the *NoNutr* and *All* simulations, and (b) in all other factorial simulations. 51

2.12 Maps of the model simulated annual average air-sea CO_2 flux density in the WTA (mol C m^{-2} yr^{-1}). Shown are the fluxes (positive outgassing) from (a) the *NoAmazon* case, (b) the *All* case, (c) the *NoNutr* case and (d) the *NoSi* case, (e) the *NoP* case, (f) the *NoDOC* case. See table 2.1 for a description of the different cases. The solid lines in each panel correspond to the average plume limits. . . . 53

2.13 Quantification of the different factors contributing to the total effect of the Amazon River on the air-sea CO_2 fluxes in different regions. Pink corresponds to the effect of the river input of freshwater, DIC, and Alk. Green reflects the contribution of the biological pump, and brown represents the outgassing driven by the riverine input of terrestrial DOC The grey bar and associated values highlight the total net effect of the Amazon. 55

2.14 Schematic summarizing the impacts of the Amazon on the biological pump, the cycling of nutrients, and the air-sea CO_2 balance. The top yellow arrows represent the air-sea CO_2 fluxes. The solid one corresponds to the *All* simulation while the dashed one represents the *NoAmazon* case. The smaller arrows inside illustrate the effect of the different riverine inputs on the air-sea CO_2 exchange. The cogs represent the cycling of different nutrients with their riverine fraction indicated in green and the marine fraction in a different color: orange for NO_3, light green for PO_4, blue for POC and yellow for $Si(OH)_4$. All values are the climatological annual mean fluxes in Tg C yr^{-1}. 60

3.1 (a) Northward pathway with the annual average streamline field and annual average limit of the plume (salinity below 35.25). (b) Eastward pathway with the average streamline field and average limit of the plume (salinity below 35.25) during the retroflection (July to November). In both panels, the values in red display the distance in km from the starting point of the pathway as used in the subsequent figures. 68

3.2 (a) Annual mean of the depth-integrated N_2 fixation in the *AllNutr* simulation and contour lines of the percentage that is supported by DDAs. (b) Measurements of depth-integrated N_2 fixation compiled in the MAREDAT database (Luo et al., 2012). We selected only the data where both DDAs and *Trichodesmium* were measured. 70

3.3 Annual mean N_2 fixation integrated in the first 100 meters (a) in the *NoNutr* simulation, (b) in the *AllNutr* simulation, (d) in the *NoP* simulation and (f) in the *NoSi* simulation. (c),(e) and (g) display the difference in annual mean N_2 fixation between each factorial simulation and the *NoNutr* simulation. The grey line in all the maps display the average limits of the plume (salinity below 35.25) 72

3.4 Annual average depth-integrated N_2 fixation in the *AllNutr* simulation (thick solid line) and monthly average (fine lines) along (a) the northward pathway and (d) the eastward pathway. The shaded area corresponds to the temporal standard deviation. Annual average depth-integrated N_2 fixation in the *NoNutr*, *NoP* and *NoSi* simulations (thick solid line) and corresponding temporal standard deviation along (b) the northward pathway and (e) the eastward pathway. Average salinity and mean, minimum and maximum limit of plume (salinity below 35.25) along (c) the northward pathway and (f) the eastward pathway. 73

3.5 Annual average biomass of each PFT in (a-d) the *AllNutr* simulation and (e-h) the *NoNutr* simulation. (i-l) Differences between the 2 simulations in percentage. Note that the color scales differ for each PFT to better visualize the areas of highest biomass. The stippled regions on the maps of DDAs locates where DDAs are mostly fixing N_2 (fixing DDAs representing more than 20 % of the biomass). 75

3.6 Phytoplankton community structure defined as the percentage of total biomass annually averaged along the northward pathway in (a) the *NoNutr* simulation, (b) in the *AllNutr* simulation, (c) in the *NoP* simulation and (d) in the *NoSi* simulation. Below the fraction is displayed the average total NPP for each simulation. All computations have been made for the surface conditions. 75

3.7 Relative growth and grazing ratios along the northward pathway between DDAs and (a-b) diatoms, (c-d) small phytoplankton and (e-f) *Trichodesmium*. The left panels correspond to the *NoNutr* simulation and the right panels to the *AllNutr* simulation 78

3.8 Growth rates of each PFT and biomass-normalized grazing rates on each PFT in (a & c) the *NoNutr* simulation and in (b & d) the *AllNutr* simulation 79

3.9 Map of the most limiting nutrient for each PFT in (a) *NoNutr* simulation and (b) in the *AllNutr* simulation 80

4.1 The measured discharge (black) and the discharge scenario excluding interannual variability (gray) (A). The discharge anomalies, computed as the difference between the measured discharge and the discharge scenario excluding interannual variability, the Oceanic Niño Index (ONI) (turquoise) and the Atlantic Meridional Mode (AMM) Index (brown) (B). Brown colorbars represent positive AMM events (dark) and negative AMM events (light), turquoise colorbars depict El Niño phases (dark) and La Niña phases (light). Monthly mean concentration of PO_4 and Dissolved Organic Phosphorus (DOP) (C), $Si(OH)_4$ (D), Dissolved Inorganic Nitrogen (DIN) and Dissolved Organic Nitrogen (DON) (E), and Fe (F) characterizing the Amazon River discharge based on (Araujo et al., 2014). 91

4.2 Map of the model domain with the averaged N_2 fixation rate in color, and with the telescopic grid depicted by every 10^{th} grid point. The white frame encloses the study region (0.5° S - 25° N; 30° W - 80° W) with the dashed line dividing the study region in a southern and northern part at 13° N. The red dot indicates the Amazon River outflow and the black dots indicate the location of the discharge measurement stations. 93

4.3 The spatially averaged SST in the study region of ROMS-BEC compared to satellite observations (A). In panel B, interannual SST anomalies are compared, which were computed by removing the modelled and observational climatology of the modelled and observational data, respectively. The satellite data was provided by the National Oceanic and Atmospheric Administration (NOAA SST V2 High Resolution) and was bilinearly interpolated to the model grid for comparison. . . 95

4.4 The mean SSS between 1983 and 2019 in colour and the modelled (black) and measured (gray) SSS at four PIRATA buoy sites. The contour line depicts the plume extent based on a SSS threshold of 35.25 psu. 96

4.5 The plume size determined based on a SSS threshold value of 35.25 psu is shown in panel A. In panel B, the interannual plume size anomalies are compared, which were computed by removing the the modelled and observational monthly mean plume size. The reanalysis data was taken from the Simple Ocean Data Assimilation (SODA 3.4.2). The satellite data, available from 2010 onwards, was taken from ESA CCI V2.31. Both datasets were bilinearly interpolated to the model grid to determine the plume size. 97

4.6 The mean of the depth-integrated N_2 fixation rate for the time period between 1983 and 2019 is shown in colors, the filled circles correspond to integrated *in situ* measurements (depth > 80m) (Luo et al., 2012) and the contour lines depict the fraction of N fixed by DDAs, whereas the remaining fraction is fixed by non-symbiotic diazotrophs. 99

4.7 The total (A), discharge variability induced (B), and climate variability induced (C) spatially averaged N_2 fixation rate variability. The gray line in panel B depicts discharge anomalies. In panel C, brown bars depict positive (dark) and negative (light) AMM events, whereas turquoise bars depict El Niño (dark) and La Niña (light) events. 101

4.8 The mean absolute deviation of the total (A), discharge variability induced (B), and climate variability induced (C) variability in theN_2 fixation rate. Contour lines depict the average N_2 fixation rate. 102

4.9 The slope between the yearly averaged N_2 fixation rate anomalies attributed to the discharge variability and the yearly averaged discharge anomalies. Stippled area represents the region exceeding the 95% confidence level. The contour line depicts the area where the SSS is influenced by discharge variability (compare to Figure 4.13D). It is defined as the area where the slope between SSS variability associated with discharge variability and discharge anomalies is smaller than -1.5 $\cdot 10^{-6}$ and significant on a 95% confidence level, including data south of 20° N and west of 45° W. 103

4.10 The N_2 fixation rate anomalies following AMM events (left column) and ENSO events (right column). The pattern is shown for positive AMM events and El Niño phases, respectively. The pattern for negative AMM events and La Niña phases corresponds to the inverse of the displayed pattern. The impact of the discharge variability is excluded, i.e., anomalies of the *VarAtm* were binned. 104

4.11 The most limiting nutrient for DDAs (A), non-symbiotic diazotrophs (B), diatoms (C), and small phytoplankton (D). 105

4.12 The slope of the linear regression fitted between N_2 fixation rate anomalies and surface nutrient anomalies (A-E) and the diazotrophic NPP anomalies and non-diazotrophic NPP anomalies. Anomalies are derived from the *VarAll* simulation. The slopes of the linear regression are scales according to an extended Si:N:P:Fe Redfield ratio amounting to 80:16:1:0.007. The contour lines depict the surface nutrient concentration in the mean state (A-E) and the fraction of NPP attributed to diazotrophs in the mean state (F). Stippled area represents the region exceeding the 95% confidence level. 106

4.13 The slope of the linear regression fitted for the yearly averaged discharge anomalies as the explanatory variable and averaged P anomalies (A), NO_3 anomalies (B), $Si(OH)_4$ (C) anomalies, and SSS anomalies (D) as the dependent variable. The slope are scaled according to a Si:N:P ratio of 80:10:1. Stippled area represents the region exceeding the 95% confidence level. 108

4.14 PO_4 anomalies following AMM events (left column) and ENSO events (right column). The pattern is shown for positive AMM events and El Niño events, respectively. The pattern for negative AMM events and La Niña events corresponds to the inverse of the displayed pattern. The impact of the discharge variability is excluded, i.e., anomalies of the *VarAtm* simulation were binned. 111

4.15 MLD anomalies following AMM events (left column) and ENSO events (right column). The pattern is shown for positive AMM events and El Niño events, respectively. The pattern for negative AMM events and La Niña events corresponds to the inverse of the displayed pattern. The impact of the discharge variability is excluded, i.e., anomalies of the *VarAtm* simulation were binned. 112

4.16 Processes resulting in interannual N_2 fixation rate variability in the WTA. In colour, the N_2 fixation rate anomalies computed as the MAD from the VarAll simulation are shown. The pie charts depict the PO_4:DOP ratio and the total P concentration in the Amazon River discharge, at the surface and at 100m depth, averaged over the whole study region. 115

A.1 DDAs biomass as a function of reported nitrate concentration. Observations come from the database established by Luo et al. (2012) (N=523) 131

A.2 Annual average sea surface height in (a) Aviso (1993-2012) and in (b) ROMS-BEC. Aviso products were processed by SSALTO/DUACS and distributed by AVISO+ (https://www.aviso.altimetry.fr) with support from CNES. 134

A.3 Maps of the annual mean surface ocean circulation in the Atlantic Ocean. (a) Average surface flow (m s^{-1}) estimated from drifters (Lumpkin et al. 2010) and (b) in ROMS-BEC (integrated in the first 15 meters to be comparable to drifter data). 134

A.4 annual average surface chlorophyll in (a) Globcolour 1998-2015 (Maritorena et al. 2010) and in (b) ROMS-BEC 135

A.5 Average integrated total N_2 fixation in ROMS-BEC, compared to integrated total N_2 fixation reported in Luo et al. (2012) (dots) 136

A.6 Annual average pCO_2 in (a) observations and in (b) ROMS-BEC. Observations are derived from the Surface Ocean CO_2 Atlas (SOCAT version 2020). All data (1970-2019) have been normalized to the year 2006. 136

B.1 Phytoplankton community structure defined as the percentage of total biomass annually averaged along the northward pathway in (a) the *NoNutr* simulation, (b) in the *AllNutr* simulation, (c) in the *NoP* simulation and (d) in the *NoSi* simulation. Below the fraction is displayed the average total NPP for each simulation. The total biomass was integrated over the first 100 meters. 137

B.2 Relative growth and grazing ratios along the eastward pathway between DDAs and (a-b) diatoms, (c-d) small phytoplankton and (e-f) *Trichodesmium*. The left panels correspond to the *NoNutr* simulation and the right panels to the *AllNutr* simulation 138

B.3 Average phytoplankton biomass versus zooplankton biomass in the *AllNutr* simulation, average over the northward pathway 139

C.1 The seasonal mean SSS simulated by ROMS-BEC (A-D) and the seasonal mean of the ESA CCI V2.31 SSS product bilinearly interpolated to the model grid (E-H) between 2010 and 2019. The difference was computed by subtracting the seasonally averaged SSS of the satellite data from the seasonally averaged SSS of the model output (I-L). Hence, positive (negative) differences are an indication of higher (lower) SSS simulated by the model than measured by the satellite. . . 142

C.2 The spatially averaged SSS in the study region of ROMS-BEC compared to reanalysis data and satellite observations (A). In panel B, interannual SSS anomalies are compared, which were computed by removing the grid cell specific seasonal cycle. The reanalysis data was taken from the Simple Ocean Data Assimilation (SODA 3.4.2). The satellite data available from 2010 onwards was taken from ESA CCI V2.31. Both datasets were bilinearly interpolated to the model grid. 144

C.3 The seasonal mean SSH simulated by ROMS-BEC (A-D) and the seasonal mean SSH of the monthly CMEMS product bilinearly interpolated to the ROMS-BEC grid (E-H) between 1993 and 2017, and the difference between the two (I-L). The SSH of both the model and the satellite measurements are absolute deviations of the SSH from the mean height of the tropical Atlantic (25° S - 25° N and 80° W - 0° W). Positive (negative) differences are an indication of higher (lower) SSH simulated by the model than measured by the satellites. 145

C.4 The seasonal mean of surface concentrations of PO_4 (A-D), $Si(OH)_4$ (E-H), NO_3 (I-L) and Fe (M-P) between 1983 and 2019. The filled circles correspond to *in situ* measurements collected during different cruises Langlois et al. (2008); Subramaniam et al. (2008a); Doherty et al. (2017a) 147

C.5 The slope of the linear regressions fitted for NPP anomalies as a function of biomass-normalized grazing pressure anomalies (A and D), biomass anomalies (B and E), and grazing anomalies (C and F). Panel A to C show the aforementioned slope for DDAs, without differentiating between symbiotic and non-symbiotic DDAs, panel D to F show the slope for non-symbiotic diazotrophs. Stippled area represents the region exceeding the 95% confidence level. 148

C.6 Vertical velocity anomalies integrated over the top 150m following AMM events (left column) and ENSO events (right column). The pattern is shown for positive AMM events and El Niño events, respectively. The pattern for negative AMM events and La Niña events corresponds to the inverse of the displayed pattern. The impact of the discharge variability is excluded, i.e., anomalies of the *VarAtm* simulation were binned. 149

C.7 Depth-integrated non-diazotrophic NPP anomalies following AMM events (left column) and ENSO events (right column). The pattern is shown for positive AMM events and El Niño events, respectively. The pattern for negative AMM events and La Niña events corresponds to the inverse of the displayed pattern. The impact of the discharge variability is excluded, i.e., anomalies of the *VarAtm* simulation were binned. 150

C.8 DOP anomalies following AMM events (left column) and ENSO events (right column). The pattern is shown for positive AMM events and El Niño events, respectively. The pattern for negative AMM events and La Niña events corresponds to the inverse of the displayed pattern. The impact of the discharge variability is excluded, i.e., anomalies of the *VarAtm* simulation were binned. 151

C.9 SiO_3 anomalies following AMM events (left column) and ENSO events (right column). The pattern is shown for positive AMM events and El Niño events, respectively. The pattern for negative AMM events and La Niña events corresponds to the inverse of the displayed pattern. The impact of the discharge variability is excluded, i.e., anomalies of the *VarAtm* simulation were binned. 152

C.10 Fe anomalies following AMM events (left column) and ENSO events (right column). The pattern is shown for positive AMM events and El Niño events, respectively. The pattern for negative AMM events and La Niña events corresponds to the inverse of the displayed pattern. The impact of the discharge variability is excluded, i.e., anomalies of the *VarAtm* simulation were binned. 153

C.11 NO_3 anomalies following AMM events (left column) and ENSO events (right column). The pattern is shown for positive AMM events and El Niño events, respectively. The pattern for negative AMM events and La Niña events corresponds to the inverse of the displayed pattern. The impact of the discharge variability is excluded, i.e., anomalies of the *VarAtm* simulation were binned. 154

List of Tables

1.1 Estimates of net air-sea CO_2 flux within the plume waters 16

1.2 Recent global estimates of N_2 fixation 17

2.1 Summary of the ROMS-BEC simulations performed for this study. The concentrations of the Amazon river input and the resulting loads are given in table A.3 . 36

2.2 Mean NPP and EP in the *NoAmazon NoNutr* cases and the changes (δ NPP, δ EP) relative to these cases for the different sub-regions and the total across the WTA analysis region (see the Methods section for the definition of these sub-regions). Listed are the results for the standard case *All* and the different factorial simulations. The absolute values for all factorial simulations can be found in Table A.5. 42

2.3 Annual mean sources of inorganic nitrogen and phosphorus in the *NoNutr* and *All* simulations integrated over the top 100m and the WTA. 46

2.4 Annually integrated CO_2 fluxes. Negative values correspond to an uptake of CO_2 by the ocean and positive values correspond to outgassing. The boundaries for the sub-regions are taken from the *All* simulation and shown in figure 2.1. 54

3.1 Comparison between the model and observations in terms of Primary Production (PP) and N_2-fixation rates in different types of waters 71

3.2 Total N_2 fixation integrated over the first 100 meters 73

4.1 Overview of the ROMS-BEC simulations performed for this study. 93

4.2 The MAD of the spatially averaged N_2 fixation rate variability. The MAD of the N_2 fixation rate variability was computed for the whole study region and the southern and northern part separately denoted in italics. 100

A.1 List of relevant BEC parameters used for the phytoplankton uptake and losses . . 132

A.2 List of relevant BEC parameters used for the cycling of DOM 132

A.3 Physical and biogeochemical properties of the Amazon River influx in our study. Monthly mean and weighted annual mean. All estimates originate from Araujo et al. (2014), except the values in gray (see main text for a description of how these values were determined). 133

A.4 Total annual atmospheric deposition of nutrients over the WTA 134

A.5 NPP and EP in the offshore Plume and Non-plume sub-regions (see the Methods section for the definition of these sub-regions) 135

A.6 Anomalous fluxes and related uptake efficiencies as defined by Jin et al. (2008), neglecting the DOC flux: $e_{uptake} = \frac{\int_A \int_t \Delta\mathrm{CO}_{2\text{air-sea}}}{\int_A \int_t \Delta EP}$ where $\Delta\mathrm{CO}_{2\text{air-sea}}$ is the change of atmosphere-ocean CO_2 exchange between the case under investigation and the *NoAmazon* case, ΔEP is the corresponding change in export production at 100 meters, and where we integrated all fluxes over the whole region of study. A positive anomaly means an anomalous uptake. 135

Bibliography

Alin, S. R., de Fátima F. L. Rasera, M., Salimon, C. I., Richey, J. E., Holtgrieve, G. W., Krusche, A. V., and Snidvongs, A. (2011). Physical controls on carbon dioxide transfer velocity and flux in low-gradient river systems and implications for regional carbon budgets. *Journal of Geophysical Research: Biogeosciences*, 116(G1). doi:https://doi.org/10.1029/2010JG001398.

Allen, G. H. and Pavelsky, T. M. (2018). Global extent of rivers and streams. *Science*, 361(6402):585–588. doi:10.1126/science.aat0636.

Aller, R. C. and Blair, N. E. (2006). Carbon remineralization in the Amazon-Guianas tropical mobile mudbelt: A sedimentary incinerator. *Continental Shelf Research*, 26(17-18):2241–2259. doi:10.1016/j.csr.2006.07.016.

Aller, R. C., Blair, N. E., Xia, Q., and Rude, P. D. (1996). Remineralization rates, recycling, and storage of carbon in Amazon shelf sediments. *Continental Shelf Research*, 16(5-6):753–786. doi:10.1016/0278-4343(95)00046-1.

Almeida, R. M., Shi, Q., Gomes-Selman, J. M., Wu, X., Xue, Y., Angarita, H., Barros, N., Forsberg, B. R., García-Villacorta, R., Hamilton, S. K., Melack, J. M., Montoya, M., Perez, G., Sethi, S. A., Gomes, C. P., and Flecker, A. S. (2019). Reducing greenhouse gas emissions of amazon hydropower with strategic dam planning. *Nature Communications*, 10(1):4281. doi:10.1038/s41467-019-12179-5.

Almeida, R. M., Tranvik, L., Huszar, V. L., Sobek, S., Mendonça, R., Barros, N., Boemer, G., Arantes, J. D., and Roland, F. (2015). Phosphorus transport by the largest amazon tributary (madeira river, brazil) and its sensitivity to precipitation and damming. *Inland Waters*, 5:275–282. doi:10.5268/IW-5.3.815.

Anderson, L. A. and Sarmiento, J. L. (1994). Redfield ratios of remineralization determined by nutrient data analysis. *Global Biogeochemical Cycles*, 8(1):65–80. doi:10.1029/93GB03318.

Araujo, M., Noriega, C., Hounsou-gbo, G. A., Veleda, D., Araujo, J., Bruto, L., Feitosa, F., Flores-Montes, M., Lefèvre, N., Melo, P., Otsuka, A., Travassos, K., Schwamborn, R., and Neumann-Leitão, S. (2017). A Synoptic Assessment of the Amazon River-Ocean Continuum during Boreal Autumn: From Physics to Plankton Communities and Carbon Flux. *Frontiers in Microbiology*, 8(JUL):1–18. doi:10.3389/fmicb.2017.01358.

Araujo, M., Noriega, C., and Lefèvre, N. (2014). Nutrients and carbon fluxes in the estuaries of major rivers flowing into the tropical atlantic. *Frontiers in Marine Science*. doi:10.3389/fmars.2014.00010.

Armstrong, R. A., Lee, C., Hedges, J. I., Honjo, S., and Wakeham, S. G. (2001). A new, mechanistic model for organic carbon fluxes in the ocean based on the quantitative association of

POC with ballast minerals. *Deep-Sea Research Part II: Topical Studies in Oceanography*, 49(1-3):219–236. doi:10.1016/S0967-0645(01)00101-1.

Aumont, O., Ethé, C., Tagliabue, A., Bopp, L., and Gehlen, M. (2015). Pisces-v2: an ocean biogeochemical model for carbon and ecosystem studies. *Geoscientific Model Development*, 8(8):2465–2513. doi:10.5194/gmd-8-2465-2015.

Baker, J. C. A., Garcia-Carreras, L., Buermann, W., de Souza, D. C., Marsham, J. H., Kubota, P. Y., Gloor, M., Coelho, C. A. S., and Spracklen, D. V. (2021). Robust amazon precipitation projections in climate models that capture realistic land–atmosphere interactions. *Environmental Research Letters*, 16:074002. doi:10.1088/1748-9326/abfb2e.

Barbier, E. B., Hacker, S. D., Kennedy, C., Koch, E. W., Stier, A. C., and Silliman, B. R. (2011). The value of estuarine and coastal ecosystem services. *Ecological Monographs*, 81(2):169–193. doi:https://doi.org/10.1890/10-1510.1.

Battin, J. and Luyssaert, S.and Kaplan, L. (2009). The boundless carbon cycle. *Nature Geoscience*, 2:598–600. doi:10.1038/ngeo618.

Benavides, M., Berthelot, H., Duhamel, S., Raimbault, P., and Bonnet, S. (2017). Dissolved organic matter uptake by Trichodesmium in the Southwest Pacific. *Scientific Reports*, 7(1):41315. doi:10.1038/srep41315.

Benavides, M. and Voss, M. (2015). Five decades of N2 fixation research in the North Atlantic Ocean. *Frontiers in Marine Science*, 2(June):1–20. doi:10.3389/fmars.2015.00040.

Bergkvist, J., Thor, P., Jakobsen, H. H., Wängberg, S. Å., and Selander, E. (2012). Grazer-induced chain length plasticity reduces grazing risk in a marine diatom. *Limnology and Oceanography*, 57(1):318–324. doi:10.4319/lo.2012.57.1.0318.

Bernard, C. Y., Dürr, H. H., Heinze, C., Segschneider, J., and Maier-Reimer, E. (2011). Contribution of riverine nutrients to the silicon biogeochemistry of the global ocean – a model study. *Biogeosciences*, 8(3):551–564. doi:10.5194/bg-8-551-2011.

Berner, R. A. and Rao, J. L. (1994). Phosphorus in sediments of the Amazon River and estuary: Implications for the global flux of phosphorus to the sea. *Geochimica et Cosmochimica Acta*, 58(10):2333–2339. doi:10.1016/0016-7037(94)90014-0.

Berthelot, H., Bonnet, S., Grosso, O., Cornet, V., and Barani, A. (2016). Transfer of diazotroph-derived nitrogen towards non-diazotrophic planktonic communities: a comparative study between &lt;i&gt;Trichodesmium&lt;/i&gt; &lt;i&gt;erythraeum&lt;/i&gt;, &lt;i&gt;Crocosphaera watsonii&amp. *Biogeosciences*, 13(13):4005–4021. doi:10.5194/bg-13-4005-2016.

Best, J. (2019). Anthropogenic stresses on the world's big rivers. *Nature Geoscience*, 12(1):7–21. doi:10.1038/s41561-018-0262-x.

Beusen, A. (2014). *Transport of nutrients from land to sea: Global modeling approaches and uncertainty analyses*. Number 58. Dept. of Earth Sciences, Utrech University.

Beusen, A. H. W., Bouwman, A. F., Van Beek, L. P. H., Mogollón, J. M., and Middelburg, J. J. (2016). Global riverine N and P transport to ocean increased during the 20th century despite increased retention along the aquatic continuum. *Biogeosciences*, 13(8):2441–2451. doi:10.5194/bg-13-2441-2016.

Bianchi, T. S. (2021). *The evolution of biogeochemistry: revisited*, volume 154. Springer International Publishing. doi:10.1007/s10533-020-00708-0.

Bianchi, T. S., Thornton, D. C., Yvon-Lewis, S. A., King, G. M., Eglinton, T. I., Shields, M. R., Ward, N. D., and Curtis, J. (2015). Positive priming of terrestrially derived dissolved organic matter in a freshwater microcosm system. *Geophysical Research Letters*, 42:5460–5467. doi:10.1002/2015GL064765.

Billen, G., Lancelot, C., Meybeck, M., Matoura, R., Martin, J., and Wollast, R. (1991). Ocean margin processes in global change. *N, P, and Si retention along the aquatic continuum from land to ocean*, pages 19–44.

Bindoff, N., Cheung, W., Kairo, J., Arístegui, J., Guinder, V., Hallberg, R., Hilmi, N., Jiao, N., Karim, L., Levin, M., O'Donoghue, S., Purca Cuicapusa, S. R., Rinkevich, B., Suga, T., Tagliabue, A., and Williamson, P. (2019). Changing Ocean, Marine Ecosystems, and Dependent Communities. In Pörtner, H.-O., Roberts, D. C., Masson-Delmotte, V., Zhai, P., Tignor, M., Poloczanska, E., Mintenbeck, K., Alegría, A., Nicolai, M., Okem, A., Petzold, J., Rama, B., and Weyer, N., editors, *IPCC Special Report on the Ocean and Cryosphere in a Changing Climate*. In press.

Bird, M., Robinson, R., Win Oo, N., Maung Aye, M., Lu, X., Higgitt, D., Swe, A., Tun, T., Lhaing Win, S., Sandar Aye, K., Mi Mi Win, K., and Hoey, T. (2008). A preliminary estimate of organic carbon transport by the ayeyarwady (irrawaddy) and thanlwin (salween) rivers of myanmar. *Quaternary International*, 186(1):113–122. doi:https://doi.org/10.1016/j.quaint.2007.08.003. Larger Asian rivers and their interactions with estuaries and coasts.

Boatman, T. G., Lawson, T., and Geider, R. J. (2017). A key marine diazotroph in a changing ocean: The interacting effects of temperature, Co2 and light on the growth of trichodesmium erythraeum IMS101. *PLoS ONE*, 12(1):1–20. doi:10.1371/journal.pone.0168796.

Bohlen, L., Dale, A. W., and Wallmann, K. (2012). Simple transfer functions for calculating benthic fixed nitrogen losses and c:n:p regeneration ratios in global biogeochemical models. *Global Biogeochemical Cycles*, 26(3). doi:10.1029/2011GB004198.

Bourlès, B., Gouriou, Y., and Chuchla, R. (1999). On the circulation in the upper layer of the Western equatorial Atlantic. *Journal of Geophysical Research*, 104:21,151–21,170. doi:10.1029/1999JC900058.

Bouwman, A. F., Bierkens, M. F. P., Griffioen, J., Hefting, M. M., Middelburg, J. J., Middelkoop, H., and Slomp, C. P. (2013). Nutrient dynamics, transfer and retention along the aquatic continuum from land to ocean: towards integration of ecological and biogeochemical models. *Biogeosciences*, 10(1):1–22. doi:10.5194/bg-10-1-2013.

Brzezinski, M. A., Dickson, M.-L., Nelson, D. M., and Sambrotto, R. (2003). Ratios of Si, C and N uptake by microplankton in the Southern Ocean. *Deep Sea Research Part II: Topical Studies in Oceanography*, 50(3-4):619–633. doi:10.1016/S0967-0645(02)00587-8.

Cabrera-Barona, P. F., Bayón, M., Durán, G., Bonilla, A., and Mejía, V. (2020). Generating and mapping amazonian urban regions using a geospatial approach. *ISPRS International Journal of Geo-Information*, 9(7). doi:10.3390/ijgi9070453.

Caffin, M., Berthelot, H., Cornet-Barthaux, V., Barani, A., and Bonnet, S. (2018). Transfer of diazotroph-derived nitrogen to the planktonic food web across gradients of N&lt;sub&gt;2&lt;/sub&gt; fixation activity and diversity in the western tropical South Pacific Ocean. *Biogeosciences*, 15(12):3795–3810. doi:10.5194/bg-15-3795-2018.

Callède, J., Cochonneau, G., Alves, F. V., Guyot, J.-L., Guimarães, V. S., and De Oliveira, E. (2010). Les apports en eau de l'Amazone à l'Océan Atlantique. *Revue des sciences de l'eau*, 23(3):247–273. doi:10.7202/044688ar.

Capone, D. G., Burns, J. A., Montoya, J. P., Subramaniam, A., Mahaffey, C., Gunderson, T., Michaels, A. F., and Carpenter, E. J. (2005). Nitrogen fixation by Trichodesmium spp.: An important source of new nitrogen to the tropical and subtropical North Atlantic Ocean. *Global Biogeochemical Cycles*, 19(2):GB2024. doi:10.1029/2004GB002331.

Capone, D. G., Zehr, J. P., Paerl, H. W., Bergman, B., and Carpenter, E. J. (1997). Trichodesmium, a globally significant marine cyanobacterium. *Science*, 276(5316):1221–1229. doi:10.1126/science.276.5316.1221.

Caputo, A., Nylander, J. A. A., and Foster, R. A. (2019). The genetic diversity and evolution of diatom-diazotroph associations highlights traits favoring symbiont integration. (January):1–11. doi:10.1093/femsle/fny297.

Caputo, A., Stenegren, M., Pernice, M. C., and Foster, R. A. (2018). A Short Comparison of Two Marine Planktonic Diazotrophic Symbioses Highlights an Un-quantified Disparity. *Frontiers in Marine Science*, 5(February):1–8. doi:10.3389/fmars.2018.00002.

Carpenter, E. J., Montoya, J. P., Burns, J., Mulholland, M. R., Subramaniam, A., and Capone, D. G. (1999). Extensive bloom of a N2-fixing diatom/cyanobacterial association in the tropical Atlantic Ocean. *Marine Ecology Progress Series*, 185(1977):273–283. doi:10.3354/meps185273.

Carpenter, E. J., Subramaniam, A., and Capone, D. G. (2004). Biomass and primary productivity of the cyanobacterium trichodesmium spp. in the tropical n atlantic ocean. *Deep Sea Research Part I: Oceanographic Research Papers*, 51(2):173–203. doi:https://doi.org/10.1016/j.dsr.2003.10.006.

Castello, L., McGrath, D. G., Hess, L. L., Coe, M. T., Lefebvre, P. A., Petry, P., Macedo, M. N., Renó, V. F., and Arantes, C. C. (2013). The vulnerability of amazon freshwater ecosystems. *Conservation Letters*, 6(4):217–229. doi:https://doi.org/10.1111/conl.12008.

Chiang, J. C. H. and Vimont, D. J. (2004). Analogous Pacific and Atlantic Meridional Modes of Tropical Atmosphere–Ocean Variability. *Journal of Climate*, 17(21):4143–4158. doi:10.1175/JCLI4953.1.

Chien, C. T., Mackey, K. R., Dutkiewicz, S., Mahowald, N. M., Prospero, J. M., and Paytan, A. (2016). Effects of African dust deposition on phytoplankton in the western tropical Atlantic Ocean off Barbados. *Global Biogeochemical Cycles*, 30(5):716–734. doi:10.1002/2015GB005334.

Claudia Benitez-Nelson (2015). The missing link in oceanic phosphorus cycling?, In *Science*. doi:10.1126/science.aab1828.

Coe, M. T., Costa, M. H., and Howard, E. A. (2008). Simulating the surface waters of the amazon river basin: impacts of new river geomorphic and flow parameterizations. *Hydrological Processes*, 22(14):2542–2553. doi:https://doi.org/10.1002/hyp.6850.

Coe, M. T., Costa, M. H., and Soares-Filho, B. S. (2009). The influence of historical and potential future deforestation on the stream flow of the amazon river – land surface processes and atmospheric feedbacks. *Journal of Hydrology*, 369(1):165–174. doi:https://doi.org/10.1016/j.jhydrol.2009.02.043.

Cole, J. J., Prairie, Y. T., Caraco, N. F., McDowell, W. H., Tranvik, L. J., Striegl, R. G., Duarte, C. M., Kortelainen, P., Downing, J. A., Middelburg, J. J., and Melack, J. (2007). Plumbing the global carbon cycle: Integrating inland waters into the terrestrial carbon budget. *Ecosystems*, 10:171–184. doi:10.1007/s10021-006-9013-8.

Coles, V. J., Brooks, M. T., Hopkins, J., Stukel, M. R., Yager, P. L., and Hood, R. R. (2013). The pathways and properties of the amazon river plume in the tropical north atlantic ocean. *Journal of Geophysical Research: Oceans*, 118:6894–6913. doi:10.1002/2013JC008981.

Coles, V. J. and Hood, R. R. (2006). Modeling the impact of iron and phosphorus limitations on nitrogen fixation in the Atlantic Ocean. *Biogeosciences Discussions*, 3(5):1391–1451. doi:10.5194/bgd-3-1391-2006.

Conroy, B. J., Steinberg, D. K., Song, B., Kalmbach, A., Carpenter, E. J., and Foster, R. A. (2017). Mesozooplankton graze on cyanobacteria in the amazon river plume and western tropical north atlantic. *Frontiers in Microbiology*, 8:1436. doi:10.3389/fmicb.2017.01436.

Conroy, B. J., Steinberg, D. K., Stukel, M. R., Goes, J. I., and Coles, V. J. (2016). Meso- and microzooplankton grazing in the Amazon River plume and western tropical North Atlantic. *Limnology and Oceanography*, 61(3):825–840. doi:10.1002/lno.10261.

Cooley, S. R., Coles, V. J., Subramaniam, A., and Yager, P. L. (2007). Seasonal variations in the Amazon plume-related atmospheric carbon sink. *Global Biogeochemical Cycles*, 21(3):1–15. doi:10.1029/2006GB002831.

Da Cunha, L. C. and Buitenhuis, E. T. (2013). Riverine influence on the tropical atlantic ocean biogeochemistry. *Biogeosciences*, 10(10):6357–6373. doi:10.5194/bg-10-6357-2013.

Dagg, M., Benner, R., Lohrenz, S., and Lawrence, D. (2004). Transformation of dissolved and particulate materials on continental shelves influenced by large rivers: Plume processes. *Continental Shelf Research*, 24(7-8):833–858. doi:10.1016/j.csr.2004.02.003.

Dai, A., Qian, T., Trenberth, K. E., and Milliman, J. D. (2009). Changes in Continental Freshwater Discharge from 1948 to 2004. *Journal of Climate*, 22(10):2773–2792. doi:10.1175/2008JCLI2592.1.

de Fátima F. L. Rasera, M., Krusche, A. V., Richey, J. E., Ballester, M. V. R., and Victória, R. L. (2013). Spatial and temporal variability of pCO2 and CO2 efflux in seven Amazonian Rivers. *Biogeochemistry*, 116(1-3):241–259. doi:10.1007/s10533-013-9854-0.

de Paiva, R. C. D., Buarque, D. C., Collischonn, W., Bonnet, M.-P., Frappart, F., Calmant, S., and Bulhões Mendes, C. A. (2013). Large-scale hydrologic and hydrodynamic modeling of the amazon river basin. *Water Resources Research*, 49(3):1226–1243. doi:https://doi.org/10.1002/wrcr.20067.

Dee, D. P., Uppala, S. M., Simmons, A. J., Berrisford, P., Poli, P., Kobayashi, S., Andrae, U., Balmaseda, M. A., Balsamo, G., Bauer, P., Bechtold, P., Beljaars, A. C. M., van de Berg, L., Bidlot, J., Bormann, N., Delsol, C., Dragani, R., Fuentes, M., Geer, A. J., Haimberger, L., Healy, S. B., Hersbach, H., Hólm, E. V., Isaksen, L., Kållberg, P., Köhler, M., Matricardi, M., McNally, A. P., Monge-Sanz, B. M., Morcrette, J.-J., Park, B.-K., Peubey, C., de Rosnay, P., Tavolato, C., Thépaut, J.-N., and Vitart, F. (2011). The era-interim reanalysis: configuration and performance of the data assimilation system. *Quarterly Journal of the Royal Meteorological Society*, 137(656):553–597. doi:10.1002/qj.828.

Del Vecchio, R. and Subramaniam, A. (2004). Influence of the Amazon River on the surface optical properties of the western tropical North Atlantic Ocean. *Journal of Geophysical Research: Oceans*. doi:10.1029/2004JC002503.

DeMaster, D. J. and C., A. R. (2001). *The Biogeochemistry of the Amazon Basin*, chapter Biogeochemical Processes on the Amazon Shelf: Changes in Diisolved and Particulate Fluxes During River/Ocean Mixing, pages 328 – 357. Oxford University Press, New York.

DeMaster, D. J., McKee, B. A., Nelson, D. M., Showers, W. J., and Jr, W. O. S. (1991). Geochemical Processes Occurring in the Waters at the Amazon River/Ocean Boundary . *Oceanography*, 4(1):15–20. doi:https://doi.org/10.5670/oceanog.1991.16.

Demaster, D. J., Smith, W. ., Nelsons, and Aller, J. Y. (1996). Biogeochemical processes in amazon shelf waters: chemical distributions and uptake rates of silicon, carbon and nitrogen, 16, pages 617–643.

Deutsch, C., Sarmiento, J. L., Sigman, D. M., Gruber, N., and Dunne, J. P. (2007). Spatial coupling of nitrogen inputs and losses in the ocean. *Nature*, 445(7124):163–167. doi:10.1038/nature05392.

Diaz, R. J. and Rosenberg, R. (2008). Spreading Dead Zones and Consequences for Marine Ecosystems. *Science*, 321(5891):926–929. doi:10.1126/science.1156401.

Dickson, A. G., Sabine, C. L., and Christian, J. R. (2007). *Guide to Best Practices for Ocean CO2 measurements. PICES Special Publication*, volume 3.

Doherty, M., Yager, P. L., Moran, M. A., Coles, V. J., Fortunato, C. S., Krusche, A. V., Medeiros, P. M., Payet, J. P., Richey, J. E., Satinsky, B. M., Sawakuchi, H. O., Ward, N. D., and Crump, B. C. (2017a). Bacterial biogeography across the Amazon River-ocean continuum. *Frontiers in Microbiology*, 8(5):1–17. doi:10.3389/fmicb.2017.00882.

Doherty, M., Yager, P. L., Moran, M. A., Coles, V. J., Fortunato, C. S., Krusche, A. V., Medeiros, P. M., Payet, J. P., Richey, J. E., Satinsky, B. M., Sawakuchi, H. O., Ward, N. D., and Crump, B. C. (2017b). Bacterial Biogeography across the Amazon River-Ocean Continuum. *Frontiers in Microbiology*, 8:882. doi:10.3389/fmicb.2017.00882.

Dore, J. E., Brum, J. R., Tupas, L. M., and Karl, D. M. (2002). Seasonal and interannual variability in sources of nitrogen supporting export in the oligotrophic subtropical North Pacific Ocean. *Limnology and Oceanography*, 47(6):1595–1607. doi:10.4319/lo.2002.47.6.1595.

Drake, T. W., Hemingway, J. D., Kurek, M. R., Peucker-Ehrenbrink, B., Brown, K. A., Holmes, R. M., Galy, V., Moura, J. M., Mitsuya, M., Wassenaar, L. I., Six, J., and Spencer, R. G. M. (2021). The pulse of the amazon: Fluxes of dissolved organic carbon, nutrients, and ions from the world's largest river. *Global Biogeochemical Cycles*, 35(4):e2020GB006895. doi:https://doi.org/10.1029/2020GB006895.

Duffy, P. B., Brando, P., Asner, G. P., and Field, C. B. (2015). Projections of future meteorological drought and wet periods in the amazon. *Proceedings of the National Academy of Sciences*, 112(43):13172–13177. doi:10.1073/pnas.1421010112.

Dugdale, R. C. and Goering, J. J. (1967). Uptake of new and regenerated forms of nitrogen in primary productivity. *Limnology and Oceanography*, 12(2):196–206. doi:10.4319/lo.1967.12.2.0196.

Dunne, J. P., Sarmiento, J. L., and Gnanadesikan, A. (2007). A synthesis of global particle export from the surface ocean and cycling through the ocean interior and on the seafloor. *Global Biogeochemical Cycles*, 21(4). doi:10.1029/2006GB002907.

Dutheil, C., Aumont, O., Gorguès, T., Lorrain, A., Bonnet, S., Rodier, M., Dupouy, C., Shiozaki, T., and Menkes, C. (2018). Modelling N2 fixation related to Trichodesmium sp.: Driving processes and impacts on primary production in the tropical Pacific Ocean. *Biogeosciences*, 15(14):4333–4352. doi:10.5194/bg-15-4333-2018.

Dutkiewicz, S., Ward, B. A., Scott, J. R., and Follows, M. J. (2014). Understanding predicted shifts in diazotroph biogeography using resource competition theory. *Biogeosciences*, 11(19):5445–5461. doi:10.5194/bg-11-5445-2014.

Enfield, D. B. and Mayer, D. A. (1997). Tropical Atlantic sea surface temperature variability and its relation to El Niño-Southern Oscillation. *Journal of Geophysical Research: Oceans*, 102(C1):929–945. doi:10.1029/96JC03296.

Espinoza, J. C., Marengo, J. A., Ronchail, J., Carpio, J. M., Flores, L. N., and Guyot, J. L. (2014). The extreme 2014 flood in south-western amazon basin: the role of tropical-subtropical south atlantic sst gradient. *Environmental Research Letters*, 9:124007. doi:10.1088/1748-9326/9/12/124007.

Espinoza, J. C., Ronchail, J., Guyot, J. L., Junquas, C., Vauchel, P., Lavado, W., Drapeau, G., and Pombosa, R. (2011). Climate variability and extreme drought in the upper solimões river (western amazon basin): Understanding the exceptional 2010 drought. *Geophysical Research Letters*, 38(13). doi:https://doi.org/10.1029/2011GL047862.

Fabregat-Safont, D., Ibáñez, M., Bijlsma, L., Hernández, F., Waichman, A. V., de Oliveira, R., and Rico, A. (2021). Wide-scope screening of pharmaceuticals, illicit drugs and their metabolites in the amazon river. *Water Research*, 200:117251. doi:https://doi.org/10.1016/j.watres.2021.117251.

Fearnside, P. M. (2015). Emissions from tropical hydropower and the IPCC. *Environmental Science & Policy*, 50(Table 1):225–239. doi:10.1016/j.envsci.2015.03.002.

Feng, Y., Menemenlis, D., Xue, H., Zhang, H., Carroll, D., Du, Y., and Wu, H. (2021). Improved representation of river runoff in Estimating the Circulation and Climate of the Ocean Version 4 (ECCOv4) simulations: Implementation, evaluation, and impacts to coastal plume regions. *Geoscientific Model Development*, 14(3):1801–1819. doi:10.5194/gmd-14-1801-2021.

Fennel, K. and Testa, J. M. (2019). Biogeochemical controls on coastal hypoxia. *Annual Review of Marine Science*, 11(1):105–130. doi:10.1146/annurev-marine-010318-095138. PMID: 29889612.

Foley, J. A., Botta, A., Coe, M. T., and Costa, M. H. (2002). El Niño-Southern oscillation and the climate, ecosystems and rivers of Amazonia. *Global Biogeochemical Cycles*, 16(4):1132. doi:10.1029/2002GB001872.

Follett, C. L., Dutkiewicz, S., Karl, D. M., Inomura, K., and Follows, M. J. (2018). Seasonal resource conditions favor a summertime increase in North Pacific diatom-diazotroph associations. *ISME Journal*, 12(6):1543–1557. doi:10.1038/s41396-017-0012-x.

Foltz, G. R., Brandt, P., Richter, I., Rodríguez-Fonseca, B., Hernandez, F., Dengler, M., Rodrigues, R. R., Schmidt, J. O., Yu, L., Lefevre, N., Da Cunha, L. C., McPhaden, M. J., Araujo, M., Karstensen, J., Hahn, J., Martín-Rey, M., Patricola, C. M., Poli, P., Zuidema, P., Hummels, R., Perez, R. C., Hatje, V., Lübbecke, J. F., Polo, I., Lumpkin, R., Bourlès, B., Asuquo, F. E., Lehodey, P., Conchon, A., Chang, P., Dandin, P., Schmid, C., Sutton, A., Giordani, H., Xue, Y., Illig, S., Losada, T., Grodsky, S. A., Gasparin, F., Lee, T., Mohino, E., Nobre, P., Wanninkhof, R., Keenlyside, N., Garcon, V., Sánchez-Gómez, E., Nnamchi, H. C., Drévillon, M., Storto, A., Remy, E., Lazar, A., Speich, S., Goes, M., Dorrington, T., Johns, W. E., Moum, J. N., Robinson, C., Perruche, C., de Souza, R. B., Gaye, A. T., López-Parages, J., Monerie, P.-A., Castellanos, P., Benson, N. U., Hounkonnou, M. N., Duhá, J. T., Laxenaire, R., and Reul, N. (2019). The Tropical Atlantic Observing System. *Frontiers in Marine Science*, 6:1–36. doi:10.3389/fmars.2019.00206.

Foltz, G. R., McPhaden, M. J., and Lumpkin, R. (2012). A Strong Atlantic Meridional Mode Event in 2009: The Role of Mixed Layer Dynamics. *Journal of Climate*, 25(1):363–380. doi:10.1175/JCLI-D-11-00150.1.

Fontes, R. F. C., Castro, B. M., and Beardsley, R. C. (2008). Numerical study of circulation on the inner Amazon Shelf. *Ocean Dynamics*, 58(3-4):187–198. doi:10.1007/s10236-008-0139-4.

Forsberg, B. R., Melack, J. M., Dunne, T., Barthem, R. B., Goulding, M., Paiva, R. C. D., Sorribas, M. V., Silva, U. L., and Weisser, S. (2017). The potential impact of new Andean dams on Amazon fluvial ecosystems. *PLOS ONE*, 12(8):e0182254. doi:10.1371/journal.pone.0182254.

Foster, R. A. and Capone, D. G. (2012). Influence of the Amazon River plume on distributions of free-living Influence and symbiotic in the western tropical north Atlantic Ocean cyanobacteria. *Limnology and Oceanography*, 52(2):517–532. doi:10.4319/lo.2007.52.2.0517.

Foster, R. A., Kuypers, M. M., Vagner, T., Paerl, R. W., Musat, N., and Zehr, J. P. (2011). Nitrogen fixation and transfer in open ocean diatom-cyanobacterial symbioses. *ISME Journal*, 5(9):1484–1493. doi:10.1038/ismej.2011.26.

Foster, R. A. and O'Mullan, G. D. (2008). Nitrogen fixing and nitrifying symbioses in the marine environment. *Nitrogen in the Marine Environment*, pages 1197–1218. doi:10.1016/B978-0-12-372522-6.00027-X.

Foster, R. A., Subramaniam, A., Mahaffey, C., Carpenter, E. J., Capone, D. G., and Zehr, J. P. (2007). Influence of the Amazon River plume on distributions of free-living and symbiotic cyanobacteria in the western tropical north Atlantic Ocean. *Limnology and Oceanography*, 52(2):517–532. doi:10.4319/lo.2007.52.2.0517.

Foster, R. A., Tienken, D., Littmann, S., Whitehouse, M. J., Kuypers, M. M. M., and White, A. E. (2021). The rate and fate of N2 and C fixation by marine diatom-diazotroph symbioses. *The ISME Journal*, (March). doi:10.1038/s41396-021-01086-7.

Foster, R. A. and Zehr, J. P. (2006). Characterization of diatom–cyanobacteria symbioses on the basis of nifH, hetR and 16S rRNA sequences. *Environmental Microbiology*, 8(11):1913–1925. doi:10.1111/j.1462-2920.2006.01068.x.

Fournier, S., Chapron, B., Salisbury, J., Vandemark, D., and Reul, N. (2015). Comparison of spaceborne measurements of sea surface salinity and colored detrital matter in the Amazon plume. *Journal of Geophysical Research: Oceans*, 120(5):3177–3192. doi:10.1002/2014JC010109.

Friedlingstein, P., Jones, M. W., O'Sullivan, M., Andrew, R. M., Bakker, D. C. E., Hauck, J., Le Quéré, C., Peters, G. P., Peters, W., Pongratz, J., Sitch, S., Canadell, J. G., Ciais, P., Jackson, R. B., Alin, S. R., Anthoni, P., Bates, N. R., Becker, M., Bellouin, N., Bopp, L., Chau, T. T. T., Chevallier, F., Chini, L. P., Cronin, M., Currie, K. I., Decharme, B., Djeutchouang, L., Dou, X., Evans, W., Feely, R. A., Feng, L., Gasser, T., Gilfillan, D., Gkritzalis, T., Grassi, G., Gregor, L., Gruber, N., Gürses, O., Harris, I., Houghton, R. A., Hurtt, G. C., Iida, Y., Ilyina, T., Luijkx, I. T., Jain, A. K., Jones, S. D., Kato, E., Kennedy, D., Klein Goldewijk, K., Knauer, J., Korsbakken, J. I., Körtzinger, A., Landschützer, P., Lauvset, S. K., Lefèvre, N., Lienert, S., Liu, J., Marland, G., McGuire, P. C., Melton, J. R., Munro, D. R., Nabel, J. E. M. S., Nakaoka, S.-I., Niwa, Y., Ono, T., Pierrot, D., Poulter, B., Rehder, G., Resplandy, L., Robertson, E., Rödenbeck, C., Rosan, T. M., Schwinger, J., Schwingshackl, C., Séférian, R., Sutton, A. J., Sweeney, C., Tanhua, T., Tans, P. P., Tian, H., Tilbrook, B., Tubiello, F., van der Werf, G., Vuichard, N., Wada, C., Wanninkhof, R., Watson, A., Willis, D., Wiltshire, A. J., Yuan, W., Yue, C., Yue, X., Zaehle, S., and Zeng, J. (2021). Global carbon budget 2021. *Earth System Science Data Discussions*, 2021:1–191. doi:10.5194/essd-2021-386.

Friedlingstein, P., O'Sullivan, M., Jones, M. W., Andrew, R. M., Hauck, J., Olsen, A., Peters, G. P., Peters, W., Pongratz, J., Sitch, S., Quéré, C. L., Canadell, J. G., Ciais, P., Jackson, R. B., Alin, S., Aragão, L. E., Arneth, A., Arora, V., Bates, N. R., Becker, M., Benoit-Cattin, A., Bittig, H. C., Bopp, L., Bultan, S., Chandra, N., Chevallier, F., Chini, L. P., Evans, W., Florentie, L., Forster, P. M., Gasser, T., Gehlen, M., Gilfillan, D., Gkritzalis, T., Gregor, L., Gruber, N., Harris, I., Hartung, K., Haverd, V., Houghton, R. A., Ilyina, T., Jain, A. K., Joetzjer, E., Kadono, K., Kato, E., Kitidis, V., Korsbakken, J. I., Landschützer, P., Lefèvre, N., Lenton, A., Lienert, S., Liu, Z., Lombardozzi, D., Marland, G., Metzl, N., Munro, D. R., Nabel, J. E., Nakaoka, S. I., Niwa, Y., O'Brien, K., Ono, T., Palmer, P. I., Pierrot, D., Poulter, B., Resplandy, L., Robertson, E., Rödenbeck, C., Schwinger, J., Séférian, R., Skjelvan, I., Smith, A. J., Sutton, A. J., Tanhua, T., Tans, P. P., Tian, H., Tilbrook, B., Werf, G. V. D., Vuichard, N., Walker, A. P., Wanninkhof, R., Watson, A. J., Willis, D., Wiltshire, A. J., Yuan, W., Yue, X., and Zaehle, S. (2020). Global carbon budget 2020. *Earth System Science Data*, 12:3269–3340. doi:10.5194/essd-12-3269-2020.

Friedman, A. R., Bollasina, M. A., Gastineau, G., and Khodri, M. (2021). Increased amazon basin wet-season precipitation and river discharge since the early 1990s driven by tropical pacific variability. *Environmental Research Letters*, 16:034033. doi:10.1088/1748-9326/abd587.

Frischknecht, M. (2018). New Perspectives on the Three-Dimensional Cycling of Carbon and Nutrients in the California Current System and its Response to ENSO. *PhD Thesis*. doi:10.3929/ethz-b-000283522.

Frischknecht, M., Münnich, M., and Gruber, N. (2018). Origin, Transformation, and Fate: The Three-Dimensional Biological Pump in the California Current System. *Journal of Geophysical Research: Oceans*, 123(11):7939–7962. doi:10.1029/2018JC013934.

Froelich, P. N., Atwood, D. K., and Giese, G. S. (1978). Influence of Amazon River discharge on surface salinity and dissolved silicate concentration in the Caribbean Sea. *Deep Sea Research*, 25(8):735–744. doi:10.1016/0146-6291(78)90627-6.

Fu, F. X., Yu, E., Garcia, N. S., Gale, J., Luo, Y., Webb, E. A., and Hutchins, D. A. (2014). Differing responses of marine N2 fixers to warming and consequences for future diazotroph community structure. *Aquatic Microbial Ecology*, 72(1):33–46. doi:10.3354/ame01683.

Gabioux, M., Vinzon, S. B., and Paiva, A. M. (2005). Tidal propagation over fluid mud layers on the Amazon shelf. *Continental Shelf Research*, 25(1):113–125. doi:10.1016/j.csr.2004.09.001.

Garcia, H. E., Locarnini, R., Boyer, T. P., Antonov, J. I., Baranova, O. K., Zweng, M. M., Reagan, J. R., and Johnson, D. R. (2013). World Ocean Atlas 2013 Volume 4 : Nutrients phosphate, nitrate, silicate). *NOAA Atlas NESDIS 76*, 4(9):396.

Gensac, E., Martinez, J. M., Vantrepotte, V., and Anthony, E. J. (2016). Seasonal and inter-annual dynamics of suspended sediment at the mouth of the amazon river: The role of continental and oceanic forcing, and implications for coastal geomorphology and mud bank formation. *Continental Shelf Research*, 118:49–62. doi:10.1016/j.csr.2016.02.009.

Gerolin, C. R., Pupim, F. N., Sawakuchi, A. O., Grohmann, C. H., Labuto, G., and Semensatto, D. (2020). Microplastics in sediments from amazon rivers, brazil. *Science of The Total Environment*, 749:141604. doi:10.1016/j.scitotenv.2020.141604.

Girault, M., Arakawa, H., and Hashihama, F. (2013). Phosphorus stress of microphytoplankton community in the western subtropical North Pacific. *Journal of Plankton Research*, 35(1):146–157. doi:10.1093/plankt/fbs076.

GLOBALVIEW-CO2 (2011). Coperative Atmospheric Data IntegrationProject – Carbon Dioxide, CD-ROM, NOAA ESRL, Boulder, Colorado [Also available on Internet via anonymous FTP toftp.cmdl.noaa.gov, path: ccg/co2/GLOBALVIEW].

Gloor, M., Brienen, R. J., Galbraith, D., Feldpausch, T. R., Schöngart, J., Guyot, J. L., Espinoza, J. C., Lloyd, J., and Phillips, O. L. (2013). Intensification of the amazon hydrological cycle over the last two decades. *Geophysical Research Letters*, 40:1729–1733. doi:10.1002/grl.50377.

Goebel, N. L., Turk, K. A., Achilles, K. M., Paerl, R., Hewson, I., Morrison, A. E., Montoya, J. P., Edwards, C. A., and Zehr, J. P. (2010). Abundance and distribution of major groups of diazotrophic cyanobacteria and their potential contribution to N2 fixation in the tropical Atlantic Ocean. *Environmental Microbiology*, 12(12):3272–3289. doi:10.1111/j.1462-2920.2010.02303.x.

Goes, J. I., Gomes, H. d. R., Chekalyuk, A. M., Carpenter, E. J., Montoya, J. P., Coles, V. J., Yager, P. L., Berelson, W. M., Capone, D. G., Foster, R. A., Steinberg, D. K., Subramaniam, A., and Hafez, M. A. (2014). Influence of the Amazon River discharge on the biogeography of phytoplankton communities in the western tropical north Atlantic. *Progress in Oceanography*, 120:29–40. doi:10.1016/j.pocean.2013.07.010.

Gomes, H. d. R., Xu, Q., Ishizaka, J., Carpenter, E. J., Yager, P. L., and Goes, J. I. (2018). The Influence of Riverine Nutrients in Niche Partitioning of Phytoplankton Communities–A Contrast Between the Amazon River Plume and the Changjiang (Yangtze) River Diluted Water of the East China Sea. *Frontiers in Marine Science*, 5(September):1–14. doi:10.3389/fmars.2018.00343.

Gong, G.-C., Chang, J., Chiang, K.-P., Hsiung, T.-M., Hung, C.-C., Duan, S.-W., and Codispoti, L. A. (2006). Reduction of primary production and changing of nutrient ratio in the East China Sea: Effect of the Three Gorges Dam? *Geophysical Research Letters*, 33(7):L07610. doi:10.1029/2006GL025800.

Gouveia, N. A., Gherardi, D. F. M., Wagner, F. H., Paes, E. T., Coles, V. J., and Aragão, L. E. O. C. (2019). The salinity structure of the amazon river plume drives spatiotemporal variation of oceanic primary productivity. *Journal of Geophysical Research: Biogeosciences*, 124:147–165. doi:10.1029/2018JG004665.

Goyet, C., Adams, R., and Eischeid, G. (1998). Observations of the co2 system properties in the tropical atlantic ocean. *Marine Chemistry*, 60(1):49 – 61. doi:https://doi.org/10.1016/S0304-4203(97)00081-9.

GRDC (2020). Major river basins of the world / global runoff data centre. 2nd, rev. ext. ed.

Grodsky, S. A. and Carton, J. A. (2003). The Intertropical Convergence Zone in the South Atlantic and the Equatorial Cold Tongue. *Journal of Climate*, 16(4):723–733. doi:10.1175/1520-0442(2003)016<0723:TICZIT>2.0.CO;2.

Grodsky, S. A., Reul, N., Lagerloef, G., Reverdin, G., Carton, J. A., Chapron, B., Quilfen, Y., Kudryavtsev, V. N., and Kao, H.-Y. (2012). Haline hurricane wake in the amazon/orinoco plume: Aquarius/sacd and smos observations. *Geophysical Research Letters*, 39(20). doi:https://doi.org/10.1029/2012GL053335.

Grosse, J., Bombar, D., Doan, H. N., Nguyen, L. N., and Voss, M. (2010). The Mekong River plume fuels nitrogen fixation and determines phytoplankton species distribution in the South China Sea during low and high discharge season. *Limnology and Oceanography*, 55(4):1668–1680. doi:10.4319/lo.2010.55.4.1668.

Gruber, N. (2016). Elusive marine nitrogen fixation. *Proceedings of the National Academy of Sciences*, 113(16):4246–4248. doi:10.1073/pnas.1603646113.

Gruber, N. (2019). Consistent patterns of nitrogen fixation identified in the ocean. *Nature*, 566(7743):191–193. doi:10.1038/d41586-019-00498-y.

Guedes, G., Costa, S., and Brondízio, E. (2009). Revisiting the hierarchy of urban areas in the brazilian amazon: a multilevel approach. *Population and environment*, 30(4-5):159–192. doi:10.1007/s11111-009-0083-3.

Guenet, B., Danger, M., Harrault, L., Allard, B., Jauset-Alcala, M., Bardoux, G., Benest, D., Abbadie, L., and Lacroix, G. (2014). Fast mineralization of land-born c in inland waters: First experimental evidences of aquatic priming effect. *Hydrobiologia*, 721:35–44. doi:10.1007/s10750-013-1635-1.

Guo, C. and Tester, P. A. (1994). Toxic effect of the bloom-forming Trichodesmium sp. (cyanophyta) to the copepodAcartia tonsa. *Natural Toxins*, 2(4):222–227. doi:10.1002/nt.2620020411.

Hansell, D. A. and Follows, M. J. (2008). *Nitrogen in the Atlantic Ocean*. Elsevier Inc. doi:10.1016/B978-0-12-372522-6.00013-X.

Harding, K., Turk-Kubo, K. A., Sipler, R. E., Mills, M. M., Bronk, D. A., and Zehr, J. P. (2018). Symbiotic unicellular cyanobacteria fix nitrogen in the Arctic Ocean. *Proceedings of the National Academy of Sciences*, 115(52):13371–13375. doi:10.1073/pnas.1813658115.

Harke, M. J., Frischkorn, K. R., Haley, S. T., Aylward, F. O., Zehr, J. P., and Dyhrman, S. T. (2018). Periodic and coordinated gene expression between a diazotroph and its diatom host. *The ISME Journal*. doi:10.1038/s41396-018-0262-2.

Hashioka, T., Vogt, M., Yamanaka, Y., Le Quéré, C., Buitenhuis, E. T., Aita, M. N., Alvain, S., Bopp, L., Hirata, T., Lima, I., Sailley, S., and Doney, S. C. (2013). Phytoplankton competition during the spring bloom in four plankton functional type models. *Biogeosciences*, 10(11):6833–6850. doi:10.5194/bg-10-6833-2013.

Hastie, A., Lauerwald, R., Ciais, P., and Regnier, P. (2019). Aquatic carbon fluxes dampen the overall variation of net ecosystem productivity in the Amazon basin: An analysis of the interannual variability in the boundless carbon cycle. *Global Change Biology*, 25(6):2094–2111. doi:10.1111/gcb.14620.

Hedges, J., Keil, R., and Benner, R. (1997). What happens to terrestrial organic matter in the ocean? *Organic Geochemistry*, 27(5):195–212. doi:https://doi.org/10.1016/S0146-6380(97)00066-1.

Hellweger, F. L. and Gordon, A. L. (2002). Tracing Amazon River water into the Caribbean Sea. *Journal of Marine Research*, 60(4):537–549. doi:10.1357/002224002762324202.

Hersbach, H., Bell, B., Berrisford, P., Hirahara, S., Horányi, A., Muñoz-Sabater, J., Nicolas, J., Peubey, C., Radu, R., Schepers, D., Simmons, A., Soci, C., Abdalla, S., Abellan, X., Balsamo, G., Bechtold, P., Biavati, G., Bidlot, J., Bonavita, M., Chiara, G., Dahlgren, P., Dee, D., Diamantakis, M., Dragani, R., Flemming, J., Forbes, R., Fuentes, M., Geer, A., Haimberger, L., Healy, S., Hogan, R. J., Hólm, E., Janisková, M., Keeley, S., Laloyaux, P., Lopez, P., Lupu, C., Radnoti, G., Rosnay, P., Rozum, I., Vamborg, F., Villaume, S., and Thépaut, J. (2020). The ERA5 global reanalysis. *Quarterly Journal of the Royal Meteorological Society*, 146(730):1999–2049. doi:10.1002/qj.3803.

Hess, L. L., Melack, J. M., Affonso, A. G., Barbosa, C., Gastil-Buhl, M., and Novo, E. M. L. M. (2015). Wetlands of the lowland amazon basin: Extent, vegetative cover, and dual-season inundated area as mapped with jers-1 synthetic aperture radar. *Wetlands*, 35(4):745–756. doi:10.1007/s13157-015-0666-y.

Holl, C. M. and Montoya, J. P. (2008). Diazotrophic growth of the marine cyanobacterium Trichodesmium IMS101 in continuous culture: effects of growth rate on N2 fixation rate, biomass and C:N:P stoichiometry. *Journal of Phycology*, 44(4):929–937. doi:10.1111/j.1529-8817.2008.00534.x.

Holling, C. S. (1959). Some characteristics of simple types of predation and parasitism. *The Canadian Entomologist*, 91(7):385–398. doi:10.4039/Ent91385-7.

Hu, C., Montgomery, E. T., Schmitt, R. W., and Muller-Karger, F. E. (2004). The dispersal of the amazon and orinoco river water in the tropical atlantic and caribbean sea: Observation from space and s-palace floats. *Deep Sea Research Part II: Topical Studies in Oceanography*, 51:1151–1171. doi:10.1016/j.dsr2.2004.04.001.

Hulth, S., Aller, R. C., Canfield, D. E., Dalsgaard, T., Engström, P., Gilbert, F., Sundbäck, K., and Thamdrup, B. (2005). Nitrogen removal in marine environments: recent findings and future research challenges. *Marine Chemistry*, 94(1):125–145. doi:https://doi.org/10.1016/j.marchem.2004.07.013. Analytical and Marine Chemistry: A Tribute to Professor David Dyrssen, the founding father of Swedish Marine Chemistry.

Hunt, B. P. V., Bonnet, S., Berthelot, H., Conroy, B. J., Foster, R. A., and Pagano, M. (2016). Contribution and pathways of diazotroph-derived nitrogen to zooplankton during the VAHINE mesocosm experiment in the oligotrophic New Caledonia lagoon. *Biogeosciences*, 13(10):3131–3145. doi:10.5194/bg-13-3131-2016.

Hutchins, D. A., Fu, F. X., Webb, E. A., Walworth, N., and Tagliabue, A. (2013). Taxon-specific response of marine nitrogen fixers to elevated carbon dioxide concentrations. *Nature Geoscience*, 6(9):790–795. doi:10.1038/ngeo1858.

Hülse, D., Arndt, S., Wilson, J. D., Munhoven, G., and Ridgwell, A. (2017). Understanding the causes and consequences of past marine carbon cycling variability through models. *Earth-Science Reviews*, 171:349–382. doi:https://doi.org/10.1016/j.earscirev.2017.06.004.

Ibánhez, J. S. P., Diverrès, D., Araujo, M., and Lefèvre, N. (2015). Seasonal and interannual variability of sea-air CO 2 fluxes in the tropical Atlantic affected by the Amazon River plume. *Global Biogeochemical Cycles*, 29(10):1640–1655. doi:10.1002/2015GB005110.

Ibánhez, J. S. P., Flores, M., and Lefèvre, N. (2017). Collapse of the tropical and subtropical North Atlantic CO2sink in boreal spring of 2010. *Scientific Reports*, 7(July 2016):1–9. doi:10.1038/srep41694.

Ilyina, T., Six, K. D., Segschneider, J., Maier-Reimer, E., Li, H., and Núñez-Riboni, I. (2013). Global ocean biogeochemistry model hamocc: Model architecture and performance as component of the mpi-earth system model in different cmip5 experimental realizations. *Journal of Advances in Modeling Earth Systems*, 5(2):287–315. doi:https://doi.org/10.1029/2012MS000178.

Inomura, K., Follett, C. L., Masuda, T., Eichner, M., Prášil, O., and Deutsch, C. (2020). Carbon Transfer from the Host Diatom Enables Fast Growth and High Rate of N2 Fixation by Symbiotic Heterocystous Cyanobacteria. *Plants*, 9(2):192. doi:10.3390/plants9020192.

Izett, J. G. and Fennel, K. (2018). Estimating the Cross-Shelf Export of Riverine Materials: Part 2. Estimates of Global Freshwater and Nutrient Export. *Global Biogeochemical Cycles*, 32(2):176–186. doi:10.1002/2017GB005668.

Jiang, H.-B., Fu, F.-X., Rivero-Calle, S., Levine, N. M., Sañudo-Wilhelmy, S. A., Qu, P.-P., Wang, X.-W., Pinedo-Gonzalez, P., Zhu, Z., and Hutchins, D. A. (2018). Ocean warming alleviates iron limitation of marine nitrogen fixation. *Nature Climate Change*, 8(8):709–712. doi:10.1038/s41558-018-0216-8.

Jin, X., Gruber, N., Frenzel, H., Doney, S. C., and McWilliams, J. C. (2008). The impact on atmospheric CO2 of iron fertilization induced changes in the ocean's biological pump. *Biogeosciences*, 5(2):385–406. doi:10.5194/bg-5-385-2008.

Kalnay, E., Kanamitsu, M., Kistler, R., Collins, W., Deaven, D., Gandin, L., Iredell, M., Saha, S., White, G., Woollen, J., Zhu, Y., Chelliah, M., Ebisuzaki, W., Higgins, W., Janowiak, J., Mo, K. C., Ropelewski, C., Wang, J., Leetmaa, A., Reynolds, R., Jenne, R., and Joseph, D. (1996). The NCEP/NCAR 40-Year Reanalysis Project. *Bulletin of the American Meteorological Society*, 77(3):437–472. doi:10.1175/1520-0477(1996)077<0437:TNYRP>2.0.CO;2.

Karl, D. M., Church, M. J., Dore, J. E., Letelier, R. M., and Mahaffey, C. (2012). Predictable and efficient carbon sequestration in the North Pacific Ocean supported by symbiotic nitrogen fixation. *Proceedings of the National Academy of Sciences*, 109(6):1842–1849. doi:10.1073/pnas.1120312109.

Korte, L. F., Brummer, G.-J. A., van der Does, M., Guerreiro, C. V., Mienis, F., Munday, C. I., Ponsoni, L., Schouten, S., and Stuut, J.-B. W. (2020). Multiple drivers of production and particle export in the western tropical North Atlantic. *Limnology and Oceanography*, pages 1–17. doi:10.1002/lno.11442.

Körtzinger, A. (2003). A significant CO2 sink in the tropical Atlantic Ocean associated with the Amazon River plume. *Geophysical Research Letters*, 30(24):2–5. doi:10.1029/2003GL018841.

Lacroix, F., Ilyina, T., and Hartmann, J. (2020). Oceanic CO&lt;sub&gt;2&lt;/sub&gt; outgassing and biological production hotspots induced by pre-industrial river loads of nutrients and carbon in a global modeling approach. *Biogeosciences*, 17(1):55–88. doi:10.5194/bg-17-55-2020.

Lacroix, F., Ilyina, T., Laruelle, G. G., and Regnier, P. (2021a). Reconstructing the preindustrial coastal carbon cycle through a global ocean circulation model: Was the global continental shelf already both autotrophic and a co2 sink? *Global Biogeochemical Cycles*, 35(2):e2020GB006603. doi:https://doi.org/10.1029/2020GB006603. e2020GB006603 2020GB006603.

Lacroix, F., Ilyina, T., Mathis, M., Laruelle, G. G., and Regnier, P. (2021b). Historical increases in land-derived nutrient inputs may alleviate effects of a changing physical climate on the oceanic carbon cycle. *Global Change Biology*, (February):1–23. doi:10.1111/gcb.15822.

Landa, M., Turk-Kubo, K. A., Cornejo-Castillo, F. M., Henke, B. A., and Zehr, J. P. (2021). Critical Role of Light in the Growth and Activity of the Marine N2-Fixing UCYN-A Symbiosis. *Frontiers in Microbiology*, 12(May):1–13. doi:10.3389/fmicb.2021.666739.

Landolfi, A., Kähler, P., Koeve, W., and Oschlies, A. (2018). Global marine N2 fixation estimates: From observations to models. *Frontiers in Microbiology*, 9(SEP):1–8. doi:10.3389/fmicb.2018.02112.

Landolfi, A., Koeve, W., Dietze, H., Kähler, P., and Oschlies, A. (2015). A new perspective on environmental controls of marine nitrogen fixation. *Geophysical Research Letters*. doi:10.1002/2015GL063756.

Landschützer, P., Gruber, N., Bakker, D. C., and Schuster, U. (2014). Recent variability of the global ocean carbon sink. *Global Biogeochemical Cycles*, 28(9):927–949. doi:10.1002/2014GB004853.

Landschützer, P., Laruelle, G. G., Roobaert, A., and Regnier, P. (2020). A uniform pco$_2$ climatology combining open and coastal oceans. *Earth System Science Data*, 12(4):2537–2553. doi:10.5194/essd-12-2537-2020.

Langlois, R. J., Hümmer, D., and LaRoche, J. (2008). Abundances and distributions of the dominant nifH phylotypes in the Northern Atlantic Ocean. *Applied and Environmental Microbiology*, 74(6):1922–1931. doi:10.1128/AEM.01720-07.

Langlois, R. J., LaRoche, J., and Raab, P. A. (2005). Diazotrophic Diversity and Distribution in the Tropical and Subtropical Atlantic Ocean. *Applied and Environmental Microbiology*, 71(12):7910–7919. doi:10.1128/AEM.71.12.7910-7919.2005.

Laruelle, G. G., Roubeix, V., Sferratore, A., Brodherr, B., Ciuffa, D., Conley, D. J., Dürr, H. H., Garnier, J., Lancelot, C., Le Thi Phuong, Q., Meunier, J.-D., Meybeck, M., Michalopoulos, P., Moriceau, B., Ní Longphuirt, S., Loucaides, S., Papush, L., Presti, M., Ragueneau, O., Regnier, P., Saccone, L., Slomp, C. P., Spiteri, C., and Van Cappellen, P. (2009). Anthropogenic perturbations of the silicon cycle at the global scale: Key role of the land-ocean transition. *Global Biogeochemical Cycles*, 23(4):n/a–n/a. doi:10.1029/2008GB003267.

Latrubesse, E. M., Arima, E. Y., Dunne, T., Park, E., Baker, V. R., D'Horta, F. M., Wight, C., Wittmann, F., Zuanon, J., Baker, P. A., Ribas, C. C., Norgaard, R. B., Filizola, N., Ansar, A., Flyvbjerg, B., and Stevaux, J. C. (2017). Damming the rivers of the Amazon basin. *Nature*, 546(7658):363–369. doi:10.1038/nature22333.

Laufkötter, C., Vogt, M., Gruber, N., Aumont, O., Bopp, L., Doney, S. C., Dunne, J. P., Hauck, J., John, J. G., Lima, I. D., Seferian, R., and Völker, C. (2016). Projected decreases in future marine export production: The role of the carbon flux through the upper ocean ecosystem. *Biogeosciences*, 13(13):4023–4047. doi:10.5194/bg-13-4023-2016.

Lauvset, S. K., Key, R. M., Olsen, A., Van Heuven, S., Velo, A., Lin, X., Schirnick, C., Kozyr, A., Tanhua, T., Hoppema, M., Jutterström, S., Steinfeldt, R., Jeansson, E., Ishii, M., Perez, F. F., Suzuki, T., and Watelet, S. (2016). A new global interior ocean mapped climatology: The 1 by 1 degree GLODAP version 2. *Earth System Science Data*, 8(2):325–340. doi:10.5194/essd-8-325-2016.

Layton, B. E., D'Souza, A. J., Dampier, W., Zeiger, A., Sabur, A., and Jean-Charles, J. (2008). Collagen's triglycine repeat number and phylogeny suggest an interdomain transfer event from a Devonian or Silurian organism into Trichodesmium erythraeum. *Journal of Molecular Evolution*, 66(6):539–554. doi:10.1007/s00239-008-9111-7.

Lee, E., Livino, A., Han, S.-C., Zhang, K., Briscoe, J., Kelman, J., and Moorcroft, P. (2018). Land cover change explains the increasing discharge of the paranáriver. *Regional environmental change*, 18(6):1871–1881. doi:10.1007/s10113-018-1321-y.

Lefévre, N., Diverrés, D., and Gallois, F. (2010). Origin of CO2undersaturation in the western tropical Atlantic. *Tellus, Series B: Chemical and Physical Meteorology*, 62(5):595–607. doi:10.1111/j.1600-0889.2010.00475.x.

Lefèvre, N., Flores Montes, M., Gaspar, F. L., Rocha, C., Jiang, S., De Araújo, M. C., and Ibánhez, J. S. P. (2017). Net Heterotrophy in the Amazon Continental Shelf Changes Rapidly to a Sink of CO2 in the Outer Amazon Plume. *Frontiers in Marine Science*, 4(September):1–16. doi:10.3389/fmars.2017.00278.

Lefévre, N., Moore, G., Aiken, J., Watson, A., Cooper, D., and Ling, R. (1998). Variability of pCO2 in the tropical Atlantic in 1995. *Journal of Geophysical Research*, 103:5623–5634.

Lefèvre, N., Tyaquiçã, P., Veleda, D., Perruche, C., and van Gennip, S. J. (2020). Amazon River propagation evidenced by a CO2 decrease at 8N, 38W in September 2013. *Journal of Marine Systems*, 211(December 2019):103419. doi:10.1016/j.jmarsys.2020.103419.

Lefèvre, N., Urbano, D. F., Gallois, F., and Diverres, D. (2014). Impact of physical processes on the seasonal distribution of the fugacity of co2 in the western tropical Atlantic. *Journal of Geophysical Research : Oceans*, pages 1–18. doi:10.1002/2013JC009248.Received.

Lentz, S. J. and Limeburner, R. (1995). The Amazon River Plume during AMASSEDS: Spatial characteristics and salinity variability. *JGR*, 100(C2):2355–2375. doi:10.1029/94JC01411.

Letelier, R. and Karl, D. (1998). Trichodesmium spp. physiology and nutrient fluxes in the North Pacific subtropical gyre. *Aquatic Microbial Ecology*, 15(1):265–276. doi:10.3354/ame015265.

Levitus, S., Boyer, T. P., Garcia, H. E., Locarnini, R. A., Zweng, M. M., Mishonov, A. V., Reagan, J. R., Antonov, J. I., Baranova, Olga K.and Biddle, M., Hamilton, M., Johnson, D. R., Paver, C. R., and Seidov, D. (2015). World Ocean Atlas 2013 (NCEI Accession 0114815). *NOAA National Centers for Environmental Information. Dataset.* doi:https://doi.org/10.7289/v5f769gt.

Lohmann, K. and Latif, M. (2007). Influence of El Niño on the Upper-Ocean Circulation in the Tropical Atlantic Ocean. *Journal of Climate*, 20(19):5012–5018. doi:10.1175/JCLI4292.1.

Louchard, D., Gruber, N., and Münnich, M. (2021). The Impact of the Amazon on the Biological Pump and the Air-Sea CO 2 Balance of the Western Tropical Atlantic. *Global Biogeochemical Cycles*, 35(6). doi:10.1029/2020GB006818.

Louchard, D., Gruber, N., and Münnich, M. (in prep.). The impact of the Amazon on the bottom-up and top-down controls on N_2 fixation in the Western Tropical Atlantic. *Global Biogeochemical Cycles*.

Lovecchio, E., Gruber, N., Münnich, M., and Lachkar, Z. (2017). On the long-range offshore transport of organic carbon from the Canary Upwelling System to the open North Atlantic. *Biogeosciences*, 14(13):3337–3369. doi:10.5194/bg-14-3337-2017.

Lumpkin, R. and Garzoli, S. L. (2005). Near-surface circulation in the Tropical Atlantic Ocean. *Deep-Sea Research Part I: Oceanographic Research Papers*, 52(3):495–518. doi:10.1016/j.dsr.2004.09.001.

Lumpkin, R. and Johnson, G. C. (2013). Global ocean surface velocities from drifters: Mean, variance, el niño–southern oscillation response, and seasonal cycle. *Journal of Geophysical Research: Oceans*, 118(6):2992–3006. doi:10.1002/jgrc.20210.

Luo, Y.-W., Doney, S. C., Anderson, L. A., Benavides, M., Berman-Frank, I., Bode, A., Bonnet, S., Boström, K. H., Böttjer, D., Capone, D. G., Carpenter, E. J., Chen, Y. L., Church, M. J., Dore, J. E., Falcón, L. I., Fernández, A., Foster, R. A., Furuya, K., Gómez, F., Gundersen, K., Hynes, A. M., Karl, D. M., Kitajima, S., Langlois, R. J., LaRoche, J., Letelier, R. M., Marañón, E., McGillicuddy, D. J., Moisander, P. H., Moore, C. M., Mouriño-Carballido, B., Mulholland, M. R., Needoba, J. A., Orcutt, K. M., Poulton, A. J., Rahav, E., Raimbault, P., Rees, A. P., Riemann, L., Shiozaki, T., Subramaniam, A., Tyrrell, T., Turk-Kubo, K. A., Varela, M., Villareal, T. A., Webb, E. A., White, A. E., Wu, J., and Zehr, J. P. (2012). Database of diazotrophs in global ocean: abundance, biomass and nitrogen fixation rates. *Earth System Science Data*, 4(1):47–73. doi:10.5194/essd-4-47-2012.

Luo, Y.-W., Lima, I. D., Karl, D. M., Deutsch, C. A., and Doney, S. C. (2014). Data-based assessment of environmental controls on global marine nitrogen fixation. *Biogeosciences*, 11(3):691–708. doi:10.5194/bg-11-691-2014.

Luo, Y. W., Shi, D., Kranz, S. A., Hopkinson, B. M., Hong, H., Shen, R., and Zhang, F. (2019). Reduced nitrogenase efficiency dominates response of the globally important nitrogen fixer Trichodesmium to ocean acidification. *Nature Communications*, 10(1):1–12. doi:10.1038/s41467-019-09554-7.

Maavara, T., Chen, Q., Van Meter, K., Brown, L. E., Zhang, J., Ni, J., and Zarfl, C. (2020). River dam impacts on biogeochemical cycling. *Nature Reviews Earth and Environment*, 1(2):103–116. doi:10.1038/s43017-019-0019-0.

Mahowald, N. M., Engelstaedter, S., Luo, C., Sealy, A., Artaxo, P., Benitez-Nelson, C., Bonnet, S., Chen, Y., Chuang, P. Y., Cohen, D. D., Dulac, F., Herut, B., Johansen, A. M., Kubilay, N., Losno, R., Maenhaut, W., Paytan, A., Prospero, J. M., Shank, L. M., and Siefert, R. L. (2009). Atmospheric Iron Deposition: Global Distribution, Variability, and Human Perturbations. *Annual Review of Marine Science*, 1(1):245–278. doi:10.1146/annurev.marine.010908.163727.

Maranger, R., Jones, S. E., and Cotner, J. B. (2018). Stoichiometry of carbon, nitrogen, and phosphorus through the freshwater pipe. *Limnology and Oceanography Letters*, 3(3):89–101. doi:10.1002/lol2.10080.

Marconi, D., Sigman, D. M., Casciotti, K. L., Campbell, E. C., Alexandra Weigand, M., Fawcett, S. E., Knapp, A. N., Rafter, P. A., Ward, B. B., and Haug, G. H. (2017). Tropical Dominance of N 2 Fixation in the North Atlantic Ocean. *Global Biogeochemical Cycles*, 31(10):1608–1623. doi:10.1002/2016GB005613.

Marengo, J. A., Borma, L. S., Rodriguez, D. A., Pinho, P., Soares, W. R., and Alves, L. M. (2013). Recent extremes of drought and flooding in amazonia: Vulnerabilities and human adaptation. *American Journal of Climate Change*, 02:87–96. doi:10.4236/ajcc.2013.22009.

Marengo, J. A. and Espinoza, J. C. (2016). Extreme seasonal droughts and floods in amazonia: causes, trends and impacts. *International Journal of Climatology*, 36(3):1033–1050. doi:https://doi.org/10.1002/joc.4420.

Marengo, J. A., Tomasella, J., Alves, L. M., Soares, W. R., and Rodriguez, D. A. (2011). The drought of 2010 in the context of historical droughts in the amazon region. *Geophysical Research Letters*, 38(12). doi:https://doi.org/10.1029/2011GL047436.

Martinez, J., Guyot, J., Filizola, N., and Sondag, F. (2009). Increase in suspended sediment discharge of the amazon river assessed by monitoring network and satellite data. *CATENA*, 79(3):257–264. doi:https://doi.org/10.1016/j.catena.2009.05.011. Sediment Sources and Sediment Delivery under Environmental Change.

Martínez-Pérez, C., Mohr, W., Löscher, C. R., Dekaezemacker, J., Littmann, S., Yilmaz, P., Lehnen, N., Fuchs, B. M., Lavik, G., Schmitz, R. A., LaRoche, J., and Kuypers, M. M. M. (2016). The small unicellular diazotrophic symbiont, UCYN-A, is a key player in the marine nitrogen cycle. *Nature Microbiology*, 1(11):16163. doi:10.1038/nmicrobiol.2016.163.

Masson, S. and Delecluse, P. (2001). Influence of the Amazon River runoff on the tropical atlantic. *Physics and Chemistry of the Earth, Part B: Hydrology, Oceans and Atmosphere*, 26(2):137–142. doi:10.1016/S1464-1909(00)00230-6.

Mayorga, E., Logsdon, M., Ballester, M., and Richey, J. (2012). Lba-eco cd-06 amazon river basin land and stream drainage direction maps. ORNL Distributed Active Archive Center. doi:10.3334/ORNLDAAC/1086.

McClain, M. E. and Elsenbeer, H. (2001). Terrestrial inputs to amazon streams and internal biogeochemical processing. In *The Biogeochemistry of the Amazon Basin*, pages 185–193. Oxford University Press.

McClain, M. E. and Naiman, R. J. (2008). Andean Influences on the Biogeochemistry and Ecology of the Amazon River. *BioScience*, 58(4):325–338. doi:10.1641/B580408.

Medeiros, P., Seidel, M., Ward, N. D., Carpenter, E., Gomes, H., Niggemann, J., Krusche, A. V., Richey, J. E., Yager, P. L., and Dittmar, T. (2015). Fate of the amazon river dissolved organic matter in the tropical atlantic ocean. *Global Biogeochemical Cycles*, pages 677–690. doi:10.1002/2015GB005115.Received.

Meyer, J., Löscher, C. R., Neulinger, S. C., Reichel, A. F., Loginova, A., Borchard, C., Schmitz, R. A., Hauss, H., Kiko, R., and Riebesell, U. (2016). Changing nutrient stoichiometry affects phytoplankton production, DOP accumulation and dinitrogen fixation – a mesocosm experiment in the eastern tropical North Atlantic. *Biogeosciences*, 13(3):781–794. doi:10.5194/bg-13-781-2016.

Miklasz, K. A. and Denny, M. W. (2010). Diatom sinking speeds: Improved predictions and insight from a modified Stoke's law. *Limnology and Oceanography*, 55(6):2513–2525. doi:10.4319/lo.2010.55.6.2513.

Molleri, G. S., Novo, E. M. M., and Kampel, M. (2010). Space-time variability of the Amazon River plume based on satellite ocean color. *Continental Shelf Research*, 30(3-4):342–352. doi:10.1016/j.csr.2009.11.015.

Monteiro, F. M., Dutkiewicz, S., and Follows, M. J. (2011). Biogeographical controls on the marine nitrogen fixers. *Global Biogeochemical Cycles*, 25(2):1–8. doi:10.1029/2010GB003902.

Montoya, J. P., Holl, C. M., Zehr, J. P., Hansen, A., Villareal, T. A., and Capone, D. G. (2004). High rates of N2 fixation by unicellular diazotrophs in the oligotrophic Pacific Ocean. *Nature*, 430(7003):1027–1031. doi:10.1038/nature02824.

Montoya, J. P., Voss, M., and Capone, D. G. (2007). Spatial variation in N2-fixation rate and diazotroph activity in the Tropical Atlantic. *Biogeosciences*, 4(3):369–376. doi:10.5194/bg-4-369-2007.

Moore, C. M., Mills, M. M., Achterberg, E. P., Geider, R. J., LaRoche, J., Lucas, M. I., McDonagh, E. L., Pan, X., Poulton, A. J., Rijkenberg, M. J. A., Suggett, D. J., Ussher, S. J., and Woodward, E. M. S. (2009). Large-scale distribution of Atlantic nitrogen fixation controlled by iron availability. *Nature Geoscience*, 2(12):867–871. doi:10.1038/ngeo667.

Moore, C. M., Mills, M. M., Arrigo, K. R., Berman-Frank, I., Bopp, L., Boyd, P. W., Galbraith, E. D., Geider, R. J., Guieu, C., Jaccard, S. L., Jickells, T. D., La Roche, J., Lenton, T. M., Mahowald, N. M., Marañón, E., Marinov, I., Moore, J. K., Nakatsuka, T., Oschlies, A., Saito, M. A., Thingstad, T. F., Tsuda, A., and Ulloa, O. (2013a). Processes and patterns of oceanic nutrient limitation. *Nature Geoscience*, 6(9):701–710. doi:10.1038/ngeo1765.

Moore, C. M., Mills, M. M., Arrigo, K. R., Berman-Frank, I., Bopp, L., Boyd, P. W., Galbraith, E. D., Geider, R. J., Guieu, C., Jaccard, S. L., Jickells, T. D., La Roche, J., Lenton, T. M., Mahowald, N. M., Marañón, E., Marinov, I., Moore, J. K., Nakatsuka, T., Oschlies, A., Saito, M. A., Thingstad, T. F., Tsuda, A., and Ulloa, O. (2013b). Processes and patterns of oceanic nutrient limitation. *Nature Geoscience*, 6(9):701–710. doi:10.1038/ngeo1765.

Moore, J., Doney, S. C., Kleypas, J. A., Glover, D. M., and Fung, I. Y. (2001). An intermediate complexity marine ecosystem model for the global domain. *Deep Sea Research Part II: Topical Studies in Oceanography*, 49(1-3):403–462. doi:10.1016/S0967-0645(01)00108-4.

Moore, J. K., Lindsay, K., Doney, S. C., Long, M. C., and Misumi, K. (2013c). Marine ecosystem dynamics and biogeochemical cycling in the community earth system model [CESM1(BGC)]: Comparison of the 1990s with the 2090s under the RCP4.5 and RCP8.5 scenarios. *Journal of Climate*. doi:10.1175/JCLI-D-12-00566.1.

Moore, J. K., Lindsay, K., Doney, S. C., Long, M. C., and Misumi, K. (2013d). Marine Ecosystem Dynamics and Biogeochemical Cycling in the Community Earth System Model [CESM1(BGC)]: Comparison of the 1990s with the 2090s under the RCP4.5 and RCP8.5 Scenarios. *Journal of Climate*, 26(23):9291–9312. doi:10.1175/JCLI-D-12-00566.1.

Moquet, J. S., Guyot, J. L., Crave, A., Viers, J., Filizola, N., Martinez, J. M., Oliveira, T. C., Sánchez, L. S. H., Lagane, C., Casimiro, W. S. L., Noriega, L., and Pombosa, R. (2016). Amazon river dissolved load: temporal dynamics and annual budget from the andes to the ocean. *Environmental Science and Pollution Research*, 23:11405–11429. doi:10.1007/s11356-015-5503-6.

Moreira-Turcq, P., Seyler, P., Guyot, J. L., and Etcheber, H. (2003). Exportation of organic carbon from the amazon river and its main tributaries. *Hydrological Processes*, 17(7):1329–1344. doi:https://doi.org/10.1002/hyp.1287.

Mu, L., Gomes, H. d. R., Burns, S. M., Goes, J. I., Coles, V. J., Rezende, C. E., Thompson, F. L., Moura, R. L., Page, B., and Yager, P. L. (2021). Temporal Variability of Air-Sea CO2 flux in the Western Tropical North Atlantic Influenced by the Amazon River Plume. *Global Biogeochemical Cycles*, 35(6):1–17. doi:10.1029/2020GB006798.

Mulholland, M. R. and Capone, D. G. (2001). Stoichiometry of nitrogen and carbon utilization in cultured populations of Trichodesmium IMS101: Implications for growth. *Limnology and Oceanography*, 46(2):436–443. doi:10.4319/lo.2001.46.2.0436.

Muller, M. (2019). Hydropower dams can help mitigate the global warming impact of wetlands. *Nature*, 566(7744):315–317. doi:10.1038/d41586-019-00616-w.

Muller-Karger, F. E., McClain, C. R., and Richardson, P. L. (1988). The dispersal of the Amazon's water. *Nature*, 333(6168):56–59. doi:10.1038/333056a0.

Nakhavali, M., Lauerwald, R., Regnier, P., Guenet, B., Chadburn, S., and Friedlingstein, P. (2021). Leaching of dissolved organic carbon from mineral soils plays a significant role in the terrestrial carbon balance. *Global Change Biology*, 27:1083–1096. doi:10.1111/gcb.15460.

Nissen, C. (2019). *Southern Ocean phytoplankton biogeography: Controlling factors and implications for biogeochemistry*. PhD thesis.

Nissen, C., Vogt, M., Münnich, M., Gruber, N., and Alexander Haumann, F. (2018). Factors controlling coccolithophore biogeography in the Southern Ocean. *Biogeosciences*, 15(22):6997–7024. doi:10.5194/bg-15-6997-2018.

Nittrouer, C. A. and DeMaster, D. J. (1996). The amazon shelf setting: tropical, energetic, and influenced by a large river. *Continental Shelf Research*, 16(5):553–573. doi:https://doi.org/10.1016/0278-4343(95)00069-0.

Nittrouer, C. A., DeMaster, D. J., Kuehl, S. A., Figueiredo, A. G., Sternberg, R. W., Ercilio, L., Faria, C., Silveira, O. M., Allison, M. A., Kineke, G. C., Ogston, A. S., Filho, P. W. M. S., Asp, N. E., Nowacki, D. J., and Fricke, A. T. (2021). Amazon sediment transport and accumulation along the continuum of mixed fluvial and marine processes. doi:10.1146/annurev-marine-010816.

Nixon, S. W., Ammerman, J. W., Atkinson, L. P., Berounsky, V. M., Billen, G., Boicourt, W. C., Boynton, W. R., Church, T. M., Ditoro, D. M., Elmgren, R., Garber, J. H., Giblin, A. E., Jahnke, R. A., Owens, N. J. P., Pilson, M. E. Q., and Seitzinger, S. P. (1996). The fate of nitrogen and phosphorus at the land-sea margin of the north atlantic ocean. *Biogeochemistry*, 35:141–180. doi:10.1007/BF02179826.

Orchard, E. D., Ammerman, J. W., Lomas, M. W., and Dyhrman, S. T. (2010). Dissolved inorganic and organic phosphorus uptake in trichodesmium and the microbial community: The importance of phosphorus ester in the sargasso sea. *Limnology and Oceanography*, 55(3):1390–1399. doi:https://doi.org/10.4319/lo.2010.55.3.1390.

Pailler, K., Bourlès, B., and Gouriou, Y. (1999). The barrier layer in the western tropical atlantic ocean. *Geophysical Research Letters*, 26(14):2069–2072. doi:10.1029/1999GL900492.

Paulsen, H., Ilyina, T., Six, K. D., and Stemmler, I. (2017). Incorporating a prognostic representation of marine nitrogen fixers into the global ocean biogeochemical model hamocc. *Journal of Advances in Modeling Earth Systems*, 9(1):438–464. doi:https://doi.org/10.1002/2016MS000737.

Philander, S. G. H. and Pacanowski, R. C. (1986). The mass and heat budget in a model of the tropical atlantic ocean. *Journal of Geophysical Research: Oceans*, 91(C12):14212–14220. doi:https://doi.org/10.1029/JC091iC12p14212.

Pierella Karlusich, J. J., Pelletier, E., Lombard, F., Carsique, M., Dvorak, E., Colin, S., Picheral, M., Cornejo-Castillo, F. M., Acinas, S. G., Pepperkok, R., Karsenti, E., de Vargas, C., Wincker, P., Bowler, C., and Foster, R. A. (2021). Global distribution patterns of marine nitrogen-fixers by imaging and molecular methods. *Nature Communications*, 12(1):4160. doi:10.1038/s41467-021-24299-y.

Pyle, A. E., Johnson, A. M., and Villareal, T. A. (2020). Isolation, growth, and nitrogen fixation rates of the Hemiaulus-Richelia (diatom-cyanobacterium) symbiosis in culture. *PeerJ*, 8:1–25. doi:10.7717/peerj.10115.

Ran, X., Yu, Z., Yao, Q., Chen, H., and Guo, H. (2013). Silica retention in the Three Gorges Reservoir. *Biogeochemistry*, 112(1-3):209–228. doi:10.1007/s10533-012-9717-0.

Raymond, P. A., Hartmann, J., Lauerwald, R., Sobek, S., McDonald, C., Hoover, M., Butman, D., Striegl, R., Mayorga, E., Humborg, C., Kortelainen, P., Dürr, H., Meybeck, M., Ciais, P., and Guth, P. (2013). Global carbon dioxide emissions from inland waters. *Nature*, 503:355–359. doi:10.1038/nature12760.

Regnier, P., Friedlingstein, P., Ciais, P., Mackenzie, F. T., Gruber, N., Janssens, I. A., Laruelle, G. G., Lauerwald, R., Luyssaert, S., Andersson, A. J., Arndt, S., Arnosti, C., Borges, A. V., Dale, A. W., Gallego-Sala, A., Goddéris, Y., Goossens, N., Hartmann, J., Heinze, C., Ilyina, T., Joos, F., Larowe, D. E., Leifeld, J., Meysman, F. J., Munhoven, G., Raymond, P. A., Spahni, R., Suntharalingam, P., and Thullner, M. (2013). Anthropogenic perturbation of the carbon fluxes from land to ocean. *Nature Geoscience*, 6:597–607. doi:10.1038/ngeo1830.

Resplandy, L., Keeling, R. F., Rödenbeck, C., Stephens, B. B., Khatiwala, S., Rodgers, K. B., Long, M. C., Bopp, L., and Tans, P. P. (2018). Revision of global carbon fluxes based on a reassessment of oceanic and riverine carbon transport. *Nature Geoscience*, 11:504–509. doi:10.1038/s41561-018-0151-3.

Richey, J. E., Melack, J. M., Aufdenkampe, A. K., Ballester, V. M., and Hess, L. L. (2002). Outgassing from amazonian rivers and wetlands as a large tropical source of atmospheric co2. *Nature*, 416(6881):617–620. doi:10.1038/416617a.

Richey, J. E., Nobre, C., and Deser, C. (1989). Amazon River Discharge and Climate Variability: 1903 to 1985. *Science*, 246(4926):101–103. doi:10.1126/science.246.4926.101.

Richey, J. E., Victoria, R. L., Salati, E., and Forsberg, B. R. (1991). *Biogeochemistry of Mqjor World Rivers*, chapter Biogeochemical Processes on the Amazon Shelf: Changes in Diisolved and Particulate Fluxes During River/Ocean Mixing, pages 57 – 74. John Wiley and Sons, New York.

Sailley, S. F., Vogt, M., Doney, S. C., Aita, M. N., Bopp, L., Buitenhuis, E. T., Hashioka, T., Lima, I., Le Quéré, C., and Yamanaka, Y. (2013). Comparing food web structures and dynamics across a suite of global marine ecosystem models. *Ecological Modelling*, 261-262:43–57. doi:10.1016/j.ecolmodel.2013.04.006.

Salati, E. and Vose, P. B. (1984). Amazon basin: A system in equilibrium. *Science*, 225(4658):129–138. doi:10.1126/science.225.4658.129.

Salisbury, J., Vandemark, D., Campbell, J., Hunt, C., Wisser, D., Reul, N., and Chapron, B. (2011). Spatial and temporal coherence between amazon river discharge, salinity, and light absorption by colored organic carbon in western tropical atlantic surface waters. *Journal of Geophysical Research: Oceans*, 116(C7). doi:https://doi.org/10.1029/2011JC006989.

Sañudo-Wilhelmy, S. A., Kustka, A. B., Gobler, C. J., Hutchins, D. A., Yang, M., Lwiza, K., Burns, J., Capone, D. G., Raven, J. A., and Carpenter, E. J. (2001). Phosphorus limitation of nitrogen fixation by Trichodesmium in the central Atlantic Ocean. *Nature*, 411(6833):66–69. doi:10.1038/35075041.

Sarmiento, J. L. and Gruber, N. (2006). *Ocean Biogeochemical Dynamics*. Princeton University Press, Princeton.

Sawakuchi, H. O., Neu, V., Ward, N. D., Barros, M. d. L. C., Valerio, A. M., Gagne-Maynard, W., Cunha, A. C., Less, D. F. S., Diniz, J. E. M., Brito, D. C., Krusche, A. V., and Richey, J. E. (2017). Carbon Dioxide Emissions along the Lower Amazon River. *Frontiers in Marine Science*, 4(March):1–12. doi:10.3389/fmars.2017.00076.

Schlosser, C., Klar, J. K., Wake, B. D., Snow, J. T., Honey, D. J., Woodward, E. M. S., Lohan, M. C., Achterberg, E. P., and Moore, C. M. (2014). Seasonal ITCZ migration dynamically controls the location of the (sub)tropical Atlantic biogeochemical divide. *Proceedings of the National Academy of Sciences*, 111(4):1438–1442. doi:10.1073/pnas.1318670111.

Schmidt, N., Fauvelle, V., Ody, A., Castro-Jiménez, J., Jouanno, J., Changeux, T., Thibaut, T., and Sempéré, R. (2019). The amazon river: A major source of organic plastic additives to the tropical north atlantic? *Environmental Science & Technology*, 53(13):7513–7521. doi:10.1021/acs.est.9b01585.

Schuster, U., McKinley, G. a., Bates, N., Chevallier, F., Doney, S. C., Fay, a. R., González-Dávila, M., Gruber, N., Jones, S., Krijnen, J., Landschützer, P., Lefèvre, N., Manizza, M., Mathis, J., Metzl, N., Olsen, A., Rios, a. F., Rödenbeck, C., Santana-Casiano, J. M., Takahashi, T., Wanninkhof, R., and Watson, a. J. (2013). An assessment of the Atlantic and Arctic sea–air CO2 fluxes, 1990–2009. *Biogeosciences*, 10(1):607–627. doi:10.5194/bg-10-607-2013.

Seidel, M., Dittmar, T., Ward, N. D., Krusche, A. V., Richey, J. E., Yager, P. L., and Medeiros, P. M. (2016). Seasonal and spatial variability of dissolved organic matter composition in the lower amazon river. *Biogeochemistry*, 131:281–302. doi:10.1007/s10533-016-0279-4.

Seitzinger, S. P. and Giblin, A. E. (1996). Estimating denitrification in north atlantic continental shelf sediments. *Biogeochemistry*, 35:235–260. doi:10.1007/BF02179829.

Seitzinger, S. P., Harrison, J. A., Dumont, E., Beusen, A. H. W., and Bouwman, A. F. (2005). Sources and delivery of carbon, nitrogen, and phosphorus to the coastal zone: An overview of Global Nutrient Export from Watersheds (NEWS) models and their application. *Global Biogeochemical Cycles*, 19(4). doi:10.1029/2005GB002606.

Sharples, J., Middelburg, J. J., Fennel, K., and Jickells, T. D. (2017). What proportion of riverine nutrients reaches the open ocean? *Global Biogeochemical Cycles*, 31(1):39–58. doi:10.1002/2016GB005483.

Shchepetkin, A. F. and McWilliams, J. C. (2005). The regional oceanic modeling system (ROMS): A split-explicit, free-surface, topography-following-coordinate oceanic model. *Ocean Modelling*, 9(4):347–404. doi:10.1016/j.ocemod.2004.08.002.

Shiozaki, T., Fujiwara, A., Ijichi, M., Harada, N., Nishino, S., Nishi, S., Nagata, T., and Hamasaki, K. (2018). Diazotroph community structure and the role of nitrogen fixation in the nitrogen cycle in the chukchi sea (western arctic ocean). *Limnology and Oceanography*, 63(5):2191–2205. doi:https://doi.org/10.1002/lno.10933.

Shipe, R. F., Curtaz, J., Subramaniam, A., Carpenter, E. J., and Capone, D. G. (2006). Diatom biomass and productivity in oceanic and plume-influenced waters of the western tropical Atlantic ocean. *Deep-Sea Research Part I: Oceanographic Research Papers*, 53(8):1320–1334. doi:10.1016/j.dsr.2006.05.013.

Sioli, H. (1984). The Amazon and its main affluents: Hydrography, morphology of the river courses, and river types. pages 127–165. doi:10.1007/978-94-009-6542-3_5.

Smith, W. O. and DeMaster, D. J. (1996). Phytoplankton biomass and productivity in the Amazon River plume: Correlation with seasonal river discharge. *Continental Shelf Research*, 16(3):291–319. doi:10.1016/0278-4343(95)00007-N.

Soetaert, K., Herman, P. M., and Middelburg, J. J. (1996). A model of early diagenetic processes from the shelf to abyssal depths. *Geochimica et Cosmochimica Acta*, 60(6):1019 – 1040. doi:https://doi.org/10.1016/0016-7037(96)00013-0.

Sohm, J. A. and Capone, D. G. (2010a). Zonal differences in phosphorus pools, turnover and deficiency across the tropical North Atlantic Ocean. *Global Biogeochemical Cycles*, 24(2):1–9. doi:10.1029/2008GB003414.

Sohm, J. A. and Capone, D. G. (2010b). Zonal differences in phosphorus pools, turnover and deficiency across the tropical North Atlantic Ocean. *Global Biogeochemical Cycles*, 24(2). doi:10.1029/2008GB003414.

Sohm, J. A., Mahaffey, C., and Capone, D. G. (2008). Assessment of relative phosphorus limitation of Trichodesmium spp. in the North Pacific, North Atlantic, and the north coast of Australia. *Limnology and Oceanography*, 53(6):2495–2502. doi:10.4319/lo.2008.53.6.2495.

Sohm, J. A., Webb, E. A., and Capone, D. G. (2011). Emerging patterns of marine nitrogen fixation. *Nature Reviews Microbiology*, 9(7):499–508. doi:10.1038/nrmicro2594.

Song, C., Gardner, K. H., Klein, S. J., Souza, S. P., and Mo, W. (2018). Cradle-to-grave greenhouse gas emissions from dams in the united states of america. *Renewable and Sustainable Energy Reviews*, 90:945–956. doi:https://doi.org/10.1016/j.rser.2018.04.014.

Stal, L. J. (2009). Is the distribution of nitrogen-fixing cyanobacteria in the oceans related to temperature?: Minireview. *Environmental Microbiology*, 11(7):1632–1645. doi:10.1111/j.1758-2229.2009.00016.x.

Steinberg, D. K. and Landry, M. R. (2017). Zooplankton and the Ocean Carbon Cycle. *Annual Review of Marine Science*, 9(1):413–444. doi:10.1146/annurev-marine-010814-015924.

Stenegren, M., Berg, C., Padilla, C. C., David, S. S., Montoya, J. P., Yager, P. L., and Foster, R. A. (2017). Piecewise Structural Equation Model (SEM) disentangles the environmental conditions favoring Diatom Diazotroph Associations (DDAs) in the Western Tropical North Atlantic (WTNA). *Frontiers in Microbiology*, 8(MAY):1–13. doi:10.3389/fmicb.2017.00810.

Stickler, C. M., Coe, M. T., Costa, M. H., Nepstad, D. C., McGrath, D. G., Dias, L. C. P., Rodrigues, H. O., and Soares-Filho, B. S. (2013). Dependence of hydropower energy generation on forests in the amazon basin at local and regional scales. *Proceedings of the National Academy of Sciences of the United States of America*, 110(23):9601–9606. doi:10.1073/pnas.1215331110.

Stocker, T., Qin, D., Plattner, G.-K., Alexander, L., Allen, S., Bindoff, N., Breon, F.-M., Church, J., Cubasch, U., Emori, S., Forster, P., Friedlingstein, P., Gillett, N., Gregory, J., Hartmann, D., Jansen, E., Kirtman, B., Knutti, R., Krishna Kumar, K., Lemke, P., Marotzke, J., Masson-Delmotte, V., Meehl, G., Mokhov, I., Piao, S., Ramaswamy, V., Randall, D., Rhein, M., Rojas, M., Sabine, C., Shindell, D., Talley, L., Vaughan, D., and Xie, S.-P. (2013). *Technical Summary*, book section TS, p. 33–115. Cambridge University Press, Cambridge, United Kingdom and New York, NY, USA. doi:10.1017/CBO9781107415324.005.

Stramma, L. and Schott, F. (1999). The mean flow field of the tropical Atlantic Ocean. *Deep Sea Research Part II: Topical Studies in Oceanography*, 46(1-2):279–303. doi:10.1016/S0967-0645(98)00109-X.

Struyf, E., Smis, A., Van Damme, S., Garnier, J., Govers, G., Van Wesemael, B., Conley, D. J., Batelaan, O., Frot, E., Clymans, W., Vandevenne, F., Lancelot, C., Goos, P., and Meire, P. (2010). Historical land use change has lowered terrestrial silica mobilization. *Nature Communications*, 1(1):129. doi:10.1038/ncomms1128.

Stukel, M. R., Coles, V. J., Brooks, M. T., and Hood, R. R. (2014). Top-down, bottom-up and physical controls on diatom-diazotroph assemblage growth in the Amazon River plume. *Biogeosciences*, 11(12):3259–3278. doi:10.5194/bg-11-3259-2014.

Subramaniam, A., Yager, P. L., Carpenter, E. J., Mahaffey, C., Björkman, K., Cooley, S., Kustka, A. B., Montoya, J. P., Sañudo-Wilhelmy, S. A., Shipe, R., and Capone, D. G. (2008a). Amazon river enhances diazotrophy and carbon sequestration in the tropical north atlantic ocean. *Proceedings of the National Academy of Sciences*, 105(30):10460–10465. doi:10.1073/pnas.0710279105.

Subramaniam, A., Yager, P. L., Carpenter, E. J., Mahaffey, C., Bjorkman, K., Cooley, S., Kustka, A. B., Montoya, J. P., Sanudo-Wilhelmy, S. A., Shipe, R., and Capone, D. G. (2008b). Amazon River enhances diazotrophy and carbon sequestration in the tropical North Atlantic Ocean. *Proceedings of the National Academy of Sciences*, 105(30):10460–10465. doi:10.1073/pnas.0710279105.

Sverdrup, H. U. (1953). On Conditions for the Vernal Blooming of Phytoplankton. *ICES Journal of Marine Science*, 18(3):287–295. doi:10.1093/icesjms/18.3.287.

Syvitski, J. P. and Saito, Y. (2007). Morphodynamics of deltas under the influence of humans. *Global and Planetary Change*, 57(3):261–282. doi:https://doi.org/10.1016/j.gloplacha.2006.12.001.

Takahashi, T., Sutherland, S. C., Wanninkhof, R., Sweeney, C., Feely, R. A., Chipman, D. W., Hales, B., Friederich, G., Chavez, F., Sabine, C., Watson, A., Bakker, D. C., Schuster, U., Metzl, N., Yoshikawa-Inoue, H., Ishii, M., Midorikawa, T., Nojiri, Y., Körtzinger, A., Steinhoff, T., Hoppema, M., Olafsson, J., Arnarson, T. S., Tilbrook, B., Johannessen, T., Olsen, A., Bellerby, R., Wong, C., Delille, B., Bates, N., and de Baar, H. J. (2009). Climatological mean and decadal change in surface ocean pco2, and net sea–air co2 flux over the global oceans. *Deep Sea Research Part II: Topical Studies in Oceanography*, 56(8):554 – 577. doi:https://doi.org/10.1016/j.dsr2.2008.12.009. Surface Ocean CO2 Variability and Vulnerabilities.

Tang, W. and Cassar, N. (2019). Data-Driven Modeling of the Distribution of Diazotrophs in the Global Ocean. *Geophysical Research Letters*, 46(21):12258–12269. doi:10.1029/2019GL084376.

Tang, W., Li, Z., and Cassar, N. (2019a). Machine Learning Estimates of Global Marine Nitrogen Fixation. *Journal of Geophysical Research: Biogeosciences*, 124(3):717–730. doi:10.1029/2018JG004828.

Tang, W., Wang, S., Fonseca-Batista, D., Dehairs, F., Gifford, S., Gonzalez, A. G., Gallinari, M., Planquette, H., Sarthou, G., and Cassar, N. (2019b). Revisiting the distribution of oceanic N 2 fixation and estimating diazotrophic contribution to marine production. *Nature Communications*, 10(1):1–10. doi:10.1038/s41467-019-08640-0.

Terhaar, J., Lauerwald, R., Regnier, P., Gruber, N., and Bopp, L. (2021). Around one third of current arctic ocean primary production sustained by rivers and coastal erosion. *Nature Communications*, 12(1):169. doi:10.1038/s41467-020-20470-z.

Ternon, J. F., Oudot, C., Dessier, A., and Diverres, D. (2000). A seasonal tropical sink for atmospheric CO2 in the Atlantic ocean: The role of the Amazon River discharge. *Marine Chemistry*, 68(3):183–201. doi:10.1016/S0304-4203(99)00077-8.

Tilman, D. (1982). *Resource Competition and Community Structure. (MPB-17), Volume 17*. Princeton University Press.

Torres-Valdés, S., Tsubouchi, T., Bacon, S., Naveira-Garabato, A. C., Sanders, R., McLaughlin, F. A., Petrie, B., Kattner, G., Azetsu-Scott, K., and Whitledge, T. E. (2013). Export of nutrients from the Arctic Ocean. *Journal of Geophysical Research: Oceans*, 118(4):1625–1644. doi:10.1002/jgrc.20063.

Tranvik, L. J., Downing, J. A., Cotner, J. B., Loiselle, S. A., Striegl, R. G., Ballatore, T. J., Dillon, P., Finlay, K., Fortino, K., Knoll, L. B., Kortelainen, P. L., Kutser, T., Larsen, S., Laurion, I., Leech, D. M., McCallister, S. L., McKnight, D. M., Melack, J. M., Overholt, E., Porter, J. A., Prairie, Y., Renwick, W. H., Roland, F., Sherman, B. S., Schindler, D. W., Sobek, S., Tremblay, A., Vanni, M. J., Verschoor, A. M., von Wachenfeldt, E., and Weyhenmeyer, G. A. (2009). Lakes and reservoirs as regulators of carbon cycling and climate. *Limnology and Oceanography*, 54(6part2):2298–2314. doi:https://doi.org/10.4319/lo.2009.54.6_part_2.2298.

Tuo, S.-H., Lee Chen, Y.-L., Chen, H.-Y., and Chen, T.-Y. (2017). Free-living heterocystous cyanobacteria in the tropical marginal seas of the western North Pacific. *Journal of Plankton Research*, 39(3):404–422. doi:10.1093/plankt/fbx023.

Tyler, A. N., Hunter, P. D., Spyrakos, E., Groom, S., Constantinescu, A. M., and Kitchen, J. (2016). Developments in earth observation for the assessment and monitoring of inland, transitional, coastal and shelf-sea waters. *Science of The Total Environment*, 572:1307 – 1321. doi:https://doi.org/10.1016/j.scitotenv.2016.01.020.

Valerio, A. M., Kampel, M., Ward, N. D., Sawakuchi, H. O., Cunha, A. C., and Richey, J. E. (2021). CO2 partial pressure and fluxes in the Amazon River plume using in situ and remote sensing data. *Continental Shelf Research*, 215(December 2020):104348. doi:10.1016/j.csr.2021.104348.

Vandemeulebrouck, R. (2020). Implementation and analysis of a weno scheme. Master's thesis, Faculty of Maths, Computational Science - CSE EPFL.

Vandevenne, F., Struyf, E., Clymans, W., and Meire, P. (2012). Agricultural silica harvest: have humans created a new loop in the global silica cycle? *Frontiers in Ecology and the Environment*, 10(5):243–248. doi:https://doi.org/10.1890/110046.

Voss, M., Bange, H. W., Dippner, J. W., Middelburg, J. J., Montoya, J. P., and Ward, B. (2013). The marine nitrogen cycle: recent discoveries, uncertainties and the potential relevance of climate change. *Philosophical Transactions of the Royal Society B: Biological Sciences*, 368(1621):20130121. doi:10.1098/rstb.2013.0121.

Voss, M., Bombar, D., Loick, N., and Dippner, J. W. (2006). Riverine influence on nitrogen fixation in the upwelling region off Vietnam, South China Sea. *Geophysical Research Letters*, 33(7):4–7. doi:10.1029/2005GL025569.

Wang, W.-L., Moore, J. K., Martiny, A. C., and Primeau, F. W. (2019). Convergent estimates of marine nitrogen fixation. *Nature*, 566(7743):205–211. doi:10.1038/s41586-019-0911-2.

Ward, B. A., Dutkiewicz, S., Moore, C. M., and Follows, M. J. (2013a). Iron, phosphorus, and nitrogen supply ratios define the biogeography of nitrogen fixation. *Limnology and Oceanography*, 58(6):2059–2075. doi:10.4319/lo.2013.58.6.2059.

Ward, N. D., Bianchi, T. S., Medeiros, P. M., Seidel, M., Richey, J. E., Keil, R. G., and Sawakuchi, H. O. (2017). Where carbon goes when water flows: Carbon cycling across the aquatic continuum. *Frontiers in Marine Science*, 4. doi:10.3389/fmars.2017.00007.

Ward, N. D., Bianchi, T. S., Sawakuchi, H. O., Gagne-Maynard, W., Cunha, A. C., Brito, D. C., Neu, V., de Matos Valerio, A., da Silva, R., Krusche, A. V., Richey, J. E., and Keil, R. G. (2016). The reactivity of plant-derived organic matter and the potential importance of priming effects along the lower amazon river. *Journal of Geophysical Research: Biogeosciences*, 121(6):1522–1539. doi:https://doi.org/10.1002/2016JG003342.

Ward, N. D., Keil, R. G., Medeiros, P. M., Brito, D. C., Cunha, A. C., Dittmar, T., Yager, P. L., Krusche, A. V., and Richey, J. E. (2013b). Degradation of terrestrially derived macromolecules in the amazon river. *Nature Geoscience*, 6(7):530–533. doi:10.1038/ngeo1817.

Ward, N. D., Krusche, A. V., Sawakuchi, H. O., Brito, D. C., Cunha, A. C., Moura, J. M. S., da Silva, R., Yager, P. L., Keil, R. G., and Richey, J. E. (2015). The compositional evolution of dissolved and particulate organic matter along the lower amazon river-Óbidos to the ocean. *Marine Chemistry*, 177:244–256. doi:10.1016/j.marchem.2015.06.013.

Watkins-Brandt, K. S., Letelier, R. M., Spitz, Y. H., Church, M. J., Böttjer, D., and White, A. E. (2011). Addition of inorganic or organic phosphorus enhances nitrogen and carbon fixation in the oligotrophic North Pacific. *Marine Ecology Progress Series*, 432:17–29. doi:10.3354/meps09147.

Webb, E. A., Jakuba, R. W., Moffett, J. W., and Dyhrman, S. T. (2007). Molecular assessment of phosphorus and iron physiology in Trichodesmium populations from the western Central and western South Atlantic. *Limnology and Oceanography*, 52(5):2221–2232. doi:10.4319/lo.2007.52.5.2221.

Weber, S. C., Carpenter, E. J., Coles, V. J., Yager, P. L., Goes, J., and Montoya, J. P. (2017). Amazon River influence on nitrogen fixation and export production in the western tropical North Atlantic. *Limnology and Oceanography*, 62(2):618–631. doi:10.1002/lno.10448.

Weber, S. C., Loick-Wilde, N., Montoya, J. P., Bach, M., Doan-Nhu, H., Subramaniam, A., Liskow, I., Nguyen-Ngoc, L., Wodarg, D., and Voss, M. (2021). Environmental Regulation of the Nitrogen Supply, Mean Trophic Position, and Trophic Enrichment of Mesozooplankton in the Mekong River Plume and Southern South China Sea. *Journal of Geophysical Research: Oceans*, 126(8):1–19. doi:10.1029/2020JC017110.

Westberry, T., Behrenfeld, M. J., Siegel, D. A., and Boss, E. (2008). Carbon-based primary productivity modeling with vertically resolved photoacclimation. *Global Biogeochemical Cycles*, 22(2). doi:10.1029/2007GB003078.

Westberry, T. K., Siegel, D. A., and Subramaniam, A. (2005). An improved bio-optical model for the remote sensing of trichodesmium spp. blooms. *Journal of Geophysical Research: Oceans*, 110(C6). doi:https://doi.org/10.1029/2004JC002517.

Williams, R. G. and Follows, M. J. (2003). Physical Transport of Nutrients and the Maintenance of Biological Production. In *Ocean Biogeochemistry*, pages 19–51. Springer Berlin Heidelberg, Berlin, Heidelberg. doi:10.1007/978-3-642-55844-3.

Winemiller, K. O., McIntyre, P. B., Castello, L., Fluet-Chouinard, E., Giarrizzo, T., Nam, S., Baird, I. G., Darwall, W., Lujan, N. K., Harrison, I., Stiassny, M. L. J., Silvano, R. A. M., Fitzgerald, D. B., Pelicice, F. M., Agostinho, A. A., Gomes, L. C., Albert, J. S., Baran, E., Petrere, M., Zarfl, C., Mulligan, M., Sullivan, J. P., Arantes, C. C., Sousa, L. M., Koning, A. A., Hoeinghaus, D. J., Sabaj, M., Lundberg, J. G., Armbruster, J., Thieme, M. L., Petry, P., Zuanon, J., Vilara, G. T., Snoeks, J., Ou, C., Rainboth, W., Pavanelli, C. S., Akama, A., van Soesbergen, A., and Sáenz, L. (2016). Balancing hydropower and biodiversity in the amazon, congo, and mekong. *Science*, 351(6269):128–129. doi:10.1126/science.aac7082.

Wrightson, L. and Tagliabue, A. (2020). Quantifying the Impact of Climate Change on Marine Diazotrophy: Insights From Earth System Models. *Frontiers in Marine Science*, 7:635. doi:10.3389/fmars.2020.00635.

Xenopoulos, M. A., Downing, J. A., Kumar, M. D., Menden-Deuer, S., and Voss, M. (2017). Headwaters to oceans: Ecological and biogeochemical contrasts across the aquatic continuum. *Limnology and Oceanography*, 62(S1):S3–S14. doi:10.1002/lno.10721.

Yang, S., Gruber, N., Long, M. C., and Vogt, M. (2017). Enso-driven variability of denitrification and suboxia in the eastern tropical pacific ocean. *Global Biogeochemical Cycles*, 31(10):1470–1487. doi:10.1002/2016GB005596.

Yeung, L. Y., Berelson, W. M., Young, E. D., Prokopenko, M. G., Rollins, N., Coles, V. J., Montoya, J. P., Carpenter, E. J., Steinberg, D. K., Foster, R. A., Capone, D. G., and Yager, P. L. (2012). Impact of diatom-diazotroph associations on carbon export in the Amazon River plume. *Geophysical Research Letters*, 39(17):1–6. doi:10.1029/2012GL053356.

Yoon, J.-H. and Zeng, N. (2010). An Atlantic influence on Amazon rainfall. *Climate Dynamics*, 34(2-3):249–264. doi:10.1007/s00382-009-0551-6.

Zehr, J. P. and Capone, D. G. (2020). Changing perspectives in marine nitrogen fixation. *Science*, 368(6492). doi:10.1126/science.aay9514.

Zehr, J. P. and Capone, D. G. (2021a). Chapter 5 measurements of organism abundances and activities. In *Marine Nitrogen Fixation*, pages 62–93. Springer International Publishing, Cham. doi:10.1007/978-3-030-67746-6.

Zehr, J. P. and Capone, D. G. (2021b). Chapter 7 biogeography of N_2 fixation in the surface ocean. In *Marine Nitrogen Fixation*, pages 117–141. Springer International Publishing, Cham. doi:10.1007/978-3-030-67746-6.

Zehr, J. P., Shilova, I. N., Farnelid, H. M., Muñoz-Marín, M. d. C., and Turk-Kubo, K. A. (2017). Unusual marine unicellular symbiosis with the nitrogen-fixing cyanobacterium UCYN-A. *Nature Microbiology*, 2(1):16214. doi:10.1038/nmicrobiol.2016.214.

Zeng, N., Yoon, J.-H., Marengo, J. A., Subramaniam, A., Nobre, C. A., Mariotti, A., and Neelin, J. D. (2008). Causes and impacts of the 2005 amazon drought. *Environmental Research Letters*, 3:014002. doi:10.1088/1748-9326/3/1/014002.

Zhao, Y., Louchard, D., Munnich, M., and Gruber, N. (in prep.). Modulation of the seawater n:p stoichiometry from the amazon river to the western tropical atlantic.

Acknowlegments

Doing a PhD has been an exhilarating, challenging, exhausting, disconcerting, demanding and incredible experience. But it has not been a solitary one and many people participated to its success.

First and foremost, I want to thank you, Niki. I am grateful beyond words for the opportunity you gave me to work in such a stimulating research environment, for all the guidance and the unfailing support. Leading by the example, you have been an inspiring figure throughout my PhD. I am also very grateful for your attentive help in finding a healthy work-life balance and in navigating the blows of fate.

Thank you also to you, Matt, for all your support, for always keeping a door open, for the endless discussions on ROMS and BEC. You showed me the importance of patience and persistence when dealing with models.

I would like to thank you, Tim, for following the project (almost) from the beginning, for your guidance during our annual meetings and for accepting to be a co-examiner.

Thank you Meike for the interesting discussions, for the nice teaching collaboration and all your advice both on PhD matter and beyond. Thank you also, Damian, for the technical support, for your patience when the simulations were not properly running and in general for your magic touch with computers.

I would also like to thank all the members of the fantastic UP group. Thank you for all the science discussions, the code debugging, the practice talks or poster presentations, the coffee/lunch breaks, the laughs. You all participated to create a great work environment that was both stimulating and joyful. Thank you, Bianca, for the great support throughout the PhD and for organizing such fun UP events. A special thank you to Dominic, Anna, Deniz and Flora for making E.31.1 the best office of the E-floor. A special thank you also to Cara for helping me make sense of the BEC code, for bouncing ideas on figures or slides and for coming to the rescue when things were difficult with the kids. Thank you Elisa, Martin, Fabio, Luke for helping me navigate the PhD, for turning the conferences into big adventures and for the fun times together. Thank you Fabio for your frenchness.

Among UP members, I want specially to thank you, Jana, for a great collaboration that will hopefully continue in the future. It was also a great pleasure to collaborate with you, Yangyang. Thank you for all the discussions on shelf processes and beyond.

I also want to thank the whole team from C-CASCADES project, especially Pierre Regnier for leading the project, Sandra Arndt and Pierre Friedlingstein for the great science discussions and Emily Mainetti for the great organization and unfailing support. Thank you to all the other

PhD students from the network for all the discussions about freshwater processes and the challenges of field work. I also particularly enjoyed sharing with you the ups and downs of PhD life at our regular C-CASCADES meetings.

Special thank you to Xavier Giraud for trusting me and accepting to take me in a Master's of science program when all I had studied before was history and political science.

I want also to thank the girls from the CHN Lesbian Lunch for the most needed and appreciated distractions, and for creating a space where I always feel that I belong.

An immense thank you to you, Céline, my wife, my partner in crime. Thank you for always following me in all my crazy ideas, like doing a PhD. Thank you for your caring presence, for your advice, for your pep talks and for staying (mostly) awake when I practiced my talks. And of course, I cannot thank you enough for making us a family. The past few years have been a rollercoaster of emotions and I am very grateful I had your hand to hold.

On a cold snowy morning of January, 6 months after I started my PhD, one day before I presented my first progress to the C-CASCADES network, Garcin and Augustine were born. They kept me up at night and deprived me of sleep to levels I did not know were humanely possible. But first and foremost, they brought so much joy in my life. Even in the hardest part of the PhD, their laughs, their genuine enthusiasm, their love of music always kept me grounded, in sight of what is really important.

I want to thank my parents for their interest in my studies since I started kindergarten, for their constant and loving support and for not asking too often when I will be done with this thesis.

I do not thank Covid for all the hardships it brought to the last stretch of my PhD. But what this pandemic has painfully reminded me is the invaluable importance of people in both my professional and personal life. And that lesson will not be forgotten.

Curriculum Vitae

Domitille Louchard

Date of Birth	May 28th, 1985
Place of Birth	Saint-Pol-sur-Ternoise (62), France
Citizen of	France

Education

Since 2016	**PhD student**, Environmental Physics, ETH Zurich, Switzerland
2014 - 2016	**M.Sc. in Physical and Biogeochemical Oceanography**, Aix-Marseille University, France
2007 - 2008	**CAPES**, competitive qualification exam for secondary education teaching
2006 - 2007	**M.A in Political Science**, Lille II University, France, Major: European Affairs
2003 - 2006	**B.A in History**, Lille III University, France, Major: Economy and Public Affairs
2000 - 2003	**Baccalaureate**, Lycée Albert Châtelet, France

Teaching experience

2020 - 2021	M.Sc. thesis advisor of Janna Härri, ”The interannual variability in marine N2 fixation in the Western Tropical Atlantic”, ETH Zurich, Switzerland
2018 - 2019	Teaching assistant for *Biogeochemical Modelling of Sediments, Lakes and Oceans*, ETH Zurich, Switzerland
2016 - 2017	Teaching assistant for *Physics lab for environmental sciences students*, ETH Zurich, Switzerland
2016	B.Sc. thesis advisor of Joséphine Meyer, ”Investigating the anti-correlation between salinity and chlorophyll concentration in the Amazon River plume”, ETH Zurich, Switzerland
2010 - 2014	High School Teacher, European Section, Lycée Beaussier in La-Seyne, France, Geography and History classes, taught in French and English
2009 - 2010	Middle School Teacher, Collège Jean Jaurès in Castanet-Tolosan, France, Geography and History classes, taught in French
2010 (01-03)	High School Teacher, Cuyahoga Falls High School in Ohio, USA, World History, 9th and !0th grades, taught in English

Research experience

Since 2016	Research Assistant, Environmental Physics, ETH Zurich, Switzerland
2015 - 2016	Student Research Assistant, European Centre for Research and Education in Environmental Geosciences, Aix-en-Provence, France
2015	Research internship, Penn State University, USA

Workshops and further training

2019	18th Internationl Swiss Climate School *Carbon and Climate in the Paris World*, C2SM ETH Zurich, Switzerland
2018	Workshop *Entrepreneurial Skills*, Université Libre de Bruxelles and Deltares, Netherlands
2018	Workshop *Python Visualization*, C2SM ETH Zurich, Switzerland
2018	7th SOLAS summer school *Surface Ocean Lower Atmosphere Study*, Institut d’Etudes Scientifique de Cargèse, France
2017	Workshop *Diagenic models and Earth system models of intermediate complexity*, UNEXE Cornwall, UK
2017	Workshop *Regional to global modelling*, IPSL Paris, France
2016	Summer School *LOAC Carbon Cycle*, Peyresq, France
2015	4th Summer School on Sustainable Climate Risk Management, Penn State University, USA

Peer-reviewed publications

Louchard, D., Gruber, N., Münnich, M. (2021). The impact of the Amazon on the biological pump and the air-sea CO_2 balance of the Western Tropical Atlantic. Global Biogeochemical Cycles, 35, e2020GB006818.doi:doi:10.1029/2020GB006818

Bakker, A.M.R., **Louchard, D.**, Keller, K. (2017). Sources and implications of deep uncertainties surrounding sea-level projections. Climatic Change 140, 339–347. doi:doi:10.1007/s10584-016-1864-1

Outreach publications

Louchard, D. (2018) Le fleuve Amazone, maillon essentiel du cycle mondial du carbone. Theconversation.com, link

Conference contributions

Oral presentations

2020	**Louchard, D.**, Gruber, N., Münnich, M. The imprint of the Amazon River on the air-sea CO2 flux in the Tropical North Atlantic. Ocean Science Meeting, San Diego, CA, USA
2019	**Louchard, D.**, Gruber, N., Münnich, M. The Amazon River imprint on the phytoplankton community and carbon export. IMBeR Future Oceans Conference, Brest, France
2018	**Louchard, D.**, Gruber, N., Münnich, M. The Amazon River imprint on the marine nutrient and carbon cycling. SOLAS Summer School, Cargèse, France
2018	**Louchard, D.**, Gruber, N., Münnich, M. The Amazon River imprint on the nutrients cycling and carbon export in the western tropical Atlantic Ocean. Ocean Science Meeting, Portland, OR, USA

Poster presentations

2021	**Louchard, D.**, Gruber, N., Münnich, M. The imprint of the Amazon River on the marine carbon cycling. 13th IBP PhD Congress, Zürich, Switzerland
2019	**Louchard, D.**, Gruber, N., Münnich, M. The Amazon River imprint on the marine biogeochemistry. 19th Swiss Global Change Day, Bern, Switzerland
2018	**Louchard, D.**, Gruber, N., Münnich, M. The imprint of the Amazon River on the marine carbon cycling. 13th IBP PhD Congress, Zürich, Switzerland
2018	**Louchard, D.**, Gruber, N., Münnich, M. The Amazon River imprint on the marine biogeochemistry. 19th Swiss Global Change Day, Bern, Switzerland
2017	**Louchard, D.**, Gruber, N., Münnich, M. The impact of the Amazon River plume on the carbon cycle in the Tropical Atlantic Ocean. 10th International Carbon Dioxide Conference, Interlakenm Switzerland
2017	**Louchard, D.**, Gruber, N., Münnich, M. The imprint of the Amazon River on the marine carbon cycling. 13th IBP PhD Congress, Zürich, Switzerland
2017	**Louchard, D.**, Gruber, N., Münnich, M. The Amazon River imprint on the marine biogeochemistry. 18th Swiss Global Change Day, Bern, Switzerland
2017	**Louchard, D.** and Gruber, N. Modeling the complex interplay of physical and biogeochemical processes in the Amazon River plume. C-CASCADES Mini Conference 2 – From land to the ocean: processes and budgets, Zürich, Switzerland

Seminar talks and other presentations

2019	**Louchard, D.** When the Amazon River meets the Atlantic: cascading effects on the marine biogeochemistry Seminar, Eawag Kastanienbaum, Switzerland
2016	**Louchard, D.**, Marescaux A., Terhaar J., Canning A., Horgby A., Uhlback J., Nydahl A., Maier M.S., Androulakakis A., Puglini M., Hastie A., Pika P., Nakhavali A., Bowring S., Lacroix F. Le Changement climatique et le cycle du carbone. Outreach, La-Colle-Saint-Michel, France

Awards

2019	Best oral presentation, IMBER Conference, Brest, France
2018	Best oral presentation, SOLAS Summer School, Cargèse, France